Computational Modelling and Electromagnetic-CFD Coupling inCasting Processes.

Luca Marioni

THÈSE DE DOCTORAT

de l'Université de recherche Paris Sciences et Lettres
PSL Research University

Préparée à MINES ParisTech

Computational Modelling and Electromagnetic-CFD Coupling in Casting Processes.

Ecole doctorale n°364: Sciences Fondamentales et Appliquées

Spécialité: Mécanique numérique et Matériaux

COMPOSITION DU JURY :

Yves FAUTRELLE
Institut Polytechnique de Grenoble (INP), France.
Président

Egbert BAAKE
Leibniz University Hannover, Germany.
Rapporteur

Ramon CODINA
Universitat Politècnica de Catalunya, Spain.
Rapporteur

Pascal GARDIN
Arcelormittal s.a., France.
Examinateur

Pascal RIVAT
Ferropem s.a., France.
Examinateur

Soutenue par **Luca MARIONI**
le **17 Novembre 2017**

Dirigée par **Francois BAY**
et **Elie HACHEM**

MINES ParisTech | PSL RESEARCH UNIVERSITY PARIS

Contents

List of Figures

List of Tables

Chapter 1

Introduction

Contents

1.1 Résumé du chapitre en français

Dans ce chapitre, les procédés traités dans cette thèse, et notamment la coulée continue, sont exposés. Une description extensive du développement historique de ce procédé est proposée et est suivie d'un résumé des différents problèmes rencontrés. La deuxième partie est dédiée à la description des technologies électromagnétiques utilisées pour faire face à ces problèmes. On décrit notamment les systèmes de freinage magnétique et de brassage électromagnétique. Les physiques à la base de ces systèmes étant différentes, leur compréhension et leur comparaison sont importantes pour comprendre les interactions entre l'écoulement de métal liquide et différents types de champs électromagnétiques. Cela amène à des choix concernant la stratégie de couplage multiphysique. Dans la dernière partie de ce chapitre, la structure de ce

manuscrit est décrite ainsi que les principaux résultats en matière de diffusion dans la littérature et la communauté scientifique.

1.2 Continuous casting

Continuous casting is a process whereby liquid metal gets solidified on a continuous basis. It is in contrast with the "ingot casting", in which large volumes of metal are cast in separate ingots. Continuous casting allowed plants to increase the production rate which can reach 60 tons per hour in the case of twin-belt continuous casting. This process is relatively new: the first patent of a continuous caster was made in 1843 by J. Laing, but it started to be used for mass production only in the 50s of the following century. Nowadays the continuous casting ratio for the world steel industry is around 96 % of crude steel output which was a mere 4 % in 1970.

1.2.1 Historical evolution of continuous casters

After the first patent in 1843 by J. Laing regarding an horizontal caster, the idea of continuous production of steel was further developed by H. Bessemer. In 1857 he patented (but never realized) the so called "twin roll caster", as depicted in figure 1.1(a). In the following decades further apparatuses were conceived to enhance the continuous casters, such as the ladle (by David D. Lewis in 1885) and an hydraulic ram to push the ingot upward (by Bessemer in 1864). The first semi-commercial caster was patented and used by Benjamin Atha in 1886, but never reached mass production. Mass production were reached only in the 1930s, when Siegfried Junghan designed a caster used by Wieland-Werke for the casting of brass (see figure 1.1(c)). Junghan implemented a vibrating mould (previously patented by Cornelius W. van Ranstin 1921) in order to prevent the solid shell to stick to the mould. In general, Junghan's machine is the first truly continuous process, which enabled the producers to output high quality products with standard processes and low complexity control. However Junghan's method did not solve all the problems of permanent mould casting, mainly due to the heat extraction being predominant through the walls of the mould. As a result, the sump of the billet was deep, the solidified shell was subject to high thermal gradients, and the air gap formation required the maintenance of low casting speeds or, in other words longer solidification times. Larger billets (300 mm – 500 mm in diameter) were characterized with inhomogeneous structure and chemical composition (macro-segregation). The long moulds which were necessary for proper cooling called for very fine finish of the internal surface. In order to eliminate these shortcomings, it was necessary to develop a technology, where the heat would be extracted predominantly through the solid part of the casting. For these

reasons, the Junghan machine was overcome by the "direct chili" (DC) technology, shown in figure 1.1(b). DC casters were firstly used by Rossi in 1937 for non-ferrous materials casting. Thanks to the high product quality and low operational costs, this concept was rapidly extended to steelmaking industries in the late 40s.

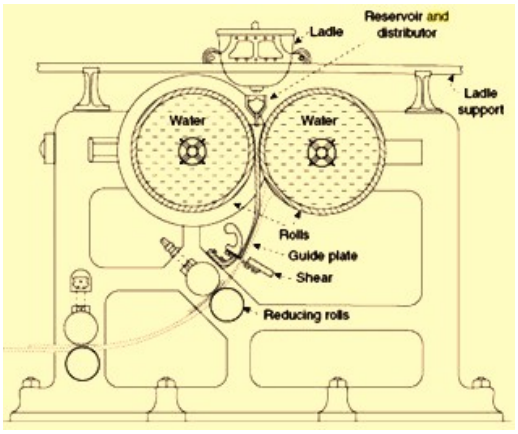

(a) Continuous casting process proposed by Henry Bessemer.

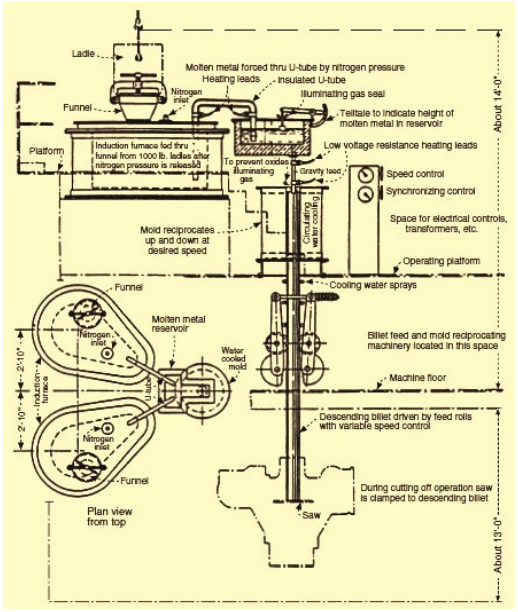

(b) Rossi caster with oscillating mould.

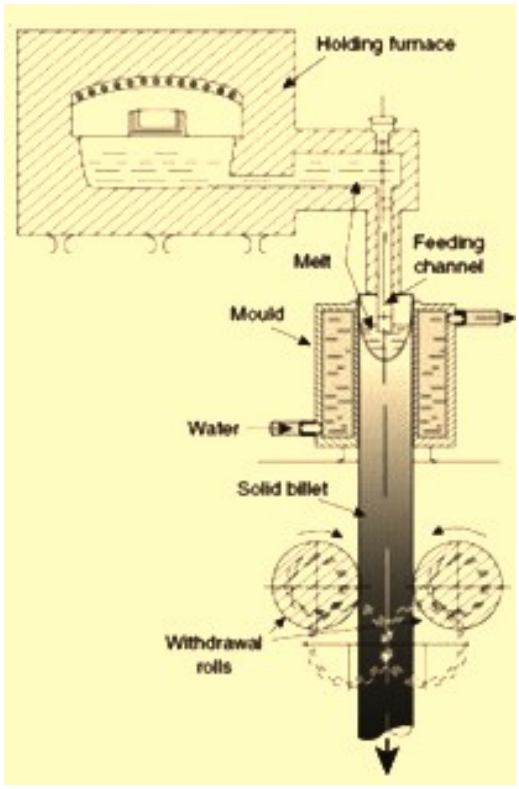

(c) Continuous casting process proposed by Junghan.

Figure 1.1: Historical casting technologies (courtesy of www.ispatguru.com).

1.2.2 Present continuous casting configuration

The present most common configuration of continuous casting is depicted in figure 1.2.2. The process is divided in the following parts:

- **Ladle**. The metal melted in the furnaces gets tapped into the ladles. At this stage, the melt undergoes refinement treatments to increase its quality such as alloying and degassing. Hence, the ladle is moved upon the caster and the melt is tapped into the tundish, feeding the continuous process. Normally two different ladles are installed upon the caster: one in position "on" (pouring metal into the tundish), and the other in position "off", ready to replace the first one and guarantee a continuous feeding of molten metal in the process.

- **Tundish**. Is a melt bath which links the non-steady flow coming from the ladles and the steady flow required by the caster. The main purpose of the tundish is to output a regular, steady and high quality flow to the caster.

- **Mould**. Metal is drained from the tundish through a submerged entry nozzle (SEN) into the top of an open-base copper mould. The mould size can range from 50 *cm* to 250 *cm* and it is water-cooled in order to solidify the hot metal directly in contact with it. Some slag is normally added on the metal meniscus and the mould is vibrated to prevent the solidified shell from sticking to the mould and decrease the friction stresses. The process within the mould is commonly named "*primary cooling*" because it leads to the first solidification.

- **Strand**. The output of the mould is called strand. It is a liquid bulk flow constrained within a solid thin shell. This shell is not think enough to bear the fluid inside, so the strand is supported by closely spaced water-cooled rollers. This rollers are used not only to support the strand, but also to mechanically treat it and to bear it, in the case of curved continuous casting. In this part of the process, the a spray cooling system is used to boost the solidification process until the bulk of the strand is solid.

- **Further treatments**. Once solidified, the strand passes through different processes (e.g. hot rolling, hardening, induction re-heating) to improve its mechanical properties.

- **Final cut**. Once the final shape and mechanical structure is achieved, the final slab is cut by a torch and moved away from the caster.

Continuous casting may be defined by their structure (e.g. horizontal, vertical or curved casters) or by the type of semi-finished produced product. Thus, continuous caster may be divided in:

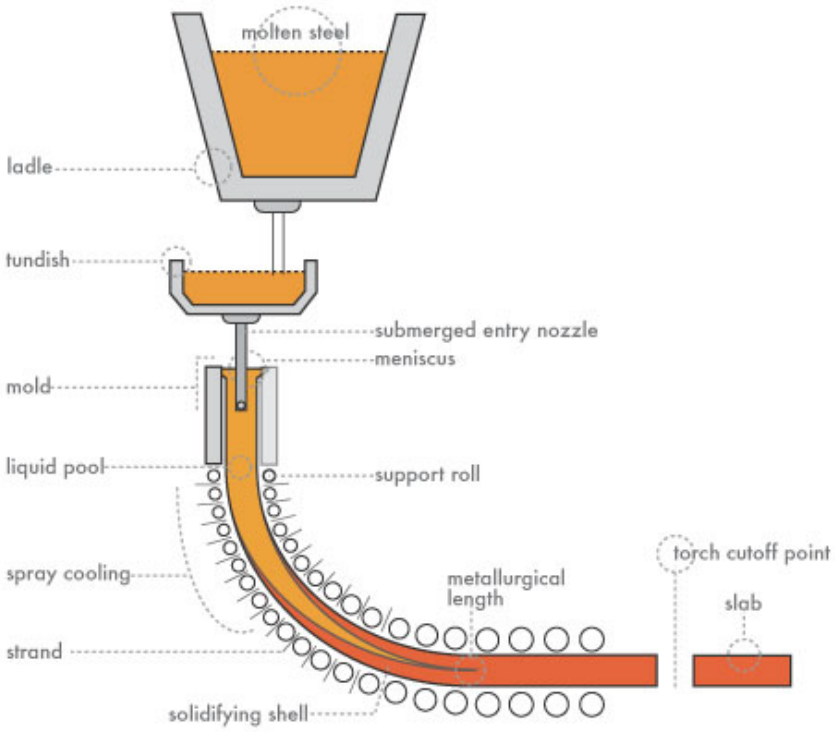

Figure 1.2: Continuous casting machine

- **Slab casters** produce slabs in the range 100–3250 *mm* wide by 40–250 *mm* thick and up to 12 *m* long with conventional casting speeds of up to 1.4 *m/minute*
- **Billet casters** cast smaller section sizes, such as below 200×200 *mm*, with lengths up to 12 *m* long. Cast speeds can reach up to 6 *m/minute* [1].
- **Bloom casters** cast sections above 200×200 *mm*. The bloom length can vary from 4 to 10 *m*.

1.3 Problems

The major technical issues related to steel production may be divided in two groups: problems related to the process itself and problems related to the quality of the final product.
Breakouts is the main process risk for continuous casting; it occurs when the solid shell is not thick enough below the bottom end of the mould and so the liquid metal leaks from the strand. This leads to safety hazards for operators and to consistent

economical damage since the process must be shut-down and restarted, losing its steady nature. Breakdowns are usually caused by problems in the solidification of the strand shell; the shell could be too thin because the casting speed is too high [2] (so the time reserved to solidification in the primary-cooling phase is too short). A second cause is the presence thermo-mechanical conditions of the flow (e.g. hot flow impacting the mould surface or high turbulence flow) which decrease the thickness or the mechanical quality of the solid shell. Another reason for poor mechanical quality of the shell is the entrapment of slag and scum in the solidified layer: these elements weaken the structure of the shell, making it not able to bear the pressure of the internal liquid metal. Another very common cause of breakouts is the stick of metal on the mould's surface; this is caused by a lack of lubrification or an erroneous vibration rate of the mould.
A second serious issue related to the process facilities is the fluctuation of the free surface of molten metal. When the free surface flow is too vigorous, some droplets risk to be spouted outside the mould (or the ingot for ingot casting) leading to safety hazards. In addition, the free surface fluctuation leads to cyclical thermal stresses in the mould, which could fail by fatigue and decrease its life expectations.
While achieving a reliable and economical production process is imperative for steelmaking industry, achieving a high quality of the final product is even more important. Especially in Europe, where the production costs are high, excellent mechanical properties are required in the final product. Poor mechanical properties may be due to the non homogeneity of the alloy because of macrosegregation. Macrosegregation is the phenomenon (see figure 1.3) in which the components of the alloy tend to separate each other during the solidification process, leading to non-uniform and non-optimal steel composition. Segregation may occur also at the microscopic scale (see figure 1.4), which leads to poor mechanical properties of the product. The microstructure (see figure 1.5(a)) is highly dependent on the solidification conditions, thus the fluid and heat flow within the process should be precisely analysed and understood in the design phase. An non-optimal fluid flow may also conduce Argon bubbles and slag impurities from the upper part of the mould to the lower solidification region, contaminating the product and leading to inclusions (see figure 1.5(b)); inclusions, together with the other aforementioned defects, lead to void merging, microcracking, macrocracking, pin holes and blow holes (see figure 1.6), which decrease the quality of the product in term to static and fatigue failures.

The causes of these problems in the product or in the process are multiple and, sometimes, not known. The crystallization of the solid part depends on the pressure, the velocity, the temperature and the local composition of the melt [8, 9, 10, 11] . Macrosegregation is formed due to the natural tendency of the different parts of the alloy to separate, due to buoyancy forces, natural convection and microscopic phenomena [12, 13, 14, 15] . Inclusions are due to the entrainment of slag or argon

bubbles in the downstream process. Bubbles behaviour has been widely studied [16, 17, 18, 19] and it is based on the interaction with the main liquid stream. Slag entrainment's causes have been studied and divided in 9 main categories [20, 21]:

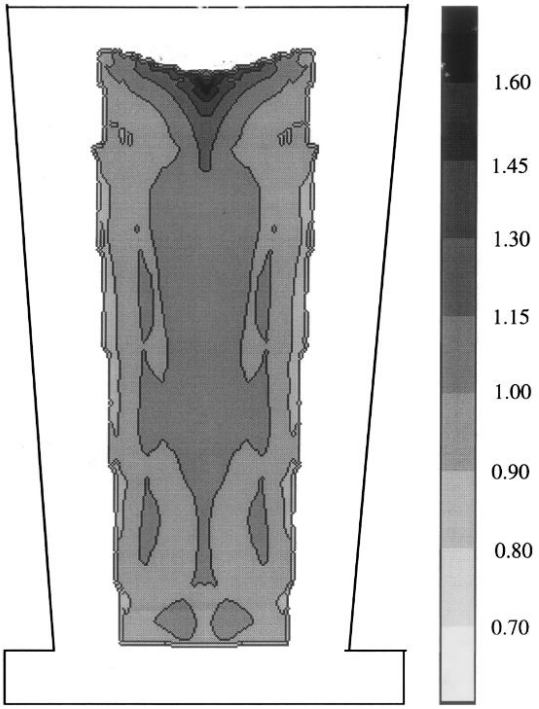

(a) Numerical simulation of macrosegregation pattern [3].

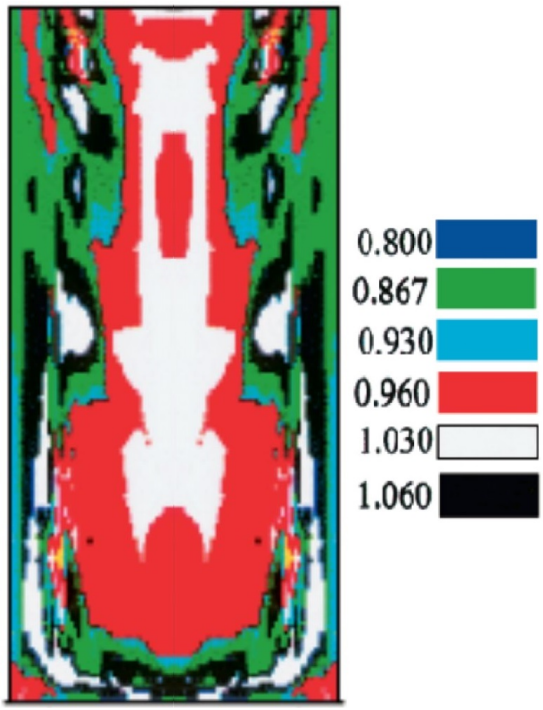

(b) Experimental analysis of macrosegregation pattern [4].

Figure 1.3: Carbon concentration in ingot casting.

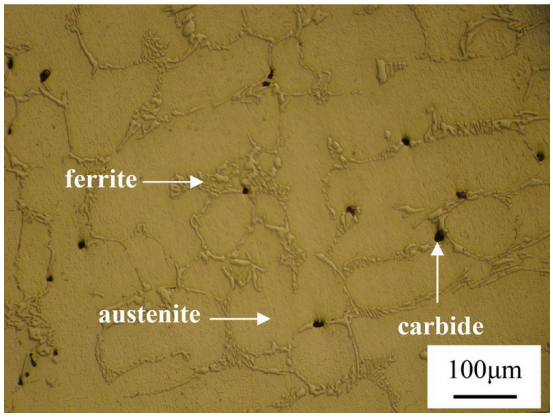

Figure 1.4: Steel microsegregation [5].

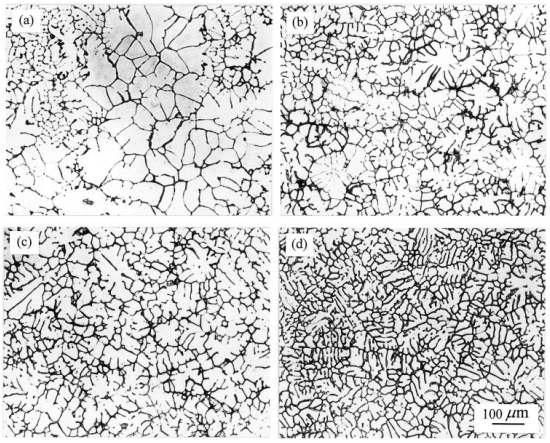

(a) Steel microstructure at different stirring rates [6].

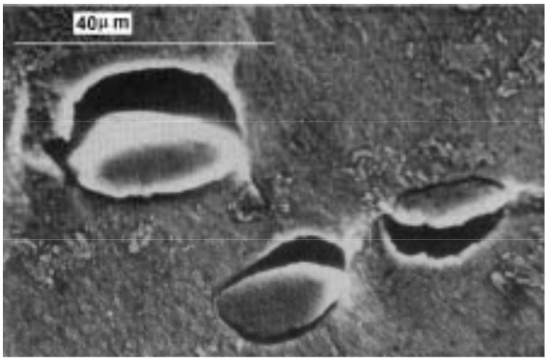

(b) Non-metallic inclusions in continuously cast steel [7].

Figure 1.5: Microscopic structure and inclusions in steel.

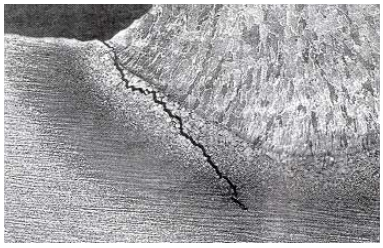

(a) Microcrack in a steel bloom.

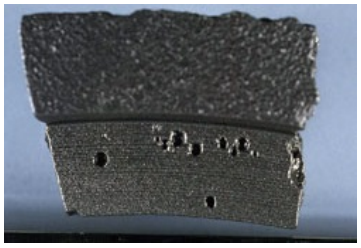

(b) Pin holes in a final product.

(c) Blow holes in a final product.

Figure 1.6: Examples of defects in the casting product.

- top surface fluctuations;
- meniscus freezing and hook formation;
- vortex formation ;
- shear layer instability;
- upward flow impinging upon the top surface;
- argon bubbles interaction;
- slag crawling;
- top surface standing wave instability;

- top surface balding.

Non-metallic inclusion may also be due to the upper part of the process, such as Tundish flow [22].
In this work we do not aim at going in depth about metallurgical considerations, for which we recall the reader to the literature references. We only want to highlight the common sources of defects, thus the variables which should be better controlled to achieve better quality of the product/process. These variables are the temperature and the velocity fields, which are mutually connected by natural convection. Thus, by controlling the velocity in the melt, we should be able to control the process and achieve the desired quality standards.

1.4 Electromagnetic applications: braking and stirring

Several techniques have been proposed to improve the continuous casting process such as mechanical stirrers [23], electrodes stirring [24], ultrasound vibrations [25, 26], electromagnetic stirring and electromagnetic braking. All these propositions should follow some criteria to be applied in an industrial framework.
First of all, they must be robust. The environment in the continuous caster is highly aggressive and extreme. Mechanical stirrers get quickly damaged by the melt, hence high maintenance costs (and short life expectancy) occur. On the other hand, also high technology machines (i.e. Industry 4.0) which use sensors and electronic chips are not able to cope with the high temperature of the melt.
Second, they should not contaminate the melt. For this reason, any application which implies a direct contact of an external apparatus (e.g. mechanical stirrers or electrode stirring) with the melt is inadvisable. This contact is very aggressive for the machine itself (which should be often changed or maintained) and leads to the input of external materials into the melt, decreasing the quality of the final product.
Third, they should be flexible. As it has been explained in section 1.3, many different phenomena may cause problems and defects. The ideal application should be able to deal with different problems and the different situations which could occur in the melt.
In this section we will introduce two common electro-technologies applied to continuous casting: electromagnetic braking (EMB or EMBr) and electromagnetic stirring (EMS).

1.4.1 Electromagnetic Braking - EMB

Electromagnetic braking consists into the superimposition of a constant magnetic field to the in-mould flow. This magnetic field is normally in the order of $0.5 - 2\,T$ and it is produced by permanent magnets or DC current coils. The basic idea is

that any conductive fluid flowing inside a magnetic field is subjected to a Lorentz force opposite to the velocity, according to the law

$$\underline{F} = \underline{j} \times \underline{B} = (-\nabla\phi + \underline{u} \times \underline{B}) \tag{1.1}$$

being $\underline{F}$ the Lorentz force, $\underline{B}$ the induced magnetic field, ϕ the electric potential and $\underline{u}$ the melt velocity (see chapter 2 for the complete description of the model). Thus, the Lorentz force works in the direction opposite to the velocity, braking the flow; but the interaction is not limited to this phenomenon, since the velocity has a backward effect on the magnetic field, by the development of induced eddy currents. Braking applications slow the flow down and decrease the turbulence in the mould. As a result, the fluctuations of the free surface decrease [27, 28, 29] which decreases the thermal fatigue in the mould resulting in a longer life of the mould itself. In addition, a slower and less turbulent flow decreases the possibilities of Argon bubbles inclusions in the lower part of the mould [30, 31], limiting the bubbles recirculation pattern to the upper part of the melt. The design of the braking system is complex because of the interaction between the turbulent flow and the external magnetic field. The motion of the liquid metal inside the external magnetic fields creates induced eddy currents which change the magnetic field by the creation of a second inducted magnetic field. This mechanics is highly dependent on the velocity inside the mould, which is difficult to be obtained. Free surface velocity can be measure by nail-boards [32, 33]; as depicted in figure 1.7, this method consists in immersing a nailed board into the liquid metal. Once removed the board, a solidified knob forms on the nail and the velocity can be computed from the height of the knob. This method lacks precision, safety and gives a clue only at the surface velocity. In addition, the contact between the nails and the melt leads to contamination of the pool and short life of the measuring system. Other methods have been proposed to overcome these limitations, such as Submeniscus Velocity Control (SVC) [33], Ultrasound Doppler Velocimeters (UDV) [34, 35] and Lorentz force velocimeters (LFV) [36, 37, 38], but all give only a partial understanding of the in-mould flow. Also large scale experiments based on a "mechanical" implementation of the electromagnetic breaker through water models [39] and polymeric grids in the flow have been used [40], but they can be used only from a qualitative point of view because of the different physical background. For these reasons, numerical simulation is the most common tool to understand the behaviour of in-mould flow [41, 42] and its interaction with the braking field [43, 44], despite the large amount of computational effort required fro this kind of computations.

Over the years, many different solutions and geometries have been proposed to optimize braking system with respect to different types of processes. In figure 1.9 different types of braking systems are shown. Local EMB are the most common

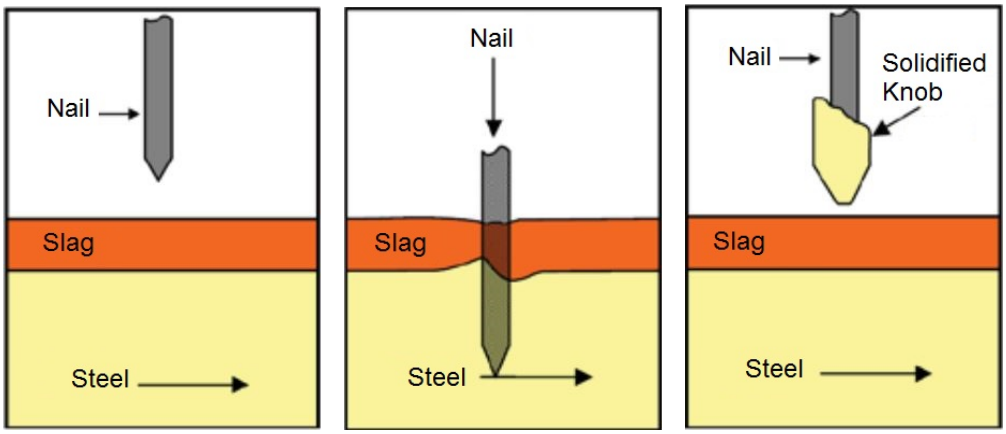

(a) Insert the nail into the liquid pool.

(b) Hold the nail in steel for a short time.

(c) Remove the nail and measure the solidified knob.

Figure 1.7: Procedure for the nail board test [33].

applications, but they require a precise design to be effective; since the flow is not just braked, but also deviated by the EMB, a local magnetic field risks to destabilize the flow and worsen the process. Single (figure 1.8(b)) and double (figure 1.8(c)) ruler EMB systems are more stable and are used to provide a strong braking in sensitive regions like the narrow face of the mould or the free surface [45, 43, 46]. In the last years, an extensive optimization work has been done [47, 48, 49] to optimize the position, size, geometry and numer of brakers, leading to the "Multi-Mode® EMB" developed by Danieli. Despite these advancements, EMB systems still have limitations. The most important limitation is the lack of flexibility: EMB systems can only brake the flow and they work for a certain flow configuration; as the flow deviates from the standard configuration, the braking effect could have no more impact or, worse, have a negative effect on the flow.

1.4.2 Electromagnetic Stirring - EMS

Electromagnetic stirring (also known as electromagnetic steering) is another widely used technique in material forming industry. It consists in the use of a time-varying electromagnetic field (EMF) produced by an AC-fed inductor; the variation in time of the EMF produces some eddy currents in the melt, thus Lorentz forces which could drive the flow, according to the law:

$$\underline{F} = \underline{j} \times \underline{B} = \left(-\nabla\phi - \frac{\partial \underline{A}}{\partial t} + \underline{u} \times \underline{B} \right), \tag{1.2}$$

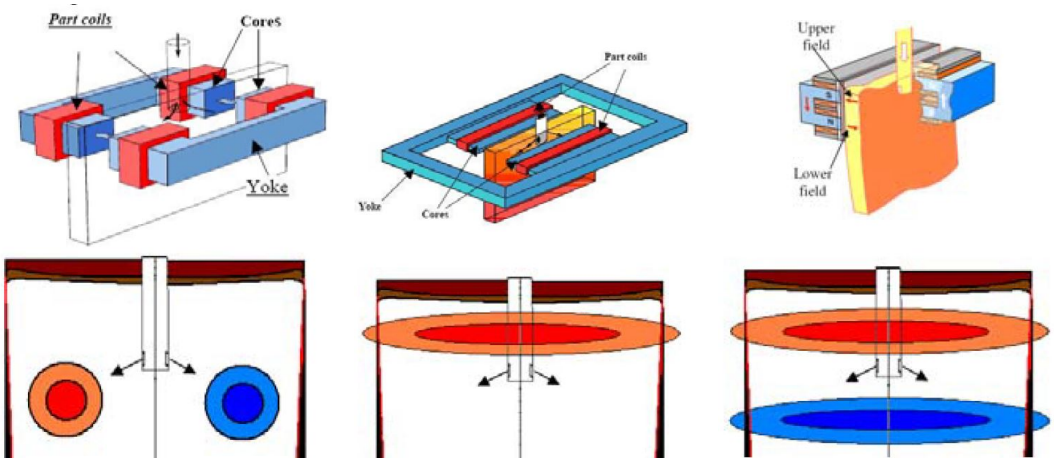

(a) Local EMB (b) Ruler EMB (c) Double ruler EMB

Figure 1.8: Different types of braking systems showng the hardware configuration (top) and field shape(below) [50].

being ϕ and $\underline{A}$ the electric and the magnetic potentials respectively (see chapter 3 for the complete description of the model). In EMS, the magnetic field is low, so the eddy current produced by the motion of the conductive fluid (i.e. the "braking term") is negligible, while an inductive part independent from the fluid motion (i.e. the "stirring term") is dominant. Hence, the main difference from the EMB is that EMS applications are mainly independent from the velocity of the liquid, while EMB is a reaction to the flow. Depending of the arrangement, the geometry and the electrical source of the system, different types of EMF and stirring can be obtained; the single coil, AC fed stirrer (figure 1.9(a)) is the most common application in ingot casting [51]. AC stirring induces a double-toroidal roll in the melt, which leads to a more uniform temperature field in the ingot ant to a finer grain microstructure. In the continuous casting frame, travelling magnetic fields (TMF) [52, 53, 54, 55], rotating magnetic fields (RMF) [56] and combinations of the both [57] are the most common types of EMF used to stir the flow. Both systems follow the principles of electrical motors and need at least 3 different phases; these systems are more complex than the AC stirrers because multiple phases and a more complex arrangement of the coils (figures 1.9(c) and 1.9(b)) are required.

The large amount of different stirring configurations give to EMS systems higher flexibility than EMB applications; EMS can be designed to increase, decrease or even invert the flow velocity and the driving force can be applied in any direction and may be used in complementation of EMB systems [60]. In addition, when compared to EMB, EMS has more design parameters (e.g. the induction frequency [61, 62])

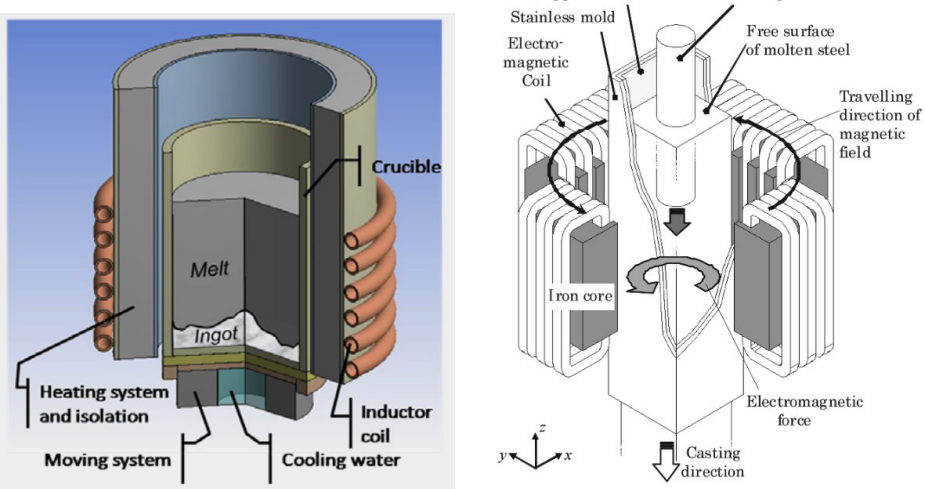

(a) AC Stirrer [51]

(b) RMF Stirrer [58]

(c) TMF Stirrer (or *Linear Stirrer*) [59]

Figure 1.9: Different types of electromagnetic stirrers.

which enables a optimal adaptation to the considered problem. These characteristics make EMS system very common in a large variety of material forming processes, such as ingot casting, continuous casting, and cold crucible casting. Also the material processed can vary from silicon [63], Aluminium [64, 65, 66], Glass [67], and Steel [68, 69, 70].
The flexibility typical of EMS enables to tackle several problems, like macrosegregation [71, 72], poor quality of the solid shell's microstructure [73, 74, 75, 76], and free surface behaviour [59, 77].
EMS systems in continuous casting process can be divided in different categories with respect to their position. The most common positions are:

- In-Mould Electromagnetic stirrers (M-EMS): positioned at the mould level,

they control the in-mould flow and, consequently, the temperature distribution, inclusions patterns, free surface variations and turbulence level.

- Strand Electromagnetic Stirrers (S-EMS): positioned at different levels of the strand. In this region, the solid shell and the mushy zone are thicker, hence the EMF is partially shielded. S-EMS produce lower level of stirring [78], focused in the central part of the strand, which decreases central segregation.

- Final Electromagnetic Stirrers (F-EMS): positioned at the end of the caster, where the piece is almost fully solidified.

Nevertheless, EMS is used at every other level of the continuous casting machine: in the Tundish it is used to prevent inclusions and melt stagnation [79, 80], while in the ladles is used to keep the temperature uniform and preventing solidification [81]. In table 1.1 the problems tackled by different types of stirrers are summarized.

Table 1.1: Benefits obtained using one or more EMS in combination. (Source: www.ergolines.it)

EMS type & combination	M-EMS	M+F-EMS	M+S+F-EMS	M+S-EMS	S-EMS	S+F-EMS
Pinhole & blowhole	+++	+++	+++	+++	/	/
Surface & subsurface cracks	+++	+++	+++	+++	/	/
Break-out reduction	+++	+++	+++	+++	+*	+*
Solidification structure & internal crack	++	++	+++	+++	++	++
Centerline segregation, center porosity	++	+++	+++	++	++	++
V segregation	/	+++	++	+	+**	++

* With S-EMS in high position. ** With S-EMS in low position.

1.5 Structure and Objectives of this work

This work aims at developing an effective and efficient numerical framework for the simulation of EMS. This means having effective models for each involved physic (e.g. fluid mechanics, electromagnetism), but also developing an efficient coupling strategy. This coupling strategy must be inexpensive in terms of computational time and computer memory, precise enough for industrial use and robust/flexible enough to be applied to different industrial configurations. The specific application we want to focus on is M-EMS, but similar applications such as AC ingot stirring have been also considered. The project is funded by Transvalor S.A. and all the developments have been implemented in THERCAST®, which is a commercial FE software for the simulation of casting processes. This work has supported the release of a beta-version of the software which enables the users to perform fully coupled mechanical-electromagnetic simulations of stirring applications.
Since we want to develop a tool able to model different stirring applications or, at least, to facilitate the implementation of further models, this work has been focused on the modelling technique itself, trying to be as independent as possible from the industrial process. Since the application to be modelled is highly multiphysical, we first analyze the model of each physics separately. In chapters 2 and 3 we will discuss the simulation techniques for the electromagnetic and the fluid mechanics modelling respectively. In chapter 4, the numerical coupling strategy between the different physics have been discussed. Finally, in chapter 5, the validation of the numerical scheme and a first application to industrial processes have been presented.

1.6 Contributions of this work

As stated before, this work deals with several research aspects, thus fits in the interests area of different scientific communities. In order to be consistent and up-to-dated to the communities' work on each studied topic, the results obtained during this thesis have been presented to 5 international conferences:

- L. Marioni, J. Alves, F. Bay, and E. Hachem. Effect of M-EMS on in-mould transient flow during continuous casting. In *International Conference on Heating by Electromagnetic sources*, pages 3-10, 2016.

- L. Marioni, F. Bay, E. Hachem. Electromagnetc-Multiphase Transient Flow Simulation via VMS approach. Application to Continuous Casting Process. In *WCCM: 12th World Congress on Computational Mechanics*, 2016.

- L. Marioni, F. Bay, and E. Hachem. Lid-driven cavity highly turbulent flow subjected to high magentic field: Determination of critical time-step for ex-

plicit MHD schemes. In *10th PAMIR International Conference - Fundamental and Applied MHD*, 2016.

- L. Marioni, E. Hachem, and F. Bay. Numerical simulation of electromagnetic stirring. In *XVIII UIE-Congress - Electrotechnologies for material forming*, 2017.

- L. Marioni, F. Bay, E. Hachem. Numerical simulation of electromagnetic stirring in steelmaking industry. In *International CAE conference and exhibition*, 2017.

The final results contained in this thesis have also been published in 5 international peer-reviewed journals:

- L. Marioni, J. Alves, F. Bay, and E. Hachem. Effect of M-EMS on in-mould transient flow during continuous casting. *International Journal of Applied Electromagnetics and Mechanics*, 2016.

- L. Marioni, F. Bay, and E. Hachem. *Numerical stability analysis and flow simulation of lid-driven cavity subjected to high magnetic field.* Physics of Fluids, 28(5):057102, 2016.

- L. Marioni, J. R. Alves Z., E. Hachem, and F. Bay. A new approach to solve complex valued systems arising from the solution of Maxwell equations in the frequency domain through real-equivalent formulations. *Numerical Linear Algebra with Applications*, 24(2):e2079, 2017.

- L. Marioni, M. Khalloufi, F. Bay, and E. Hachem. Two-fluid flow under the constraint of external magentic field: revisiting the dam-break benchmark. *International Journal of Numerical Methods for Heat and Fluid Flow*, 27(11), 2017.

- L. Marioni, F. Bay, E. Hachem. Numerical coupling strategy for the simulation of electromagnetic stirring. *Magnetohydrodynamics*, 53(3), 547-557, 2017.

In addition to the aforementioned scientific contributions, this work led to specific industrial results. The simulation algorithm has been implemented in THERCAST®, produced by Transvalor s.a.. The developments have been presented to 2 international user meeting:

- F. Bay and L. Marioni. Modelling of Magnetic Coupling in industrial processes. In *THERCAST®international user meeting*, 2015.

- L. Marioni. Electromagnetic coupled simulations in continuous casting process. In *THERCAST®international user meeting*, 2016.

The EMS-simulation module ha been included in the α-release of THERCAST®, which has been used for the external consultancy problems shown in chapter 5. Thanks to the encouraging results obtained in this phase, the module is now ready for the β-release.

Chapter 2

Electromagnetic problem

Contents

2.1 Résumé du chapitre en français

Dans ce chapitre, une présentation du modèle électromagnétique et des outils utilisés pour la simulation numérique du problème électromagnétique sont proposés. Les équations gouvernant le problème électromagnétique sont initialement décrites et commentées, notamment par rapport à des phénomènes spécifiques tel que l'effet de peau et l'interaction avec des milieux en mouvement. En outre, le système de Maxwell a été réécrit selon la formulation potentielle (A, ϕ), en accord avec l'état de l'art concernant la simulation des phénomènes d'induction. La formulation du problème a été complétée par une description extensive des différents comportements

magnétiques de matériaux ainsi que sur la comparaison de différentes lois de comportement pour la simulation des matériaux ferromagnétiques et paramagnétiques. La deuxième partie du chapitre traite de la discrétisation spatiale du problème analytique susmentionné. L'approche numérique a été basée sur la méthode des éléments finis; en particulier les éléments finis d'arêtes (de type Nédelec) ont été utilisés. La dernière partie du chapitre décrit la stratégie de résolution en temps. En particulier, on présente deux alternatives : la résolution du problème dans le domaine temporel, ou la résolution dans le domaine des fréquences (harmonique). Cette dernière alternative a été notamment développée dans ce chapitre. Le système linéaire obtenu à partir de cette approche est un système impliquant des nombres complexes. Afin de remédier aux problèmes d'efficacité lors de la résolution de ce système linéaire, notamment par rapport à la parallélisation du code et le conditionnement de l'opérateur linéaire, on a choisi de résoudre le problème avec une formulation réelle équivalente. La dernière partie du chapitre est dédiée à la formulation et à la validation de cette nouvelle méthode, notamment le développement d'un système de préconditionnement spécifique pour cette application physique. Les validations ont été effectuées en termes de précision et de ressources de calcul requises.

2.2 Mathematical model

2.2.1 Maxwell Equations

The basic laws of electromagnetism can be summarized in the following system:

$$\begin{cases} Faraday's\ Induction\ Law: & \oint_C \underline{E} \cdot d\underline{l} = -\dfrac{d}{dt}\displaystyle\int_{\partial\Omega} \underline{B} \cdot \hat{n} dS \\ Maxwell - Ampere's\ Law: & \oint_C \underline{H} \cdot d\underline{l} = -\dfrac{d}{dt}\displaystyle\int_{\partial\Omega} \underline{D} \cdot \hat{n} dS \\ Gauss'\ Law: & \displaystyle\oint_{\partial\Omega} \underline{D} \cdot \hat{n} = \int_{\Omega} \rho^e d\Omega \\ Gauss'\ Law\ for\ the\ magnetic\ field: & \displaystyle\oint_{\partial\Omega} \underline{B} \cdot \hat{n} = 0, \end{cases} \tag{2.1}$$

with:

- $\underline{E}$ being the electric field,
- $\underline{H}$ being the magnetic field,
- $\underline{D}$ being the electric flux density,

- $\underline{B}$ being the magnetic flux density,
- ρ^e being the charge density.

System (2.1) is defined on a finite domain Ω whose boundary is $\partial\Omega$. The strong formulation is expressed by the following system:

$$\begin{cases} \nabla \times \underline{E} = -\dfrac{\partial \underline{B}}{\partial t} \\ \nabla \times \underline{H} = \dfrac{\partial \underline{D}}{\partial t} + \underline{j} \\ \nabla \cdot \underline{D} = \rho^e \\ \nabla \cdot \underline{B} = 0. \end{cases} \tag{2.2}$$

This development, which is widely used in articles and textbooks, relies on the specific hypothesis that the domain of integration is independent of time, namely, it does not move. This assumption makes system (2.2) not valid for moving domains, as Einstein remarked in 1905 [82]: "*It is known that Maxwell's electrodynamics - as usually understood at the present time - when applied to moving bodies, leads to asymmetries which do not appear to be inherent with the phenomena*". This limit of the classic Maxwell theory is also proven from the fact that the force of a moving particle can't be derived directly from the field equations, but should be postulated a-posteriori as:

$$\underline{F} = q\left(\underline{E} + \underline{u} \times \underline{B}\right), \tag{2.3}$$

being q the charge of the particle and $\underline{u}$ the velocity of the material particle. Starting from this limitation of the classic Maxwell's formalism, a different approach has been proposed [83, 84] to derive the differential model for electrodynamics of moving objects. While the classic development for non-moving objects uses a spatial derivative of the Gauss' Law, the proposed development adopts the use of a material derivative to guarantee the time-invariance of the derivative defined as:

$$\frac{d}{dt}\int_{\partial\Omega} \underline{B} \cdot \hat{n} dS = \int_{\partial\Omega} \frac{D}{Dt}\underline{B} \cdot \hat{n} dS. \tag{2.4}$$

From equation (2.4) we retrieve an equivalent *upper convected oldroyd* derivative of the vector field:

$$\frac{D}{Dt}\underline{B} = \frac{\partial}{\partial t}\underline{B} + (\underline{u} \cdot \nabla)\underline{B} + (\nabla \cdot \underline{u})\underline{B} - (\underline{B} \cdot \nabla)\underline{u}. \tag{2.5}$$

By means of the vector calculus identity

$$\nabla \times (\underline{B} \times \underline{u}) = (\underline{u} \cdot \nabla)\underline{B} + \underline{B}(\nabla \underline{u}) - (\underline{B} \cdot \nabla)\underline{u} - \underline{u}(\nabla \underline{B}), \tag{2.6}$$

we can reduce equation (2.5) to:

$$\frac{D}{Dt}\underline{B} = \frac{\partial}{\partial t}\underline{B} - \nabla \times (\underline{u} \times \underline{B}) + \underline{u}(\nabla \cdot \underline{B}). \tag{2.7}$$

Equation (2.7) together with Stoke's and Gauss' integral theorems, enable the transformation of system (2.1) into:

$$\begin{cases} \nabla \times \underline{E} = -\dfrac{\partial \underline{B}}{\partial t} + \nabla \times (\underline{u} \times \underline{B}) \\ \nabla \times \underline{H} = \dfrac{\partial \underline{D}}{\partial t} - \nabla \times (\underline{u} \times \underline{D}) + \rho^e \underline{u} \\ \nabla \cdot \underline{D} = \rho^e \\ \nabla \cdot \underline{B} = 0. \end{cases} \tag{2.8}$$

The last fundamental equation is the conservation of charge (or the continuity equation for the electric charge); it can be obtained by taking the divergence of the Maxwell-Ampere's Law:

$$\nabla \cdot [\nabla \times \underline{E}] = \nabla \cdot \left[\frac{\partial \underline{D}}{\partial t} - \nabla \times (\underline{u} \times \underline{D}) + \underline{j} \right] \tag{2.9}$$

$$0 = \frac{\partial}{\partial t}\rho^e + \nabla \cdot \underline{j}. \tag{2.10}$$

Skin depth.

In this section we will introduce a parameter related to induction problems: the skin depth. We know that the eddy electric current will tend to flow close to the surface and will drop exponentially with respect to the depth according to the following equation:

$$\underline{j} = \underline{j}_s e^{-d/\delta}, \tag{2.11}$$

where $\underline{j}_s$ is the current density at the surface, d is the depth beneath the surface and δ is the skin depth defined as:

$$\delta = \sqrt{\frac{1}{\pi \sigma f \mu}} \tag{2.12}$$

being f the induction frequency. The penetration depth represents the region where the 87% of the power is developed into the domain by induction (figure 2.1(a)) and the 63% of the current flows (figure 2.1(b)). The 98% of the inducted current

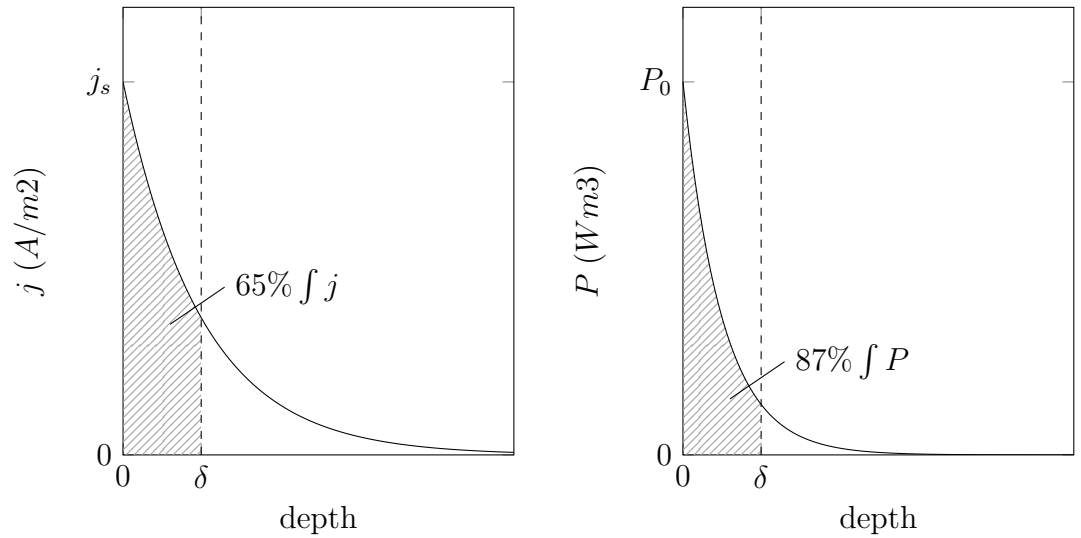

(a) Depth drop of the current density.

(b) Depth drop of the developed power.

Figure 2.1: Physical meaning of the skin depth.

flows in a thickness of 4δ. An optimal skin depth may be found for each application: for induction heating the skin depth is usually $\delta^* = D/8$ (where D is the diameter of the billet), while for AC stirring we expect $\delta^* = D/6$.

2.2.2 Potential formulation

A common way to solve system (2.8) is to use a potential formulation. Different potential formulations have been proposed to solve the EMF model; for EMS applications, two different techniques are commonly used: the electric vector potential $(\Psi, \underline{T})$ [85] and the magnetic vector potential $(\underline{A}, \phi)$ [58] approaches. The latter approach is the one mostly used in the literature and thus has been used in the current work.

Because of the Gauss' Law (i.e. $\nabla \cdot \underline{B} = 0$), it is possible to introduce a potential field $\underline{A}$, namely the magnetic vector potential, defined as follows:

$$\underline{B} = \nabla \times \underline{A}. \tag{2.13}$$

The Faraday's law can thus be re-arranged as:

$$\nabla \times \underline{E} = -\frac{\partial}{\partial t}(\nabla \times \underline{A}) + \nabla \times (\underline{u} \times \nabla \times \underline{A}) \tag{2.14}$$

$$\nabla \times \left(\underline{E} + \frac{\partial \underline{A}}{\partial t} - \underline{u} \times \nabla \times \underline{A} \right) = 0. \tag{2.15}$$

Since for any scalar function ϕ, $\nabla \times (-\nabla \phi) = 0$ is verified, thus:

$$\underline{E} + \frac{\partial \underline{A}}{\partial t} - \underline{u} \times \nabla \times \underline{A} = -\nabla \phi \tag{2.16}$$

$$\underline{E} = -\nabla \phi - \frac{\partial \underline{A}}{\partial t} + \underline{u} \times \nabla \times \underline{A}. \tag{2.17}$$

Hence, we can retrieve the electric current density as

$$\underline{j} = \sigma \left(-\nabla \phi - \frac{\partial \underline{A}}{\partial t} + \underline{u} \times \nabla \times \underline{A} \right), \tag{2.18}$$

with σ being the electrical conductivity.
Let's now introduce the constitutive equation for the magnetic material:

$$\underline{H} = \mu^{-1} \underline{B}, \tag{2.19}$$

where μ is the magnetic permeability.
By substitution of equations (2.18) and (2.19) in the Maxwell-Ampere's law, and the quasi-static approximation for the electric field we obtain

$$\nabla \times \mu^{-1} \nabla \times \underline{A} = \sigma \left(-\nabla \phi - \frac{\partial \underline{A}}{\partial t} + \underline{u} \times \nabla \times \underline{A} \right). \tag{2.20}$$

The double curl in equation (2.20) requires conditions to be specified not only on the magnetic potential but also on its first derivative in order to guarantee uniqueness of the solution. This additional condition is given by an extra equation, namely the *gauge* equation. Several gauge equations have been proposed in the literature, and in this work we will use the *Coulomb gauge*:

$$\nabla \cdot \underline{A} = 0. \tag{2.21}$$

Equation (2.20) is completed by the conservation of charge equation:

$$\nabla \cdot \underline{j} = 0 \tag{2.22}$$

$$\nabla \cdot \sigma \left(-\nabla \phi - \frac{\partial \underline{A}}{\partial t} + \underline{u} \times \nabla \times \underline{A} \right) = 0. \tag{2.23}$$

The Lorentz force acting on a moving object through an EMF can be naturally derived from the described framework:

$$f_L = \underline{j} \times \underline{B} \tag{2.24}$$

$$f_L = \sigma \left(-\nabla\phi - \frac{\partial \underline{A}}{\partial t} + \underline{u} \times \nabla \times \underline{A} \right) \times \nabla \times \underline{A}. \tag{2.25}$$

2.2.3 Material behaviour

As seen in equation (2.20), the EMF modelling needs two parameters (μ and σ) to be solved, given the following constitutive equations:

$$\underline{j} = \sigma(\underline{E}_{Maxwell} + \underline{u} \times \nabla \times \underline{A}) \tag{2.26a}$$

$$\underline{B} = \mu \underline{H}. \tag{2.26b}$$

In this section we will explain the physics and the mathematical models used to describe the electromagnetic behaviour of materials. While the electrical conductivity σ used in equation (2.26a) is commonly represented as a function of temperature, the magnetic constitutive equation is more complex to model. The magnetic permeability does not depend only on the temperature, but also on the magnetic field itself. This material non-linearity is due to the physical characteristics of the material and can be studied through the magnetization law.

Magnetization Law.

The magnetization law can be written as:

$$\underline{B} = \mu_0 \underline{H} + \underline{M} \tag{2.27}$$

where μ_0 is the magnetic permeability of vacuum (invariant $\mu_0 = 4\pi \times 10 - 7H/m$) and $\underline{M}$ is the magnetic dipole moment per unit volume, namely the material's magnetization. Material's magnetization may be expressed as

$$\underline{M} = \mu_0 \chi_v \underline{H}, \tag{2.28}$$

with χ_v being the volume magnetic susceptibility, which is an adimensional parameter. Equation (2.27) can therefore being re-written as

$$\underline{B} = \mu_0(\underline{H} + \chi_v \underline{H}) = \mu_0(1 + \chi_v)\underline{H}. \tag{2.29}$$

From equation (2.29) we can introduce the relative magnetic permeability:

$$\mu_r := (1 + \chi_v). \tag{2.30}$$

The evolution and values of this magnetic parameter (i.e. χ_v either μ_r) depends on the physics of the material. Materials can be distinguished in a few different classes with respect to their behaviour when subjected to an external magnetic field; in this section we will discuss the three most common classes: ferromagnetic, diamagnetic and paramagnetic materials.

Ferromagnetic materials. Ferromagnetic materials are highly susceptible to external magnetic fields (i.e. $\chi_v \in (1000 \div 200000)$)[86]. Ferromagnetic bulk materials are structured in subdomains [87] (figure 2.2) called *magnetic domains* or *Weiss domains*, from the name of Pierre-Ernest Weiss who, in 1906, suggested existence of magnetic domains in ferromagnets.

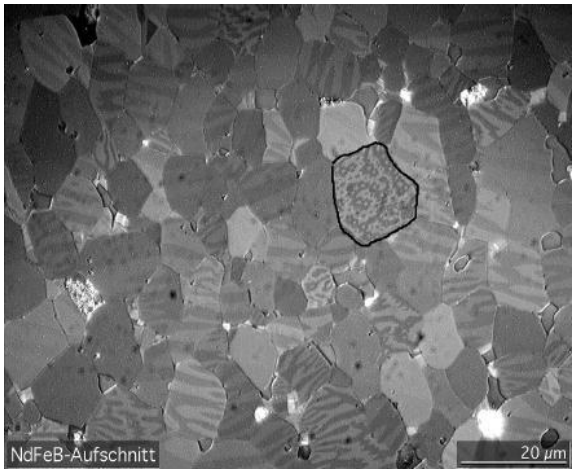

Figure 2.2: Microcrystalline grains within a piece of NdFeB with magnetic domains made visible with a Kerr microscope. The domains are the light and dark stripes visible within each grain. (Source: Wikipedia)

The magnetic spin is uniform in each sub-domain, but the different domains are randomly oriented due to thermal energy, as depicted in figure 2.3(a). This is the configuration with minimum energy and results in a global null magnetic field. When an external magnetic field is imposed (figure 2.3(b)) all the Weiss domains polarize in the same direction as the external field. This global alignment transforms the material in a magnet with its own magnetic field which could be higher than the external one. This is a gradual phenomena: the global alignment of the polarization of the domains occurs when a certain value of the external field H_s, namely

saturation magnetic field, is reached. Anyway, H_s is relatively low for ferromagnetic materials, so ferromagnets usually behave as flux concentrators for engineering applications. When the external magnetic field is removed, the global alignment is partially lost, but is still high enough to produce a magnetic field for a certain period (figure 2.3(c)). After a certain time, a random configuration is retrieved due to the demagnetization process.

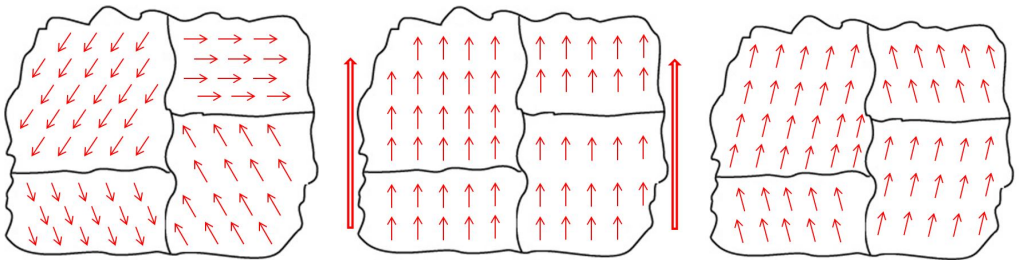

(a) Unmagnetized status

(b) Magnetization under an external magnetic field

(c) Residual magnetization status

Figure 2.3: Behaviour of ferromagnets when subjected to an external magnetic field.

The ability of maintaining the magnetic polarization after the external magnetic field is removed come from hysterical behaviour of the magnetization phenomenon. In figure 2.4, the magnetization hysteresis curve for a ferromagnetic material is plotted. From point (a) to point (b) the first magnetization occurs: the external magnetic field is not strong enough to align all the Weiss domains but it is strong enough to impose a general orientation and, consequently, to develop a flux density in the material with $\mu_r \gg 1$. Point (b) represents the saturation point ($H(b) = H_s$): for any load $H > H_s$ there is no more magnetic susceptibility, hence $\chi_v = 0$ and $\mu_r = 1$. At point (c), the external magnetic field has been removed, but a residual flux density B_R remains. Point (c) shows the coercive force: a magnetic field opposite to the first magnetization field has to be applied to neutralize the residual flux in the material. The shape of the hysteresis depends on the material properties and it is important to notice that the area of the loop represents energy lost by heating to turn the magnetic poles in the material. For this reason, ferromagnetic materials are excellent for induction heating applications (for which the hysteresis heat is added to the Joule heat).

Paramagnetic materials. Paramagnetic materials are, like ferromagets, attracted by magnetic fields. The difference is that the magnetic moment induced in paramagnetic materials is linear with the external field and rather weak. The magnetic spins in paramagnetic material are not uniform and no magnetic domain are present, so

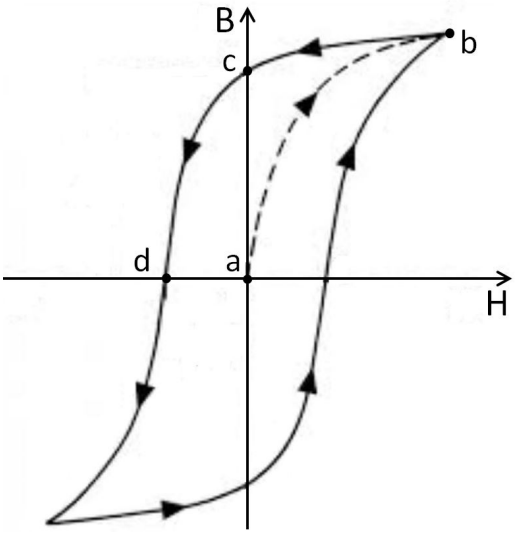

Figure 2.4: Magnetization hysteresis curve for a ferromagnetic material.

no global polarization occurs (figure 2.5).

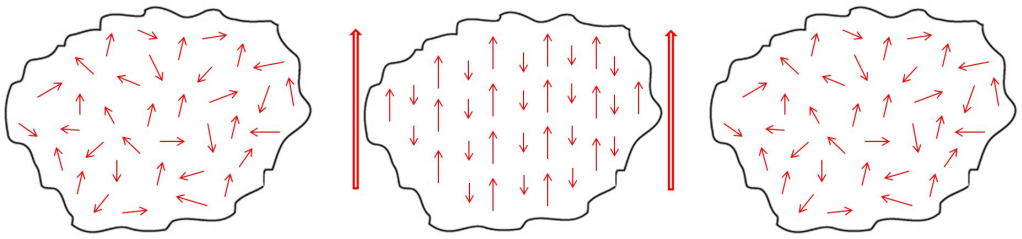

(a) Unmagnetized status (b) Magnetization under an external magnetic field (c) Retrieved unmagnetized status

Figure 2.5: Behaviour of paramagnetic materials when subjected to an external magnetic field.

Diamagnetic materials. Diamagnetism is a quantum effect present in all materials and leads the material to be repelled by the magnetic field. This means that, when subjected to an external magnetic field, dielectric materials get polarized opposite to the external field (see figure 2.6). Anyway, the strength of this polarization is low so it is negligible when the material shows ferromagnetic or paramagnetic behaviours. For this reasons, dielectric materials like silver, water, carbon are normally considered non-magnetic; the magnetic susceptibility of dielectric materials is negative, but very low ($\chi_v \in (-0.5; -50) \times 10^{-5}$), while the relative magnetic

permeability is slightly lower than 1.

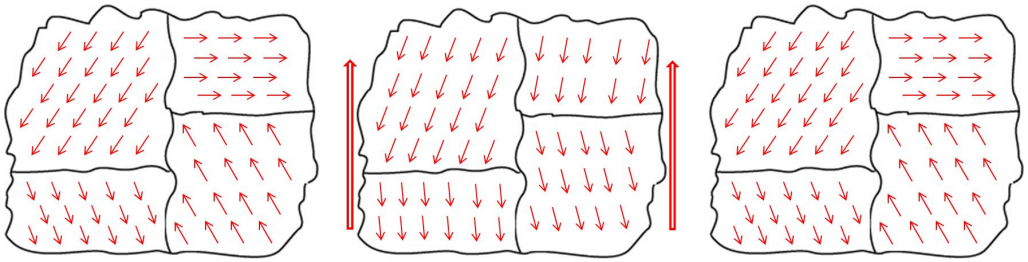

(a) Unmagnetized status (b) Magnetization under an external magnetic field (c) Retrieved unmagnetized status

Figure 2.6: Behaviour of dielectric materials when subjected to an external magnetic field.

The magnetic nature of the material affects not only the magnetic field within the material itself, but also the surrounding field. As depicted in figure 2.7, ferromagnetic materials behave like flux concentrators and they increase the induction magnetic field. Paramagnetic and diamagnetic materials, on the opposite, have a low influence on the external induction magnetic field.

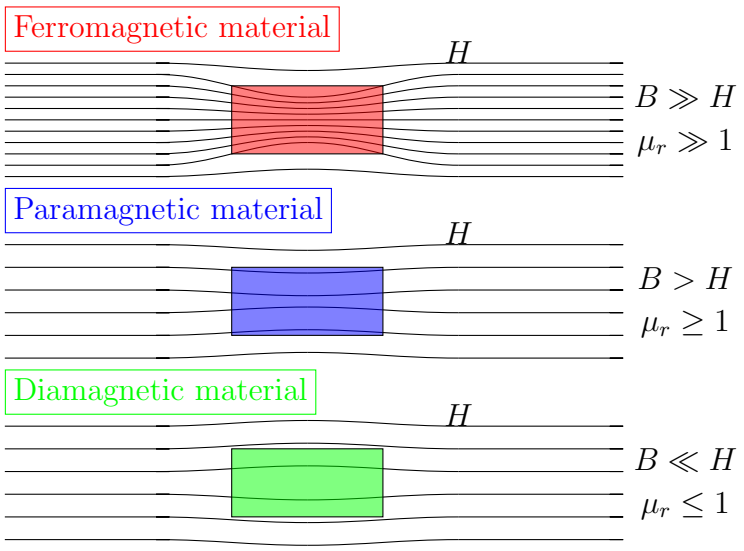

Figure 2.7: Comparison between the magnetic behaviour of material at a different magnetic state.

Curie temperature. The categories described above (i.e. ferromagnetism, paramagnetism, and diamagnetism) are not intrinsic of the material, but they are relative

at the conditions of the material itself. The magnetization properties are determined by the magnetic moment, i.e. a dipole moment within an atom which originates from the angular momentum and spin of electrons. Materials have different structures of intrinsic magnetic moments that depend on temperature; the Curie temperature is the critical point at which a material's intrinsic magnetic moments change direction. Ferromagnetic materials behave as paramagnetic when the temperature is higher than the Curie point (figure 2.8). The Curie temperature depends on many variables; in the case of steel, it strongly depends on the composition and it can be derived by the Fe-C equilibrium diagram. In this work we limit to notice that the Curie temperature of steel is $T_C \approx 770°C$, which is significantly lower than the temperature in the mould. This means that the in-mould melt in continuous casting behaves as a paramagnetic fluid. This consideration will be important, as explained in chapter 4. It is also important to notice that this assumption is not valid for lower parts of the casting process (e.g. for low S-EMS or F-EMS) and in the case of ferromagnetic moulds (possible for ingot casting), which are anyway not efficient for EMS applications.

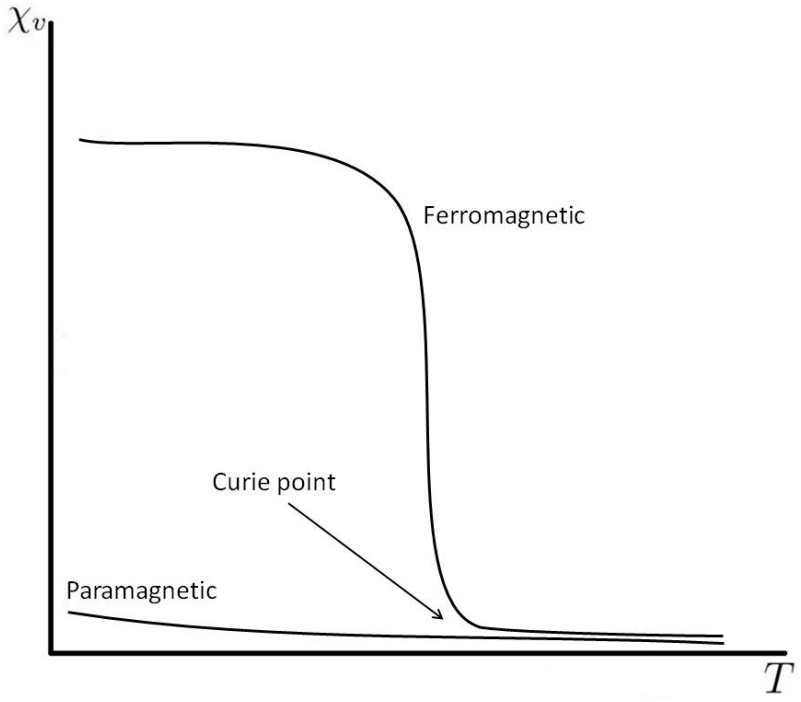

Figure 2.8: Curie Point influence on the magnetic behaviour.

Magnetization curve approximation. As stated before, the hysteresis curve for ferromagnetic materials is extremely important. In the literature, many different

constitutive equations have been proposed to approximate the magnetization curve in an efficient and effective way. In 2015, Q. Tang published an article [88] comparing 11 different models. In this work we limit to report the models in table 2.2, referring to the original work for the extensive comparison.

Table 2.1: Approximation expressions for the B-H curve

Expression	N. Parameters
$H = a_0 + a_1 B + ... + a_9 B^9$	10
$H = aB + bB^n$	3
$H = ae^{bB}$	2
$H = \left(ae^{bB^2} + c\right) B$	3
$B = a_0 + a_1 H - a_2 H^{-1}$	3
$B = \dfrac{a_0 + a_1 H + a_2 H^2}{1 + b_1 H + b_2 H^2} + \mu_0 H$	6
$B = a - be^{-cH}$	3
$B = a_0 + a_1 e^{-b_1 H} + L + a_4 e^{-b_4 H}$	9
$B = a\, tan^{-1}(bH) + cH$	3
$B = a\left(coth\left(\dfrac{H}{b}\right) - \dfrac{b}{H}\right) + c$	3

In this section we limit to compare 5 different models.

Model A.

It is used in FLUX®and it is commonly used in the literature [89]. The magnetic permeability is approximated with the formula:

$$\mu_r(T,H) = 1 + f(T) \cdot \mu_{20}(H), \tag{2.31}$$

where μ_{20} is the field-dependent permeability at the room temperature $T = 20°C$, and the function $f(T)$ is calculated with the relationships:

$$\begin{cases} f(T) = 1 - e^{\left(\dfrac{T - T_C}{C}\right)}, & \forall T < T_1 \wedge T_1 = T_C + Cln0.9 \\ f(T) = e^{\left(\dfrac{10(T2 - T}{C}\right)}, & \forall T > T_1 \wedge T_2 = T_1 + 0.1Cln0.1 \end{cases} \tag{2.32}$$

Another way of approximating the B-H curve is based on the following relationship:

$$B(H) = \mu_0 H + B_S \frac{H_a + 1 - \sqrt{(H_a + 1)^2 - 4H_a\,(1 - a)}}{2(1 - a)} \tag{2.33}$$

with $H_a = \mu_0 H(\mu_{r,i} - 1)B_s^{-1}$.

Model B.

Is the isotropic analytical model implemented in FLUX®. The magnetic flux can be computed as:

$$B(H,T) = \mu_0 H + \frac{2J_0}{\pi} arct\left(\frac{\pi\,(\mu_{r0} - 1)\,\mu_0 H}{2J_0}\right)\alpha(T), \tag{2.34}$$

where $\alpha(T)$ is a scalar parameter depending on the temperature.

Model C.

Is the model proposed by Tang [88] and reported in table 2.1:

$$B = a\left(coth\left(\frac{H}{b}\right) - \frac{b}{H}\right) + c, \tag{2.35}$$

with a,b and c being scalar parameters to be turned.

Model D.
Is the model used in Forge®:

$$\begin{cases} B(H,T) = \mu_0 \mu_{rmax}(T) H, & \forall B < B_{int} \\ B(H,T) = \mu_0(H) + B_s(T), & \forall B \geq B_{ind} \end{cases} \tag{2.36}$$

with μ_{rmax} being the maximum permeability and $B_s(T)$ being the saturation flux.

Model E.
Is a model proposed in the current work. The relative magnetic permeability is computed as:

$$\begin{cases} \mu_r = aH^2 + bH + \mu_{ri}, & \forall B < B_{ind} \\ \mu_r = cH^d, & \forall B \geq B_{ind} \end{cases} \tag{2.37}$$

where μ_{ri} is the relative magnetic permeability at $H = 0$ for the first magnetization. The parameter can be retrieved by some geometrical features of the B-H curve:

- the peak of the relative permeability: $(H^p; \mu_r(H^p))$, and
- the point where we want the approximated and experimental curves to be coincident $(H^*; \mu_r(H^*))$.

Consequently, we obtain the following set of formulae:

$$\begin{cases} a = \dfrac{\mu_r(H^p) - \mu_r i}{H^*} \\ b = 2aH^* \\ c = exp\left(\dfrac{ln\left(\mu_r(H^p)\right) ln\left(H^*\right) - ln\left(\mu_r(H^*)\right) ln\left(H^p\right)}{ln\left(H^*\right) - ln\left(H^p\right)} \right) \\ d = \dfrac{ln\left(\dfrac{\mu_r(H^p)}{c}\right)}{ln\left(H^p\right)}. \end{cases} \tag{2.38}$$

In figure 2.9, the comparison between the different models is shown with respect to experimental data of a cast iron billet.

The approximation error computed as:

$$err = \sum_{i=0}^{i=n.data} \frac{2(B_{appr,i} - B_{exp,i})^2}{H_{i+1} - H_{i-1}} \tag{2.39}$$

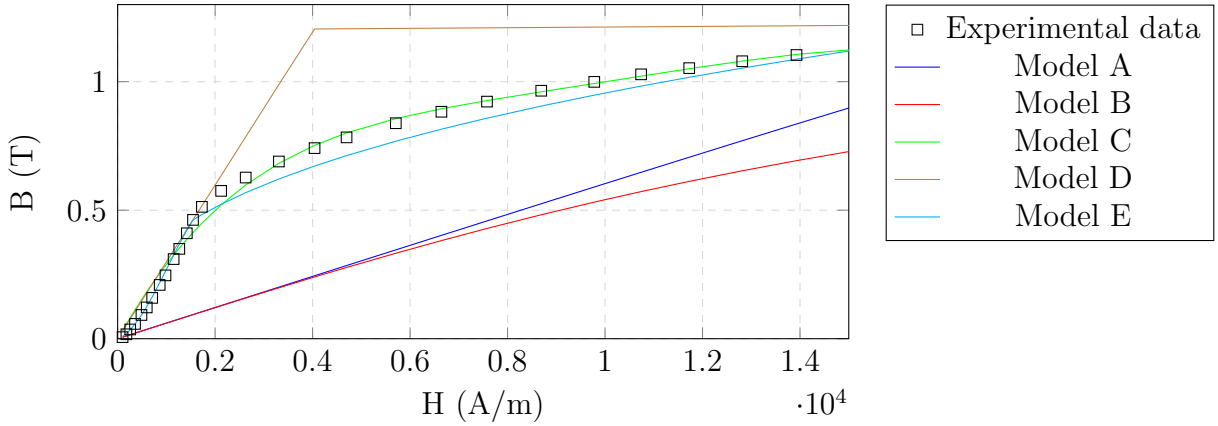

(a) B-H magnetization curve

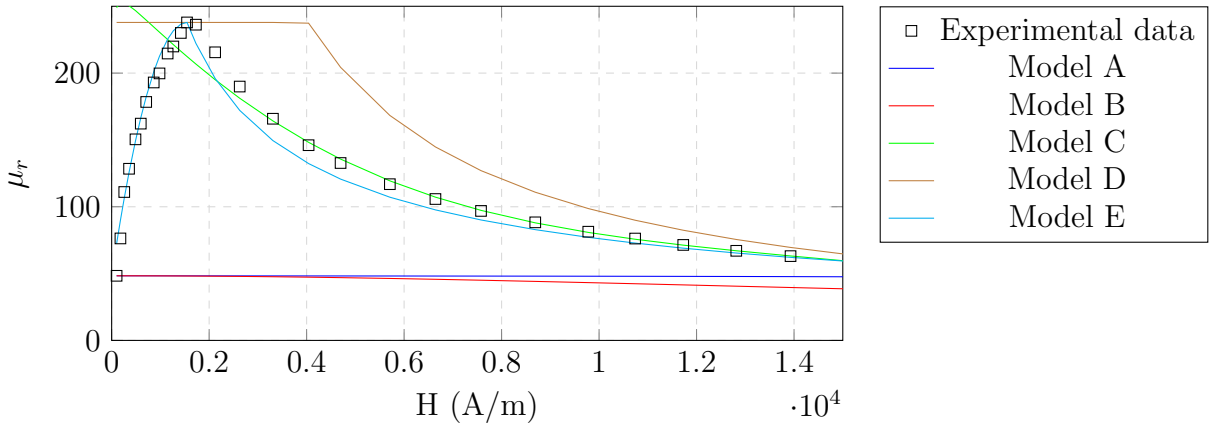

(b) μ-H magnetization curve

Figure 2.9: Comparison of approximation of the magnetization curves by different models.

is reported in table 2.2. In terms of interpolation, models C and E seem the best. In this work we will use model E because it is the simpler, since it relies on geometrical features of the BH curve; on the opposite, model C needs a non-linear equation solution to find the optimal parameters, which are purely numerical and have not physical meaning. But in terms of extrapolation, the results of the comparison are highly different. We see in figure 2.10 that models E and C are the worse; in this case we do not have an experimental comparison (which is often the case for the data input in simulations), but it is clear that they do not model a physical behaviour of the material. Thus, in this work, we will use models A and D when an extrapolation of the BH curve is needed, so when the external magnetic field is high.

Table 2.2: BH curve interpolation errors.

Model	err ($\times 10 - 5$)
A	710
B	770
C	24
D	140
E	6.7

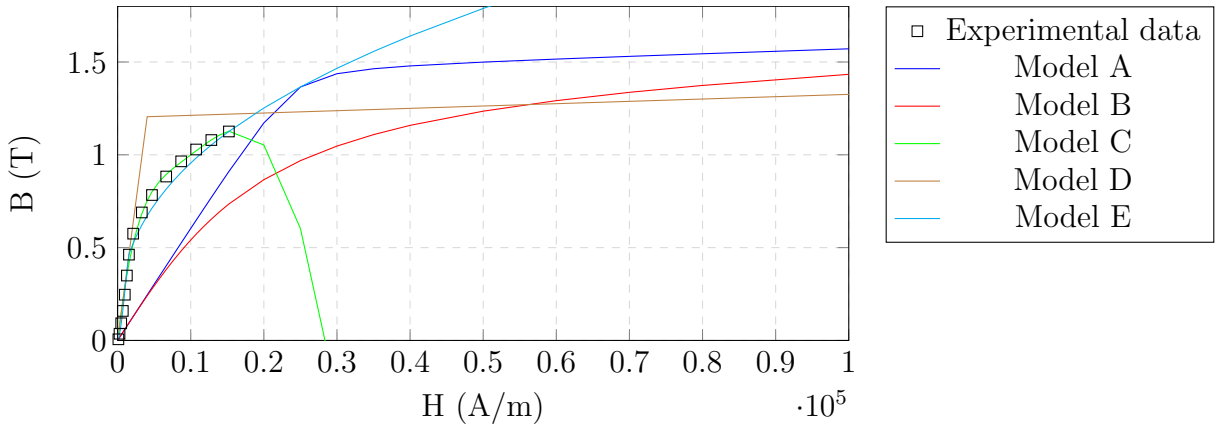

(a) B-H magnetization curve

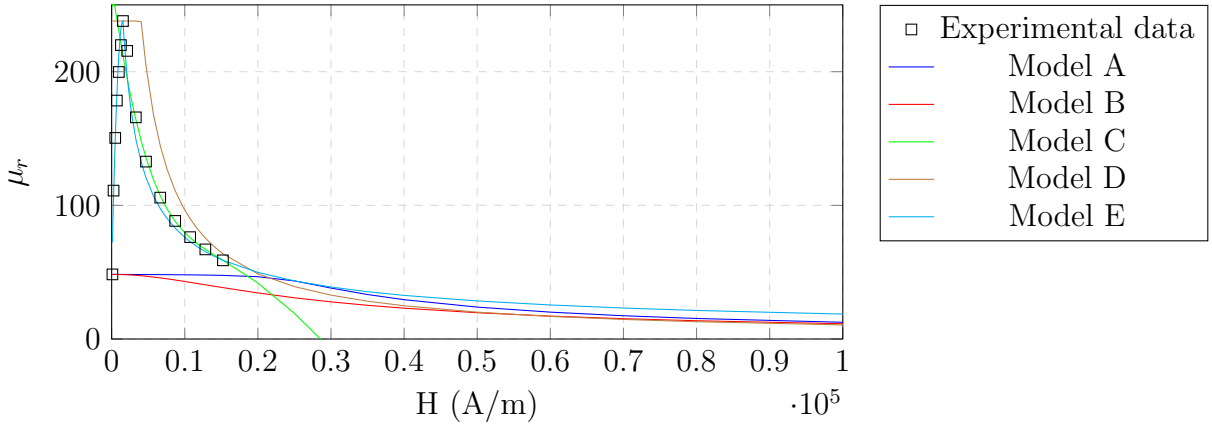

(b) μ-H magnetization curve

Figure 2.10: Comparison of approximation of the magnetization curves by different models.

2.3 Space discretization

The strong formulation to be solved is the potential-based model described in section 2.2:

$$\begin{cases} \nabla \times \mu^{-1} \nabla \times \underline{A} = \sigma \left(-\nabla \phi - \dfrac{\partial \underline{A}}{\partial t} + \underline{u} \times \nabla \times \underline{A} \right) \\ \nabla \cdot \left[\sigma \left(-\nabla \phi - \dfrac{\partial \underline{A}}{\partial t} + \underline{u} \times \nabla \times \underline{A} \right) \right] = 0. \end{cases} \tag{2.40}$$

System (2.40) can be simplified by neglecting the convective term (i.e. $\underline{u} \times \nabla \times \underline{A}$); this choice is based on the physics of EMS, as further detailed in chapter 4.
The charge conservation equation can be further simplified through the gauge condition (eq. (2.21)): under the assumptions of local uniformity of σ (acceptable in a finite element framework, since σ is considered element-wise constant) and interchangeability of $\nabla \cdot$ and ∂_t operators, we obtain

$$\begin{cases} \nabla \times \mu^{-1} \nabla \times \underline{A} = \sigma \left(-\nabla \phi - \dfrac{\partial \underline{A}}{\partial t} \right) \\ \Delta \phi = 0. \end{cases} \tag{2.41}$$

As we see, system (2.41) is weakly coupled, since the second equation is independent from the first. For this reason, it will be solved in a decoupled way: the second equation will be solved in the inductor domain (the only region where ϕ is non-zero) and the solution will be used as a source term in the solution of the first equation.

2.3.1 Finite Elements

The classic finite element schemes are based on nodal variable, thus they approximate the vectorial unknown field on the elements' nodes. This choice ensures the $\mathcal{C}^0$ continuity on the normal components of vector fields which is important when dealing with gradient and divergence operators. For this reason, the second equation of system (2.41) will be solved by the classic $\mathcal{P}^1$ nodal elements. But this approach is not effective for the magnetic potential resolution. The main problem is that the curl operator needs only the tangential component of the vectorial field to be reinforced and not also the normal component, which is the case when nodal elements are used. This over-constraint leads to spurious and non-physical solutions when nodal elements are used to solve curl-based models [90]. In order to solve this issue, a different finite element formulation were developed by Nédélec [91], which avoid the rise of spurious solutions [92, 93, 94, 95]; the degrees of freedom are, in this case, assigned at the edges of the element.

Nédélec Elements.

In this section we will describe the main characteristics of Nedélec edge finite elements. For the sake of simplicity, we will develop the 2D case, with reference to the triangular parametric element depicted in figure 2.11. Let's introduce a scalar defined as:

$$p(t, \underline{x}) = \sum_n p_n(t)\varphi_n(\underline{x}), \tag{2.42}$$

where $\varphi_n(\underline{x})$ is the $n-th$ scalar nodal basis function. For the 2D triangular element, the scalar basis functions are computed as follows:

$$\begin{aligned} \varphi_1(\underline{x}) &= 1 - x - y \\ \varphi_2(\underline{x}) &= x \\ \varphi_3(\underline{x}) &= y. \end{aligned} \tag{2.43}$$

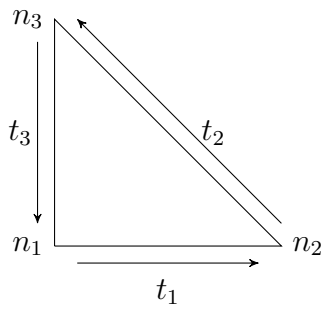

Figure 2.11: 2D reference element.

The vectorial basis function defined on the element's edges are computed from the nodal basis functions according to the equation:

$$\Psi_d(\underline{x}) = \varphi_i(\underline{x})\nabla\varphi_j(\underline{x}) - \varphi_j(\underline{x})\nabla\varphi_i(\underline{x}). \tag{2.44}$$

For the 2D element, the vectorial basis functions (figure 2.12) can be extensively written as:

$$\begin{aligned} \Psi_1(\underline{x}) &= \varphi_1(\underline{x})\nabla\varphi_2(\underline{x}) - \varphi_2(\underline{x})\nabla\varphi_1(\underline{x}) = (1-y, x)^T \\ \Psi_2(\underline{x}) &= \varphi_2(\underline{x})\nabla\varphi_3(\underline{x}) - \varphi_3(\underline{x})\nabla\varphi_2(\underline{x}) = (-y, x)^T \\ \Psi_3(\underline{x}) &= \varphi_4(\underline{x})\nabla\varphi_2(\underline{x}) - \varphi_2(\underline{x})\nabla\varphi_4(\underline{x}) = (-y, x-1)^T. \end{aligned} \tag{2.45}$$

According to the classical finite element method (FEM) approach, the unknown field (in our case the magnetic vector potential $\underline{A}$) is computed as the linear combination of the base functions:

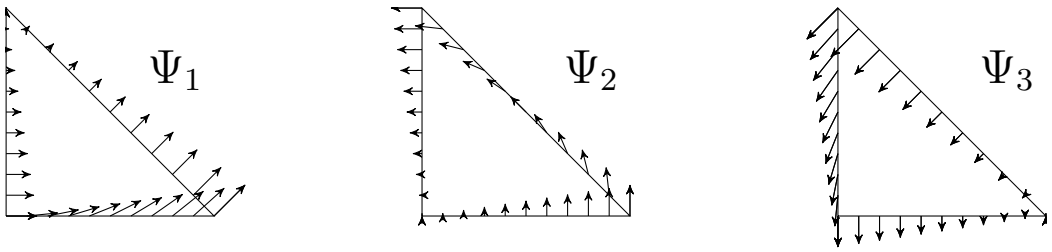

Figure 2.12: Edge base functions for the 2D element.

$$\underline{A}(t,\underline{x}) = \sum_d a_d(t)\Psi_d(\underline{x}) \tag{2.46}$$

where $a_d = \underline{A}\cdot\hat{t}$ represents the mean value of the integral of $\underline{A}$ along the edge d, with $\hat{t}$ being the versor tangent to the edge.
The weak formulation of the magnetic potential equation can be written as:

$$\mu_0^{-1}\cdot\left(\mu_r^{-1}\nabla\times\underline{\Psi};\nabla\times\underline{\Psi}\right)\mathbf{A} = -\sigma\left(\partial_t\underline{\Psi};\underline{\Psi}\right)\underline{A} - \sigma\left(\nabla\phi;\underline{\Psi}\right). \tag{2.47}$$

Let's notice that μ_r has been removed from the curl operator since it is considered uniform within each element.

A good advantage of Nédélec elements is that the Coulomb gauge is naturally guaranteed:

$$\nabla\cdot\underline{A} = \nabla\cdot\sum_d a_d(t)\underline{\Psi}_d(\underline{x}) = \sum_d a_d(t)\nabla\cdot\underline{\Psi}_d(\underline{x}) \tag{2.48}$$

$$\nabla\cdot\underline{\Psi}_d(\underline{x}) = \left[\nabla\varphi_i\cdot\nabla\varphi_j - \nabla\varphi_j\cdot\nabla\varphi_i\right] + \left[\varphi_i\cdot\nabla^2\varphi_j - \varphi_j\cdot\nabla^2\varphi_i\right]. \tag{2.49}$$

The first part of equation (2.49) is always equal to zero and the second part is null because $\mathcal{P}^1$ elements are used, hence

$$\nabla\cdot\underline{\Psi} = 0. \tag{2.50}$$

It is interesting to notice that the calculated field $\underline{A}$ will be inherently divergence-free within the element, but a long debate has risen in the literature about the global respect of the gauge condition. As stated before, edge finite elements guarantee the continuity of the tangential component of the field, but not the normal component. This is extremely helpful when treating singularities (e.g. edges and corners) between different materials, but may lead to discontinuities also at the interface between adjacent elements in the same material. As claimed by Gerrit Mur in several papers between 1985 and 1995 [96, 97, 98], for this kind of elements the continuity of the normal flux densities in between adjoining edge elements containing the same

material is guaranteed no more. Thus an extra compatibility condition should be added to the model or certain initial conditions have to be chosen [99]. Recently, additional work has been dedicated to this problem and new type of basis functions have bee proposed to guarantee all the compatibility conditions related to Maxwell's equation [100].

Boundary conditions.

Charge conservation equation. This equation is solved by the use of nodal elements in the inductor domain (Ω_I). The boundary conditions are imposed on the boundary sections of the inductor by sets of two, composed by one output section (Γ_O) and one input section (Γ_I). An homogeneous Dirichlet boundary (and initial) condition has been applied to the boundaries:

$$\begin{aligned} \phi(t, \underline{x}) &= 0 \quad \forall \underline{x} \in \Gamma_O \wedge \forall t \in \Omega_t \\ \phi(t, \underline{x}) &= V(t, \underline{x}) \quad \forall \underline{x} \in \Gamma_I \wedge \forall t \in \Omega_t \end{aligned} \tag{2.51}$$

with Ω_t the time interval (see section 2.4 for further details on the time integration algorithm) and $V(t, \underline{x})$ the input electric potential. Also when the input data was the current density, a Dirichlet boundary condition has been applied according to the method reported in the work of J. Alves [84].

Magnetic vector potential equation. The magnetic vector potential equation has been solved in a single domain Ω which includes the inductor domain Ω_I, the air domain Ω_A and the work piece domain Ω_W, which include the molten metal, the mould and the iron core of the inductor in our case.The boundary conditions to be imposed are:

$$\underline{A}(0, \underline{x}) = \frac{\partial}{\partial t}\underline{A}(0, \underline{x}) = 0 \quad \forall \underline{x} \in \Omega \tag{2.52a}$$

$$\underline{B} \cdot \hat{n} = 0 \Rightarrow \hat{n} \cdot \nabla \times \underline{A} = 0 \quad \forall \underline{x} \in \Gamma_B \subseteq \Gamma \tag{2.52b}$$

$$\underline{H} \times \hat{n} = 0 \Rightarrow \nabla \times \underline{A} \times \hat{n} \quad \forall \underline{x} \in \Gamma_H \subseteq \Gamma \tag{2.52c}$$

where Γ is the boundary of the computational domain.
Boundary condition (2.52b) is equivalent to $\underline{A} \times \hat{n} = 0$, which represents also the symmetry condition for $\underline{B}$. This condition can be further developed to find a simply-to-impose formulation:

$$\underline{A} \times \hat{n} = 0 \Rightarrow \underline{A} \cdot \hat{t} = 0, \tag{2.53}$$

where $\hat{t}$ is any given unit vector belonging to the boundary surface. Equation (2.53) is also the homogeneous Dirichlet boundary condition of the problem. On the other

hand, condition (2.52c) is a Neumann boundary condition. It can be re-written as [101]:

$$\nabla \times \underline{A} \times \hat{n} \Leftarrow \underline{A} \cdot \hat{n} = 0 \tag{2.54}$$

which is the natural condition emerging from the finite element approximation and thus is naturally satisfied with no need of an explicit imposition.

Dimension of the air domain. The dimension of the air domain surrounding the inductor and the metal regions has a great influence on the quality of results. The Dirichlet condition describes in equation (2.53) forces the magnetic field to be tangent to the boundaries of the domain or, in other words, it forces all the field lines to be fully contained in the domain. This is true only if an infinite region is modelled; for real simulations, this kind of boundary condition represents an approximation which should be carefully analysed. The homogeneous Dirichlet condition is equivalent to the modelling of a magnetic shield (e.g. a ferromagnetic core) on the boundary surfaces, which concentrates the magnetic flux inside the domain. As a result, if the modelled air domain is not large enough, the simulation will lead to an overestimation of the magnetic field and the power injected in the system.
Let's consider the simple case of a solenoid with a metallic cylinder core as shown in figure 2.13. It is a very basic benchmark used in this work to test the EM simulations. The inductor is fed with AC current. The internal radius of the solenoid is $20mm$ and the wire's section is a square with the edge $5mm$ length. Inside the solenoid the is a para-magnetic copper cylinder, whose surface was insulated from the current in the wire. Only 30° was simulated because of the axial symmetry of the problem. Its conductivity was set to $\sigma = 5\,E07\,S/m$ and $\mu_r = 1\,H/m$. The dimension of the air domain has been varied as well as the induction frequency. For each simulation, the error of the magnetic field at the center of the solenoid has been computed and the error with respect to a reference solution obtained with $1mln$ nodes has been plotted in figure 2.14. Figure 2.14 shows that the error is a damped-sinusoidal function of the air domain; the error seems not being a function of the skin depth δ (figure 2.14(a)). From figure 2.14(b) the error seems depending on the domain's size, or at least on its scaled value. In this case, give the simplicity of the geometry, the domain size has been scaled by the radius of the billet. In a more general way we limit to observe the low impact of the skin depth and the boundary conditions choice.

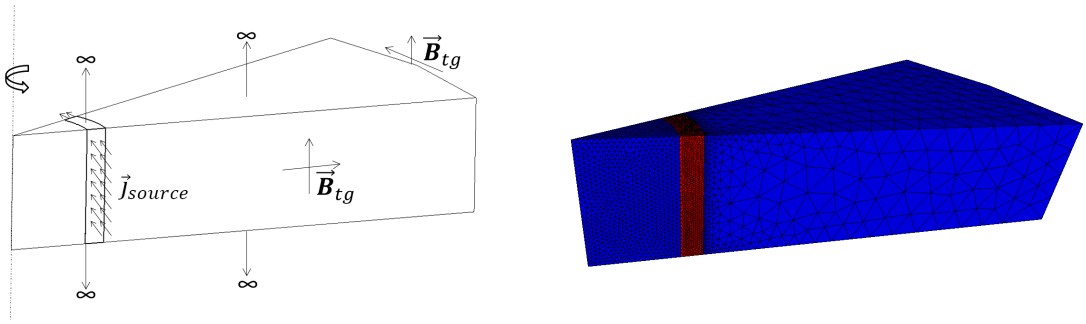

(a) Boundary conditions

(b) Mesh of the domain. In red is the region of the domain occupied by the inductor

Figure 2.13: Simulation set-up: domain, mesh and boundary conditions

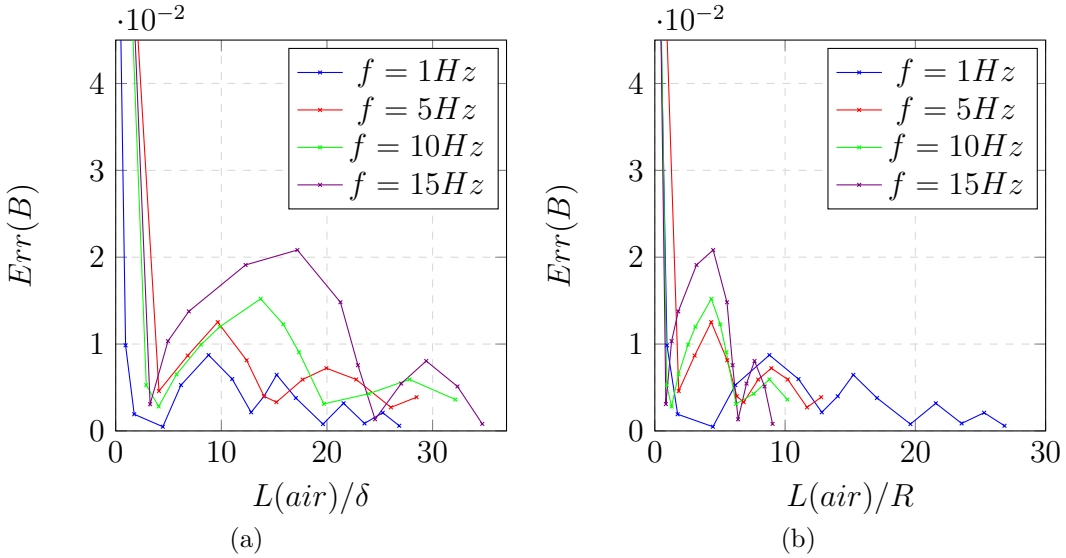

(a) (b)

Figure 2.14: Error of the simulated maximum magnetic field *vs* the air domain's size

2.4 Time integration

The electromagnetic model in equation (2.41) is time-dependent; the second equation (i.e. the charge conservation equation) depends on time because its boundary condition do. Hence ϕ is a time-dependent source term for the first equation, whose solution depends on time in the term $\partial_t \underline{A}$. In this section we will show the different techniques used in this work for the time integration of equation (2.41) both in the time and in the frequency domain.

2.4.1 Integration in the time-domain

Let's re-write equation (2.47) in vectorial notation. For the sake of simplicity, let's set:

$$\begin{aligned}\mathbf{R} :=& (\nabla \times \underline{\Psi}; \nabla \times \underline{\Psi}) \\ \mathbf{F} :=& (\underline{\Psi}; \underline{\Psi}).\end{aligned} \tag{2.55}$$

Equation (2.47) can thus be written as:

$$\mu^{-1}\mathbf{R}\underline{A} = -\sigma\partial_t\mathbf{F} - \sigma(\nabla\phi\underline{\Psi}). \tag{2.56}$$

Equation (2.56) is still continuous in time because of the operator ∂_t and because $\phi(t)$. Two different time-integration schemes have been considered in this work: *forward Euler* (EE) and the *Quasi-Static Second-Order-Central Differences* (QSSC).

Forward Euler. Forward Euler is the simplest and one of the most common explicit method for the integration of ODE. EE can be applied for the time-integration of equation (2.56), leading to the following algebraic system:

$$[\Delta t\mathbf{R} + \mu\sigma\mathbf{F}]\,\underline{A} = \mu\sigma\mathbf{F}\underline{A}^{-} - \Delta t\sigma\mu(\nabla\underline{\Psi}; \underline{\Psi})\phi^{-}, \tag{2.57}$$

where Δt is the time step and x^{-} is the value of x at the previous time-step.

Quasi-Static Second-Order-Central Differences. QSSC is a two-steps march scheme used to integrate ODE. It has been used for the time integration of electromagnetic application and it shows good stability properties [102]. By using the QSSM method, equation (2.56) can be written as:

$$\left[\frac{2}{3}\Delta t\mathbf{R} + \mu\sigma\mathbf{F}\right]\underline{A} = \frac{4}{3}\mu\sigma\mathbf{F}\underline{A}^{-} - \frac{1}{3}\mu\sigma\mathbf{F}\underline{A}^{=} + \frac{2}{3}\Delta t\sigma\mu(\nabla\underline{\Psi}; \underline{\Psi})\phi^{-}, \tag{2.58}$$

where $\underline{A}^{=}$ is the value of $\underline{A}$ at the ante-previous time-step.

Convergence criterion.

The integration on time is performed until the periodic state is reached. This condition could be verified in two ways: once for each simulated EM period or at each time-step. The first way is the classical method used in Forge®: the energy input in each inductor during the EM period is compared to the energy input in the previous period and the steady state is considered to be achieved when the difference between the two energies is sufficiently low. This method has the main drawback that no stop-condition is implemented within the period; this means that, if the steady state is achieved at the beginning of a period, one full period will be simulated, increasing

the computational time with no gain in accuracy. For this reason, a second method has been implemented, in order to stop the simulation at the time step in which the steady state is achieved. The method is based on three scalar quantities defined for each inductor:

$$\begin{aligned} &Power\ current: \ P = \frac{1}{2}\int_{\Omega} \sigma E^2 \, d\Omega \\ &Energy\ current: \ \mathcal{E} = \int_0^{\bar{t}} P \, dt \\ &Average\ power: \ \bar{P} = \frac{\mathcal{E}}{\bar{t}}. \end{aligned} \tag{2.59}$$

The qualitative evolution of the fields in equation (2.59) is depicted in figure 2.15.

When the mean of the averaged power between two peaks is lower than a certain threshold, the stopping criterion is satisfied and the simulation ends.

2.4.2 Integration in the frequency domain

Instead of solving equation (2.47) in the time domain, it is possible to solve it in the frequency domain [103, 104, 105]. This is a very common modelling procedure for electromagnetic application and several studies have been performed to enhance the resolution techniques of the rising complex-valued systems [106, 107].
We can substitute the evolution in time of each field with the rotation of a phasor in the complex plane by using the *Euler's formula*:

$$e^{\varphi i} = \cos(\varphi) + i \sin(\varphi) \tag{2.60}$$

where $\varphi \in \Re$, e is the Napier's number and i is the imaginary unit.
This transformation (which is a pure algebraic substitution and not a Fourier transformation) is acceptable under the hypothesis that under the constriction of an harmonic source term (like ϕ is in the presence of a AC current fed wire) the whole system reacts harmonically and with the same pulsation. Let's now set the phasor $\tilde{\underline{A}} := \underline{A} e^{\omega i}$, where ω is the angular frequency of the source, and replace it in equation (2.56); the $(\underline{A}, \phi)$ formulation can be so re-written in the frequency domain as:

$$[\mathbf{R} + \mu\sigma\omega i \mathbf{F}] \, \tilde{\underline{A}} = \sigma\mu(\nabla\underline{\Psi}; \underline{\Psi})\phi_0 i \tag{2.61}$$

where ϕ_0 is the real average value of ϕ computed from the current density conservation equation.
System (2.61) is a complex-valued system. The problem is that many numerical packages used in commercial software, e.g. PETSc [108] and Aztec [109], focus on real-valued systems, while complex-valued systems are seen as a late addition. In

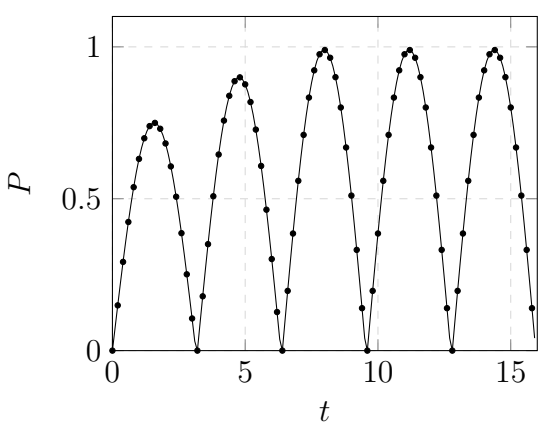

(a) Power evolution in the inductors

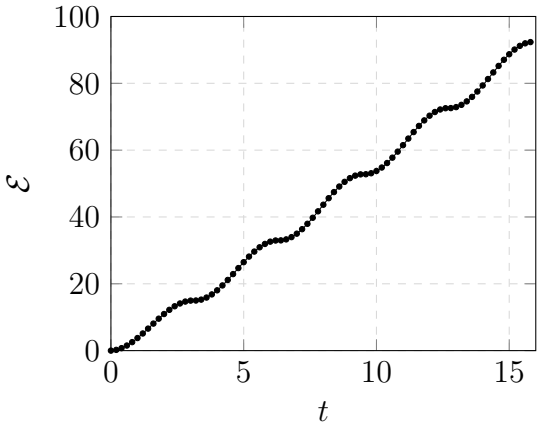

(b) Energy evolution in the inductors

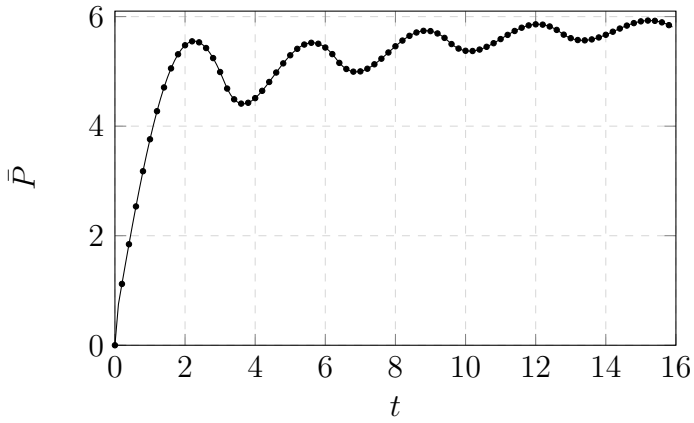

(c) Average power evolution in the inductors

Figure 2.15: Qualitative evolution of the energy-based fields used for the convergence criterion.

our case, real-valued PETSc libraries have been used for the software, thus high effort and low advantages would have been gained by the use of complex-valued libraries in THERCAST®. Consequently, transforming the complex system into a real-equivalent system could be convenient.

Real-equivalent formulation.

Several formulations have been proposed in the literature and they start from the basic *EK* real-valued formulations [110]. These formulations have very different spectral properties, as reported in [111], and their theoretical efficiency could reach the complex system's one [112]. Additional issues arise when these formulations are applied to electromagnetic simulations, whose intrinsic ill-conditioning requires that

the formulations be enhanced in order to be still efficient. This enhancing of the matrix conditioning can be carried out by changing the preconditioning technique [113] or by using different solving algorithm [114, 115, 116]. In order to completely exploit the usage of PETSc libraries, we propose to change the equivalent real formulation itself in order to obtain a better conditioned system in the case of electromagnetic applications, as described in [117].
Real-equivalent formulations are based on the fact that any complex equation can be written as a $[2 \times 2]$ real-valued system:

$$(a+bi)(x+yi) = c+di \quad \Longrightarrow \quad \begin{cases} ax - by = c \\ bx + ay = d \end{cases} \tag{2.62}$$

where $a, b, c, d, x, y \in \Re$ and i is the imaginary unit $i = \sqrt{-1} \in \Im$.
From this scalar observation, it is possible to transform any $[N \times N]$ complex valued system defined as:

$$[\mathbf{A} + \mathbf{B}i]\{x + yi\} = \{b + ci\}$$

into the four real-equivalent formulations described in equation (2.63).

$$\begin{bmatrix} \mathbf{A} & -\mathbf{B} \\ \mathbf{B} & \mathbf{A} \end{bmatrix} \begin{Bmatrix} x \\ y \end{Bmatrix} = \begin{Bmatrix} b \\ c \end{Bmatrix} \tag{2.63a}$$

$$\begin{bmatrix} \mathbf{A} & \mathbf{B} \\ \mathbf{B} & -\mathbf{A} \end{bmatrix} \begin{Bmatrix} x \\ -y \end{Bmatrix} = \begin{Bmatrix} b \\ c \end{Bmatrix} \tag{2.63b}$$

$$\begin{bmatrix} \mathbf{B} & \mathbf{A} \\ -\mathbf{A} & \mathbf{B} \end{bmatrix} \begin{Bmatrix} x \\ y \end{Bmatrix} = \begin{Bmatrix} c \\ -b \end{Bmatrix} \tag{2.63c}$$

$$\begin{bmatrix} \mathbf{B} & \mathbf{A} \\ \mathbf{A} & -\mathbf{B} \end{bmatrix} \begin{Bmatrix} x \\ y \end{Bmatrix} = \begin{Bmatrix} c \\ b \end{Bmatrix} \tag{2.63d}$$

Equations from (2.63a) to (2.63d) are known as $EK1$, $EK2$, $EK3$, $EK4$ respectively [110]. These formulations are equivalent in terms of results, but present very different spectral properties and structures. Let $\Sigma(C)$ denote the spectrum of the original complex matrix $\mathbf{C} = \mathbf{A} + \mathbf{B}i$, and $\bar{\Sigma}(C)$ the set of conjugates of elements of $\Sigma(C)$. The spectrum of the equivalent-real formulations is then $\Sigma(EK) = \Sigma(C) \cup \bar{\Sigma}(C)$. If the complex matrix respects the *half-plane condition*

$$\Sigma(C) \subset \{\lambda \in \mathscr{C} \mid Re\{\lambda\} \geq 0\} \quad \vee \quad \Sigma(C) \subset \{\lambda \in \mathscr{C} \mid Im\{\lambda\} \geq 0\} \tag{2.64}$$

one of $EK1$ and $EK3$ formulations will be positively defined and will also respect the *half-plane condition*, which is a desirable property for many Krylov subspace solvers. Whene considering linear systems rising from the solution of the Maxwell problem, the $EK1$ formulation is the one which is positive defined; thus we decided

to use the non-symmetric $EK1$ formulation instead of a symmetric formulation in order to reach a good solving efficiency. For any further discussion about the spectral properties of EK formulations we refer to [118].

One of the main drawbacks in these formulations is that the final matrix does not conserve the original structure: in FEM (finite element method) applications the global matrix is usually sparse and diagonally dominant, but by splitting this matrix into four sub-blocks we obtain four diagonally dominant blocks which form a non diagonally dominant global matrix. In order to recover the original structure, which is better conditioned, it is possible to apply the EK formulations locally instead of globally, i.e. we replace each complex entry of the matrix by a $[2 \times 2]$ EK matrix instead of replacing the $[N \times N]$ complex-valued matrix with four real valued blocks sized $[N \times N]$.
For the sake of simplicity, let's consider a general $[3 \times 3]$ system:

$$\begin{bmatrix} a_{11}+b_{11}i & a_{12}+b_{12}i & a_{13}+b_{13}i \\ a_{21}+b_{21}i & a_{22}+b_{22}i & a_{23}+b_{23}i \\ a_{31}+b_{31}i & a_{32}+b_{32}i & a_{33}+b_{33}i \end{bmatrix} \begin{Bmatrix} x_1+y_1i \\ x_2+y_2i \\ x_3+y_3i \end{Bmatrix} = \begin{Bmatrix} f_1+g_1i \\ f_2+g_2i \\ f_3+g_3i \end{Bmatrix} \tag{2.65}$$

where $a_{mn}, b_{mn}, x_n, y_n, f_n, g_n \in \Re \, \forall m, n = 1, 2, 3$.
This general complex-valued system can be related to a "*global*" *EK1* formulation (2.66) or to a "*local*" EK1 formulation (2.67).

$$\left[\begin{array}{ccc|ccc} a_{11} & a_{12} & a_{13} & -b_{11} & -b_{12} & -b_{13} \\ a_{21} & a_{22} & a_{23} & -b_{21} & -b_{22} & -b_{23} \\ a_{31} & a_{32} & a_{33} & -b_{31} & -b_{32} & -b_{33} \\ \hline b_{11} & b_{12} & b_{13} & a_{11} & a_{12} & a_{13} \\ b_{21} & b_{22} & b_{23} & a_{21} & a_{22} & a_{23} \\ b_{31} & b_{32} & b_{33} & a_{31} & a_{32} & a_{33} \end{array}\right] \left\{\begin{array}{c} x_1 \\ x_2 \\ x_3 \\ \hline y_1 \\ y_2 \\ y_3 \end{array}\right\} = \left\{\begin{array}{c} f_1 \\ f_2 \\ f_3 \\ \hline g_1 \\ g_2 \\ g_3 \end{array}\right\} \tag{2.66}$$

$$\left[\begin{array}{cc|cc|cc} a_{11} & -b_{11} & a_{12} & -b_{12} & a_{13} & -b_{13} \\ b_{11} & a_{11} & b_{12} & a_{12} & b_{13} & a_{13} \\ \hline a_{21} & -b_{21} & a_{22} & -b_{22} & a_{23} & -b_{23} \\ b_{21} & a_{21} & b_{22} & a_{22} & b_{23} & a_{23} \\ \hline a_{31} & -b_{31} & a_{32} & -b_{32} & a_{33} & -b_{33} \\ b_{31} & a_{31} & b_{32} & a_{32} & b_{33} & a_{33} \end{array}\right] \left\{\begin{array}{c} x_1 \\ y_1 \\ \hline x_2 \\ y_2 \\ \hline x_3 \\ y_3 \end{array}\right\} = \left\{\begin{array}{c} f_1 \\ g_1 \\ \hline f_2 \\ g_2 \\ \hline f_3 \\ g_3 \end{array}\right\} \tag{2.67}$$

Therefore, given a generally diagonally dominant structure of **A** and **B** reported in figure 2.16, we pass from the global (figure 2.17(a)), to the local (figure 2.17(b)) application of the EK formulations. By the use of the local formulation, we are able to focus the elements of the local diagonals (the diagonals of **A** and **B**) on the global diagonal, which allows to use a wider range of preconditioner. On the other side, the global formulation leads to high valued entries far from the main diagonal, which requires special preconditioner to be efficiently solved.

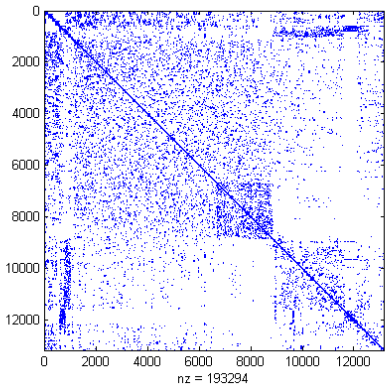

(a) Matrix **A**'s sparsity pattern example

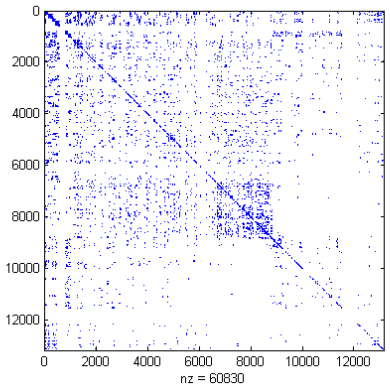

(b) Matrix **B**'s sparsity pattern example

Figure 2.16: Sparsity patterns of a couple of sparse and diagonally dominant matrices corresponding to the matrices used for the validation cases presented in the following paragraphs.

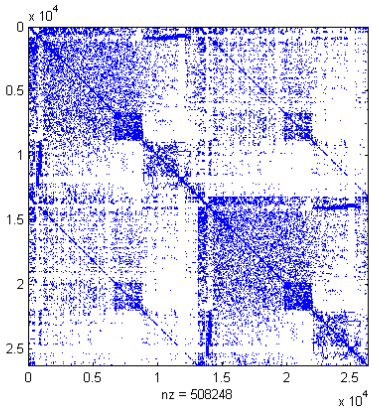

(a) Global *EK1* formulation

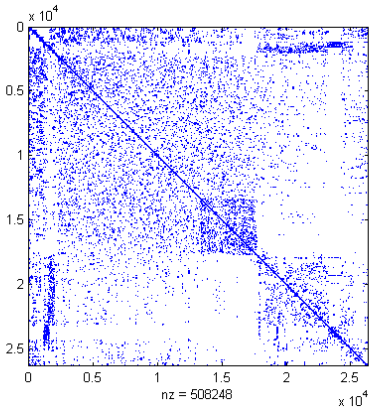

(b) Local *EK1* formulation

Figure 2.17: Sparsity patterns for the EK1 real valued formulation

When simulating a physical problem, **A** and **B** usually arise from different physics of the phenomenon, thus **A** and **B** may present very different eigenvalues and non-zero structures. In this case, the combined matrix according to *EK* formulation usually present worse conditioning properties than the original **A** and **B** matrices themselves. Therefore we can reformulate the *EK1* system (2.63a) by a linear

combination between the lines as following:

$$\begin{matrix}(1)+\beta(2): \\ \beta(1)-\quad(2): \end{matrix}\begin{bmatrix}\mathbf{A}+\beta\mathbf{B} & \beta\mathbf{A}-\mathbf{B} \\ \beta\mathbf{A}-\mathbf{B} & -(\mathbf{A}+\beta\mathbf{B})\end{bmatrix}\begin{Bmatrix}x\\y\end{Bmatrix}=\begin{Bmatrix}b+\beta c\\ \beta b-c\end{Bmatrix} \tag{2.68}$$

where $\beta \in \Re$ is a scalar coupling parameter. In the new EK formulation the symmetry is recovered and the parameter β allows to control the relative magnitude between the different entries in the matrix.

Resolution of the EM problem through real-equivalent formulation.

The real-equivalent method can be used to solve the complex-valued system (2.61) arising from the EM modelling. By applying the *EK1* formulation described in equation (2.63a) we obtain:

$$\begin{bmatrix}\mathbf{R} & \mu\sigma\omega\mathbf{F} \\ -\mu\sigma\omega\mathbf{F} & \mathbf{R}\end{bmatrix}\begin{Bmatrix}Re\{\tilde{\mathbf{A}}\}\\ Im\{\tilde{\mathbf{A}}\}\end{Bmatrix}=\begin{Bmatrix}0\\ \sigma\mu(\nabla\mathbf{\Psi};\mathbf{\Psi})\phi_0\end{Bmatrix}. \tag{2.69}$$

The problems in this formulation stem from the difference of structure and magnitude between the real contributions ($\mathbf{R}$) and the imaginary contributions ($\pm\mu\sigma\omega\mathbf{F}$); while the first is present all over the domain, the second is non-zero only in the elements whose conductivity is different than zero, so not in the air. This difference makes the matrix in system (2.69) very ill-conditioned. So we can enhance the formulation by applying the linear combination proposed in equation (2.68), which leads to the system

$$\begin{bmatrix}\mathbf{R}+\beta\mu\sigma\omega\mathbf{F} & \beta\mathbf{R}-\mu\sigma\omega\mathbf{F} \\ \beta\mathbf{R}-\mu\sigma\omega\mathbf{F} & -(\mathbf{R}+\beta\mu\sigma\omega\mathbf{F})\end{bmatrix}\begin{Bmatrix}Re\{\underline{\tilde{A}}\}\\ Im\{\underline{\tilde{A}}\}\end{Bmatrix}=\begin{Bmatrix}\beta\sigma\mu(\nabla\underline{\Psi};\underline{\Psi})\phi_0\\ -\sigma\mu(\nabla\mathbf{\Psi};\underline{\Psi})\phi_0\end{Bmatrix}. \tag{2.70}$$

The parameter β allows to control the conditioning of the formulation. In this work we propose to smooth the entries by imposing

$$\beta=-\frac{B+A}{B-A}. \tag{2.71}$$

Let's notice that if we apply the global form of $EK1$, A and B are matrices and expression (2.71) is meaningless. But when we apply the local form of $EK1$, A and B are the scalars which compose the $[2\times 2]$ equivalent formulation that replace each entry. Since β must be constant for each couple of lines $(2n-1;2n)$ with $n=1,2,...,N$, we cannot evaluate it separately for each entry, but an average value must be computed by evaluating the contributions coming from $\mathbf{R}$ and $\mathbf{F}$. For

Nedelec FE we can compute the element contribution to the global matrix as:

$$\begin{aligned} \mathbf{A}_{el} = \mathbf{R}_{el} = (\nabla \times \underline{\Psi}; \nabla \times \underline{\Psi}) = \frac{2}{3\alpha h_R^4} \mathbb{M}_R(\alpha) \\ \mathbf{B}_{el} = \sigma\omega\mu_0 \mathbf{F}_{el} = \sigma\omega\mu_0 (\underline{\Psi}; \underline{\Psi}) = \sigma\omega\mu_0 \frac{1}{30\alpha h_F^2} \mathbb{M}_F(\alpha) \end{aligned} \tag{2.72}$$

where h_R and h_F are characteristic values of the mesh in the whole domain and in the conductor respectively, α is the element's shape factor and $\mathbb{M}_R(\alpha)$ and $\mathbb{M}_F(\alpha)$ are 6×6 coefficients matrices. Similarly, the eigenvalues of the element matrices are computed as:

$$eig(\mathbf{R}_{el}) = \frac{2}{3\alpha h_R^4} \underline{v}_R(\alpha); \qquad eig(\sigma\omega\mu_0 \mathbf{F}_{el}) = \sigma\omega\mu_0 \frac{1}{30\alpha h_F^2} \underline{v}_F(\alpha); \tag{2.73}$$

where $\underline{v}_R(\alpha)$ and $\underline{v}_F(\alpha)$ are vectors of coefficients. For the complete development, please refer to [102]. By considering isotropic elements, i.e. $\alpha = 1$, we are able to estimate the contribution coming from the two different matrices and to calculate the constant averaged smoothing parameter β as:

$$\beta = -\frac{\sigma\omega\mu_0 h_R^4 + 20 h_F^2}{\sigma\omega\mu_0 h_R^4 - 20 h_F^2} \tag{2.74}$$

obtained by replacing each matrix in equation (2.71) by its maximum eigenvalue. The main advantage arising from using this kind of approach is that no loop over the time steps is needed. In figure 2.18 the resolution scheme for system (2.41) is resumed. When the system is solved in the time domain, the resolution of the real valued system is inside two loops: one loop over the electromagnetic periods to reach the steady state, and the second over the time steps inside each period. On the other side, the solution in the frequency domain requires to solve the complex valued system just once and then apply this solution (the phasor of $\underline{A}$) to a certain number of time steps.

Numerical procedures and Validation of the real-equivalent approach.

All the developments presented in the present work are introduced in Matelec®, which is the electromagnetic module used by the commercial software application Forge®. The assembly, parallelization, preconditioning are performed by PETSc libraries. The preconditioning algorithm is the classic Jacobi, while the system is solved by fGMRES [119] algorithm. All the simulations were performed on a CPU Intel®i7-3770. The reference case is depicted in figure 2.13 and it has been used in two configurations: with or without a metallic core.

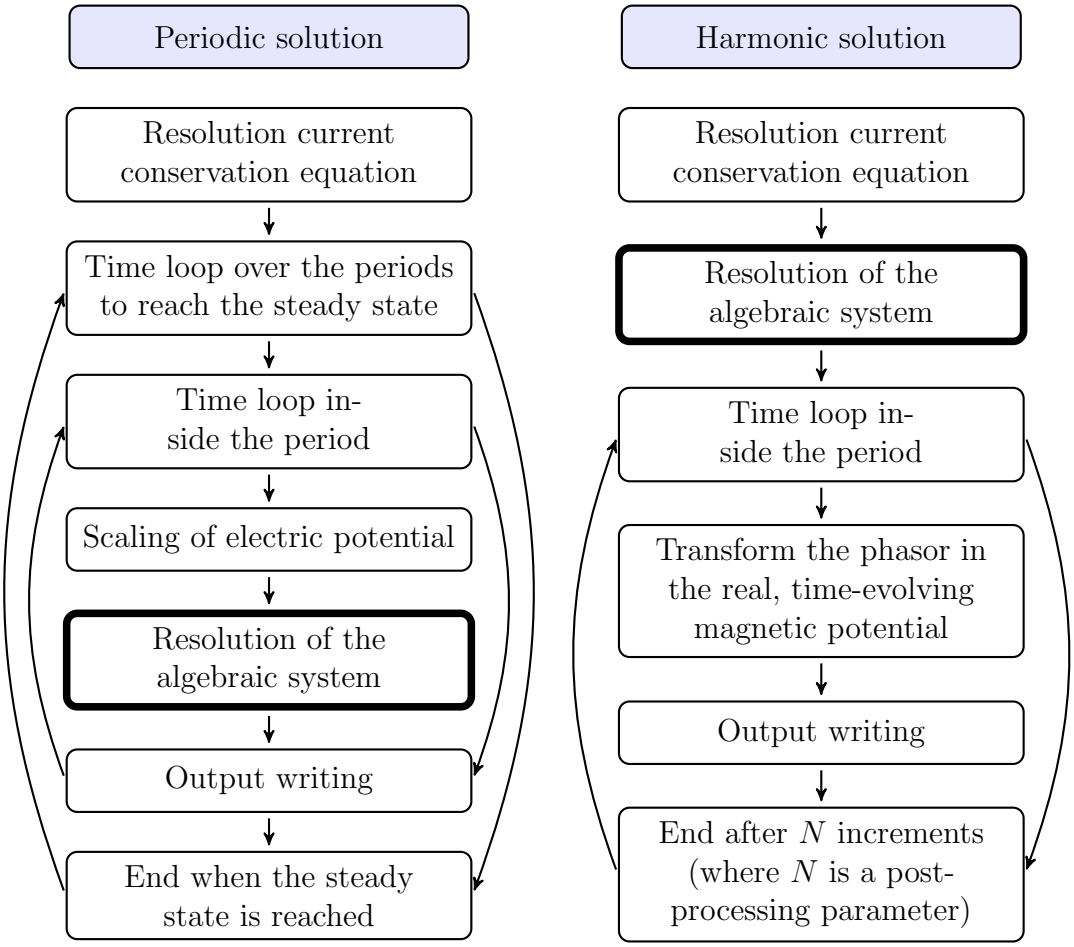

Figure 2.18: Comparison between the flow of computation to solve system (2.41) in the time domain (periodic approach) or in the frequency domain (harmonic approach)

Air-core solenoid. The problem's configuration is very similar to the one described for figure 2.13, with the difference that a $100\,mm$ thick layer of air was considered around the solenoid and that the copper cylinder has been replaced with air. The mesh is composed of 19360 nodes, 100862 elements and 124706 edges: a sketch of the global mesh is shown in figure 2.13(b). The reference is the value of the magnetic induction field evaluated at the central axis of the coil: for any infinitely long solenoid it is analytically calculated as:

$$B^{\infty} = \mu n I^{RMS} = 0.4188790205\,T \tag{2.75}$$

where n is the spire density and I^{RMS} is the *root mean square* of the AC current. The second reference used to validate the results is the integral of the vertical component of $\underline{B}$ at the center of the solenoid in a quarter of electromagnetic period. The two errors, i.e. the error on the magnetic field ($ErrB$) and on its integral ($ErrI$), were computed in norm L^2

In figures 2.19 and 2.20 a comparison between the numerical and analytical results is proposed. In figure 2.19 we notice that no gain in accuracy is achieved when the number of time-steps per period is increased. Since the air core has zero-conductivity, the magnetic field is not perturbed by induced eddy currents and and is easily predicted even by a small number of time-steps. In the case of resolution in the time domain (EE and QSSC) the error fast converges to the value $6.09E-06$ which is due to the spatial approximation. The results obtained in the frequency domain are in accordance with the analytical prediction as well. Four time-steps per period were used in order to catch the maximum, minimum and zero levels in the period, but we remark again that it is just a post-process choice. In figure 2.20 we see that the error of the integral follows the linear interpolation in time, so it converges as $\mathcal{O}(\Delta t^2)$. In this case, the harmonic solution can be post-process in a higher number of time-steps to reach the expected precision.

The computational time required by the harmonic solver is half of the time required by the time-evolving approaches, as plotted in figure 2.21. This gain in time is due to the fact that the system is solved only once instead of, in the case of 16 time-steps, 48 times. In addition the final equivalent real system has good properties because it is barely affected by $\mathbf{F}$ (present only in the conductive part of the domain).

The computational time does not change linearly with the time step because the time step plays a role in the conditioning of the system, affecting the number of linear iterations needed to solve the system at each time step. In figure 2.22 the actual CPU time is compared to the potential linear evolution computed from the results obtained with higher time-steps. It is clear that the optimal time discretization is the division of the period in 64 steps independently from the adopted time-scheme.

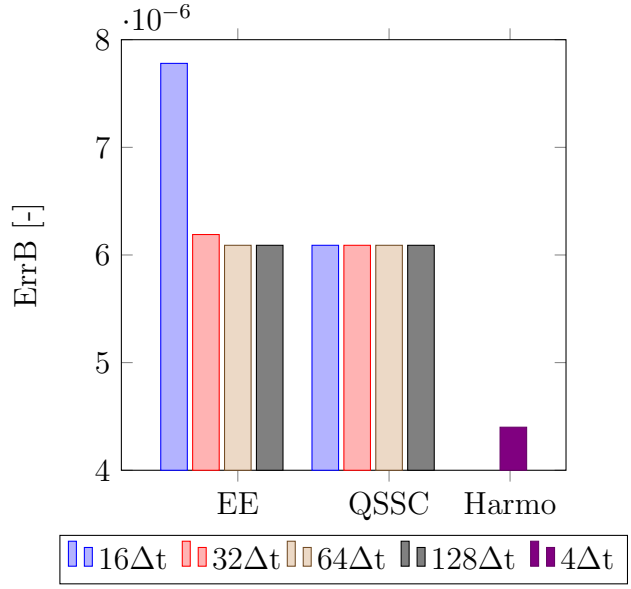

Figure 2.19: Error of the predicted value of B in comparison with the analytical solution.

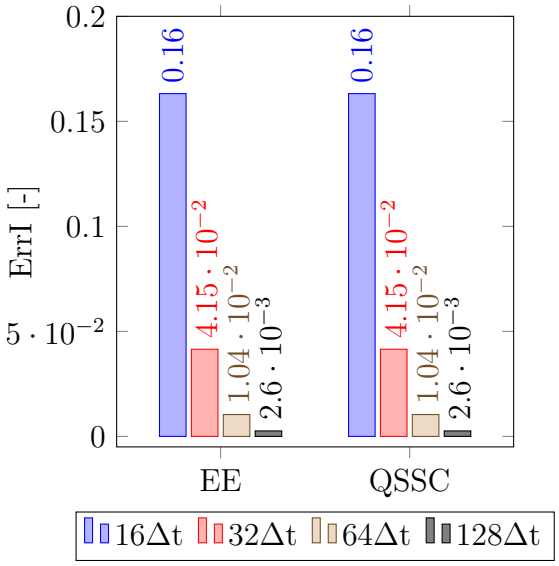

Figure 2.20: Error of integral of the predicted value of B in comparison with the analytical solution over a quarter of period.

In figure 2.23 it is shown how the time-discrete solutions need more than one period to reach the steady state, while the solution in the frequency domain is naturally steady. Despite the differences in the results obtained at the beginning

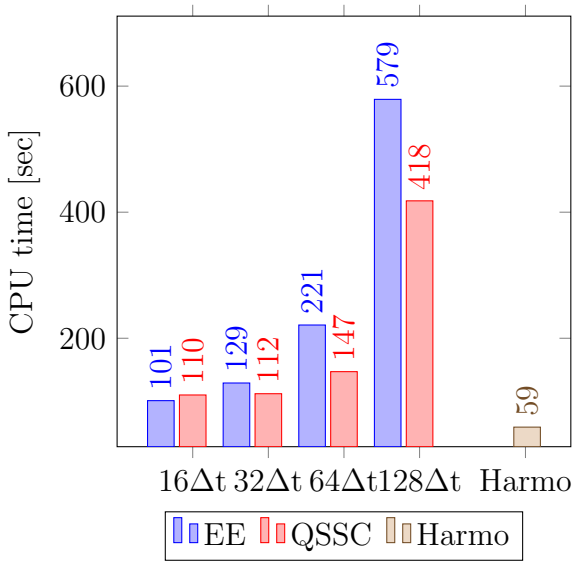

Figure 2.21: Computing time over 1 CPU

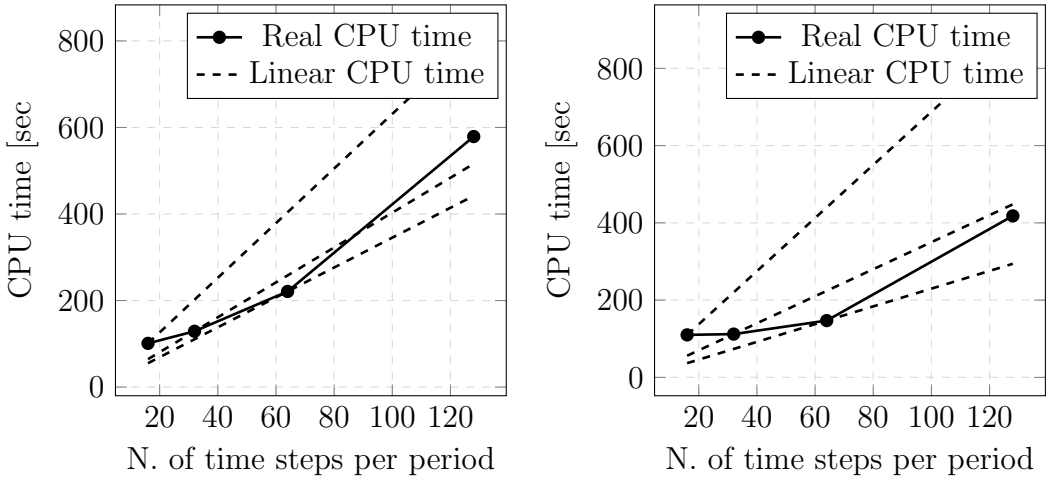

(a) Comparison between actual CPU time and its potentially linear evolution with explicit Euler scheme

(b) Comparison between actual CPU time and its potentially linear evolution with QSSC scheme

Figure 2.22: Comparison between actual CPU time and its potentially linear evolution with different time-schemes in the air-cored solenoid case.

of the computation, we see that the differences once the steady state is reached are minimal.

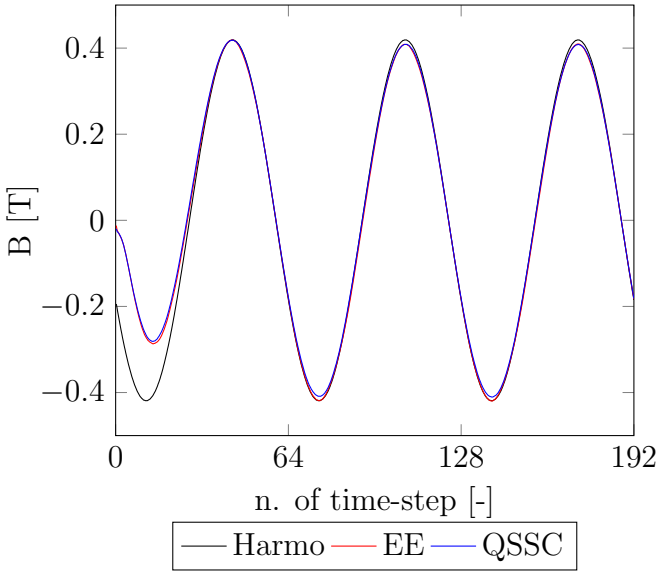

Figure 2.23: Variation of the vector B on solenoid's axis over the time-steps.

Metallic-core solenoid. The second case has the same layout: the same solenoid in the same domain, but the air inside the solenoid was replaced by a para-magnetic copper cylinder, whose surface was insulated from the current in the wire. Its conductivity was set to $\sigma = 5\,E07\,S/m$ and $\mu_r = 1\,H/m$. The mesh is composed of 22598 nodes, 119278 elements and 146268 edges. The case of the metallic-core solenoid is also interesting because it both maintains its geometrical simplicity and introduces a region in the domain where induced eddy current can develop. From a purely algebraic point of view, the introduction of the metallic part increases the ill-conditioning due to the $\beta\mu\sigma\omega\mathbf{F}$ term in equation (2.70).
These two reference cases were simulated by using different temporal schemes with different time steps and the harmonic solver.
The magnitude of vector B in the center of the solenoid is reported in figure 2.24: differently from the first test case (figure 2.19), we notice that the solution is dependent over the time-step used to discretize the period. Both algorithms seem seem to converge to the same value, which is approximately coincident with the value obtained by the harmonic resolution. The solution obtained by using QSSC time-scheme is closer to the convergence value and the difference between the two results (with the same amount of time-steps) is between 4% and 0.8%. This is the first effect of the metal core: the induced eddy currents perturb the propagation of the magnetic field, so the time-discretization is more important than before to catch this phenomenon. In term of error on the integral, we see from figure 2.25 that the two solutions converge to the correct integral, but less than $\mathcal{O}(h^2)$. So, in this case more than before, a great advantage could be taken from the large amount

of time-steps obtained in the post-processing of the harmonic resolution.

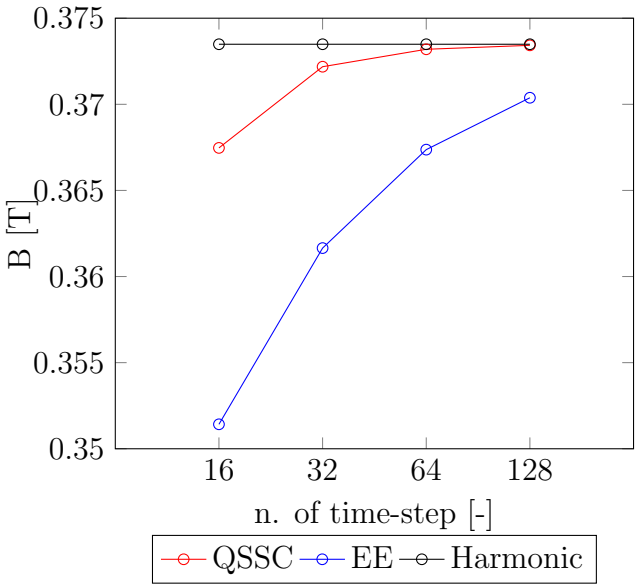

Figure 2.24: Magnitude of the vector B on solenoid's axis over the time-steps used to discretize the period.

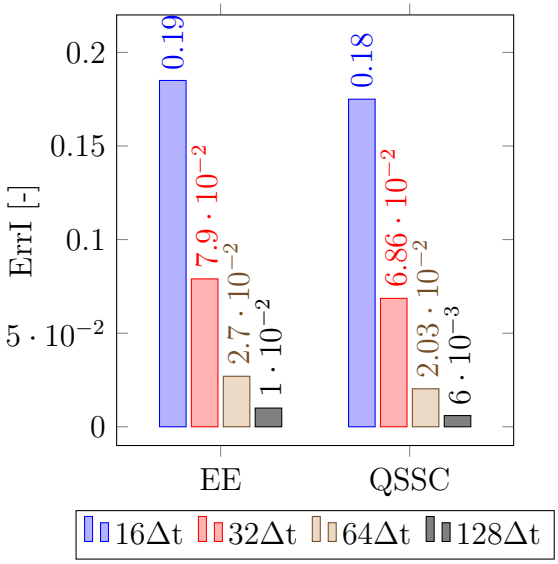

Figure 2.25: Error of integral of the predicted value of B in comparison with the theoretical sinusoidal solution over a quarter of period.

The presence of the conductor makes the conditioning of the problem worse. As

it is shown in figure 2.26, the average time to perform the simulation is much higher than before: this is partially due to the increase of degrees of freedom (+17% of edges), but mainly to the bad conditioning deriving from the conductive part of the domain. Notice also that EE takes less time to finish when it uses $64\,\Delta t$ instead of $32\,\Delta t$, since it takes one period less to reach the steady state. In this framework, the harmonic approach faces the major problems of conditioning: the time needed to reach convergence is about 50 times the case with the air-core. Despite this problem, let's note in figure 2.28 that the modification made on the equivalent-real formulation has sensibly increased the convergence rate; while convergence was obtained in more than 1000000 iterations (and hours of computing) in the original *EK1* formulation, the new formulation reaches convergence after 55000 iterations and 1280 *sec* .

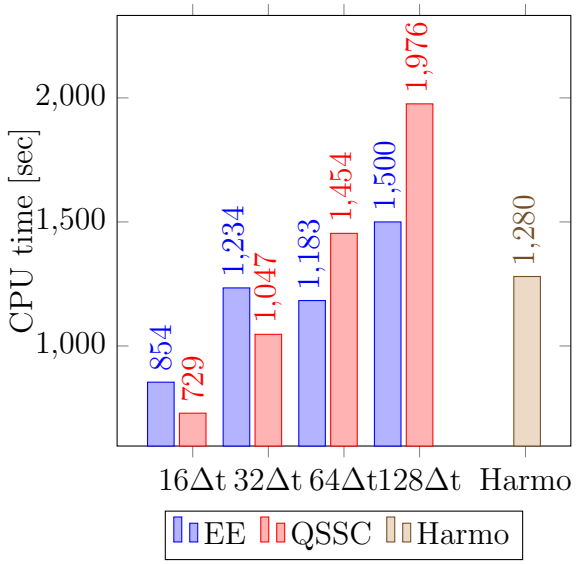

Figure 2.26: Computing time over 1 CPU

In figure 2.27 the actual CPU time is compared to the potential linear evolution computed from the results obtained with higher time-steps. In this case the solver benefits from the decrease of the time step, thus the optimal time step is smaller than 1/128 of the period. The difference between figures 2.22 and 2.27 is due to the fact that the solution in the air is highly regular, while the propagation of eddy currents inside the metal core produce perturbations which make the linear solve convergence more challenging.

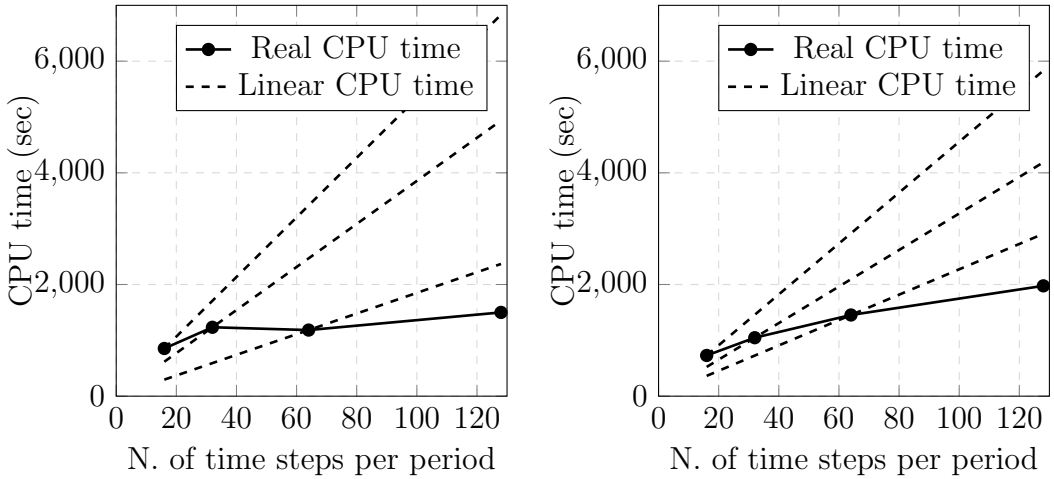

(a) Comparison between actual CPU time and its potentially linear evolution with explicit Euler scheme

(b) Comparison between actual CPU time and its potentially linear evolution with QSSC scheme

Figure 2.27: Comparison between actual CPU time and its potentially linear evolution with different time-schemes in the metal-cored solenoid case.

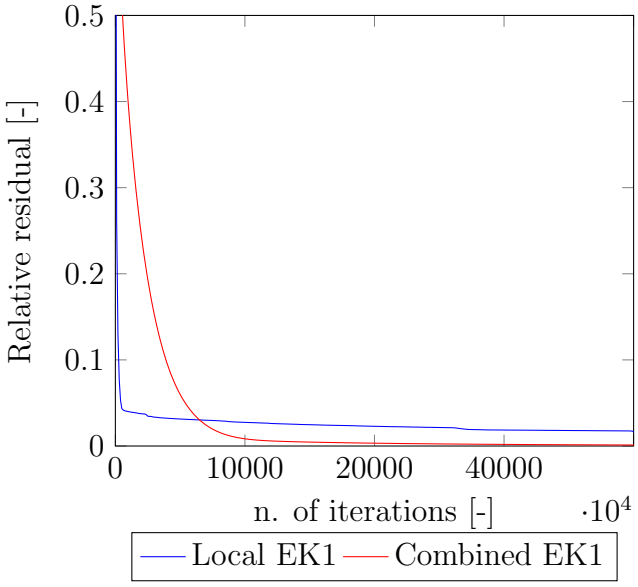

Figure 2.28: Comparison between the convergence of the original EK1 real-equivalent formulation and the modified one

Final comments on the time integration scheme.

In this work both the resolution in the time domain and in the frequency domain have been used. The proposed real equivalent formulation is more efficient than

the periodic resolution when no metallic piece is present in the domain (not the case of EMS) or when only one frequency have been used for the induction (which is the case of AC stirring). For more complex EM configurations such as stirring by TMF or RMF, the integration in the time domain is more efficient in term of computational time and thus it has been preferred to the harmonic resolution.

2.5 Conclusions

In this chapter we have presented the numerical methods used to solve the EM problem. The existing software based on edge finite elements have been explained.
A comparison of different constitutive models and implementation of the model which better fits the industrial applications simulated in this work.
Then we have studied the elements which affect the choice of the air domain to be modelled around the electromagnetically active parts. This study is a contribution helps to understand how to correctly model the desired process and has to be considered as a contribution to the "best practice" of THERCAST®.
The time-dependent resolution algorithm already implemented has been enhanced with a new convergence criteria, which better fits the coupling strategy chosen for the simulation of EMS.
Finally, the resolution of the EM problem in the frequency domain ha been implemented. The complex-valued system has been solved by a local real-equivalent formulation proposed in this work.

Chapter 3

Fluid Mechanics

Contents

3.1 Résumé du chapitre en français

Dans ce chapitre, on décrit la modélisation du problème de mécanique des fluides. Dans la première partie, on montre la formulation analytique du problème basé sur les équations de Navier-Stokes pour des écoulements incompressibles. La résolution de ce système d'équations aux dérivées partielles a été faite au moyen de la méthode des éléments finis. La formulation mixte classique de Galerkin a été modifiée, et le système a été reformulé selon une approche variationelle multi-échelle (VMS-Variational Multiscale). Cette formulation garantit une stabilisation naturelle du

problème numérique dans les régimes de convection dominante et de simuler la turbulence à un niveau d'efficacité comparable à celui des méthodes LES. Dans la partie centrale de ce chapitre, on étend cette approche à des écoulements multiphasiques dont les phases sont suivies par l'intermédiaire de la méthode level-set. Cette méthode, très classique, a été renforcée par le développement de différentes techniques numériques (réinitialisation convective, filtrage de la fonction level-set, correction de la level-set pour garantir la conservation de masse dans le domaine). En fin chapitre, on montre la technique d'adaptation anisotrope du maillage qui permet d'adapter dynamiquement le maillage à la physique du problème et à la solution de l'écoulement.

3.2 Governing equations

Let's consider the motion of a Newtonian fluid in a region $\Omega \subset \mathcal{R}^3$ and a time period $[0;T]$; its dynamics can be described by the velocity $\underline{u}(\underline{x},t)$ and the pressure $p(\underline{x},t)$ fields which satisfy the momentum and mass conservation of the system:

$$\frac{\partial}{\partial t}(\rho\underline{u}) + \nabla\cdot(\rho\underline{u}\otimes\underline{u}) = s_1 \quad \text{in } \Omega\times[0;T] \tag{3.1a}$$

$$\frac{\partial}{\partial t}\rho + \nabla\cdot(\rho\underline{u}) = s_2 \quad \text{in } \Omega\times[0;T], \tag{3.1b}$$

where ρ is the fluid mass density, and s_1 and s_2 are the source/sink terms for momentum and mass respectively.

3.2.1 Mass continuity equation

Equation (3.1b) represents the mass balance within an infinitesimal volume and through its boundaries. It can be re-written in terms of material derivative as:

$$\frac{D\rho}{Dt} - \underline{u}\cdot\nabla\rho + \nabla\cdot(\underline{u}\rho) = s_2. \tag{3.2}$$

The first term (i.e. $D\rho/Dt$) is related to the compressibility of the fluid. We know from the internal fluid-dynamics principles that fluids behave as incompressible when the following condition is satisfied:

$$\mathcal{M} = \frac{u}{c} < 0.3, \tag{3.3}$$

being $\mathcal{M}$ the Mach number and c the speed of sound in the medium. The speed of sound can be directly deduced from the material's compressibility at isentropic conditions β_S:

$$c = \sqrt{\frac{1}{\rho \beta_S}}. \tag{3.4}$$

In the case of liquid steel, we have $\beta_S \approx 6.25 \times 10^{-12}$, thus the speed of sound is $c \approx (4600 \div 4820) m/s$ and the incompressibility condition

$$u < 0.3\, c = 1380\, m/s \tag{3.5}$$

is satisfied for industrial applications. Thus, we can state that any material particle has constant density, hence equation (3.2) can be simplified to

$$-\underline{u} \cdot \nabla \rho + \nabla \cdot (\underline{u} \rho) = s_2, \tag{3.6}$$

$$-\underline{u} \cdot \nabla \rho + \rho \nabla \cdot \underline{u} + \underline{u} \cdot \nabla \rho = s_2, \tag{3.7}$$

and finally

$$\nabla \cdot \underline{u} = 0 \tag{3.8}$$

under the assumption of no mass sink nor source.

3.2.2 Momentum conservation equation

Equation (3.1a) can be developed as following:

$$\underline{u} \frac{\partial \rho}{\partial t} + \rho \frac{\partial}{\partial t} \underline{u} + (\underline{u} \otimes \underline{u}) \cdot \nabla \rho + \rho \underline{u} \cdot \nabla \underline{u} + \rho \underline{u} \nabla \cdot \underline{u} = \underline{s}_1, \tag{3.9}$$

which can be further re-arranged in the form

$$\underline{u} \left(\frac{\partial \rho}{\partial t} + \nabla \cdot (\rho \underline{u}) \right) + \rho \left(\frac{\partial}{\partial t} \underline{u} + \underline{u} \cdot \nabla \underline{u} \right) = \underline{s}_1. \tag{3.10}$$

By substitution of the continuity equation (3.1b) in equation (3.10), we obtain

$$\rho \left(\partial_t \underline{u} + \underline{u} \cdot \nabla \underline{u} \right) = \underline{s}_1, \tag{3.11}$$

where the "$\partial / \partial t$" operator has been replace by "∂_t" for notation's simplicity. For Newtonian fluids, equation (3.11) can be re-written by developing the source term:

$$\rho \left(\partial_t \underline{u} + \underline{u} \cdot \nabla \underline{u} \right) = \nabla \cdot \underline{\underline{\sigma}} + \underline{f}, \tag{3.12}$$

being $\underline{\underline{\sigma}}$ the Cauchy stress tensor and $\underline{f}$ the external volumetric load.
The Cauchy stress tensor can be computed according to the following constitutive equation:

$$\underline{\underline{\sigma}} = 2\mu \underline{\underline{\varepsilon}}(\underline{u}) - p \underline{\underline{I}} \tag{3.13}$$

where μ is the dynamic viscosity, $\underline{\underline{I}}$ is the identity tensor, and p is the pressure. The strain rate tensor $\underline{\underline{\varepsilon}}(\underline{u})$ is defined as:

$$\underline{\underline{\varepsilon}}(\underline{u}) := \frac{1}{2}\left(\nabla\underline{u} + \nabla^T\underline{u}\right). \tag{3.14}$$

Thus, the momentum conservation equation can be written as:

$$\rho\left(\partial_t\underline{u} + \underline{u}\cdot\nabla\underline{u}\right) - 2\mu\nabla\cdot\underline{\underline{\varepsilon}}(\underline{u}) + \nabla p = f. \tag{3.15}$$

3.2.3 Boundary and initial conditions

The initial condition on velocity at $t = 0$ must satisfy $\nabla\cdot\underline{u}_0 = 0$ in order to obtain a well-posed problem and has the following form:

$$\underline{u} = \underline{u}_0 \quad \text{in}\,\Omega\times(0). \tag{3.16}$$

On the opposite, no initial condition on the pressure is needed for incompressible flows.
Let's define Γ as the boundary of Ω and introduce the following sub-division of the boundary:

$$\Gamma_D\cup\Gamma_N = \Gamma \wedge \Gamma_D\cap\Gamma_N = \emptyset, \tag{3.17}$$

where Γ_D and Γ_N are the portions of the boundary on which Dirichlet and Neumann boundary conditions will be applied. The general set of mixed boundary conditions are defined as follow:

$$\underline{u}(\underline{x},t) = \underline{u}_D \quad \forall(\underline{x},t)\in\Gamma_D\times(0,T) \tag{3.18a}$$
$$\hat{n}\cdot\underline{\underline{\sigma}}(\underline{x},t) = h_N \quad \forall(\underline{x},t)\in\Gamma_N\times(0,T) \tag{3.18b}$$

with $\hat{n}$ being the unit outward vector to Γ_N.
From the application point of view (e.g. in-mould flow) we have the following cases:

- The inflow boundary, modelled through a Dirichlet boundary condition or a non-homogeneous Nuemann condition.
- The outflow boundary, for which several approaches have been proposed in the literature. Uniform and non-uniform Dirichlet boundary condition [28] are widely used, but also homogeneous or negative Neumann conditions are.
- Wall condition, usually modelled through a non-slip Dirichelt boundary condition, i.e. $u_\perp = 0$.

- Pressure condition, which is needed when only Dirichlet boundary conditions on velocity are imposed. In this situation, the computed pressure is scaled of an arbitrary factor and has no unique solution. This kind of system is physically equivalent to a closed system, so a reference value of pressure should be given. For this reason, an homogeneous Dirichlet condition on the pressure should be applied to one arbitrary point of the boundary.

3.3 Numerical resolution

In this work, a finite element method (FEM) approach has been used to solve the Navier-Stokes equations. The function spaces for the velocity, the weighting function space and the scalar function space for the pressure are respectively defined by:

$$\begin{cases} \mathcal{V} = \left\{ \underline{u} |\, \underline{u} \in \left(H^1(\Omega)\right)^d \,|\, \underline{u} = \underline{g} \; on \; \Gamma_D \right\} \\ \mathcal{W} = \left\{ \underline{w} |\, \underline{w} \in \left(H^1(\Omega)\right)^d \,|\, \underline{u} = 0 \; on \; \Gamma_D \right\} \\ \mathcal{Q} = \left\{ p |\, p \in L^2(\Omega) \right\}. \end{cases} \tag{3.19}$$

Let us now introduce the following integral notation:

$$(a, b) := \int_\Omega ab \, dx. \tag{3.20}$$

After applying the Green theorem, we can derive the weak form of equations (3.15) and (3.8) consisting in finding $(\underline{u}, p) \in (\mathcal{V}, \mathcal{Q})$ so that

$$\begin{cases} (\rho \partial_t \underline{u}, \underline{w}) + (\rho \underline{u} \cdot \nabla \underline{u}, \underline{w}) + (2\mu \underline{\underline{\varepsilon}}(\underline{u}) : \underline{\underline{\varepsilon}}(\underline{w})) - (p, \nabla \cdot \underline{w}) = (\underline{f}, \underline{w}) + (h_N, \underline{w})_{\Gamma_N} \\ (\nabla \cdot \underline{u}, q) = 0 \end{cases}. \tag{3.21}$$

The discretization has been done by the classic Galerkin approach; the domain has been subdivided in tetrahedral (for $\Omega \subset \mathcal{R}^3$) and triangular (for $\Omega \subset \mathcal{R}^2$) $\mathcal{P}^1$ elements so that

$$K_i \subset \mathcal{T}_h \cong \Omega, \tag{3.22}$$

being K_i the i-th element.. Using this partition, the above-defined functional spaces are approximated to finite dimensional spaces panned by continuous piecewise polynomials defined as

$$\begin{cases} \mathcal{V}_h = \left\{ \underline{u}_h \in \left(C^0(\Omega)\right)^d \wedge \underline{u}_{h|K} \in P^1(K)^d, \forall K \in (T)_h \right\} \\ \mathcal{W}_{h|\Gamma} = \left\{ \underline{w}_h \in \mathcal{V} \wedge \underline{w}_{h|\Gamma} = 0 \right\} \\ \mathcal{Q}_h = \left\{ q_h \in \left(C^0(\Omega)\right) \wedge q_{h|K} \in P^1(K), \forall K \in (T)_h \right\}. \end{cases} \tag{3.23}$$

The Galerkin discrete problem consists now in solving the mixed problem by finding $(\underline{u}_h, p_h) \in (\mathcal{V}_h, \mathcal{Q}_h)\ \forall (\underline{w}_h, q_h)$ such that

$$\begin{cases} (\rho \partial_t \underline{u}_h, \underline{w}_h) + (\rho \underline{u}_h \cdot \nabla \underline{u}_h, \underline{w}_h) + (2\mu \underline{\underline{\varepsilon}}(\underline{u}_h) : \underline{\underline{\varepsilon}}(\underline{w}_h)) - (p_h, \nabla \cdot \underline{w}_h) = (\underline{f}, \underline{u}_h) + \\ \qquad\qquad\qquad\qquad\qquad\qquad\qquad\qquad\qquad\qquad\qquad\qquad (h_N, \underline{w}_h)_{\Gamma_N} \\ (\nabla \cdot \underline{u}_h, q_h) = 0. \end{cases} \tag{3.24}$$

The finite element approximation described in equation (3.24) may fail because of two reasons. The first reason is the dominance of the non-linear convective term which may yield to spurious oscillation and spoil the final solution. The second main problem is the fail in satisfying the convergence criterion for mixed finite elements, namely the inf-sup (or Babuska-Brezzi) condition [120]. This condition requires an appropriate pair of function spaces for the approximation of velocity and pressure, which should respect the following criterion:

$$\inf_{q_h \in \mathcal{Q}_h} \sup_{u_h \in \mathcal{V}_{h|\Gamma}} \frac{(\nabla \cdot \underline{u}_h, q_h)_\Omega}{|q_h|_0 \, |\underline{u}_h|_1} \geq \beta > 0 \tag{3.25}$$

with β being a constant independent of h.
It is well know that the P1-P1 Galerkin approximation for the velocity and pressure functional domains does not respect the inf-sup condition. For this reason a stabilization algorithm can be used to guarantee the convergence of the solution.

3.3.1 Variational Multiscale Method (VMS)

Once system (3.24) is obtained, we need three modelling steps to reach a robust and efficient model:

- **Choice of the Galerkin spaces**. As stated before, we know that the P1-P1 modelling does not respect the inf-sup condition. On the other hand, this is the simplest choice to implement and the most competitive in terms of computational effort, thus we would like to enhance this formulation to make it comply with the inf-sup condition. This enhancement can be achieved by introducing the so called "MINI" element and the consequent static condensation, as already proposed for the Stokes [121, 122] and Navier-Stokes [123, 124] problems.

- **Turbulence model**. In-mould flow is often characterized by a Reynolds number $Re \approx 2 \times 10^6$, for which full turbulence is normally developed in the flow. Direct numerical simulation (DNS) of system (3.24) is impossible from the practical point of view because of the high required computational effort. In order to model all the scales of turbulence, the minimum mesh size should

be of the same order of magnitude with the minimum turbulence scale; this quantity is computed by the Kolmogorov theory as

$$\eta = \left(\frac{\nu^3}{\varepsilon}\right)^{1/4} \tag{3.26}$$

where ν is the kinematic energy and ε is the rate of energy dissipation. The turbulence scale is, in our case (as well in the majority of industrial cases) too small to be directly solved. For this reason, a turbulence model is needed to simulate the transient flow regime without the need of an explicit model of all turbulence's scales.

In this section, the time-dependent Navier-Stokes problem will be solved via a variation multiscale approach proposed firstly by T. Hughes [125, 126] and lately applied to highly turbulent flows [127]. The VMS formulation will enrich the functions' spaces and provide a natural stabilization, avoiding the spurious solutions for convection dominated regimes. The VMS formulation also satisfies the inf-sup condition. on the contrary of classic Galerkin formulations. Finally, this formulation has been proofed to be equivalent to LES methods [128] for the modelling of turbulence effects. The effect of the small scale turbulence is modelled implicitly, without the need of its explicit resolution.
The basic idea is to split the unknown functional spaces in two parts, corresponding to different modelling scales: the resolvable coarse-scale and unresolved fine-scale so that $\underline{u} = \underline{u}_h + \tilde{\underline{u}}$ and $p = p_h + \tilde{p}$. Likewise, we apply the same decomposition for the shape functions $\underline{w} = \underline{w}_h + \tilde{\underline{w}}$ and $q = q_h + \tilde{q}$.

The unresolved fine-scales are modelled using residual based terms that are derived consistently. The static condensation consists of substituting the fine-scale solution into the large-scale problem providing additional terms, tuned by a local stabilizing parameter. These stabilizing terms enhance the classic Galerkin formulation and improve the method's stability. The enrichment of the functional spaces is performed as follows: $\mathcal{V} = \mathcal{V}_h \oplus \tilde{\mathcal{V}}$, $\mathcal{W}_0 = \mathcal{W}_{h|\Gamma} \oplus \tilde{\mathcal{W}_{h|\Gamma}}$ and $\mathcal{Q} = \mathcal{Q}_h \oplus \tilde{\mathcal{Q}}$. Thus, the mixed-finite element approximation of problem (3.24) can be written as:

find $(u, p) \in (\mathcal{V}, \mathcal{Q})$ such that

$$\begin{cases} \left(\rho\dfrac{\partial(\underline{u}_h + \tilde{\underline{u}}_h)}{\partial t}, \underline{w}_h + \tilde{\underline{w}}_h\right) + \left(\left(\rho\underline{u}_h + \tilde{\underline{u}}_h \cdot \nabla\left(\underline{u}_h + \tilde{\underline{u}}_h\right), \underline{w}_h + \tilde{\underline{w}}_h\right) + \right. \\ \quad - \left(p_h + \tilde{p}, \nabla \cdot \left(\underline{w}_h + \tilde{\underline{w}}_h\right)\right) + \left(2\mu\underline{\underline{\varepsilon}}(\underline{u}_h + \tilde{\underline{u}}_h) : \underline{\underline{\varepsilon}}(\underline{w}_h + \tilde{\underline{w}}_h)\right) = \left(\underline{f}, \underline{w}_h + \tilde{\underline{w}}_h\right) + \\ \quad \left. + \left(h_N, \underline{w}_h + \tilde{\underline{w}}_h\right)_{\Gamma_N} \quad \forall \underline{w}_h + \tilde{\underline{w}}_h \in \tilde{\mathcal{W}}_0 \right. \\ \\ \left(\nabla \cdot \left(\underline{u}_h + \tilde{\underline{u}}_h\right), q_h + \tilde{q}_h\right) = 0 \quad \forall q_h + \tilde{q}_h \in \mathcal{Q}_h \oplus \tilde{\mathcal{Q}}. \end{cases} \tag{3.27}$$

This system can be split into two sub-problems, namely the coarse-scale problem and the fine-scale problem, as follows:

Coarse-cale problem

$$\begin{cases} \left(\rho\dfrac{\partial(\underline{u}_h+\underline{\tilde{u}}_h)}{\partial t},\underline{w}_h\right)+(\rho(\underline{u}_h+\underline{\tilde{u}}_h)\cdot\nabla(\underline{u}_h+\underline{\tilde{u}}_h),\underline{w}_h)-(p_h+\tilde{p},\nabla\cdot\underline{w}_h)+ \\ \quad+\left(2\mu\underline{\underline{\varepsilon}}(\underline{u}_h):\underline{\underline{\varepsilon}}(\underline{w}_h)\right)=\left(\underline{f},\underline{w}_h\right) \quad \forall\underline{w}_h\in\mathcal{W}_0 \\ \\ (\nabla\cdot(\underline{u}_h+\underline{\tilde{u}}_h),q_h)=0 \quad \forall q_h\in\mathcal{Q}_h. \end{cases} \tag{3.28}$$

Fine-scale problem

$$\begin{cases} \left(\rho\dfrac{\partial(\underline{u}_h+\underline{\tilde{u}}_h)}{\partial t},\underline{\tilde{w}}_h\right)+(\rho(\underline{u}_h+\underline{\tilde{u}}_h)\cdot\nabla(\underline{u}_h+\underline{\tilde{u}}_h),\underline{\tilde{w}}_h)-(p_h+\tilde{p},\nabla\cdot\underline{\tilde{w}}_h)+ \\ \quad\left(2\mu\underline{\underline{\varepsilon}}(\underline{\tilde{u}}_h):\underline{\underline{\varepsilon}}(\underline{\tilde{w}}_h)\right)=\left(\underline{f},\underline{\tilde{w}}_h\right) \quad \forall\underline{\tilde{w}}_h\in\tilde{\mathcal{W}}_0 \\ \\ (\nabla\cdot(u_h+\tilde{u}),\tilde{q}_h)=0 \quad \forall\tilde{q}_h\in\tilde{\mathcal{Q}}. \end{cases} \tag{3.29}$$

At this level, three assumptions may be done to deal with the non-linearity of the momentum equation:

- the subscales are not tracked in time, hence a quasi-static approximation has been adopted in this work. This choice is justified by the fact that the subscale equation remains quasi time-dependent since it is driven by the large-scale time-dependent residual
- the non-linearity linked to the convective term has been treated by ignoring the convective contribution of the small-scale velocity, hence: $(\underline{u}_h+\underline{\tilde{u}}_h).\nabla(\underline{u}_h+\underline{\tilde{u}}_h)\approx\underline{u}_h.\nabla(\underline{u}_h+\underline{\tilde{u}}_h)$ [127]
- the nonlinear cross-product terms are neglected.

The residuals $\mathcal{R}_M$ and $\mathcal{R}_C$ of the fine-scale problem can be directly computed as

$$\begin{aligned} \mathcal{R}_M &= \underline{f}-\rho\partial_t\underline{u}_h-\rho\underline{u}_h^i\cdot\nabla\underline{u}_h-\nabla p_h+\nabla\cdot\left(2\mu\underline{\underline{\varepsilon}}\left(\underline{u}_h\right)\right) \\ \mathcal{R}_C &= -\nabla\cdot\underline{u}_h \end{aligned} \tag{3.30}$$

where $\underline{u}_h^i$ is the velocity at Newton iteration i. Since we work with linear shape functions, the second order term in the expression of the residual of the momentum equation is null, thus:

$$\mathcal{R}_M=\underline{f}-\rho\partial_t\underline{u}_h-\rho\underline{u}_h^i\cdot\nabla\underline{u}_h-\nabla p_h. \tag{3.31}$$

The solution of the fine-scale problems considered to be residual-driven, and thus is computed as:

$$\begin{aligned}
\tilde{p} &\approx \tau_C \mathcal{R}_C \\
\underline{\tilde{u}} &= \sum_{K \in \mathcal{T}_h} \underline{\tilde{u}}_{hk} b_k \approx \sum_{K \in \mathcal{T}_h} \tau_K \mathcal{R}_M b_k \\
\underline{\tilde{w}} &= \sum_{K \in \mathcal{T}_h} \underline{\tilde{w}}_{hk} b_k \approx \sum_{K \in \mathcal{T}_h} \tau_K \mathcal{R}_M b_k^*
\end{aligned} \tag{3.32}$$

where b_k are the $\mathcal{C}^0$-continuous shape function used to approximate the small scale solution, and τ_C and τ_K are stabilization parameters appropriately computed [129].

Therefore, the residual-based solution of the small-scale problem can be substituted in the fine scale problem:

$$\begin{cases}
(\rho \partial_t \underline{u}_h, \underline{w}_h)_\Omega + (\rho \underline{u}_h^i . \nabla \underline{u}_h, \underline{w}_h)_\Omega - \sum_{K \in \mathcal{T}_h} (\tau_K \mathcal{R}_M, \rho \underline{u}_h \nabla \underline{w}_h)_K + (2\mu \underline{\underline{\varepsilon}}(\underline{u}_h) : \underline{\underline{\varepsilon}}(\underline{w}_h))_\Omega \\
\qquad -(p_h, \nabla \cdot \underline{w}_h)_\Omega + \sum_{K \in \mathcal{T}_h} (\tau_C \mathcal{R}_C, \nabla \cdot \underline{w}_h)_K = (\underline{f}, \underline{w}_h)_\Omega \\
\\
(\nabla \underline{u}_h, q_h)_\Omega - \sum_{K \in \mathcal{T}_h} (\tau_K \mathcal{R}_M, \nabla q_h)_K = 0.
\end{cases} \tag{3.33}$$

By comparing the standard Galerkin method with the proposed stable formulation, additional integrals that are evaluated element-wise are involved. These additional terms, obtained by replacing the approximated $\underline{\tilde{u}}_h$ and $\tilde{p}_h$ into the large-scale equation, represent the effects of the sub-grid scales. They are introduced in a consistent way to the Galerkin formulation and enable to overcome the instability of the standard formulation arising in convection dominated flows and to deal with the pressure instabilities.

The proposed VMS approach has been demonstrated [128] to be equivalent to standard LES methods. Thanks to this equivalence, it models the turbulence structure better than RANS models (e.g. the $k-\varepsilon$ model, which is very common in the literature). On the other hand, it does not model precisely the small scale turbulence, but this is not a problem for the applications we aim to simulate: steel-base industrial processes are not extremely turbulent and the application of EMS decreases the turbulence of the flow.

3.4 Multiphase flow

In-mould flow can be divided in several CFD subdomains, whose interfaces must be modelled. The metal flows in different phases (liquid and mushy) and the interface

with the solid region must be tracked as well. In addition, in-mould domain contains several immiscible fluid (e.g. molten steel, Argon bubbles, slag, air). Thus, an appropriate model should be used to take into account the interaction between the different phases of the flow. The multi-phase nature of the phenomenon is modelled through the non-uniformity of material parameters in the momentum equation (equation (3.15)). In this work, the non-uniformity of the material parameters has been numerically modelled through the Level-Set method (LSM). The level-set method is an Eulerian method to track interfaces. Firstly proposed by S. Osher in 1988 [130], it was further developed and applied to incompressible flows by Y.C. Chang et al. in 1996 [131]. The method has been used in a large variety of applications, such as fast phase change in boiling [132, 133], image segmentation [134, 135, 136], fluid-structure interaction [137], computer graphics and rendering [138], multi-fluid flow [139] and microstructural simulations in metallurgy [140, 141, 142]. In this section we will show the principles of the method and propose a set of numerical algorithms in order to provide an efficient and robust method for multi-fluid flows.
The basic idea of the LSM is that the interface can be implicitly tracked as the zero-isovalue of a scalar function α named *level-set function* defined as follows:

$$\alpha(\underline{x}) = d(\underline{x}, \Gamma) \quad \forall \underline{x} \in \Omega \tag{3.34}$$

where d stands for the signed Eulerian distance function operator and Γ is the interface computed such as:

$$\Gamma = \{\underline{x} \in \Omega \mid \alpha(\underline{x}) = 0\}. \tag{3.35}$$

It is important to remind that for any Eurlerian distance function, the following property is achieved:

$$|\nabla \alpha| = 1. \tag{3.36}$$

The level-set function enables to identify the different phases (or sub-domains) by checking its sign:

$$\begin{cases} \underline{x} \in \Omega_1 & \Leftrightarrow \quad \alpha(\underline{x}) > 0 \\ \underline{x} \in \Gamma & \Leftrightarrow \quad \alpha(\underline{x}) = 0 \\ \underline{x} \in \Omega_2 & \Leftrightarrow \quad \alpha(\underline{x}) < 0 \end{cases} \tag{3.37}$$

being Ω_i the i-th subdomain. The main advantage is that as many as needed parameters may be retrieved by the tracking of a single scalar function (i.e. α) as follows:

$$\xi_i = H(\alpha)\xi_{1i} + (1 - H(\alpha))\xi_{2i} \tag{3.38}$$

where ξ_i is the i-th parameter and H is the Heaviside function or any smoothed version of it.
The function α evolves according to the flow through the transport equation

$$\frac{D\alpha}{Dt} = \frac{\partial \alpha}{\partial t} + \underline{u} \cdot \nabla \alpha = 0. \tag{3.39}$$

It is known that equation (3.39) does not preserve the geometry of the solution for any value of $\underline{u}$. The interface's motion is still well modelled from the analytical point of view, but two numerical problems arise from the solution of the transport equation:

- the smoothed Heaviside function (normally used for numerical stability) evolves during the transport, so a non-physical evolution of the mixing law occurs
- the gradient of the solution $\nabla \alpha$ has no theoretical limitation, thus it could tend to infinity, yielding to numerical problems in the resolution.

Therefore, a further step is needed to preserve the property of the level-set function which should remain a signed Eulerian distance function during the whole computation. The most classic way is to re-initialize the level-set function by solving the following Hamilton-Jacobi problem [139]:

$$\begin{cases} \dfrac{\partial \beta}{\partial \tau} + s(|\nabla \beta| - 1) = 0 \\ \beta(\tau = 0, \underline{x}) = \alpha(t, \underline{x}) \end{cases} \tag{3.40}$$

where β is the level-set function under the re-initialization process, s is the sign function of the level-set, and τ is a virtual time space in which the re-initialization equation (3.40) is solved at each increment of the physical time domain. The steady state solution for (3.40) is the value of α for the following physical time-step. It is also important to underline that the zero isovalue of the re-initialized and the non-re-initialized LS functions are coincident, thus the solution maintains its physical meaning.
The described formulation is the most common way of using the LSM for multiphase flows, however it yields to several numerical issues. In the following sections we will propose a set of enhancements of the method used to increase its efficiency and numerical robustness.

3.4.1 Filtered LS

The use of an eulerian signed distance function has several drawbacks:

- **Impossibility of imposing Dirichlet b.c.**. Open boundaries are insidious for numerical resolutions: because of the absence of robust b.c. for the NS problem and the difficulty of computing gradients, spurious oscillations in the velocity field may occur. The same problem may occur in the resolution of the

transport equation. For this reason, Dirichlet b.c. are preferable to Neumann b.c..

- **Need to solve the field on the whole domain**. The physical meaning of the LS function was given in equation (3.38), hence it affects the physical solution either through its sign or through its real value only where the Heaviside function is smoothed (i.e. close to the interface). This means that the LS function itself is used only close to the interface, while for the rest of the domain only its sign counts. In particular, a uniform LS would be advantageous because $|\nabla\alpha| = 0$ on the majority of the domain would simplify a lot the resolution of equation (3.39).

- **It is at least $\mathcal{C}^0$ continuous**. For non-planar interfaces, the signed distance function is $\mathcal{C}^0$ continuous at least in one point of the domain, which lead to the impossibility to compute an appropriate gradient of the LS function as needed in equation (3.39). Classic 2D examples are the center of a circular interface or the diagonals of a square.

A better numerical behaviour of the LSM may be achieved by filtering the LS function. Several filters have been proposed in literature. The comparison between these filters is complex, since each application of the LSM leads to different requirements for the choice of the filter. In this section we limit to propose different choices and to underline their differences in terms of continuity. We choose continuity as the key parameter because many filters are not $\mathcal{C}^\infty$ and we noticed that instabilities often appear in the low-continuity points of the LS function.

A. Linear truncated LS. It is the simplest example of filter:

$$\hat{\alpha}(\alpha) = \begin{cases} -E & \forall\alpha \in (-\infty; -E] \\ \alpha & \forall\alpha \in (-E; -E) \\ E & \forall\alpha \in [-E; \infty) \end{cases} \tag{3.41}$$

where $\hat{\alpha}$ is the filtered LS and E is a scalar parameter defining the thickness of truncation. In figure 3.1 the 1D plot of $\hat{\alpha}$ and its derivatives is depicted.

Figure 3.1 shows that $\hat{\alpha} \in \mathcal{C}^0$. This is a problem because the LSM method inherently needs $\mathcal{C}^1$ continuity and because some parameters are computed from higher derivatives of the LF function, such as the curvature

$$\hat{k} = \nabla \cdot \left(\frac{\nabla\hat{\alpha}}{|\nabla\hat{\alpha}|} \right). \tag{3.42}$$

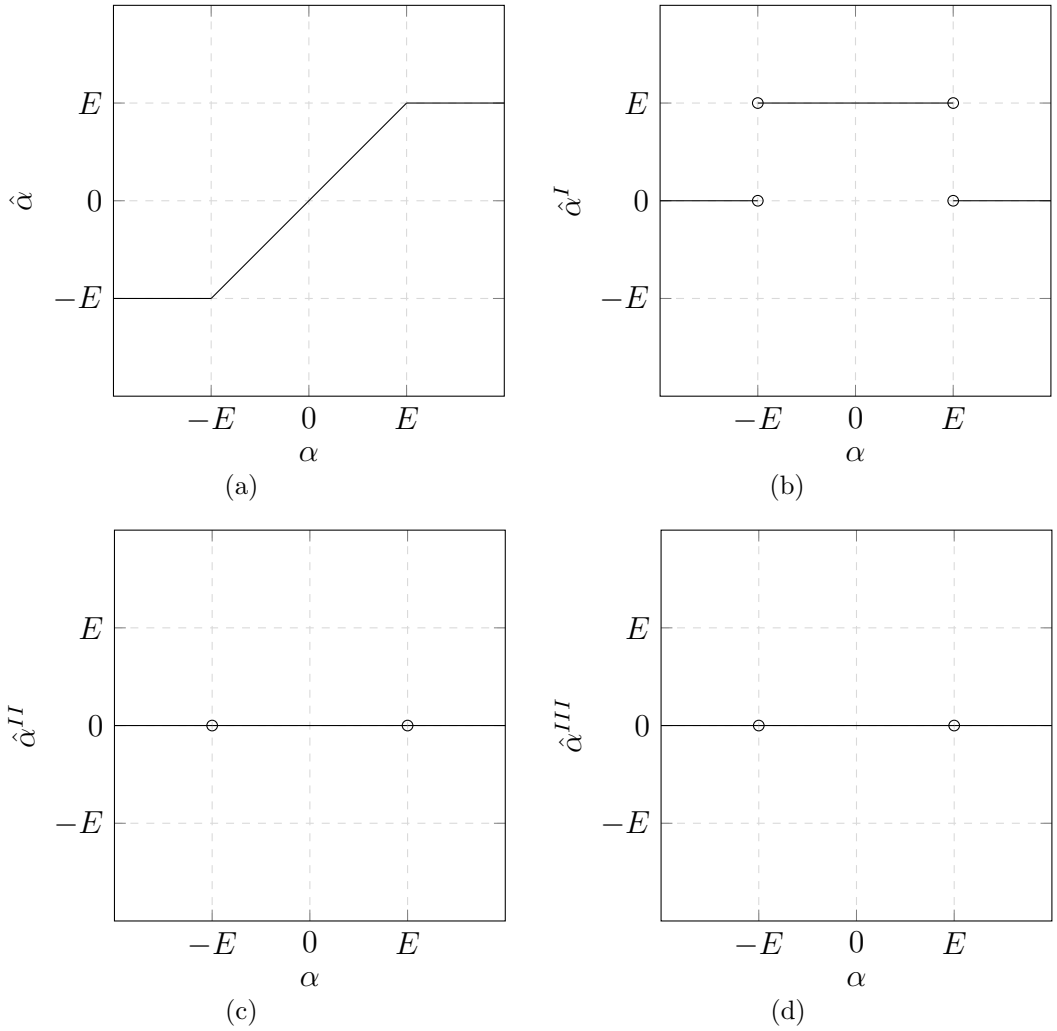

Figure 3.1: Linear truncated 1D LS and its derivatives.

B. Scaling Sinusoidal LS. The filtered LS function is defined as:

$$\hat{\alpha}(\alpha) = \begin{cases} -A & \forall \alpha \in (-\infty; -E] \\ \dfrac{A}{2}\left(\dfrac{\pi\alpha}{E} + \sin\left(\dfrac{\pi\alpha}{E}\right)\right) & \forall \alpha \in (-E; -E) \\ A & \forall \alpha \in [-E; \infty) \end{cases} \tag{3.43}$$

From figure 3.2 we see that $\hat{\alpha} \in \mathcal{C}^2$; the main drawback is that it is not periodic and that the maximum value of the derivatives grow with respect to the derivative order i proportionally to $(\pi/E)^i$ or, in other words, the gradients of each derivative

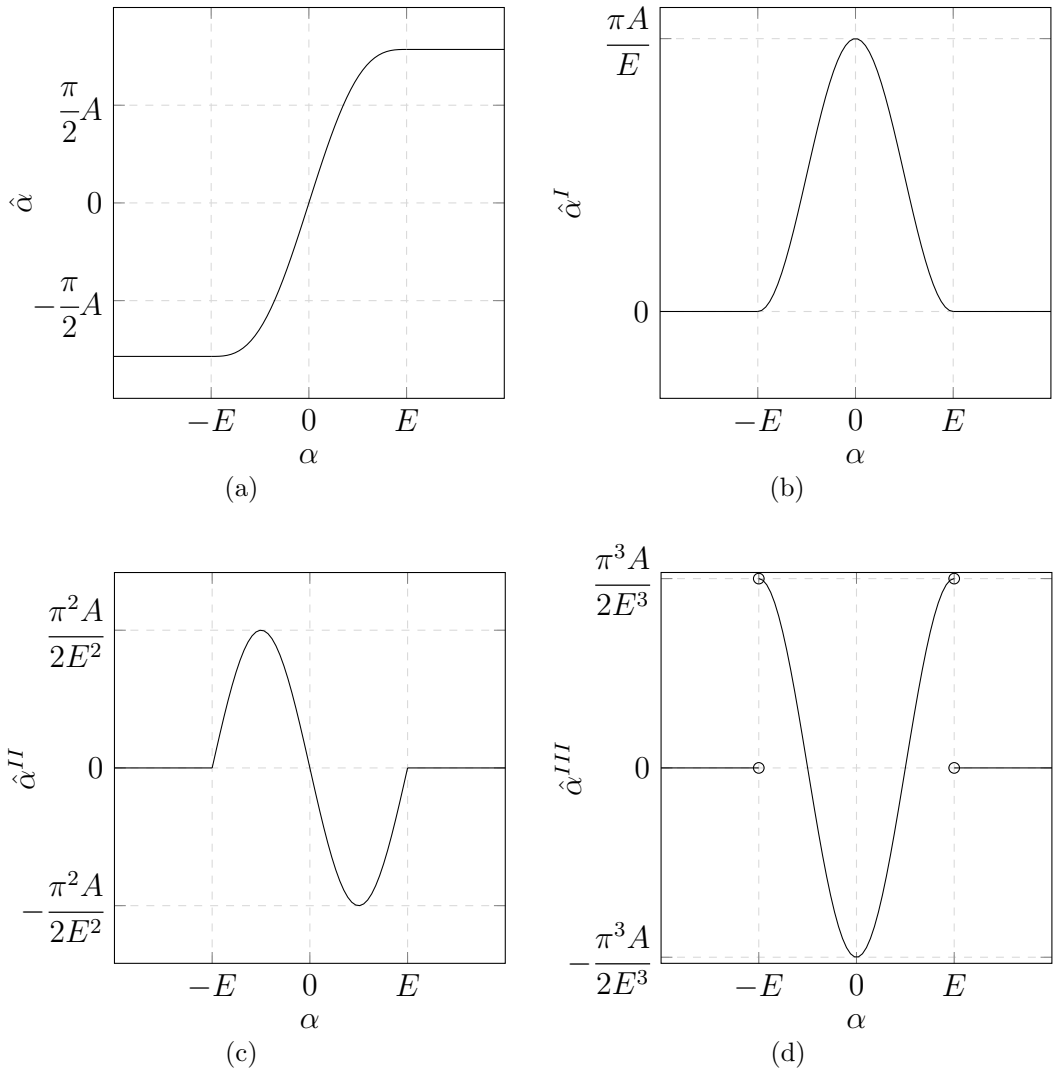

Figure 3.2: Scaled Sinusoidal 1D LS and its derivatives.

are higher than the gradients of the previous order derivative.

C. Hyperbolic Tangent. Many different filters have been based on the hyperbolic tangent function. The so-called "conservative level-set" method [143, 144, 145] is based on the following filter:

$$\hat{\alpha} = \frac{1}{2}\left(\tanh\left(\frac{\alpha}{2E}\right) + 1\right), \tag{3.44}$$

being E a scalar parameter.

A similar filter is [146]:

$$\hat{\alpha} = E \tanh\left(\frac{\alpha}{E}\right). \tag{3.45}$$

The difference between the two formulations consists only in scaling and translating constants, hence the two filters have been treated together.

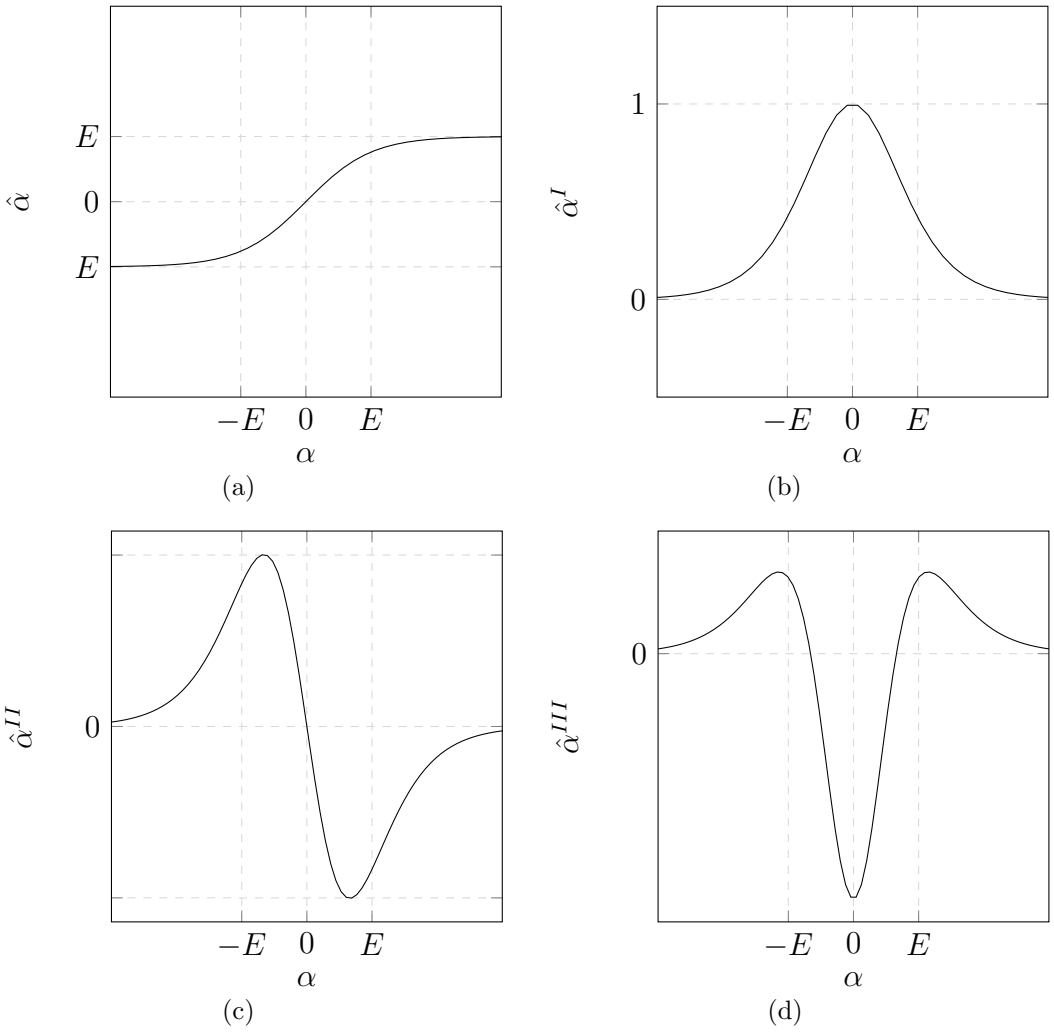

Figure 3.3: Hyperbolic tangent based 1D LS and its derivatives.

From figure 3.3 we see that the the filter based on the hyperbolic tangent is $\mathcal{C}^\infty$ continuous. The main drawback is that it is never analytically uniform, namely $\nabla\hat{\alpha} = 0$. This means that no Dirichlet b.c. can be imposed and that the transport

equation must be solved in the whole domain. However, we see that

$$\lim_{\alpha\to\pm\infty}\hat{\alpha}=\pm E \quad \text{and} \quad \lim_{\alpha\to\pm\infty}\hat{\alpha}^I=0$$

are true and that this asymptotic tendency is quite fast for $\alpha > E$ and $\alpha < -E$, hence Dirichlet b.c. can be imposed without introducing a significant error and $|\nabla\hat{\alpha}| \approx 0$ except close to the interface.

D. Sinusoidal filter. It is often used for the "convected re-initialized" level-set method [147]. It is based on a piece-wise defined filter based on the sinus function:

$$\hat{\alpha}(\alpha)=\begin{cases} -\dfrac{2E}{\pi} & \forall\alpha\in(-\infty;-E] \\ \dfrac{2E}{\pi}\sin\left(\dfrac{\pi}{2E}\alpha\right) & \forall\alpha\in(-E;-E) \\ \dfrac{2E}{\pi} & \forall\alpha\in[-E;\infty) \end{cases} \tag{3.46}$$

In figure 3.4 we see that the filter in sinus is $\mathcal{C}^1$ continuous. It has the desirable property of having periodic derivatives in $[-E;E]$.

E. Piecewise defined hyperbolic tangent. It can be seen as an extension of the classical hyperbolic filter: the difference is that it is piecewise defined and the part of the filter in the neighbourhood of $\alpha = 0$ is linear. In this way, the region close to the interface (which is the most important) is better approximated by linear finite elements. The filter can thus be defined as:

$$\hat{\alpha}(\alpha)=\begin{cases} -e+E\tanh\left(\dfrac{\alpha+e}{E}\right) & \forall\alpha\in(-\infty;-E] \\ \alpha & \forall\alpha\in(-E;E) \\ e+E\tanh\left(\dfrac{\alpha-e}{E}\right) & \forall\alpha\in[E;\infty) \end{cases} \tag{3.47}$$

F. Convolution filter. More complex filters based on the convolution of the distance function have been proposed for rendering applications [148]. This filter is aimed at guaranteeing a $\mathcal{C}^1$ continuity for any interface shape and it is defined as:

$$\hat{\alpha}=\int_\Omega \alpha(\underline{x},\underline{s}h(\underline{x}))\omega(\underline{x})d\underline{s}, \tag{3.48}$$

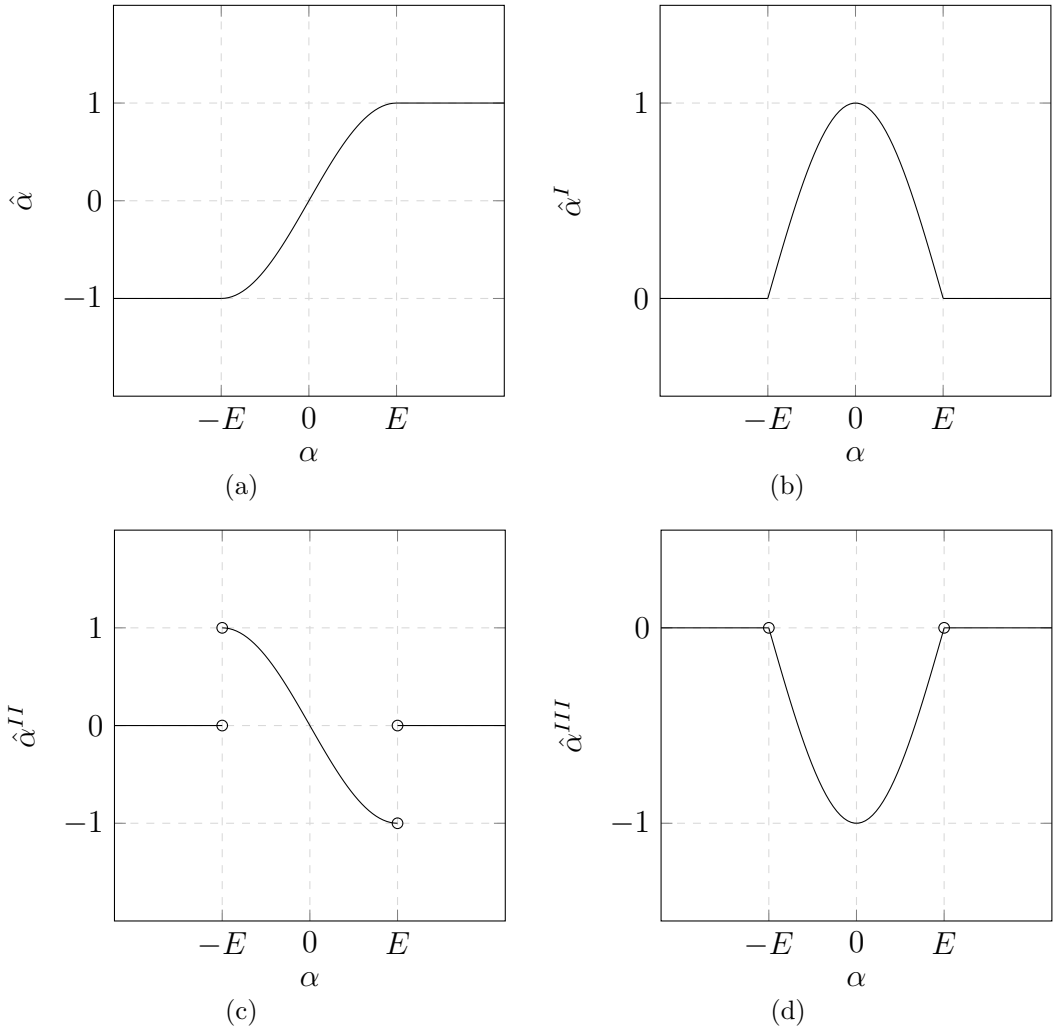

Figure 3.4: Sinusoidal 1D LS and its derivatives.

where ω is a normalized smooth kernel function, h is a functions that controls the kernel size such that $h(\underline{x}) = 0$ if $\alpha(\underline{x}) = 0$, and $\underline{s}$ is a displacement vector. The function h is introduced to interpolate the values from 0 to 1 as we move away from the interface. It must be monotonically increasing in $\mathbb{R}^+$, smooth and such that $h(0) = 0$ and $h(t) = 1$ for $t \geq f_c$ giving a capping value f_c. The most common choice for h is:

$$h(\underline{x}) = 3r(\underline{x})^3 - 2r(\underline{x})^3, \tag{3.49}$$

where $r(\underline{x}) = min(|f(\underline{x})|/f_c, 1)$. The kernel function can be computed in different ways [148]. One proposition is the classic Gaussian curve, but it is tricky to control

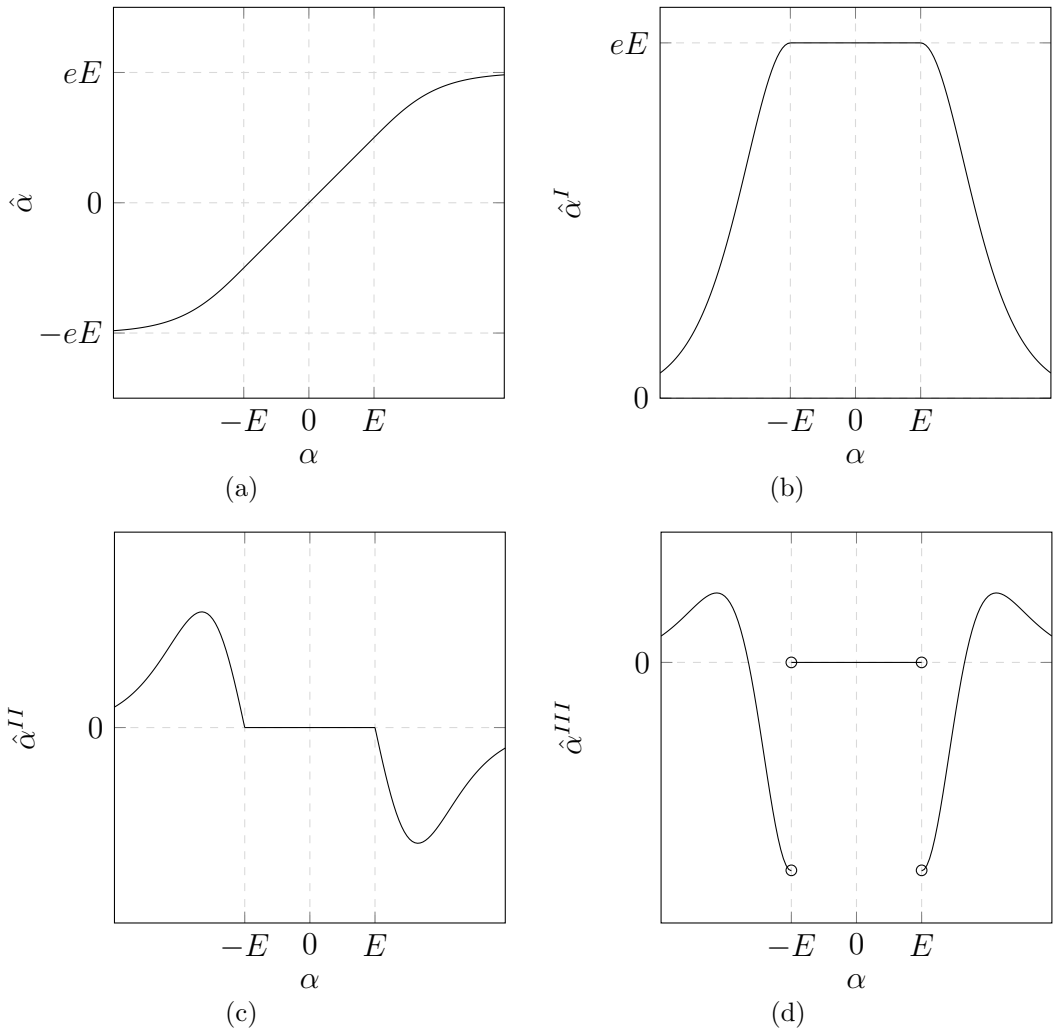

Figure 3.5: Piece-wise defined tangent based 1D LS and its derivatives.

and integrate since does not have compact support. The function used in our tests is the so calles "*bump function*" defined as:

$$\omega(\underline{x}) = b^{-3}\omega_b\left(\frac{\underline{x}}{b}\right), \tag{3.50}$$

where b controls the width of the bump function. The support function ω_b is computed as:

$$\omega_b = \begin{cases} Ce^{\frac{1}{|\underline{x}|^2 - 1}} & \forall \underline{x} \mid |\underline{x}| < 1 \\ 0 & \forall \underline{x} \mid |\underline{x}| \geq 1 \end{cases} \tag{3.51}$$

where C is such that $\int \omega = 1$. The resulting filter is very similar to the non-filtered LS where $\alpha \in \mathcal{C}^\infty$, but it is smoother where the non-filtered function is non-derivable. To highlight this property, let us consider a 1D problem with $\Gamma = \{0, 1\}$ as depicted in figure 3.6. This represents the same situation occurring on the diameter of a circle in 2D or a sphere in 3D.

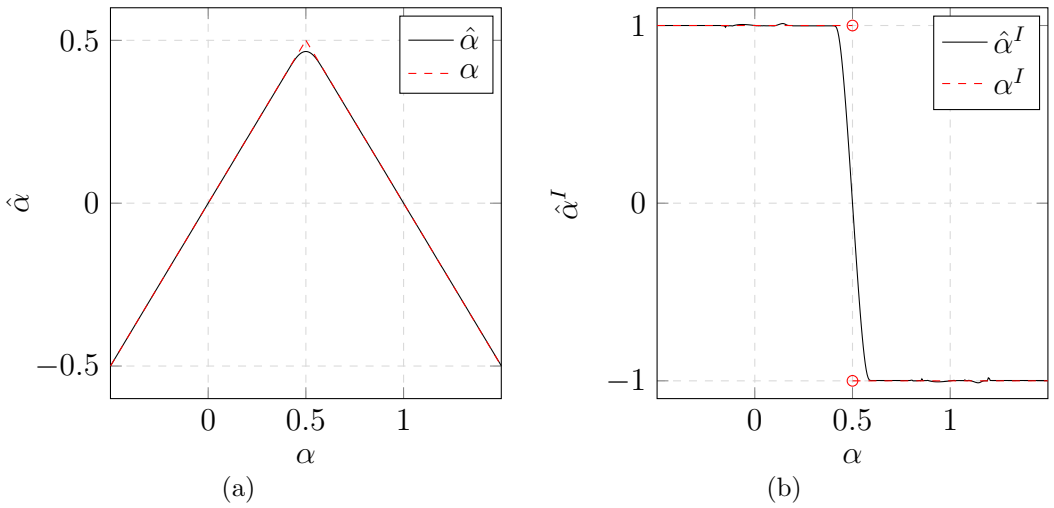

Figure 3.6: Convolution 1D LS and its derivative ($b = 0.1$ and $f_c = 0.2$).

In table 3.1, the summary of the main properties of the different filters is proposed. The hyperbolic tangent filter is the filter which combines the better properties: it is continuous, it is almost uniform far from the interface and its derivative can be written as a function of the $\hat{\alpha}$ itself, which is a property fundamental for the reasons explained in the next section.

3.4.2 Convective re-initialization

The standard LSM is a two-steps method: at each time step of the LS transport (equation (3.39)), the Hamilton-Jacobi problem should be solved (equation (3.40)) to re-initialize the LS function. This approach is accurate, but time-consuming; one way to enhance it is to merge the two problems and embed the re-initialization in the transport problem [149]. To do this, we first need to have the same variable in

Table 3.1: Properties of the filtered LS functions.

Filter	$\mathcal{C}^k$		$\lvert\nabla\hat{\alpha}\rvert_\Gamma = 1$	$\lvert\nabla\hat{\alpha}\rvert_\infty = 0$	$\hat{\alpha}^I = f(\hat{\alpha})$
	min	max			
A	0	0	++	++	no
B	0	2	+	++	no
C	0	∞	+	+	yes
D	0	1	+	++	yes
E	0	2	++	+	yes
F	∞	∞	++	no	no

the two problems, thus to correlate the physical time t and the virtual time τ. The time evolution term can be re-written as:

$$\frac{\partial\alpha}{\partial\tau} = \frac{\partial\alpha}{\partial t}\frac{\partial t}{\partial\tau}. \tag{3.52}$$

Let us introduce the parameter

$$\lambda := \frac{\partial\tau}{\partial t} \tag{3.53}$$

so that we can write equation (3.40) in the physical time space:

$$\frac{\partial\alpha}{\partial t} + \lambda s(|\nabla\alpha| - 1) = 0, \tag{3.54}$$

where the re-initializing LS function β has been replaced by the real LS function. From the practical point of view, only a numerical expression for λ is missing. From equation (3.53) we can derive that

$$\lambda = \frac{\Delta\tau}{\Delta t}, \tag{3.55}$$

but we should choose an appropriate value for $\Delta\tau$, which is not simple because the Hamilton-Jacobi problem is not explicitly solved in the virtual time space, but it is implicitly solved in the physical time space. Let's re-arrange the terms in equation (3.40):

$$\frac{\partial\beta}{\partial\tau} + s\left(\frac{\nabla\beta}{|\nabla\beta|}\cdot\nabla\beta - 1\right) = 0 \tag{3.56}$$

$$\frac{\partial\beta}{\partial\tau}\underline{U}\cdot\nabla\beta = s \tag{3.57}$$

with $\underline{U}$ being the *re-initialization velocity* defined as:

$$\underline{U} := s\frac{\nabla\beta}{|\nabla\beta|}. \tag{3.58}$$

Equation (3.57) is the Hamilton-Jacobi problem written in the form of convection equation. The proper value of the time-step can thus be computed according to the CFL condition:

$$\Delta\tau = \frac{h}{|\underline{U}|} = h, \tag{3.59}$$

where h is the mesh size and $|\underline{U}| \equiv 1$ because β is an euler distance function satisfying the relation (3.36). By substitution of this value in equation (3.55) we obtain:

$$\lambda = \frac{h}{\Delta t}. \tag{3.60}$$

We can now merge the transport and the re-initializations steps in the following one-equation model:

$$\frac{\partial\alpha}{\partial t} + \underline{u}\cdot\nabla\alpha = \lambda s(|\nabla\alpha| - 1) = 0. \tag{3.61}$$

Equation (3.61) enables to re-initialize the non-filtered level-set while convecting it; however it need to be adapted when a filtered LS is used. In fact, the condition (3.36) is not valid, thus the new value of $|\nabla\hat{\alpha}|$ should be found. For the sake of simplicity we will develop the computation for the hyperbolic tangent filter, which is the one used in this work.
Given the filter

$$\hat{\alpha} = E\,tanh\left(\frac{\alpha}{E}\right) = E\frac{1 - e^{-2\alpha/E}}{1 + e^{-2\alpha/E}}, \tag{3.62}$$

we can compute its derivative as

$$\frac{\partial\hat{\alpha}}{\partial\alpha} = 2\nabla\alpha\frac{e^{-2\alpha/E}\left(1 + e^{-2\alpha/E}\right) + \left(1 - e^{-2\alpha/E}\right)e^{-2\alpha/E}}{\left(1 + e^{-2\alpha/E}\right)^2}. \tag{3.63}$$

By imposing the Eulerian-distance-function condition to α, we obtain:

$$|\nabla_\alpha\hat{\alpha}| = \frac{4e^{-2\alpha/E}}{\left(1 + e^{-2\alpha/E}\right)^2} = 1 - \left(\frac{\hat{\alpha}}{E}\right)^2. \tag{3.64}$$

By using this new condition, we can write the Hamilton-Jacobi problem (3.40) as

$$\begin{cases} \dfrac{\partial \hat{\beta}}{\partial \tau} + s\left(|\nabla \hat{\beta}| - \left(\dfrac{\hat{\beta}}{E}\right)^2\right) = 0 \\ \hat{\beta}(\tau = 0, \underline{x}) = \hat{\alpha}(t, \underline{x}) \end{cases} \tag{3.65}$$

and the convection-re-initialization equation (3.61) as:

$$\frac{\partial \hat{\alpha}}{\partial t} + \underline{u} \cdot \nabla \hat{\alpha} = \lambda s \left(|\nabla \hat{\alpha}| - \left(\frac{\hat{\alpha}}{E}\right)^2\right). \tag{3.66}$$

Local re-initialization parameter.

Equation (3.66) has the advantage of being fast, but the disadvantage of not solving the Hamilton-Jacobi problem. The re-initialization term which is added to the classic transport equation plays indeed a role in re-initializing the LS function, but it is a non-physical term added all over the domain. When the amount of needed re-initialization is small, no problem occur. On the opposite, when the LS is highly deformed by the velocity field, this term may be not sufficient. Therefore, a local scaling of the re-initializing term is important in order to increase the re-initialization capacity in the regions of the domain where the deformation is higher and reducing the re-initialization where it is not needed. This can be done by introducing a local parameter θ called re-initialization parameter, such that

$$\frac{\partial \hat{\alpha}}{\partial t} + \underline{u} \cdot \nabla \hat{\alpha} = \theta \lambda s \left(|\nabla \hat{\alpha}| - \left(\frac{\hat{\alpha}}{E}\right)^2\right). \tag{3.67}$$

where

$$\theta = < \nabla \left(\underline{u} \cdot \frac{\nabla \hat{\alpha}}{|\nabla \hat{\alpha}|}\right); \frac{\nabla \hat{\alpha}}{|\nabla \hat{\alpha}|} > \Delta t. \tag{3.68}$$

The parameter θ aims at measuring the "need" of re-initialization, considered proportional to the strain rate in the direction perpendicular to the interface. This procedure has been tested on the following 2D case.
Let's consider the circular interface defined as:

$$\Gamma(\underline{x}) = \{\underline{x} \mid d((x_0, y_0), \underline{x}) = 0.1\}. \tag{3.69}$$

The tests consists in convecting such interface by the following velocity field:

$$\underline{u} = 2(x - x_0)^3 \, \hat{i} + 2(y - y_0)^2 \, \hat{j}. \tag{3.70}$$

The velocity streamlines and the interface are depicted in figure 3.7.This test case is interesting because the interface is subjected to various strain states:

- Increasing stretching along x: the gradient of velocity along x grows quadratically as the interface moves away from the center. This means that the interface thickness is subjected to increasing stretching and re-initialization need during the convection
- Decreasing stretching along y: the gradient of velocity along y decreases linearly as the interface moves towards the center. This means that the interface thickness is subjected to decreasing stretching and re-initialization need during the convection
- Velocity tangent to the interface: at each moment of the simulation, four points of the interface are convected by a velocity tangent to the interface itself, meaning that no re-initialization is needed during that time-step.

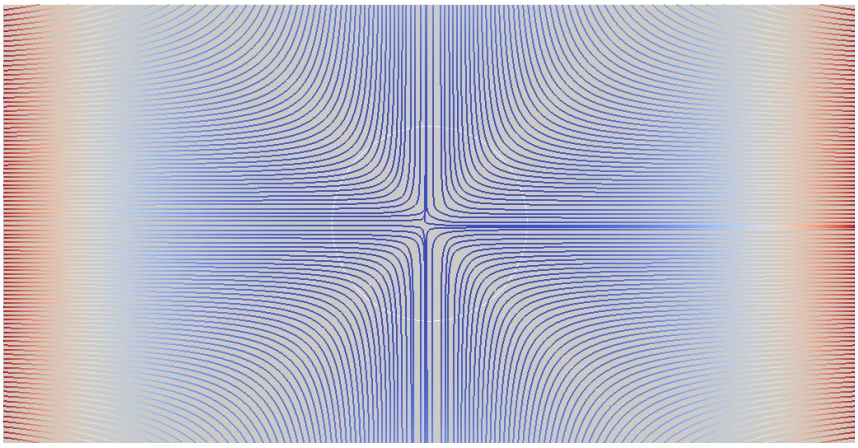

Figure 3.7: Test case: stretching circle.

The presence of these three regions is modelled by the local re-initialization parameter, as shown in figure 3.8. The simulation has been performed with a high time-step, in order to exceed the re-initialization capacity of the classic method, with $\theta \equiv 1$. In figure 3.9 the spoiling of the geometrical properties of the LS function is shown. In figure 3.9(b) we notice how the lack of re-initialization capacity has yielded to oscillations and to the growth of the interface thickness (which, in this case, should be $E = 0.04$). On the opposite, with the use of a local-defined re-initialization parameter it is possible to scale the re-initialization and focus where it is needed, as showed in figure 3.10. A global comparison of the convected interface is shown in figure 3.11 where the results obtained with a uniform θ (up-left and

down-right) are compared to the ones obtained by the use of a local θ (up-right and down-left).

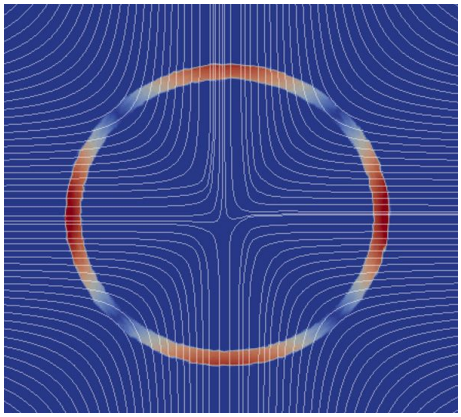

Figure 3.8: Local re-initialization parameter.

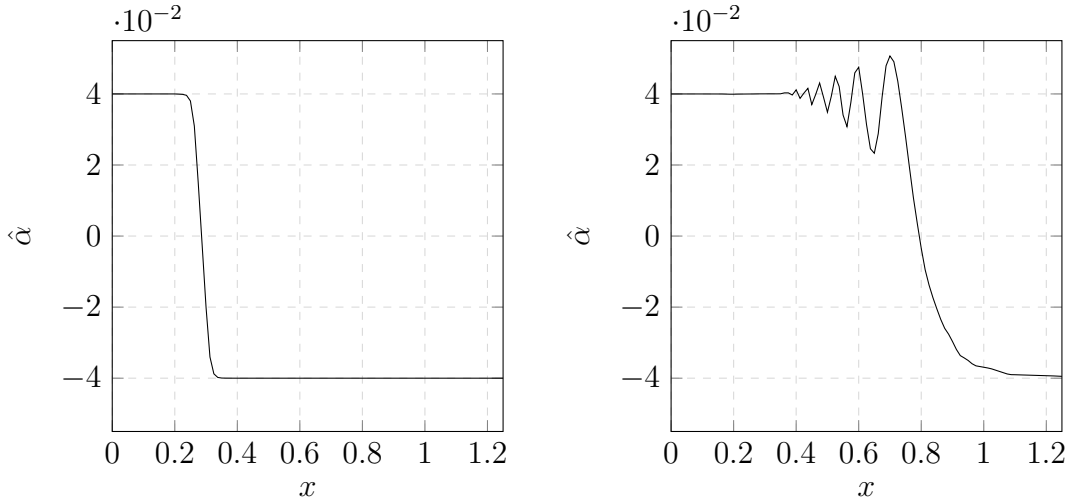

(a) Initial LS function

(b) LS function after 300 time-steps

Figure 3.9: Evolution of the LS function along the x axis with $\theta \equiv 1$.

3.4.3 Volume conservation

The main drawback of the LSM is that it is not volume-conservative. Many methodologies have been proposed to correct this drawback; the so called "conservative level-set" has been proposed by Olsson and Kreiss in 2005 [143] and further developed in 2007 [144]. This method is based on the correction of the transport equation

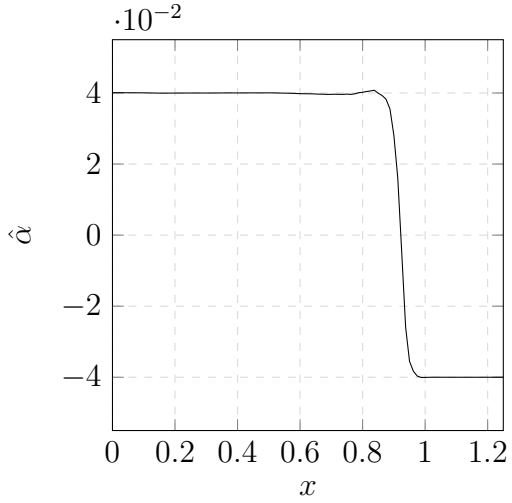

Figure 3.10: Evolution of the LS function along the x axis with local θ after 300 time-steps.

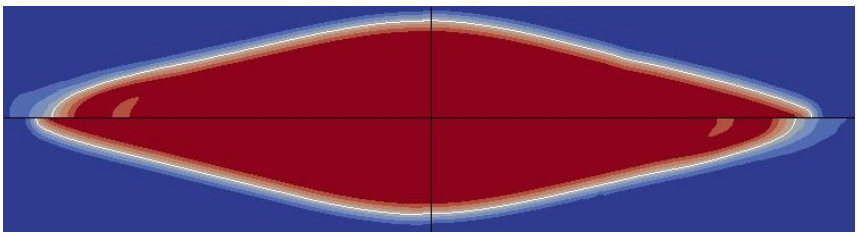

Figure 3.11: LS function at the end of the simulation with uniform θ (up-left and down-right) and local θ (up-right and down-left).

by a diffusive term, which compensates the volume loss. The conservative level-set greatly improved the volume conservation, but it introduces a non-physical distortion of the interface, as noticed by L. Zhao et al. in [150]. In addition, it involves the use of scalar parameters whose value should be determined. Further improvements have been obtained by the use of higher order schemes [145], by coupling the LSM with the volume of fluids methods (VOF) [151] or by the use of semi-Lagrangian methods and material particles [152]. These methods are theoretically consistent and ensure a local volume conservation, but they lack of computational speed and numerical robustness. On the opposite, global volume correction have been proposed. This second family of methods simply move the interface in its normal direction until the global correct volume is retrieved. The advantage is that perfect volume conservation is obtained, while the main drawback is that the volume loss is recovered by artificially adding volume along the whole interface; this means that only a global conservation is guaranteed, which turns to be an important limi-

tation for non-connected phases. However, in our case we need to model the molten metal in the mould, which is a simply-connected domain, so this class of volume-correction methods has been chosen. Let's see now how this correction (done after the transport of the LS) can be computed. Recently, L. Betancour proposed to solve a non-linear scalar equation in order to find the value δ_v to be added to the level-set function to retrieve the global correct volume [153]. This method works well in terms of volume-conservation, but no theoretical proof of the uniqueness of this correction is provided. In addition we need not to deform the LSF for the reasons explained in section 3.4, which is not guaranteed by this method for any filter used. Inspired by the work of Baiges et al. [154] on mass correction of non-filtered level set functions, we propose a mass correction uniform on the interface. Thus, the correction can be computed as:

$$\hat{\alpha}_c = \hat{\alpha} + \frac{\Delta V}{S}, \tag{3.71}$$

where $\hat{\alpha}_c$ is the corrected level-set, ΔV is the volume loss and S is the interface's surface (for 3D cases). This works perfectly for non-filtered $\hat{\alpha}$ because any vertical translation correspond to an equivalent horizontal translation. But when the level-set is filtered, this formula is no more valid. The method has been enhanced by considering the spacial derivative of the LS function:

$$\hat{\alpha}_c = \hat{\alpha} + \frac{\Delta V}{S} \cdot ||\nabla \hat{\alpha}||_{\Omega_e}, \tag{3.72}$$

where Ω_e is the single finite element crossed by the interface. This method takes into account the case in which $||\nabla \hat{\alpha}|| \neq 1$, but is not applicable for filtered level-set functions since it would create a discontinuity. When a filtered level-set function is used (for instance with the hyperbolic tangent filter described in paragraph 3.4.1C we need a correction term which does not change the value of the LS far from the interface and does not deform the re-initialized LS. Basically, we want to translate the level-set horizontally instead of vertically, thus:

$$\hat{\alpha}_c = tanh\left(\frac{\alpha + \delta_h}{E}\right) E, \tag{3.73}$$

with

$$\delta_h = \frac{\Delta V}{S}. \tag{3.74}$$

By developing equation (3.73), we obtain

$$\hat{\alpha}_c = \frac{tanh\left(\frac{\alpha}{E}\right)\left(\frac{\delta_h}{E}\right)}{1+\left(\frac{\alpha}{E}\right)\left(\frac{\alpha}{E}\right)}E \tag{3.75}$$

$$\hat{\alpha}_c = \frac{\hat{\alpha}+\hat{\delta}_h}{1+\hat{\alpha}\hat{\delta}/E^2}, \tag{3.76}$$

being

$$\hat{\delta} = \frac{1}{2}\left(tanh\left(\frac{\delta_h}{2E}\right)+1\right). \tag{3.77}$$

The method enables a perfect volume conservation, but it introduces a non-physical movement (but not distortion) of the interface. In order to limit this numerical error, the horizontal correction has been imposed to of one order of magnitude lower than the displacement due to the transport equation; in the case of higher correction, the full time-step (Navier-Stokes, convective re-initialization and mass correction) is re-done with a lower time-step.

Validation: rotating circle

Since the volume loss is not a central problem of M-EMS applications, we will not go in depth in the validation and benchmarking of this method, but we will limit to show one benchmark case as validation. The chosen benchmark is the so called "rotating circle", whose configuration is depicted in figure 3.12. Given the domain $\Omega = [-1;1] \times [0;7]$ and an initial circle with radius 0.25, the benchmark consists in its transport by the rigid body motion defined by the following velocities:

$$u_x = Y; \quad u_y = -X, \tag{3.78}$$

being (X, Y) the spatial coordinates. The space domain has been discretized by 30000 elements, while the time step was $\Delta t = 0.04$. The variation of the circle surface is plotted in figure 3.13. As expected, the classic LSM leads to a constant rate of mass loss, up to 10%. The conservative level set method improves mass conservation, which still occurs; this method may probably lead to better results, but an appropriate choice of time-step and numerical parameters should be done. Finally, we can see that the proposed mass conservation works as expected, leading to null mass loss. It is important to underline that this method could artificially deform the interface and lead to inconsistent results for non simply connected domains. However, it is not the case for in-mould free surface fluctuation.

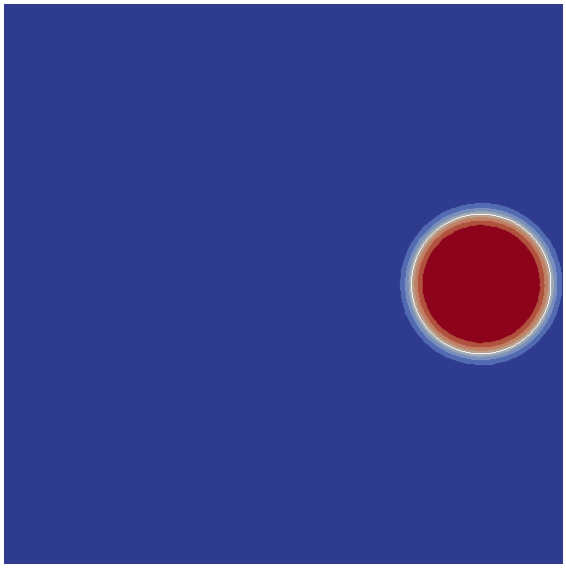

Figure 3.12: Initial level set function

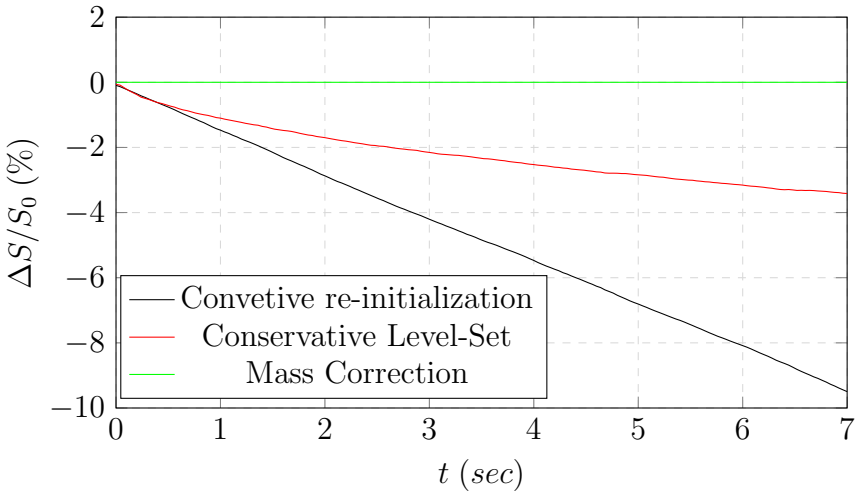

Figure 3.13: Variation of the circle's surface.

3.4.4 Mesh adaptation

The mesh is dynamically adapted to the solution, i.e. velocity and interface position. The aim is to refine the discretization in the areas of the domain where the solution fields are mostly non-linear. The refinement affects both the density of elements and their shape, which is anisotropically adapted and stretched along the direction where the considered solution field is linear. The mesh adaptation algorithm used in this work is based on the paper of [155], who proposed a method based on the

edges length distribution tensor and the associate edge based error analysis. The principle is to compute the error along the edges and to adapt the mesh in order to minimize it.
In this section, we propose a synthesis of the method based on the work of [155] and further developed by [129] in the case of Navier-Stokes equations with multi-field re-meshing.
Let us introduce the set of fields we want to remesh according to:

$$\underline{w} = \{w_1, w_2, ..., w_N\}. \tag{3.79}$$

Let's then denote the error of each field along the edges as:

$$\mathbf{e}_{ij} = \{e_{ij}^1, e_{ij}^2, ..., e_{ij}^N\} \tag{3.80}$$

where e_{ij} is the error along the edge linking the $i-th$ node to the $j-th$ node. This error can be expressed as:

$$e_{ij}^n = \mathbf{g}^{ij} \cdot \mathbf{X}^{ij} \tag{3.81}$$

with $\mathbf{X}^{ij}$ being the length of the edge linking the $i-th$ node to the $j-th$ node, and $\mathbf{g}^{ij} = \mathbb{H}(u)\mathbf{X}^{ij}$, where $\mathbb{H}$ is the Hessian associated with $\underline{u}$. The current length distribution tensor $\mathbf{X}^{ij}$ has to be modified to obtain the resultant disposition of edges length; to define this transformation, let's introduce the stretching factors s_{ij} as the ratio between the original edge length and the length of the adapted edge:

$$s_{ij} \in \mathcal{S} = \{s_{ij} \in \mathbb{R}^+ \, i = 1, ..., \Lambda, \, j = 1, ..., \Lambda, \, \Gamma(i) \cap \Gamma(j) \neq \emptyset\} \tag{3.82}$$

with Λ being the number of nodes of the mesh and $\Gamma(i)$ being the set of nodes directly linked to the $i-th$ node .
Hence we can express the error in relation to the change in the edges' length, expressed in term of stretching factors , so that:

$$\begin{cases} \tilde{\mathbf{X}}^{ij} = s_{ij}\mathbf{X}^{ij} \\ \tilde{e}_{ij}^n = s_{ij}^2 \mathcal{G} \cdot \mathbf{x}^{ij} \end{cases} \tag{3.83}$$

where $\tilde{\mathbf{X}}^{ij}$ and $\tilde{e}_{ij}^n$ are the target edge length and the target error respectively and $\mathcal{G}$ a recovery-gradient operator defined in [155].
We can therefore derive the associate metric $\mathbb{M}$ as:

$$\mathbb{M}^i = \left(\frac{1}{d} \sum_{j \in \Gamma(i)} s_{ij}^2 \mathbf{X}^{ij} \bigotimes \mathbf{X}^{ij} \right)^{-1}. \tag{3.84}$$

For the complete derivation of the metric, please refer to the work of [155].
Set the metric framework, we need now to choose the input field to remesh according

to. For high-Reynolds multiphase incompressible flows, we propose the following set of fields:

$$w = \left\{ N_u \frac{\underline{u}^i}{|\underline{u}^i|} \, , \; N_s \frac{|\underline{u}^i|}{\max\limits_{\Omega} |\underline{u}|} \, , \; N_p \frac{\hat{\alpha}_j}{\max\limits_{\Omega} |\hat{\alpha}|} \, , \; N_u \frac{\underline{f}_L^i}{|\underline{f}_L^i|} \, , \; N_s \frac{|\underline{f}_L^i|}{\max\limits_{\Omega} |\underline{f}_L|} \right\} \tag{3.85}$$

where Ω is the computational domain, N_u, N_s and N_p are weighting parameters. In the current work we have chosen $N_u = 0.2$, $N_s = 0.2$, $N_p = 1$, meaning that the quality of the mesh across the interface is considered the main target for the remeshing algorithm. To better understand the re-meshing algorithm, we refer to the test cases shown in chapter 4.

3.5 Conclusions

In this chapter we have presented the numerical methods used to solve the CFD problem.
The VMS approach has been used to solve the NS equations. This method provides natural and consistent stabilization, enabling the user to simulate convective-dominated flows with no numerical spurious instabilities. It is also an efficient and effective way of modelling the fully developed turbulence which occurs in steel casting flows because it has been proofed to be equivalent to LES methods.
In the second part of the chapter, we have introduced the multiphase model, base on the level-set method. The transport and re-initialization phases of the classic level set method have been merged in a single-step method named *convective re-initialization level set*. This method requires to filter the level set function. Several filters have been compared and the pros and cons of each filter have been highlighted. Furthermore,an a-posteriori global mass correction algorithm has been proposed and tested, resulting to guarantee perfect mass conservation in the domain.
Finally, an anisotropic mesh adaptation algorithm has been shown. The re-meshing algorithm is based on a multi-field criterion such that the obtained mesh minimized the interpolation error of the user-defined fields on the elements' edges.

Chapter 4

Coupling scheme

Contents

4.1 Résumé du chapitre en français

Ce chapitre a pour objectif de proposer une stratégie de couplage entre les physiques décrites dans les chapitres précédents. Dans la première partie du chapitre, on montre tous les paramètres physiques qui lient le problème électromagnétique et la mécanique des écoulements multiphasiques. Cette partie est suivie par une description plus technique de la stratégie de couplage, en détaillant l'implémentation de ce travail dans le logiciel commercial « THERCAST ». On souligne la pertinence du terme convectif dans les forces de Lorentz, qui est discrétisé explicitement en temps. Ce terme pose des problèmes de convergence, lorsqu'un pas de temps critique n'est pas respecté. L'expression de ce pas de temps critique, basé sur le travail des forces de Lorentz et qui garantit la convergence, a été proposé dans ce chapitre. Pour valider cette approche, deux cas tests sont proposés. Le premier est le cas de la cavité entraînée auquel un champ magnétique est appliqué. Ce test a notamment été utilisé pour valider le pas de temps critique proposé dans ce chapitre. Le deuxième cas est le cas de l'écroulement d'une colonne de fluide avec application d'un champ magnétique. Ce cas a permis de tester l'outil numérique également en présence d'écoulements multiphasiques. La dernière partie du chapitre traite du problème multiphysique dans une optique plus globale. Différentes stratégies de couplage sont présentées et des comparaisons entre celles-ci sont effectuées. Un couplage bidirectionnel a été proposé et validé par des comparaisons avec des résultats expérimentaux et numériques (ANSYS).

4.2 Coupling model

In chapters 2 and 3 we have presented the mechanical and the electro-magnetic phenomena as separate standalone problems. Indeed, this is not true. The thermo-mechanical and electro-magnetic problems are mutually interconnected by several factors, as summarized in figure 4.1. A consistent way to solve the coupled problem is to solve it as an unique system, but this would be very heavy in terms of computational resources. At the opposite, numerical coupling strategies could be used to link the different solvers. Thus, the so-called "two meshes two solvers" (2M2S) approach [156] is used: the mechanical and the EM problems are solved in different domains, with different meshes and solvers. This choice leads to a greater freedom of simulation and enables the user to use specific (and more efficient) solvers for each physics. The EM domain includes the caster's parts, the molten metal, the inductor and an air layer around. The mesh is refined in the skin depth and in the inductor, while it is coarse in the air and at the centre of the liquid; in facts, the EMF penetrates in the centre of the liquid region only at very low frequency, but this is quite rare in industrial applications. The fluid mechanics domain includes only the liquid

region, and the mesh is anisotropically adapted according to the fields in equation (3.85). The coupling between the two solvers must be developed; a weakly coupled, 1-way approach is the most common used [157, 158, 159, 160, 161, 162] method: the EM problem is solved and the average Lorentz force is added in the mechanical problem after being interpolated between the two meshes. So, the EM problem is solved only once. On the opposite, 2-ways methods involve a stronger coupling. The EM problem is solved periodically in order to consider the variation of temperature or of the liquid domain. Also quasi-2-ways algorithms have been proposed in order to correct the EM results without solving the whole differential problem again [163]. The best way (in terms of accuracy) is to solve each physics at each time step and explicitly link its output to the following solver. This is quite accurate as far as the time step is low with respect to the characteristic time of the problem. The main drawback of this approach is that it is computationally expensive; this is usually used for short-time processes like material pulse forming [102] or in fully magnetohydrodynamic (MHD) problems. It is also used for some EMS application with rapid free surface variation, but its high requirements in terms of computational time limit its use to 2D simulations [164]. The purpose of this chapter is to propose a dedicate coupling scheme which fits EMS applications, providing accurate results in a short amount of time and needing low computer memory. In addition, this scheme should be robust and flexible, thus applicable to different industrial applications, because the final commercialized software must be ready-to-use and user friendly, with no need of either parameters calibration or tailor-made corrections.

The coupling between the CFD and the thermo-metallurgical problem is not treated in this chapter because already developed in Thercast®. On the opposite, the relations between the EM problem and the other physics have been considered and they can be divided into different problems, as described in the following sections.

4.2.1 Elements which affect the EM problem

Material parameters

Material parameters change in function of the variation of temperature (T) and geometrical location (Ω). The EM computation must be updated when the variations are so high to change the EM results. The variations due to the free surface fluctuation are very low in the mould, and thus can be neglected. On the opposite, the air layer due to shrinkage effects and the solidification front for ingot casting have high impact on the EM computation since the electromagnetic nature of the material changes (solid ferromagnetic steel or non conductive air layer), thus it should be somehow taken into account. However, these effects are small in the mould, in the tundish and in the ladles. In the present work, a weak 2 ways approach has

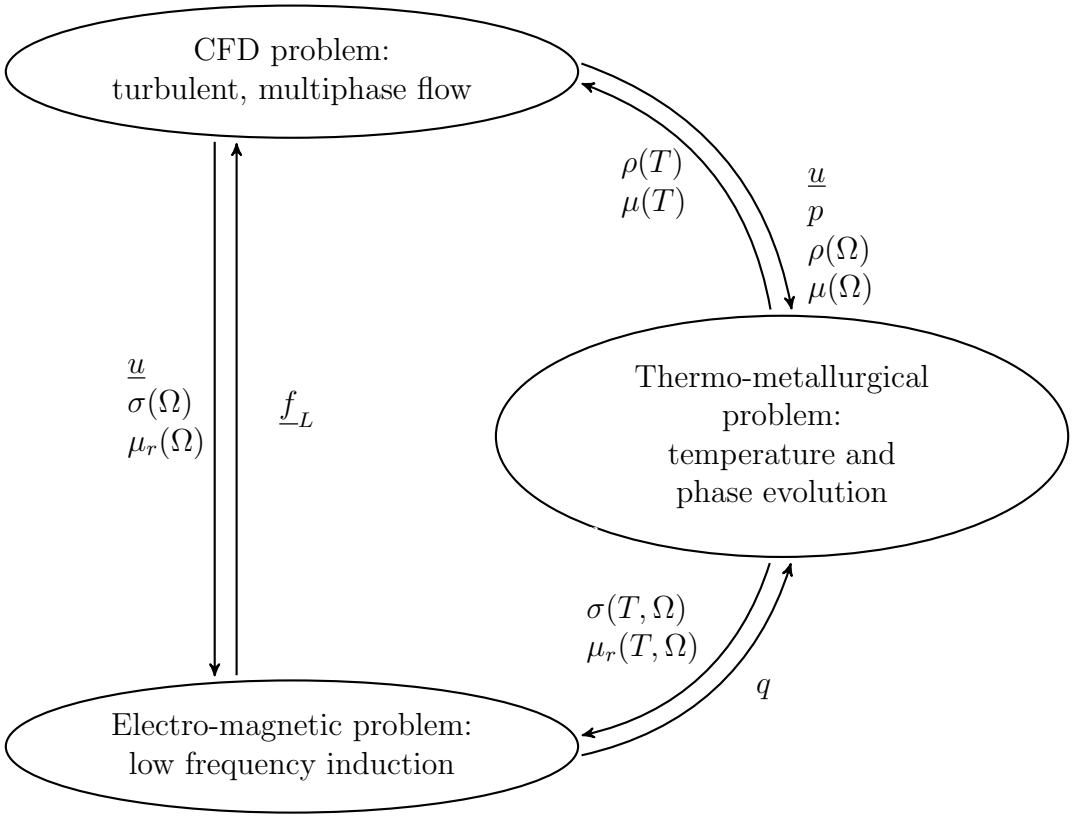

Figure 4.1: Multi-physics coupling scheme

been used to update the EM results. During the resolution of the NS equations, the variation of the relative magnetic permeability field is computed as

$$v = \int_{\Omega} \left| \frac{\mu_r(T, \underline{x}) - \mu_{r,EM}(\underline{x})}{\mu_{r,EM}(\underline{x})} \right| d\underline{x} \tag{4.1}$$

where $\mu_{r,EM}$ is the value of the relative magnetic permeability used in the EM simulation. When the variation is higher than a certain threshold , i.e. $v > \varepsilon$, it means that the domain has significantly changed its electro-magnetic properties, thus the EM simulation is re-launched. The variation of electro-magnetic properties is due to two main phenomena:

- The temperature variation changes the material properties.
- The phases motion (e.g. free surface fluctuation or phase change) leads to the high variation of material properties in the region which has changed phase/material.

This condition has the main drawback of needing the possibility to import the material properties (defined on the Gauss points) from the EM solver to the mechanical solver; in addition it implies to compute the updated relative magnetic permeability field inside the mechanical solver. These operations are relatively expensive in terms of computational resources and, most of all, seem not fundamental in M-EMS applications. As stated before, the phase change or the free surface fluctuation in the mould have little impact on the EM field. The main variation of the material parameters is due to the temperature. In facts, the temperatures computed before and during stirring are very different, since the convection is deeply affected by the electro-magnetic steering. Thus, a second and simpler condition has been defined through an Ω_n^m-condition on the temperature field:

$$\Omega_n^m \left[\left(\frac{T - T_{EM}}{T_{EM}} \right) < \varepsilon \right], \tag{4.2}$$

where T_{EM} is the reference temperature field used in the EM simulation and T is the temperature field at the current mechanical time-step. The Ω_n^m operator means that the condition on the temperature must be satisfied on $n\%$ of the active volume, which is defined as the volume where the Lorentz force is higher than $m\%$ of the maximum Lorentz force during the EM period.

Conductive fluid motion

The molten metal velocity ($\underline{u}$) affects the EM computation by creating convective eddy currents in the melt, i.e. $\underline{j}_c = \sigma \underline{u} \times \underline{B}$. This term is crucial because it is the only external factor which affects the EM problem for mono-phase flows with nearly constant temperature (which is the case for the in-mould flow after a starting period). For EMB applications, this is the only contribution to electrical currents inside the melt, but for EMS applications it is combined with the AC term, i.e. $\underline{j}_c = \sigma \partial_t \underline{A}$.

At very low frequencies such that the magnetic field is almost uniform over the fluid domain, we have:

$$\frac{\underline{u} \times \underline{B}}{\partial \underline{A} / \partial t} \approx \frac{U}{\omega L}, \tag{4.3}$$

where ω is the pulsation of the EM field, U is the characteristic velocity of the flow and L is the characteristic length of the conductive domain. This ratio can be expressed in function of the Raynolds magnetic number, defined as

$$Rem := \mu \sigma U L, \tag{4.4}$$

hence

$$\frac{\underline{u} \times \underline{B}}{\partial_t \underline{A}} \approx \frac{Rem}{\omega L^2 \mu \sigma}. \tag{4.5}$$

Thus, the eddy currents produced by the liquid's motion can be neglected when

$$Rem \ll R_\omega := \omega L^2 \mu \sigma, \tag{4.6}$$

where $R\omega$ is the shielding parameter. This is the theoretical condition for which the convective term of the eddy current can be neglected, as stated by Moreau [165]. This condition is usually respected for EMS applications, but it must be checked, especially when the induction frequency is low.
In this section, we also want to point out two common mistakes done in the simulation of EMS. The first mistake is to consider $Rem \ll 1$ instead of (4.6). This is due to the fact that, at high frequencies, the field penetration is limited to the skin depth δ, such that

$$R_\omega = \omega L^2 \mu \sigma = \omega \delta^2 \mu \sigma \approx 1. \tag{4.7}$$

But this condition is valid only for high frequencies, so for just a part of EMS applications, whose working range varies from few Hertzs to thousands of Hertzs.
The second error is to automatically neglect the convective term $\underline{u} \times \underline{B}$ from the mechanics point of view. Relation (4.6) says that the convective electrical current is small if compared to the AC-induced electrical current, but does not guarantee that

$$f_{Lb} = \sigma \underline{u} \times \underline{B} \times \underline{B} \tag{4.8}$$

is negligible with respect to

$$f_{Ls} = \sigma \left(\nabla \phi + \partial_t \underline{A} \right) \times \nabla \times \underline{A}. \tag{4.9}$$

On this topic, different works have been published. While the most common choice is to neglect the electromotive terms from both the EM and the mechanical point of view [162], a few authors claim its relevance [166]. In this work, this term has been modelled explicitly (section 4.4) and its impact has been investigated in section 4.6.

4.2.2 How the EM problem affects the thermo-mechanical problems

Lorentz forces

Lorentz forces ($\underline{f}_L$) are the core of EMS applications, but two aspects have to be analysed for the coupling scheme. The first, is the influence of the convective (or

braking) term of the force defined as

$$\underline{f}_{Lb} = \sigma \underline{u} \times \underline{B} \times \underline{B}.$$

This term is important because it depends on the solution of the NS problem (i.e. the velocity). This term, while fundamental for EMB, has small impact on EMS, thus its mechanical influence on the flow should be discussed, as stated in the previous section. The neglection of this term would allow the modelling of the Lorentz forces in the NS equation through a source term. While, in the case of consideration of this term, the Lorentz force would be modelled as a reaction term. In the case of modelling through a source term, a second point must be discussed: the choice between the use of the Lorentz forces averaged over the EM period, or the use of their time-dependent value. In the first case, only one field should be stored and interpolated, while, in the second case, a higher computational effort would be demanded for the storage and interpolation of several fields, corresponding to the force at different moments in the period. Different criteria on which base this choice have been proposed in the literature. Barna et al. [167] propose to base this choice on the interaction parameter (or Stuart number), defined as

$$N := \frac{B^2 L \sigma}{\rho U} = \frac{Ha^2}{Re}, \tag{4.10}$$

Ha being the Hartmann number, L the characteristic length of the liquid domain and U its characteristic velocity. This adimensional number is defined as the ratio of electro-magnetic to inertial forces: if it is low, the flow will react slowly to the steering because of its inertia, so only the average part of the Lorentz force will influence the flow. A different condition has been proposed by Felten et al. [168]. This work proposes to compare the turnover time of the turbulent structure, according to the Kolmogorov theory [169], and the frequency of the Lorentz force. From Prandtl's theory, the estimate of the turnover time τ_r is:

$$\tau_t = \mathcal{O}\left(|\bar{S}|^{-1}\right), \tag{4.11}$$

being $|\bar{S}|$ the second invariant of the shear rate tensor. The idea is that if the period of the EM force is of the same order of magnitude than τ_t, the transient part will affect the turbulence structure. On the opposite, if the time-scale of the EM force is smaller than the one of the turbulence, only the average part of the force will affect the flow. Hence, the condition to be verified to neglect the transient part of the Lorentz force can be written as

$$\frac{\tau_t}{\tau_f} \gg 1, \tag{4.12}$$

$$\frac{f}{|\bar{\bar{S}}|} \gg 1, \tag{4.13}$$

being f the frequency of the Lorentz force. From a practical point of view, the threshold value is proposed in [168] to be

$$f \geq 5|\bar{\bar{S}}|. \tag{4.14}$$

The main drawback of this criterion is that it is local, since $|\bar{\bar{S}}|$ is element-wise computed (hence, $P0$) in the FE framework. This condition may not be satisfied locally without any global interaction between the transient Lorentz force and the turbulence structure. This is the case when only a little region is concerned, or the region is not mechanically active (thus a low EM force is induced) or numerical errors affect the computation of $|\bar{\bar{S}}|$ (which is common at the boundary elements). For these reasons, a global condition has to be imposed. As done in section 4.2.1 for the criterion on the temperature-coupling-scheme, we propose a second Ω_n^m-condition on the Lorentz force-turbulence interaction criterion:

$$\Omega_n^m \left[f \geq 5|\bar{\bar{S}}| \right]. \tag{4.15}$$

The value of the couple of parameters (m, n) will be computed in section 4.6 with respect to a laboratory benchmark case.

4.3 Technical implementation of the coupling scheme

In this section the coupling scheme is summarized, adding some technical description of the development. These technical choices are not fundamental from a research point of view, but they are important in terms of industrial interests. As stated before, we use a 2M2S approach implemented within THERCAST®which links an EM solver and a CFD solver. All the terms which link the two solvers should be interpolated between the meshes and stored in memory, and both these actions require heavy computational resources. By simply storing these variables in RAM (as done in [164]), a lighter coupling interface is obtained; but this choice requires to always neglect the transient part of the Lorentz force, which is not acceptable for the range of application we want to simulate. On the opposite, a file-based coupling is heavier in terms of HDD memory and coupling time, but gives more flexibility to the software. Thus we have decided to implement a file-based coupling scheme in THERCAST®structured as follows:

1. Run the EM simulation, either in the time domain or in the frequency domain. In any case, the output consists in a set of N binary files containing the Lorentz

force corresponding to the N discretization points of the EM period plus one binary file containing the average Lorentz force. The same output is produced for the induced magnetic field. A common drawback of file-based coupling schemes is that files can be read/written only in sequential, resulting in a bottleneck for parallel simulations. In order to avoid this and obtain good parallel computing performance, each core writes the output file relative to itself. In this way the reading/writing and the interpolation processes can be done in parallel, reducing the computational effort required by the coupling interface.

2. Run the CFD transient computation.

3. Every M time steps of the CFD computation, verify the Ω_n^m-condition on the temperature (equation (4.2)): if it is not respected, the EM simulation is launched again.

4. Every M time steps of the CFD computation, verify the condition on the electromotive part of the eddy currents (equation (4.6)). If it is fulfilled, only the files containing the Lorentz forces are used in the coupling interface. Otherwise, the files containing the induced magnetic field will also be used. For the sake of clarity, we will not follow the latter case in this description because it is very uncommon for the cases we want to simulate.

5. Every M time steps of the CFD computation, verify the Ω_n^m-condition on the Lorentz force-turbulence interaction (equation (4.15)): if it is fulfilled, only the time average value of the force will be used. Otherwise, at each time step the corresponding value of the force will be used.

6. If necessary, read the output of the EM analysis, interpolate it to the CFD mesh, and write the interpolated field in a binary file. These new files are stored because they can be used in future time steps with no need of re-interpolation between the mesh (which is the heaviest part of the algorithm).

7. In case of anisotropic remeshing, erase all the files containing the interpolated fields.

8. Perform the time interpolation.

9. Add the EM force as a source term in the Navier-Stokes equations. If the electromotive term is considered, it is modelled explicitly, hence as a source term as well (see sections 4.4 and 4.6).

10. Continue the CFD simulation.

This coupling scheme is also depicted in figure 4.2, where the superscripts X^{em} and X^{cfd} mean that the field refers to the mesh used in the electro-magnetic and the fluid mechanics simulations respectively. For the sake of clarity, some actions like the CFD algebraic solution, the time-step computation and the stopping criteria have been omitted and included implicitly in the action "CFD time-step".

4.4 Explicit modelling of the electromotive part of the Lorentz force

As stated before, we have chosen to model the braking term of the Lorentz force explicitly, it will therefore be an additional source term in the NS equations instead of being on the LHS of the NS equation. This choice implies to used the velocity field corresponding to the previous time-step and enables to use the classic CFD solver and its stabilization algorithm shown in chapter 3. In order to validate its implementation, we choose to put ourselves in a configuration where this is the only term, i.e. a fluid flow subjected to an uniform external magnetic field. In this case, the Lorentz force can be written as

$$\underline{f}_L = \underline{j} \times \underline{B}_0, \tag{4.16}$$

$\underline{B}_0$ being the imposed magnetic field. The current density is then reduced to

$$\underline{j} = \sigma(-\nabla\phi + \underline{u} \times \underline{B}_0). \tag{4.17}$$

The electric potential (ϕ) has to respect the current density conservation condition

$$\begin{aligned} &\nabla \cdot \underline{j} = 0 \\ &\Delta\phi = \nabla \cdot (\underline{u} \times \underline{B}_0) \end{aligned} \tag{4.18}$$

which is naturally satisfied for any in-plane magnetic field vector superimposed to a 2D flow, since

$$\Delta\phi = \partial_z(u_x B_y - u_y B_x) \equiv 0. \tag{4.19}$$

The choice of considering only the 2D case is motivated in section 4.6. The braking Lorentz force can thus be easily computed as

$$\underline{f}_L = \sigma(\underline{u}^- \times \underline{B}_0) \times \underline{B}_0, \tag{4.20}$$

$\underline{u}^-$ being the velocity field at the previous time step. The problem is that this explicit modelling is not unconditionally stable and, especially at high values of $\underline{B}_0$, it leads to numerical instabilities of the model. The convergence of the pure

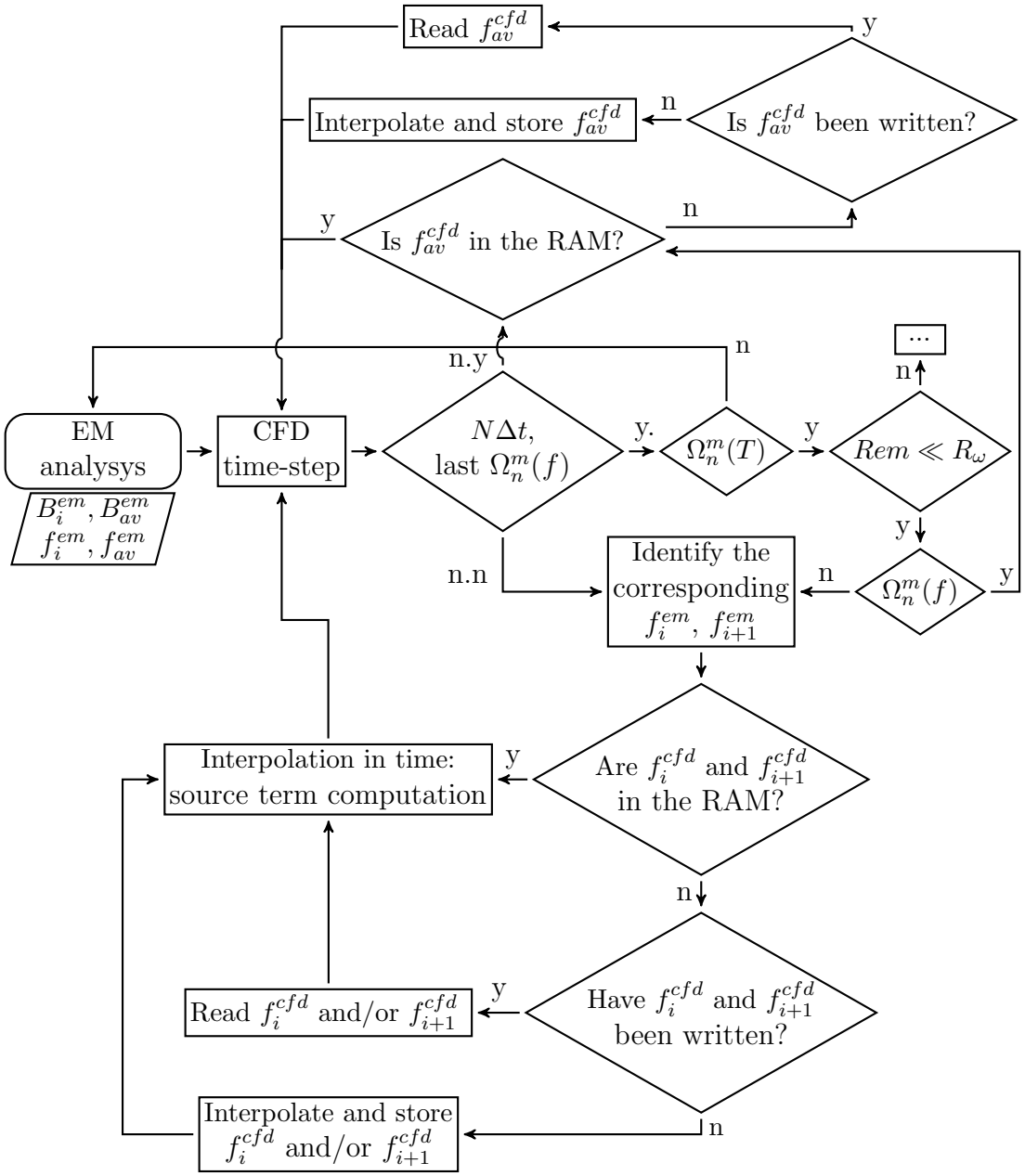

Figure 4.2: Coupling scheme

CFD formulation is guaranteed from a restriction on the time-step, which must be computed according to the *CFL* condition:

$$\Delta t_{CFL} < \frac{C\Delta x}{u} \tag{4.21}$$

where u is the fluid velocity, C is a coefficient and Δx is the characteristic dimension of the element.

Different problems arise when the magnetic interaction parameter is increased. For high values of N, the transient flow's time scale could be of the same magnitude as the Δt_{CFL}: in this configuration a different Δt has to be calculated to obtain both accuracy and convergence, as shown in [170, 171]. To do this, we consider a purely inertial flow, which is reasonable at high Re. This is also justified with respect to continuous casting, where the metal density is high as well as the turbulence . We want to find the time-step by which the piece-wise constant Lorentz force completely brakes the flow in one time-step. So we compare the work of the external force to the internal energy, approximated to the kinematic energy:

$$\int d\mathcal{E} = \int \delta\mathcal{W}. \tag{4.22}$$

We consider the force to be constant in time and opposite to the velocity, thus:

$$\frac{1}{2}\rho u_0^2 = f_L s(t). \tag{4.23}$$

where $s(t)$ is the displacement of a material particle during the time step.
By considering a material particle far enough from the boundary, and by assuming the magnetic field normal to the velocity (most restrictive case), we can reduce the motion of the particle to a constant decelerating motion

$$s = ut + \frac{1}{2}at^2 = ut - \frac{1}{2}\frac{f_L}{\rho}t^2. \tag{4.24}$$

By substituting equations (4.16) and (4.24), we can rewrite equation (4.23) as:

$$\begin{gathered} -\frac{1}{2\rho}(\sigma B^2)^2\Delta t^2 + \sigma B^2 \Delta t - \frac{1}{2}\rho = 0 \\ \Delta t^* = \rho\frac{1}{\sigma B^2} \end{gathered} \tag{4.25}$$

where Δt^* is the threshold where the work of the external force is high enough to dissipate all the kinetic energy in one time-step. Similarly, $\Delta t = 2\Delta t^*$ will be the time step which will allow the force to induce a flow opposite to the flow at the previous time-step in the areas far enough from the boundary. In the following section, a validation of this limit time step is proposed in relation to a reference case.

4.4.1 Validation of the limit time-step condition in reference to the lid-driven cavity benchmark case

The flow in a cavity induced by the motion of one of the walls is a classical benchmark for fluid mechanics analyses and it has been widely studied in literature [172, 173, 174]. The most interesting part of the flow is the area close to the corners, where high turbulence and discontinuous velocity occur [175]. The flow has been studied at different range of Reynolds number (Re) up to 100000 in [176]. Approaches similar to the one used in the present work have been used to study Reynolds from 10000 in [177, 178] and up to 50000 in [127, 129]. The number of induced eddies increases with the increasing of the Reynolds number, their size decreases and the flow turns to be chaotic [179]. This flow can be braked by the superimposition of a constant magnetic field [180]. This case has been used as benchmark for different applications, from biomagnetic fluids [181], to nanofluids [182]. The stabilisation due to the external magnetic field in the cavity has also been studied [183, 184, 185]. Deeper investigations have been done on the natural convected cavity under an external magnetic field both numerically [186, 187, 188, 189] and experimentally [190]. At the best of our knowledge, the flow behaviour at high Stuart number has not been object of studies. The idea is to use this benchmark to test the numerical coupling between the fluid flow and the magnetic field at different configurations, in order to find possible limitations and convergence conditions. The considered test case has been sketched in figure 4.3. The 2D square cavity has length $L = 1$; no-slip boundary conditions have been imposed at three borders while a constant tangent unity velocity has been imposed at the last border. The zero level pressure has been imposed to the vertex opposite to the applied shear velocity. The gravity is set to zero and the magnetic field is imposed in different configurations.

A newtonian, incompressible and conductive fluid has been considered. The density has been set to $\rho = 10^3\, kg/m^3$ and the dynamic viscosity μ has been set in accordance to the target Reynolds number $Re = \frac{\rho u L}{\mu}$. The electric conductivity is set to $\sigma = 7.14 \times 10^5\, \Omega m$. The external magnetic field (B_0) is constant; the Reynolds magnetic number is assumed to be less than one, hereby the induced magnetic field produced by the conductor's motion is neglected.

Horizontal magnetic field and validation

For the first test case, we set B_0 in the same direction as the x axis. In figure 4.4, u_x profile along the vertical middle-line is plotted. The benchmark is taken from [183] and $Re = 5000$ and $N = 5, 30$ are reported in figure 4.4(a) and 4.4(b) respectively. In figure 4.5 the velocity magnitude in the upper part of the cavity is plotted. We can notice that the braking effect increases as N increases and the vertical velocity

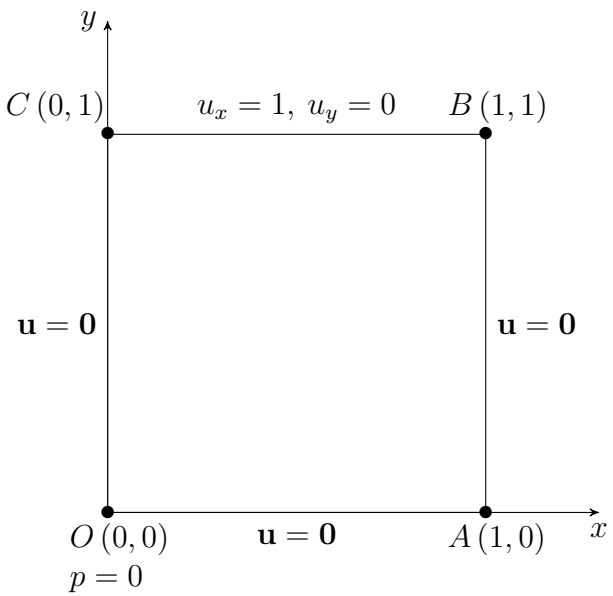

Figure 4.3: Schematic representation of the lid-driven cavity test: geometrical features and boundary conditions

(normal to B_0) is dumped. This leads to a more horizontal flow and thinner eddies, as shown in figure 4.6.

Even with higher Re the stabilizing effect of the magnetic field occurs: in figure 4.7 the evolution of the flow with respect to the magnetic interaction parameter is shown. The number of eddies is directly related to the Stuart number, as reported in figure 4.8. Note that in figure 4.8 a non-continuous variable, the number of eddies, is plotted so the linear function represents the tendency of a piece-wise constant function. As we see from figure 4.7, the different N adopted do not represent the last (and most unstable) eddy at the same level of development. The increasing of N is a constrain over the vertical flow which leads to almost horizontal re-circulation patterns. In figure 4.9 the average slope of the interface between the two upper eddies is plotted; by increasing N an alternating horizontal flow is induced and the vertical re-circulation is confined at the external boundaries. In figure 4.10 the horizontal velocity along the vertical middle-line is plotted. By increasing the magnetic field, the main horizontal flow moves upwards and the thickness is almost constant. At high N, the eddy is pushed against the lid, its thickness decreases and its velocity increases. Note also that the horizontal velocity of the secondary eddies is much lower than the velocity of the first upper eddy.
As the eddies' thickness decreases with the increasing of B, remeshing is fundamental in order to catch the small eddies without increasing the number of elements. In

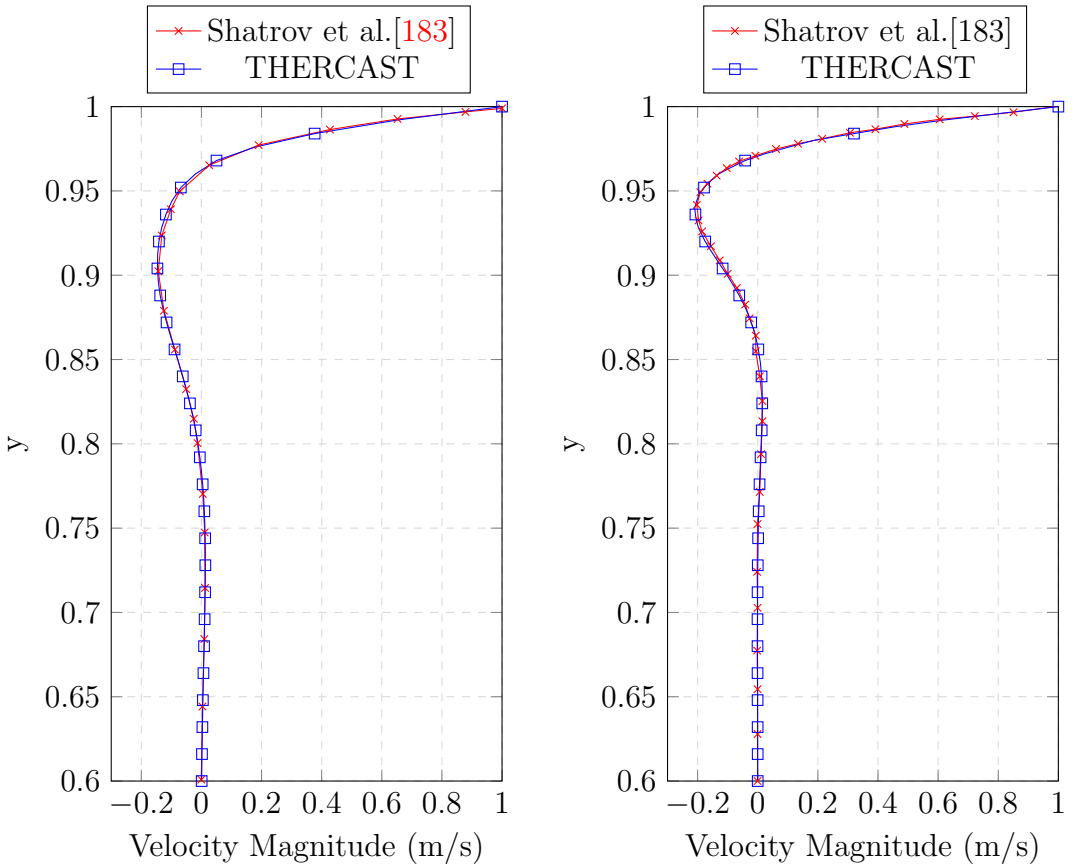

(a) Velocity profile along the middle-line, $Re = 5000$, $N = 5$

(b) Velocity profile along the middle-line, $Re = 5000$, $N = 30$

Figure 4.4: Velocity profile along the middle-line: validation.

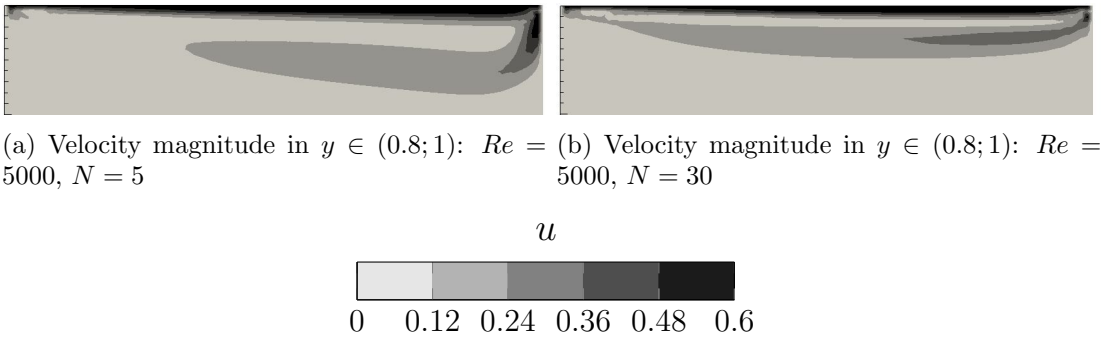

(a) Velocity magnitude in $y \in (0.8; 1)$: $Re = 5000$, $N = 5$

(b) Velocity magnitude in $y \in (0.8; 1)$: $Re = 5000$, $N = 30$

Figure 4.5: Velocity magnitude in the upper part of the cavity.

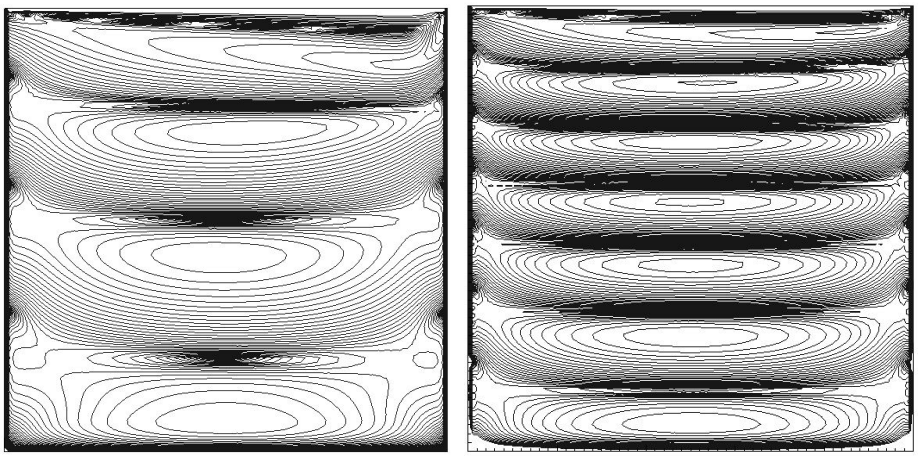

(a) Velocity magnitude isocontour: $Re = 5000$, $N = 5$

(b) Velocity magnitude isocontour: $Re = 5000$, $N = 30$

Figure 4.6: Isocontour of velocity field magnitude. The isovalues are in logarithmic scale: 20 in the range $||u|| \in (0.01; 0.5)$ and 100 in the range $||u|| \in (0; 0.01)$.

figure 4.11 we see how the mesh anisotropically adapts to the flow. From figure 4.11(c) it is possible to notice that the algorithms does not catch the low velocity eddies by itself. For this reason, the weighting parameter N_s and N_n are computed according to the magnetic interaction parameter. The anisotropic non-structured mesh allows the user to well model the boundary layers and the area close to the corners, where instabilities due to the discontinuity of boundary conditions may occur.

Vertical magnetic field

In the lid-driven cavity test, the horizontal flow is the primary one, since it's forced by the boundary condition. An horizontal magnetic field opposes to the vertical circulation of the flow, stimulating the horizontal flow. In this way we decrease the importance of the secondary vertical flow, so we create different eddies almost independent; the upper b.c. induces a first eddy, whose bottom part induces the second eddy below and so on. In order to fully interact with the mechanical behaviour we decided to consider a magnetic field facing the primary flow. In the second test case the orientation of the magnetic field was changed, so that $B_y = const.$ and $B_x = B_z = 0$. In this configuration the primary flow, driven by b.c., must cross the magnetic field, so a higher level of braking is expected. In figure 4.12 the flow at different Stuart numbers is described. The first effect of the magnetic field is to sharpen the flow at the upper-right corner and to suppress the smallest eddies (figure 4.12(b)). By increasing the Stuart number the main eddy gets squeezed along

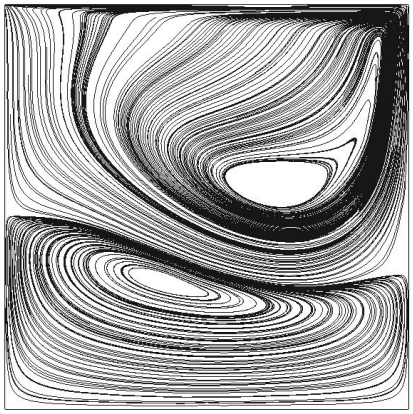

(a) Velocity streamlines: $Re = 10000$, $N = 0.5$

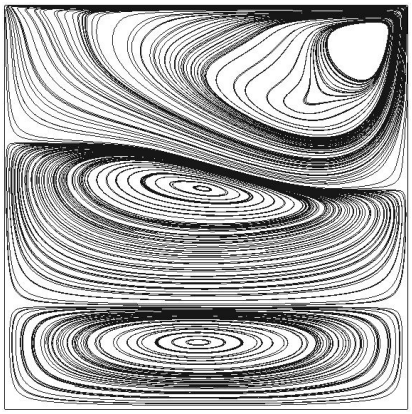

(b) Velocity streamlines: $Re = 10000$, $N = 1$

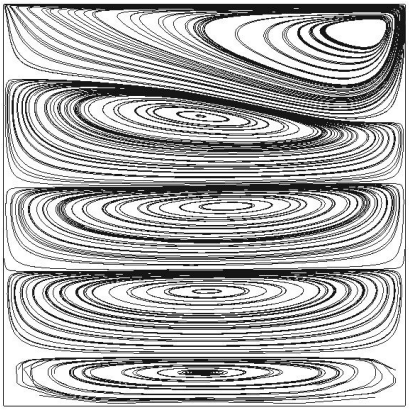

(c) Velocity streamlines: $Re = 10000$, $N = 2$

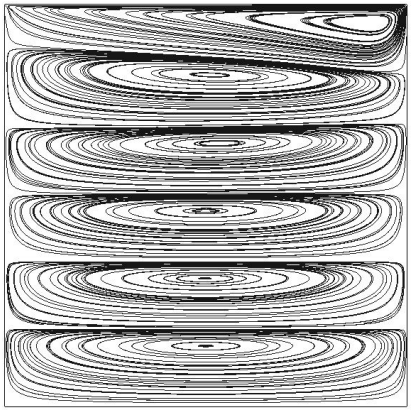

(d) Velocity streamlines: $Re = 10000$, $N = 5$

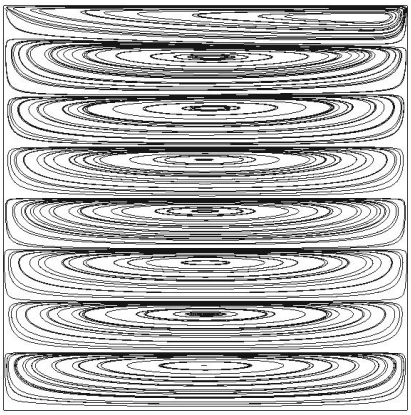

(e) Velocity streamlines: $Re = 10000$, $N = 15$

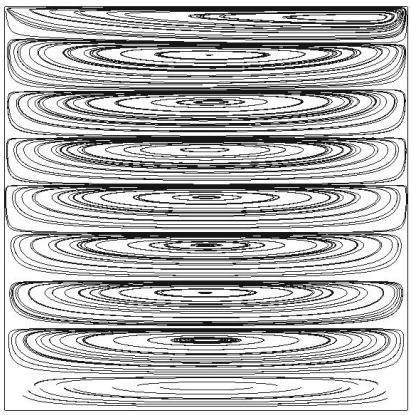

(f) Velocity streamlines: $Re = 10000$, $N = 20$

Figure 4.7: Velocity streamlines of the flow subjected at different external magnetic field's magnitudes.

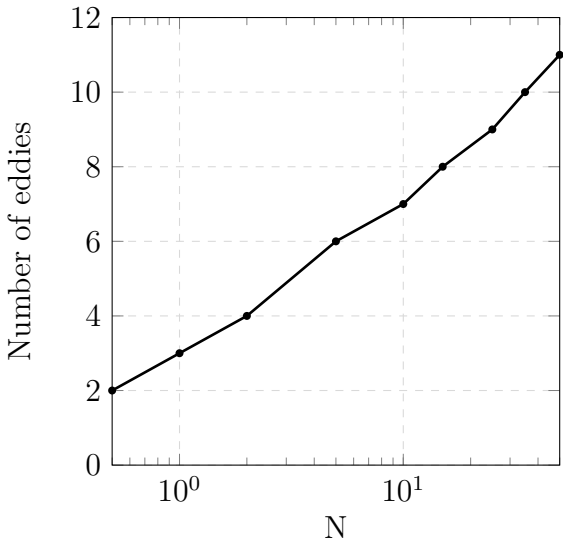

Figure 4.8: Number of horizontal eddies with respect to the magnetic interaction parameter.

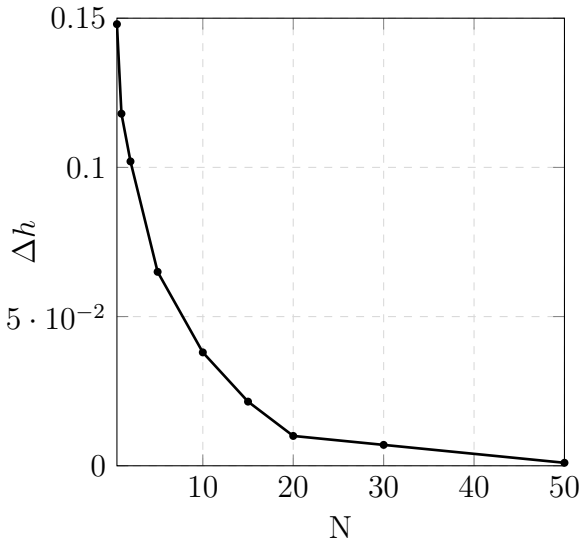

Figure 4.9: Average slope of the interface between the two upper eddies.

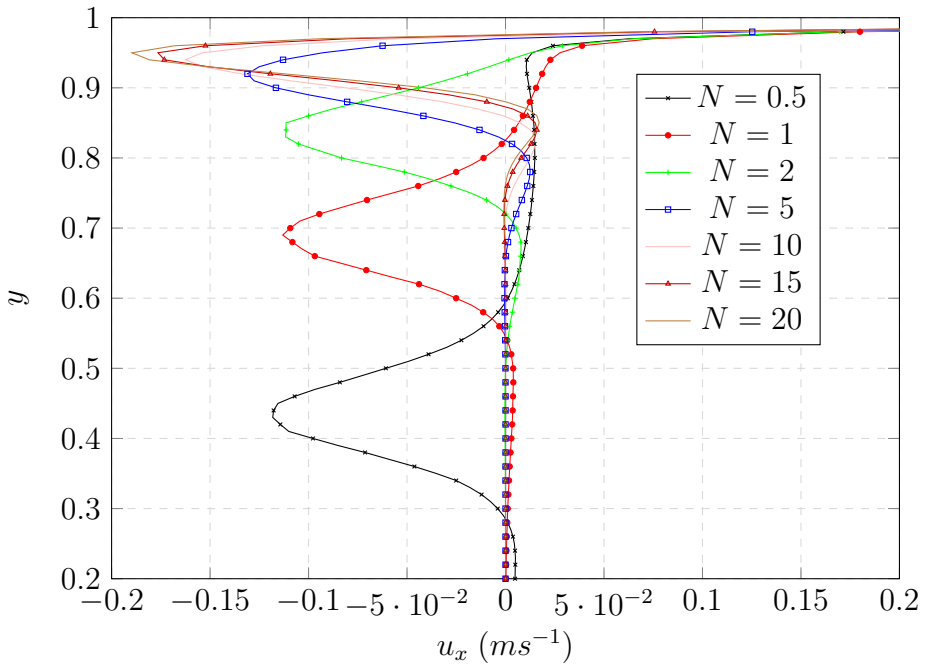

Figure 4.10: Horizontal velocity profile along the vertical middle-line

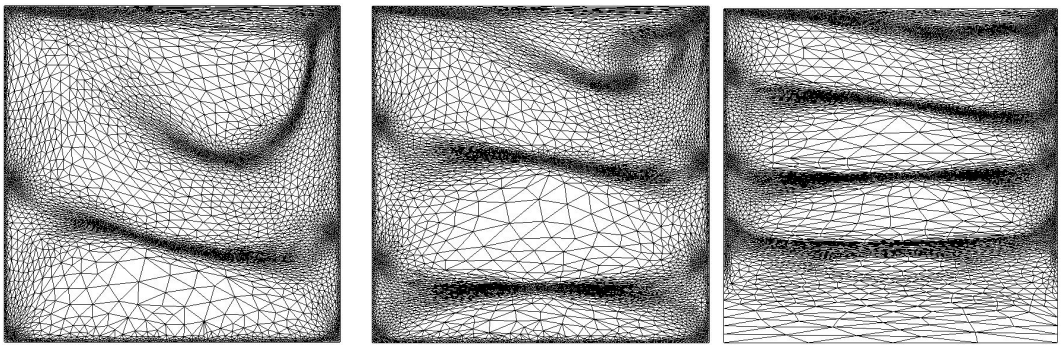

(a) Final mesh: $Re = 10000$, $N = 0.5$

(b) Final mesh: $Re = 10000$, $N = 1$

(c) Final mesh: $Re = 10000$, $N = 2$

Figure 4.11: Dinamically adapted anisotropic mesh.

the right boundary, where the kinetic energy input by the b.c. is highest. Finally, in figure 4.12(f), the flow is controlled by the magnetic field. The fluid coming from the upper boundary deviates in the y direction since the magnetic field prevents the horizontal flow. Despite this, the flow has to move to the left side because of the boundary conditions on velocity and so it can not form an independent eddy. For this reason a slow, laminar flow is formed in the middle of the cavity. Over this value of N, the vertical eddy's size would decrease as well as the magnitude of velocity in the center band. The height of the right eddy depends on the Reynolds number: as reported in table 4.1 a higher Reynolds number leads to a higher vertical excursion of the eddy. It is also shown a very known result, by which a high Stuart number can regularize the turbulent flow and make it steady. In figure 4.13 the horizontal velocities along the horizontal middle-line are reported. We notice that the constant velocity band in the middle is wider when Re is higher (and μ lower); the low-viscosity flow is therefore constrained into a thin and high eddy close to the right boundary. The same process is clear from the same plot for a higher Stuart number (figure 4.14). The curve for the same Re ($Re = 10000$ and $Re = 20000$) are more braked, thus the velocity peaks decrease and the plateau is wider (until almost $x = 0.8$ against about $x = 0.55$).

Table 4.1: Minimum height of $||u|| = 0.05$ isovalue.

Re	$y_{N=7.14}$	$y_{N=1.785}$
200000	0.11	non-steady
100000	0.165	non-steady
50000	0.22	0.09
20000	0.33	0.148
10000	0.44	0.175
5000	0.5	0.21
1000	0.52	0.258

In figure 4.15 we plot the number of nodes where the velocity normal to the magnetic fields reverses over one time step, i.e. $u^n \cdot f^n > 0$; in this case the Lorentz force brakes the flow and then accelerates it inside the same time increment. Since the Lorentz force does not follow the velocity inside the time step, it happens that for fast transient phenomena the Δt_{CFL} is of the same magnitude than the transient flow itself. From figure 4.15 we see that $\Delta t = 3 \cdot 10^{-3}\, sec$ leads to invert the flow in 55% of the domain. It is important to underline that in a Eulerian framework, this is a natural phenomenon: the velocity variation is related to the spatial deformation of the flow and not on the material particle itself. In this case the pathological behaviour is evident from the fast increase of the number of these points, as clear

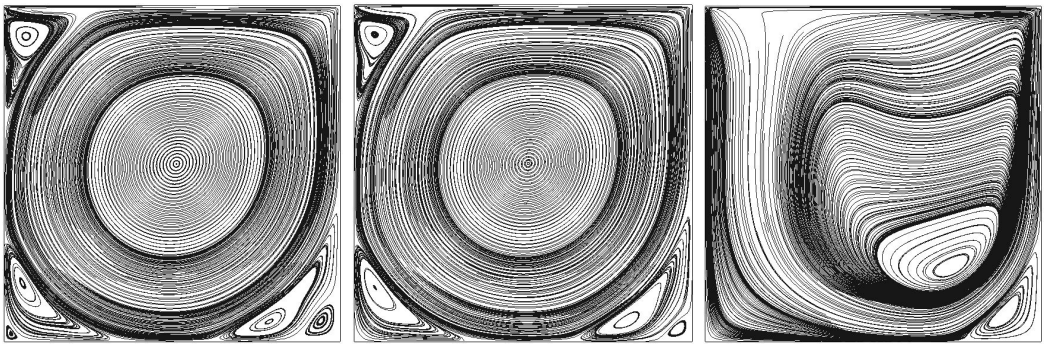

(a) Velocity streamlines, $Re = 10000$,$N = 0$

(b) Velocity streamlines, $Re = 10000$, $N = 0.01785$

(c) Velocity streamlines, $Re = 10000$, $N = 0.2856$

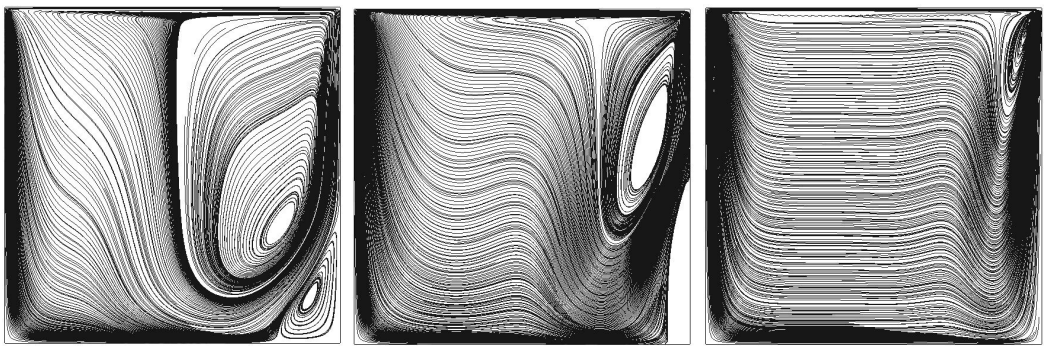

(d) Velocity streamlines, $Re = 10000$, $N = 0.6426$

(e) Velocity streamlines, $Re = 10000$, $N = 1.785$

(f) Velocity streamlines, $Re = 10000$, $N = 7.14$

Figure 4.12: Velocity streamlines of the lid-driven cavity flow under a vertical magnetic field.

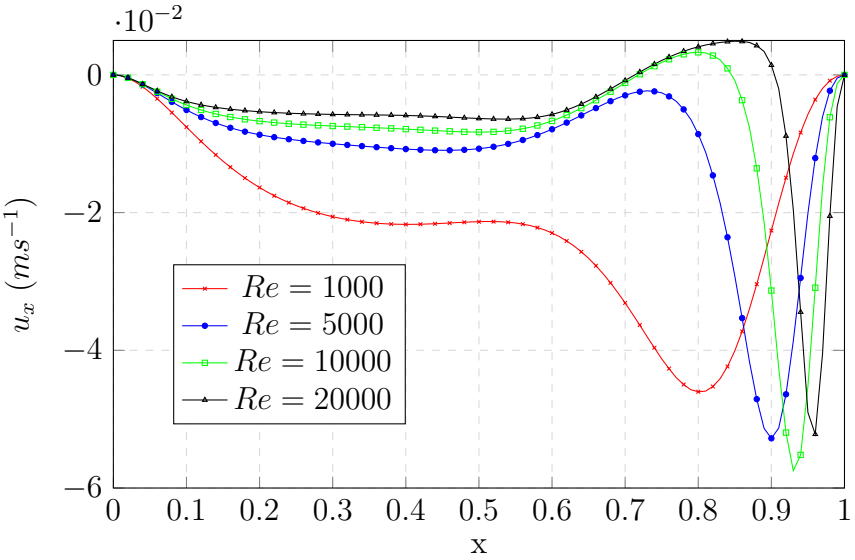

Figure 4.13: u_x plot over the center-line $y = 0.5$ at different Re and $N = 1.785$.

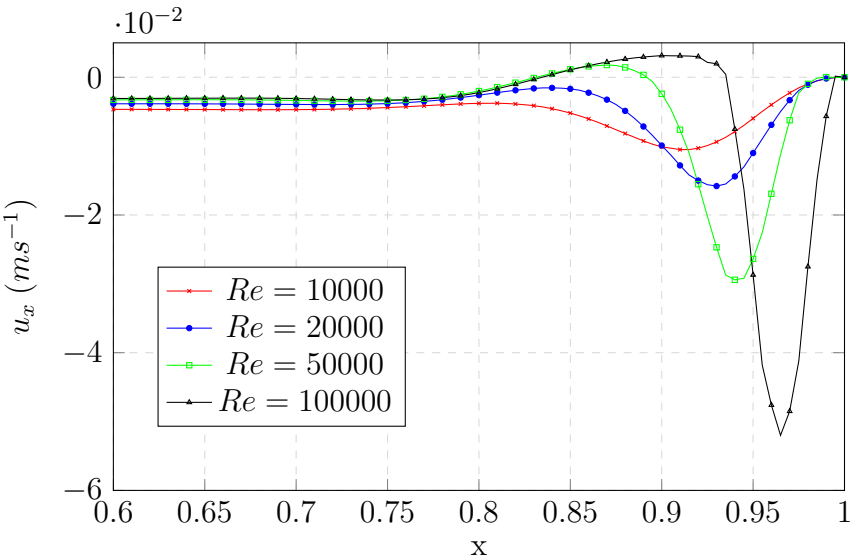

Figure 4.14: u_x plot over the center-line $y = 0.5$ at different Re and $N = 7.14$.

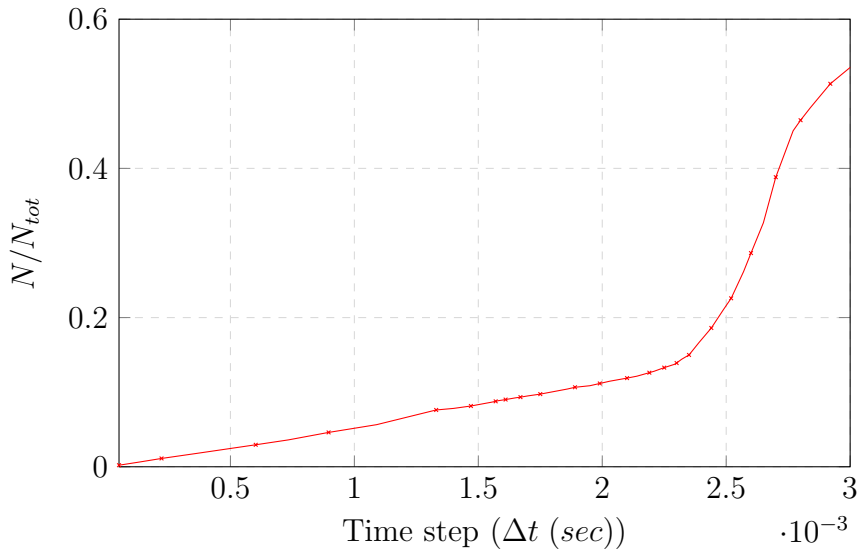

Figure 4.15: Number of reverse-velocity nodes normalized to the total number of free nodes, $N = 7.14$.

from figure 4.15. To better analyse this problem, we will consider the most restrictive case in section 4.4.1.

Perfect braking case

In this section we will present a numerical test in order to better catch the numerical problem shown in figure 4.15. We propose to consider a Lorentz force opposite to velocity on the whole domain (perfectly braking) and equal to:

$$f_L = \sigma u B^2. \tag{4.26}$$

By this test we will be able to:

- *Minimize the flow deformation.* As stated in section 4.4.1, "reverse velocity" point could be naturally produced by the flow deformation in Eulerian simulations. By imposing a perfectly braking force, the flow will be slowed but not heavily deformed. The pathological velocity inversion will occur on the whole domain for the same time step, so it will be easily detected.

- *Extend the numerical problem on the whole domain.* In the cases of vertical and horizontal magnetic field, the numerical problems occurred in the regions where magnetic reaction to the flow was maximum, so where the velocity was normal to the magnetic field. By imposing a perfectly braking force we will be able to extend the same conditions to the whole domain.

This numerical test case represents all the physical cases in which the Lorentz force is opposite to the velocity globally (e.g. vertical flow with an horizontal magnetic field) or locally (e.g. cases in sections 4.4.1 and 4.4.1).

Several tests similar to the one reported in figure 4.15 have been conducted and the results are reported in figure 4.17. In all these configurations we notice that the turn of velocity is much faster than in the case of vertical magnetic field. In figure 4.15 the velocity turning is smoother because part of the Lorentz force's work is spent to deform the flow; in this case the extra-constraint on deformation leads to an almost instantaneous velocity turning, where the energy dissipated inside the time step is high enough to balance the inertia. We can also notice that the expression (4.25) predicts well the time-step which leads to this phenomenon, represented by the dotted lines (notice that few different time steps were used for each simulation, so the whole band is included between the smaller and larger time steps used). We do not report the complete curves for all the configurations analyzed, but in figure 4.18 we show the variation of the critical time step over the variation of the main problem variables: from this figure we see the the dependencies are conform to the one adopted in (4.25). As depicted in figure 4.16, this condition could be more restrictive than the CFL condition for cases with high Stuart number, so it must be considered for the explicit modelling of the Lorentz force.

The choice of Δt affects also the convergence. In figure 4.19 the convergence of the L^2 error is plotted; the error is here computed with respect to an overkilled solution with $\Delta t \ll min(\Delta t)$. From this plot we see that for $\Delta t \geq 2\Delta t^*$ the simulation diverges, even if we respect the *CFL* condition. In this case the Lorentz force (constant inside the time-step) is high enough to reverse the flow and increase the velocity magnitude in the opposite direction, which leads to a diverging acceleration of the flow, thus we have

$$\begin{cases} u^n \cdot u^{n-1} < 0 \quad \vee \quad ||u^n|| \geq ||u^{n-1}|| \\ f_L^n \cdot u^n > 0 \quad \vee \quad ||f_L^n|| \geq ||f_L^{n-1}||. \end{cases} \tag{4.27}$$

For $\Delta t \in (\Delta t^*; 2\Delta t^*)$ the solution converges, but the convergence rate is small. In this interval, the transient flow is not well predicted since the punctual velocity reverses its direction at each time-step. The flow will oscillate across an equilibrium point but the reverse velocity's magnitude is still lower than the one at the previous time step, so the oscillations decrease amplitude. This configuration is defined as:

$$\begin{cases} u^n \cdot u^{n-1} \leq 0 \quad \vee \quad ||u^n|| < ||u^{n-1}|| \\ f_L^n \cdot u^n \geq 0 \quad \vee \quad ||f_L^n|| < ||f_L^{n-1}||. \end{cases} \tag{4.28}$$

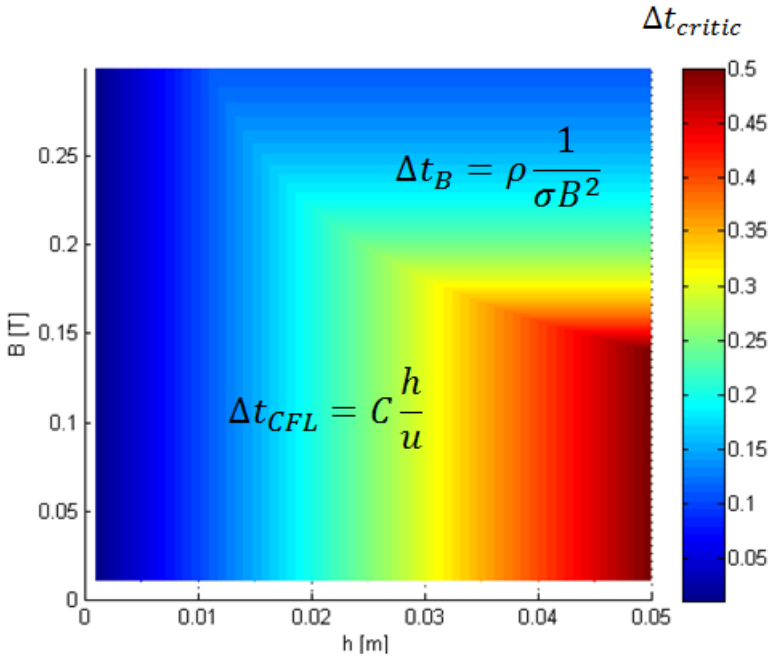

Figure 4.16: Comparison between the CFL condition and the MHD limit time-step.

For $\Delta t < \Delta t^*$ the converge rate is higher and no verse-changing takes place and the following conditions are satisfied:

$$\begin{cases} u^n \cdot u^{n-1} > 0 \quad \vee \quad ||u^n|| < ||u^{n-1}|| \\ f_L^n \cdot u^n < 0 \quad \vee \quad ||f_L^n|| < ||f_L^{n-1}||. \end{cases} \tag{4.29}$$

In this case the Lorentz force monotonically brakes down the flow. The velocity's evolution is qualitatively convex and monotonically decreasing, so the piece-wise constant approximation of the Lorentz force leads to an over-estimation of the braking effect, which still does not affect the convergence. These considerations are directly connected to the prediction of the transient state; in figure 4.20, the time required to reach the steady state is plotted. For $\Delta t = 2\Delta t^*$ the required time tends to infinity because the system oscillates between two opposite velocity fields. For $\Delta t < \Delta t^*$ the solution tends to a constant value, $T_s = 0.52$ in the current simulation.

In figure 4.21 the horizontal velocity at $P(0.5; 0.75)$ is plotted over the time-steps. As expected, we see that the simulation with $\Delta t = 0.0072 > 2\Delta t^*$ diverges and the one with $\Delta t = 0.0001 < \Delta t^*$ converges providing a good description of the transient state. Between these cases, we see that for $\Delta t \in (\Delta t^*; 2\Delta t^*)$ the simulations converge to the correct steady state, but the transient state is oscillatory, due

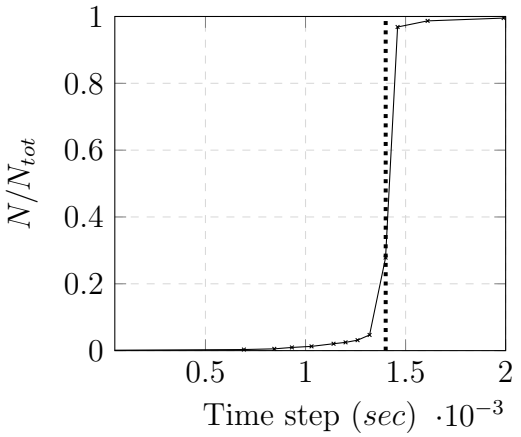

(a) Reverse-velocity points: $\mu = 0.1$, $B_z = 1$, $\rho = 1000$, $\sigma = 714000$

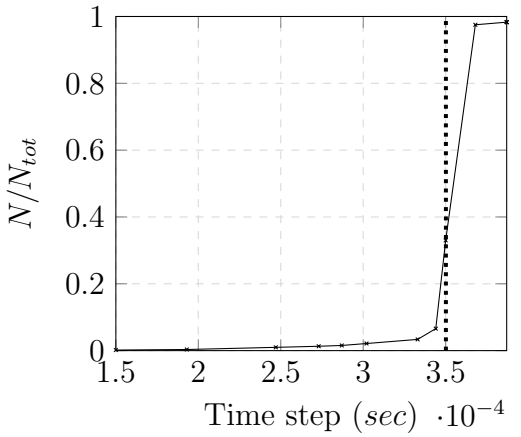

(b) Reverse-velocity points: $\mu = 0.1$, $B_z = 2$, $\rho = 1000$, $\sigma = 714000$

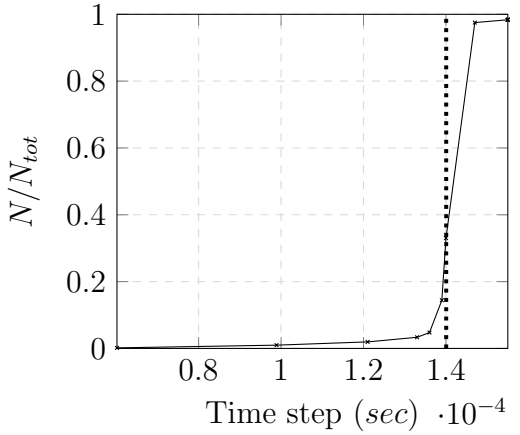

(c) Reverse-velocity points: $\mu = 0.1$, $B_z = 1$, $\rho = 100$, $\sigma = 714000$

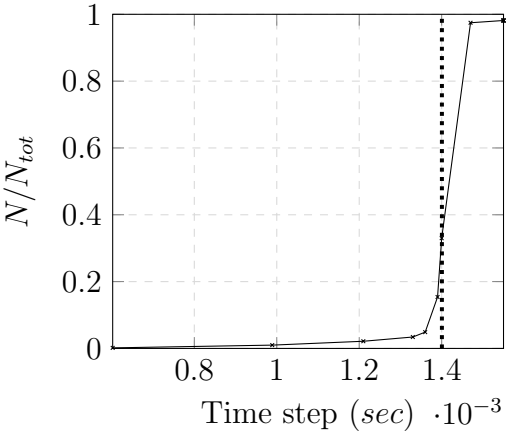

(d) Reverse-velocity points: $\mu = 0.1$, $B_z = 1$, $\rho = 1000$, $\sigma = 714000$, $u_{b.c.} = 2$

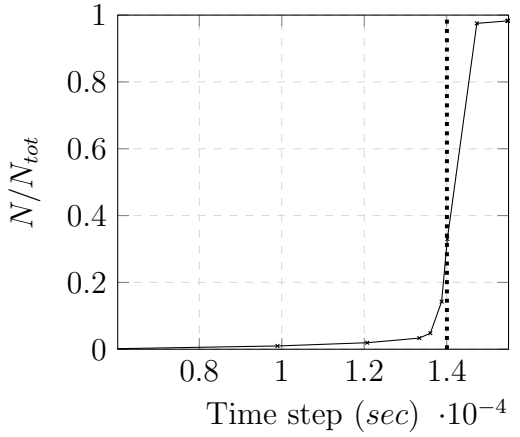

(e) Reverse-velocity points: $\mu = 0.1$, $B_z = 1$, $\rho = 1000$, $\sigma = 7140000$

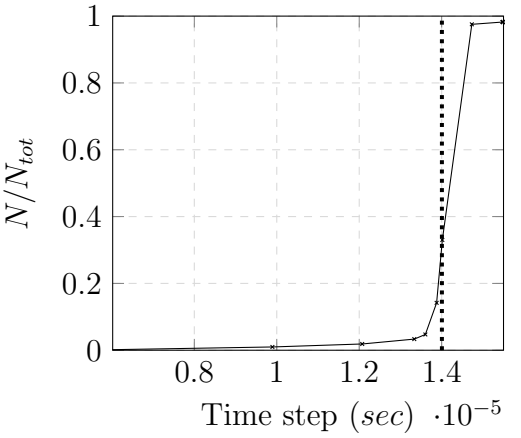

(f) Reverse-velocity points: $\mu = 0.1$, $B_z = 1$, $\rho = 1000$, $\sigma = 71400000$

Figure 4.17: Normalized reverse-velocity points in different problem configurations.

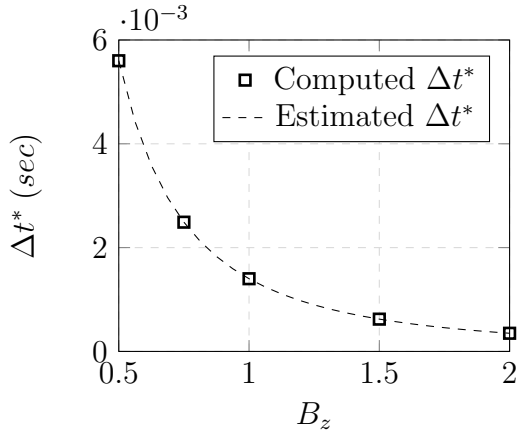

(a) Critical time-step variation at different magnetic field magnitudes

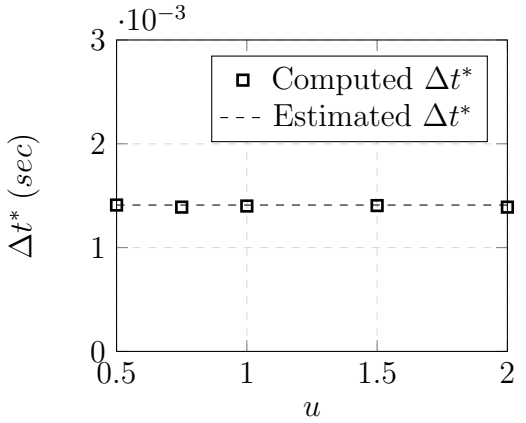

(b) Critical time-step variation at different velocity magnitudes

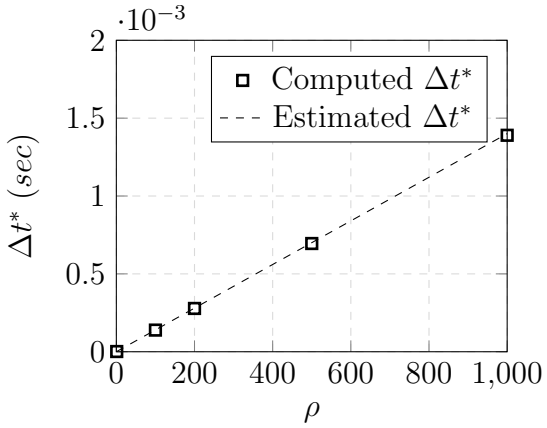

(c) Critical time-step variation at different velocity magnitudes

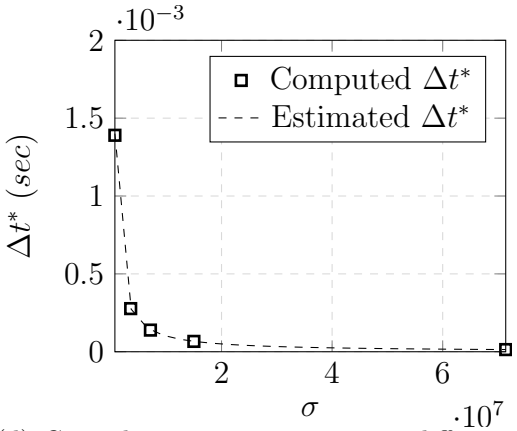

(d) Critical time-step variation at different material's conductivity

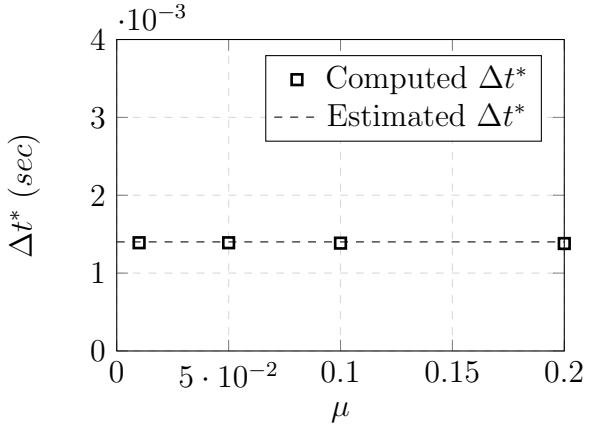

(e) Critical time-step variation at different material's viscosity

Figure 4.18: Critical time-step variation with respect to main physical parameters' variation.

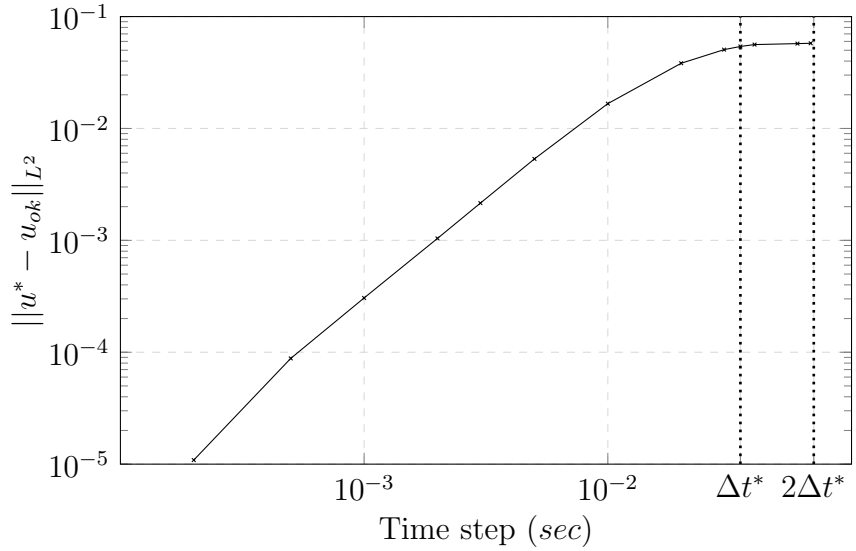

Figure 4.19: Convergence of error with respect to the refinement in the time discretization.

to the numerical problems connected to the time-step. It is also important to note that the velocity, in those cases, does not reverse at each time step forever (like for $\Delta t = 0.0072 > 2\Delta t^*$): when the velocity is low enough so that the viscous energy is dominant with respect to the kinetic energy, the external work is no more sufficient to dissipate the whole energy and equation (4.25) is no longer valid. In figure 4.21, we see that the simulation with $\Delta t = 0.006$ stops oscillating at the $16th$ step. For $\Delta t = 0.0068$, this point is reached at the $68th$ step.

4.5 Two phase flow under a uniform magnetic field: extension of the dam-break benchmark case

In this section, a multiphase flow under external uniform magnetic field is simulated and benchmarked [191]. The objective is to test the convergence condition described in section 4.4 and the set of numerical methods proposed in chapter 3 for the CFD problem. The coupling scheme is not the full one described in sections 4.2 and 4.3, because a uniform external magnetic field is modelled. For this reason, there is no need of an EM simulation performed on a different mesh, thus the magnetic field evolution is computed on the CFD mesh through the induction equation and the

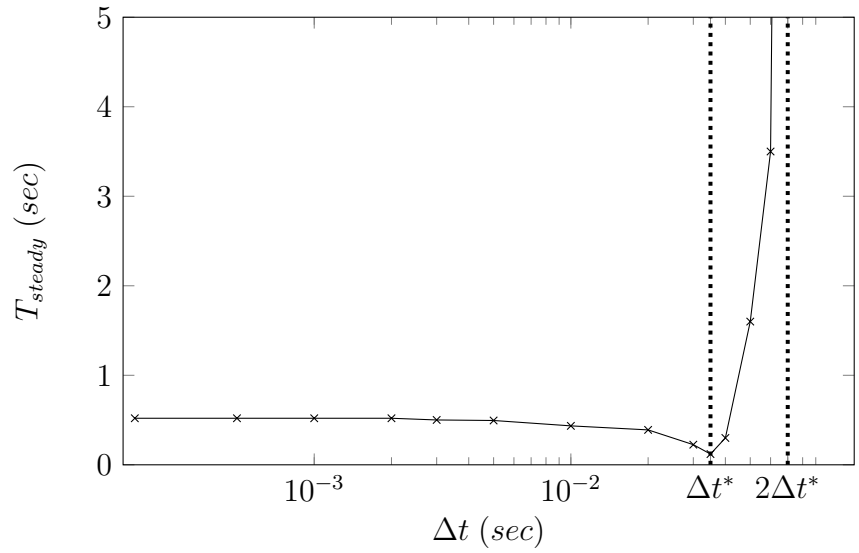

Figure 4.20: Physical time to reach the steady state with respect to the time-step.

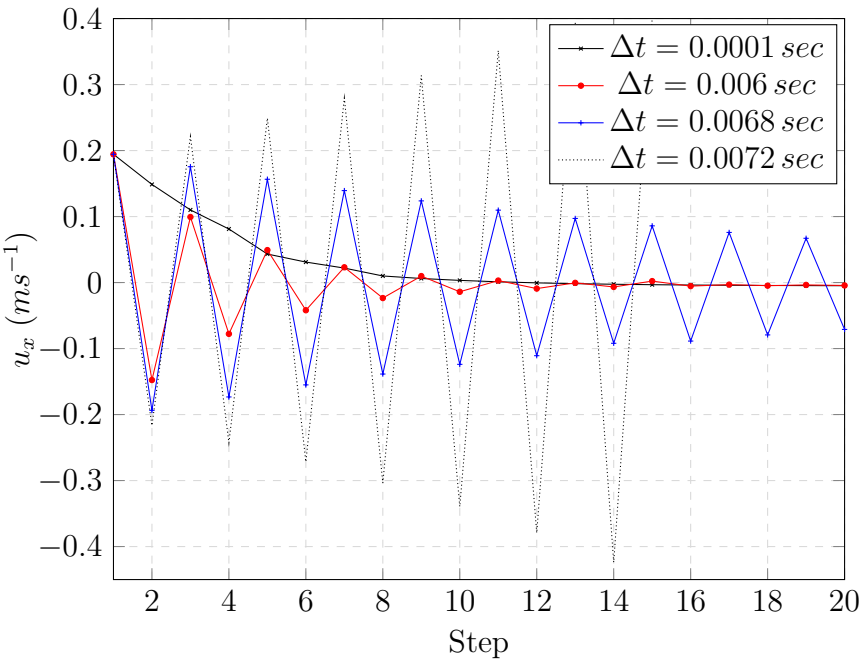

Figure 4.21: Evolution of the horizontal velocity at $P(0.5; 0.75)$ with different time-steps and $\Delta t^* = 0.0035\,sec$.

Gauss' law of magnetism:

$$\begin{aligned} \frac{\partial \underline{B}}{\partial t} &= \eta \nabla^2 \underline{B} + \nabla \times (\underline{u} \times \underline{B}) \\ \nabla \cdot \underline{B} &= 0 \end{aligned} \tag{4.30}$$

with η being the magnetic diffusivity. $\underline{B}$ is the global magnetic flux density defined as

$$\underline{B} = \underline{B}_{ext} + \underline{b} \tag{4.31}$$

where $\underline{B}_{ext}$ is the external constant and uniform magnetic field and $\underline{b}$ is the induced magnetic field.

Since in this work we will consider the behaviour of a liquid metal column ($\eta \approx 1.1$), we can compute the Reynolds magnetic number as $Rem = UL/\eta = 2 \times 10^{-2}$, where L is a characteristic dimension of the physical problem and U is the average fluid velocity. For this range of magnetic Reynolds number, the magnetic field convection due to fluid motion is negligible with respect to its diffusion, thus $|\underline{b}| \ll |\underline{B}_{ext}|$. All the proposed computations have been made without the convective term, with the exception of those proposed in section 4.5.2, in order to check the validity of the hypothesis. The induction equation has been solved according to the method proposed by [192].

The time-step has been computed to respect the CFL condition, the explicit MHD critical time step proposed in section 4.4 and to force the interface to remain in the re-meshed thickness. Thus, the final expression for the time-step is:

$$\Delta t = \min \left\{ C \cdot \left(\frac{\Delta x}{u_x} + \frac{\Delta y}{u_y} \right) ;\ \rho \frac{1}{\sigma B^2};\ \varphi \frac{E}{u_\perp \cdot p} \right\} \tag{4.32}$$

where C is the CFL constant, Δx and Δy are the elements size, p is the period of re-meshing in time-steps and φ is a coefficient depending on the temporal derivative of the velocity field. The velocity normal to the interface $u_\perp$ has been computed as:

$$u_\perp =< u; \frac{\nabla \tilde{\alpha}}{||\nabla \tilde{\alpha}||} > \tag{4.33}$$

being $\hat{\alpha}$ the filtered level-set function.

4.5.1 Problem set-up: the dam-break benchmark

In this section, the dam-break benchmark has been chosen to validate the pure CFD scheme and to be extended to MHD cases. This problem was firstly formulated by

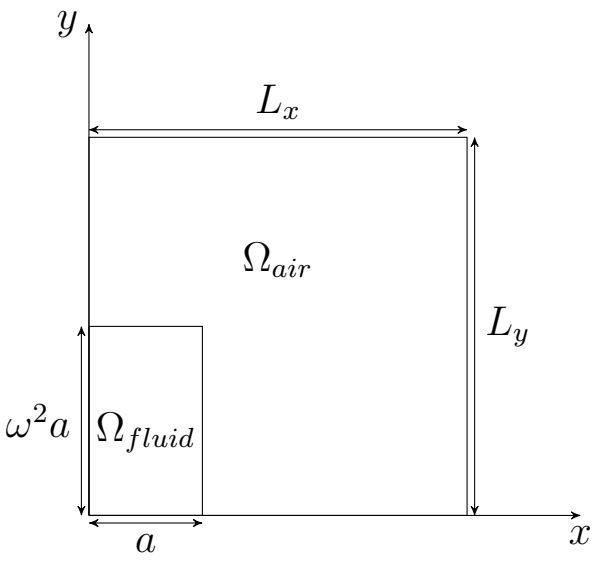

Figure 4.22: Schematic representation of the dam-break test: geometrical features and initial phases disposition.

[193]. The problem was than studied by several authors both experimentally and numerically ([194, 195, 196, 197, 198]). Different conditions have been considered ([199, 200]) in order to provide results closer to real engineering cases such as dam failures and floods. The case has finally become a benchmark to test advanced numerical techniques for multi fluid simulations ([201, 202, 203, 204, 205]), grid adaptation ([206]), unstructured mesh adaptation ([207]) and multiphase simulation techniques ([208, 209, 210]).
The dam-break benchmark represents the study of the collapse of a fluid column in an air cavity. In this work a 2D simplification is used and only half of the domain is simulated by taking advantage of the symmetry line; a sketch of the simulation domain is presented in figure 4.22, where a and ω are geometrical parameters defining the width of the liquid column and the ratio between its height and its width.

4.5.2 Results

Validation

In the present section the validation of the test case with no external magnetic field is reported. The kinematics of the fall (see figure 4.23) has been studied and the benchmark results have been taken from the work of [193] (experimental data), Murrone [202] (numerical results) and Elias [211] (numerical results for the 3D simulation). The main problem parameters used in the simulation have been reported

in table 4.2.

Table 4.2: Main problem parameters: validation test case.

ρ_{fluid}	$1000\ kg/m^3$
ρ_{air}	$1\ kg/m^3$
μ_{fluid}	$1 \cdot 10^{-3}\ Pa \cdot m^3$
μ_{air}	$1 \cdot 10^{-6}\ Pa \cdot m^3$
L_x	$0.5 \quad m$
L_y	$0.15 \quad m$
a	$0.06 \quad m$
ω^2	2

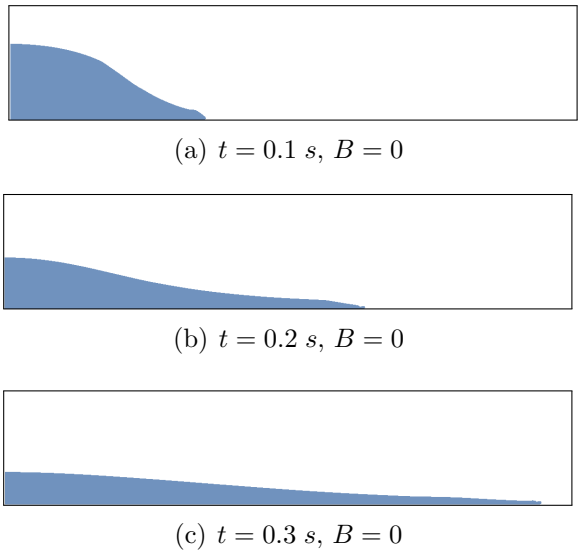

(a) $t = 0.1\ s$, $B = 0$

(b) $t = 0.2\ s$, $B = 0$

(c) $t = 0.3\ s$, $B = 0$

Figure 4.23: Column fall evolution.

In figure 4.24 the non-dimensional front position versus the non-dimensional time is plotted, while in figure 4.25 a second comparison has been done, referring to the height of the liquid column. In this case note that the non-dimensional times are different in order to keep the same notation as the original works. The obtained results are in good agreement with both experimental and numerical benchmarks, especially in the computation of the height of the column, which lacked accuracy in the previous numerical work.

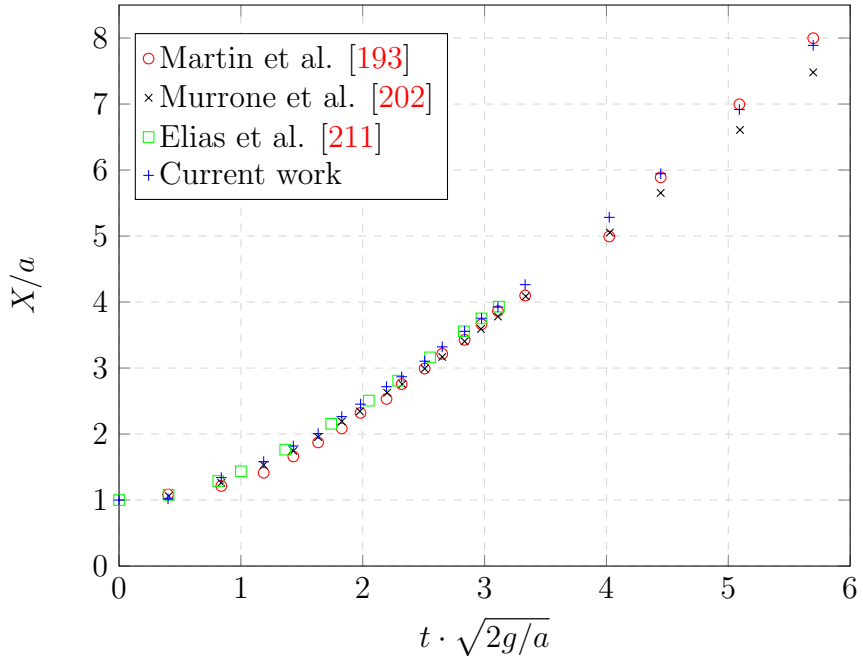

Figure 4.24: Non-dimensional front position evolution.

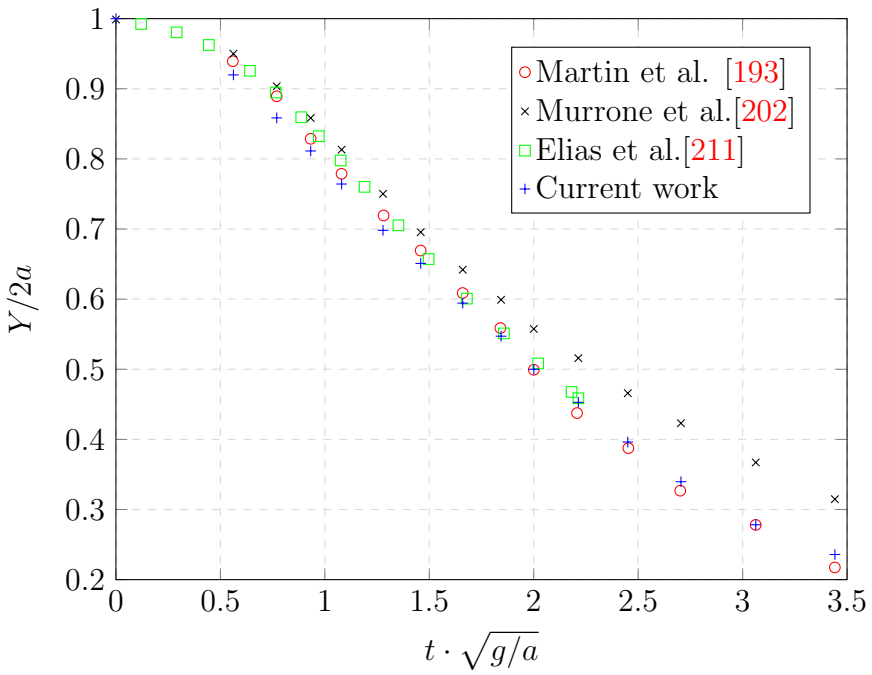

Figure 4.25: Non-dimensional column height evolution.

Mesh adaptation

For the extension of the test case, some parameters have been changed as reported in table 4.3 in order to fit the case of a conductive fluid, e.g. molten steel.

Table 4.3: Main problem's parameters: conductive fluid.

ρ_{fluid}	$7000 : kg/m^3$
μ_{fluid}	$6 \cdot 10^{-3}\ Pa \cdot m^3$
L_x	$0.5 \quad m$
L_y	$0.5 \quad m$
a	$0.09 \quad m$
ω^2	0.888

In [202], 12000 nodes have been used to mesh the domain. In the current work, anisotropic mesh adaptation allows to dramatically decrease the ratio between degrees of freedom and accuracy. In figure 4.26 the mesh after $0.1\,s$ is shown; it is clear how the automatic adaptation refines the mesh close to the interface and in the boundary layers, where the spatial variation of velocity is maximum. In figure 4.27 the coordinates of the barycenter of the fluid have been plotted versus the physical time. The simulation with the coarsest mesh (which employs 10% of the nodes used in [202]) provides good results during the falling of the column and lacks of accuracy only in the last part, when the fluid impacts on the right-hand boundary. In order to measure the quality of the simulations, the results have been compared to the ones obtained by an overkilled simulation (400,000 nodes); the main comparison has been made on the barycentre velocity and the error has been computed as:

$$Err(\underline{u}) = \frac{(u_x - u_x^*)^2 + (u_y - u_y^*)^2}{(u_x^* + u_y^*)^2}, \tag{4.34}$$

where the starred quantities refer to the overkilled solution.
In figure 4.28 the error of the velocity of the barycentre has been plotted versus the physical time; except for the two coarsest meshes, the error decreases over the whole computation with the increase of the number of nodes. In figure 4.29 the average error during the simulation is plotted versus the number of nodes of the mesh, showing the convergence of the numerical scheme.

External magnetic field

In this section the classic benchmark variables have been computed in the case of the presence of an external magnetic field $B = 0.5\,T$, which corresponds to a Stuart number $N = B^2 L\sigma/\rho U = 2.5$. The kinematics of the fall is highly affected by the presence of the magnetic field as shown in figure 4.30. When a vertical magnetic

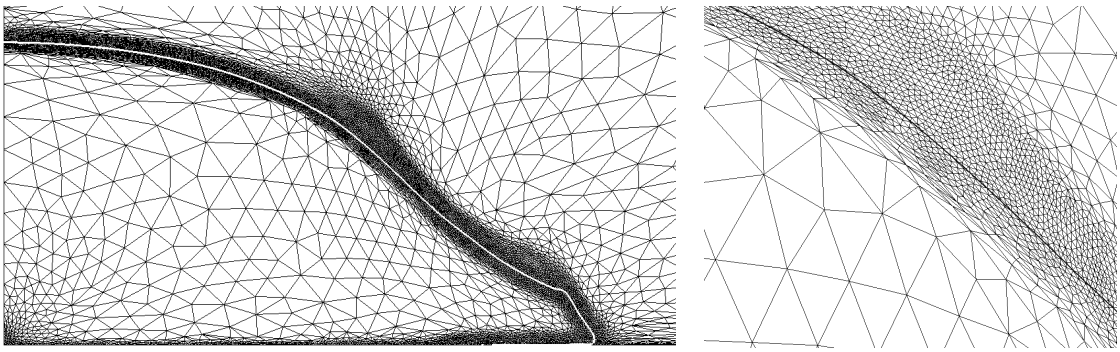

(a) Refined mesh in the liquid domain.

(b) Refined mesh in the liquid domain: detail across the interface

Figure 4.26: Anisotropic, unstructured mesh.

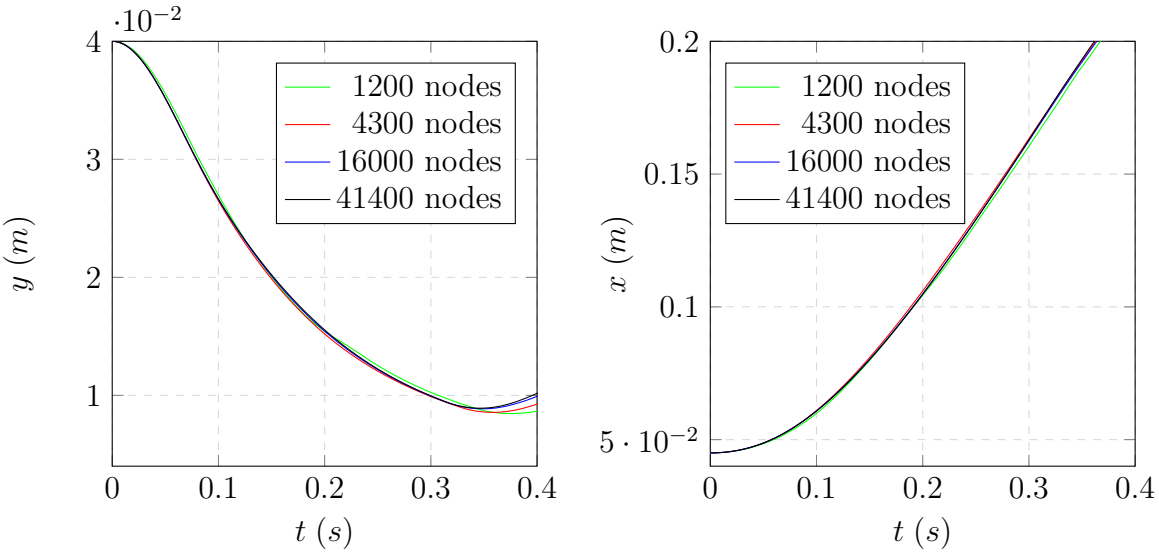

(a) Vertical position of the barycenter of the fluid domain.

(b) Horizontal position of the barycenter of the fluid domain.

Figure 4.27: Barycenter position evolution at different mesh-refinement levels.

field is applied we note a sharpening of the front (see figure 4.30(b)) because it is the area of the domain with the highest velocity, hence the highest electromagnetic reaction. In addition, the fluid domain is convex, while it is concave in the other cases. This qualitative difference is clear from figure 4.31, since the smoothness of the fluid domain leads to obtain the minimum height of the column at the same front position.

Following, the benchmark data of the front position (see figure 4.32) and the column height (see figure 4.33) are proposed. It is clear how the vertical magnetic

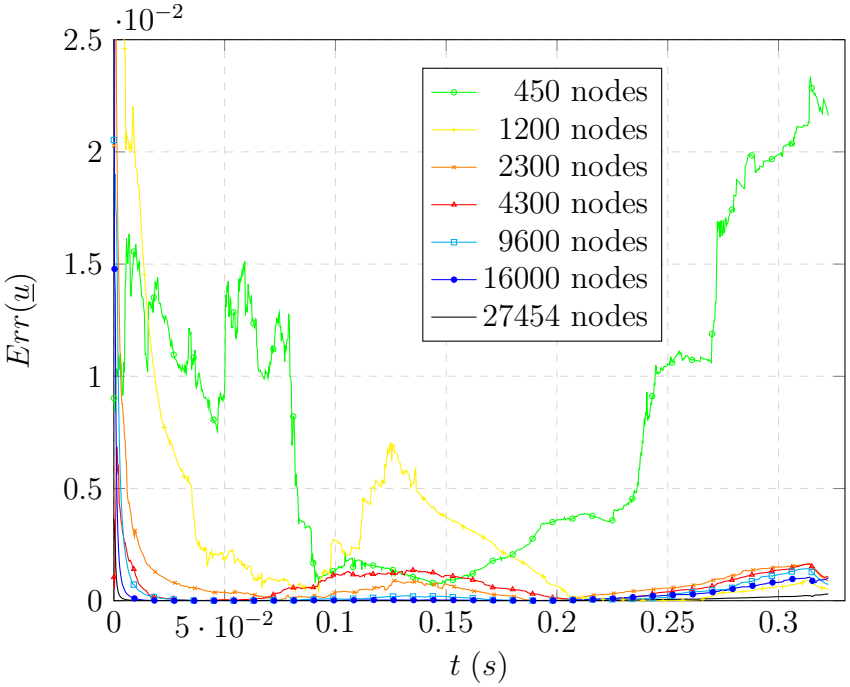

Figure 4.28: Error of the barycenter velocity.

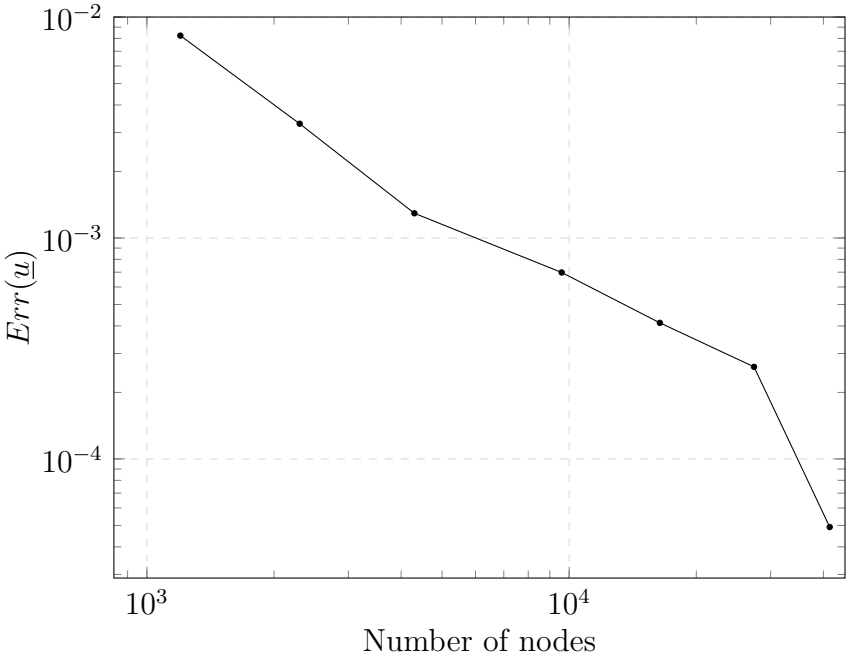

Figure 4.29: Convergence of the numerical scheme.

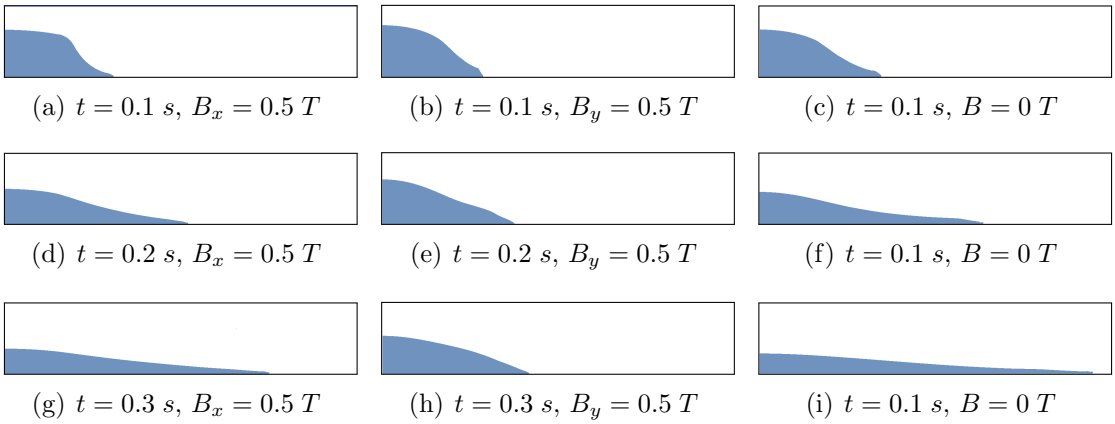

(a) $t = 0.1\ s$, $B_x = 0.5\ T$ (b) $t = 0.1\ s$, $B_y = 0.5\ T$ (c) $t = 0.1\ s$, $B = 0\ T$

(d) $t = 0.2\ s$, $B_x = 0.5\ T$ (e) $t = 0.2\ s$, $B_y = 0.5\ T$ (f) $t = 0.1\ s$, $B = 0\ T$

(g) $t = 0.3\ s$, $B_x = 0.5\ T$ (h) $t = 0.3\ s$, $B_y = 0.5\ T$ (i) $t = 0.1\ s$, $B = 0\ T$

Figure 4.30: Column fall evolution with different external uniform magnetic fields.

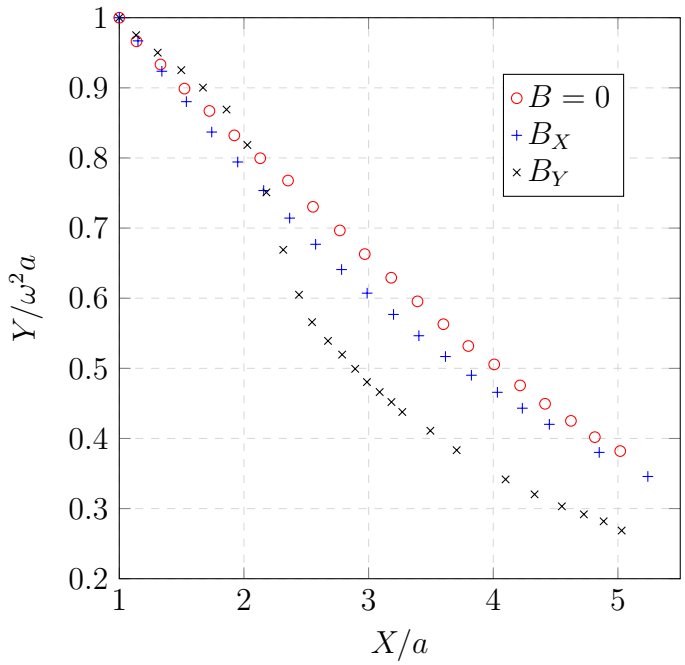

Figure 4.31: Column shape evolution.

field has a stronger impact on the flow than the horizontal magnetic field, which leads to a high braking of the falling column.

The braking due to the vertical magnetic field is proportional to N and no turbulence occurs in the liquid flow; in figure 4.34, the kinematic results of the column fall under the imposition of different magnetic fields are presented.

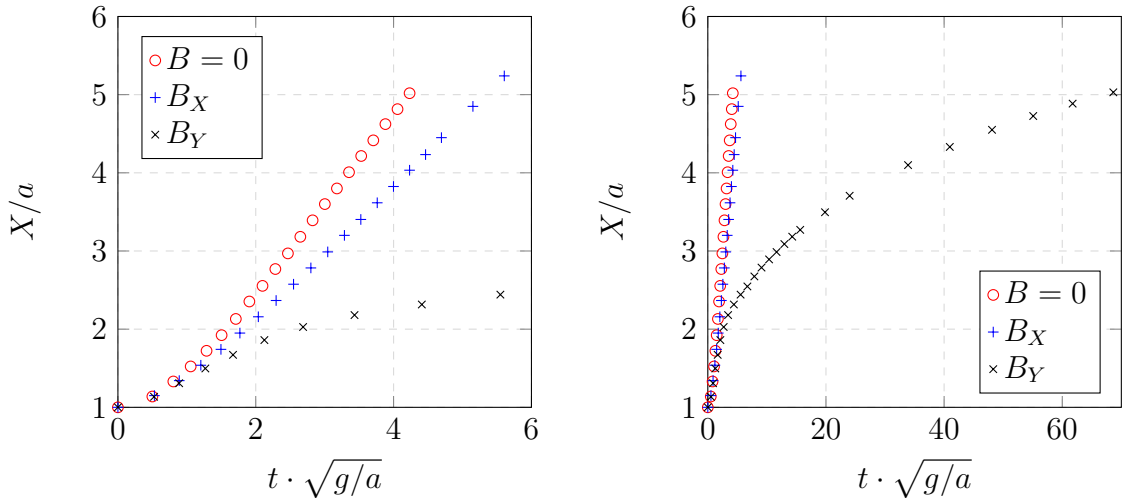

(a) Short time (b) Long time

Figure 4.32: Front position evolution.

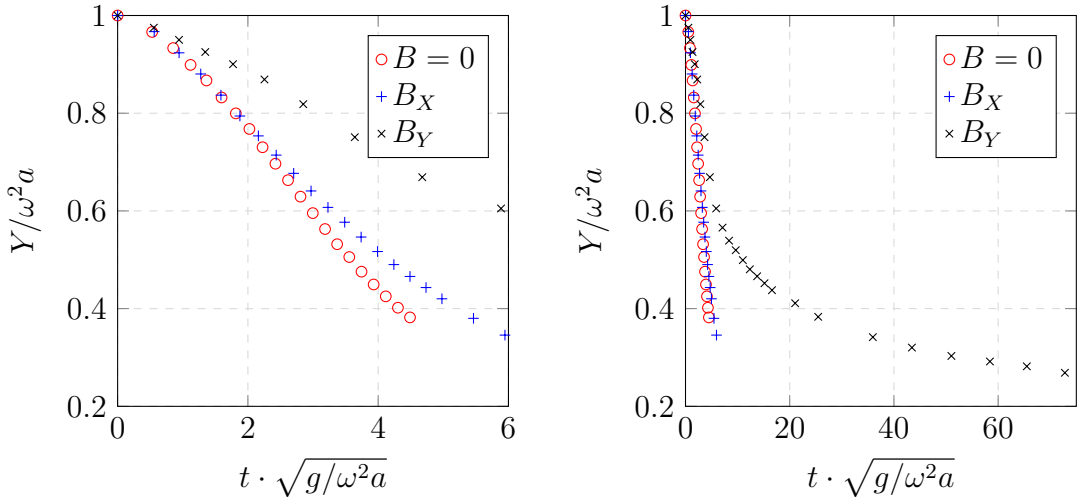

(a) Short time (b) Long time

Figure 4.33: Column height evolution.

Induced magnetic field

The material parameters used in the simulation (tab 4.3) correspond to a low Reynolds magnetic number, i.e. $Rem = 2 \times 10^{-2}$, so the induced magnetic field is low. The difference between the induced magnetic field and the external magnetic

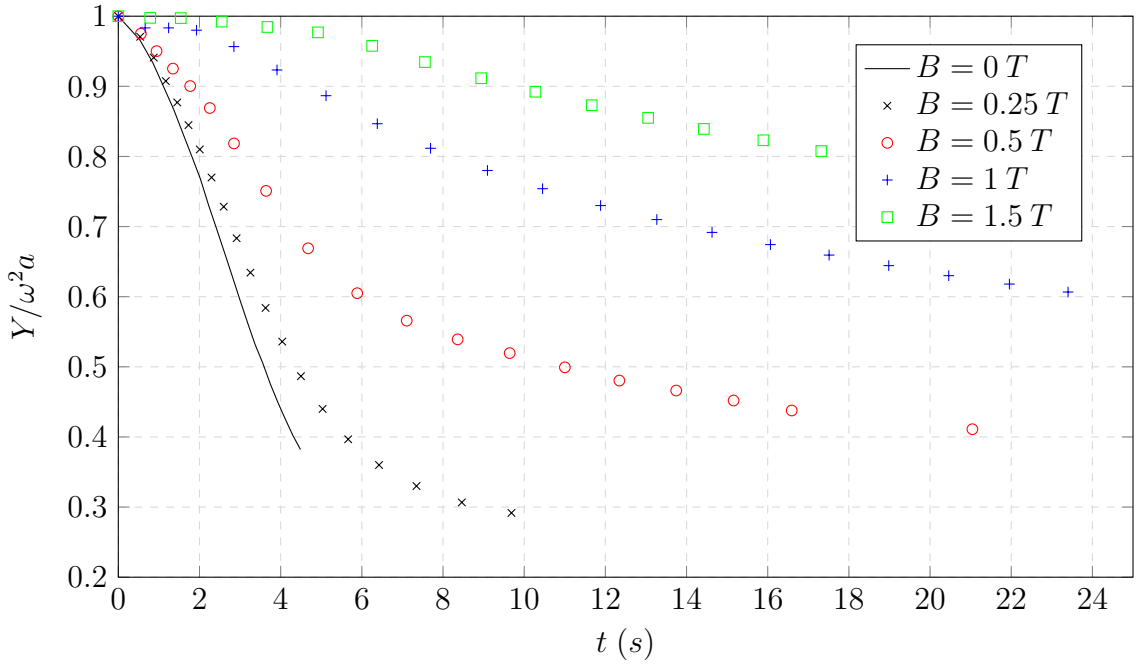

(a) Non-dimensional column height.

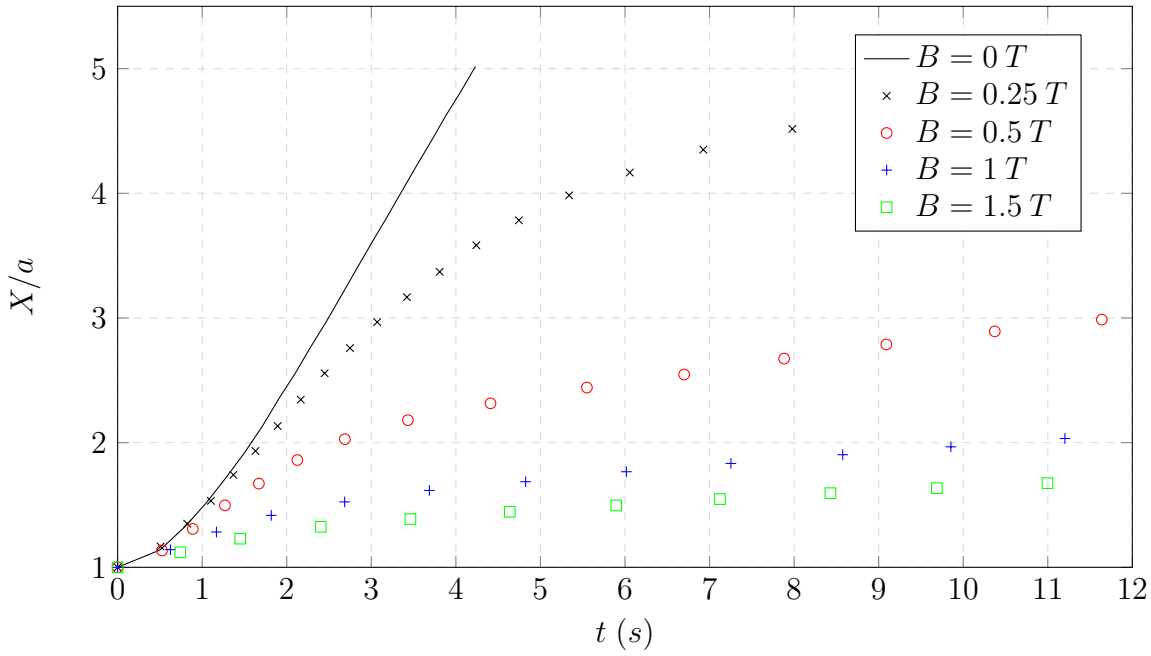

(b) Non-dimensional front position

Figure 4.34: Kinematics of the fluid flow at different level of magnetic field

field have been evaluated according to the following expression:

$$\delta B = \frac{(b_x^- B_x^{ext})^2 + (b_y - B_y^{ext})^2}{(B_x^{ext} + B_y^{ext})^2}. \tag{4.35}$$

In figure 4.35 the maximum value of the induced magnetic field (relative to the external magnetic field) versus the front position is plotted. The induced magnetic field decreases as the external magnetic field increases; this is a common feature in gravity driven problems, i.e. with no injection of energy, because the Lorentz force brakes the flow reducing the convective term in the induction equation. The position of the peak in the induced magnetic field depends on the velocity of the developed flow: since the velocity monotonically grows within the simulation, the peak in the magnetic field is reached as soon as the velocity is high enough to induce a reaction able to face the acceleration of the front.

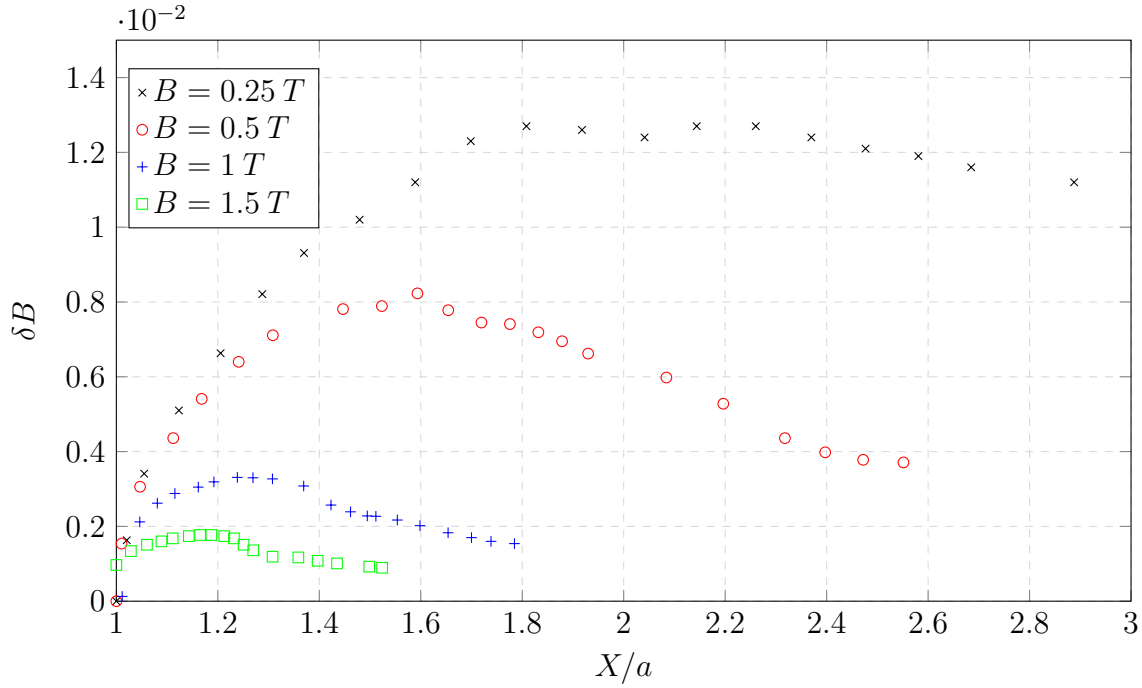

Figure 4.35: Relative variation of induced magnetic field.

In figure 4.36 the variation of the relative magnetic field over a horizontal line at $y = 0.005m$ is plotted in the instant when the maximum variation occurs. In this figure it is confirmed that the increase in the external magnetic field decreases the moment when the maximum induced magnetic field develops; it is also shown that the peak in the magnetic field occurs closer to the interface as the external magnetic field increases.

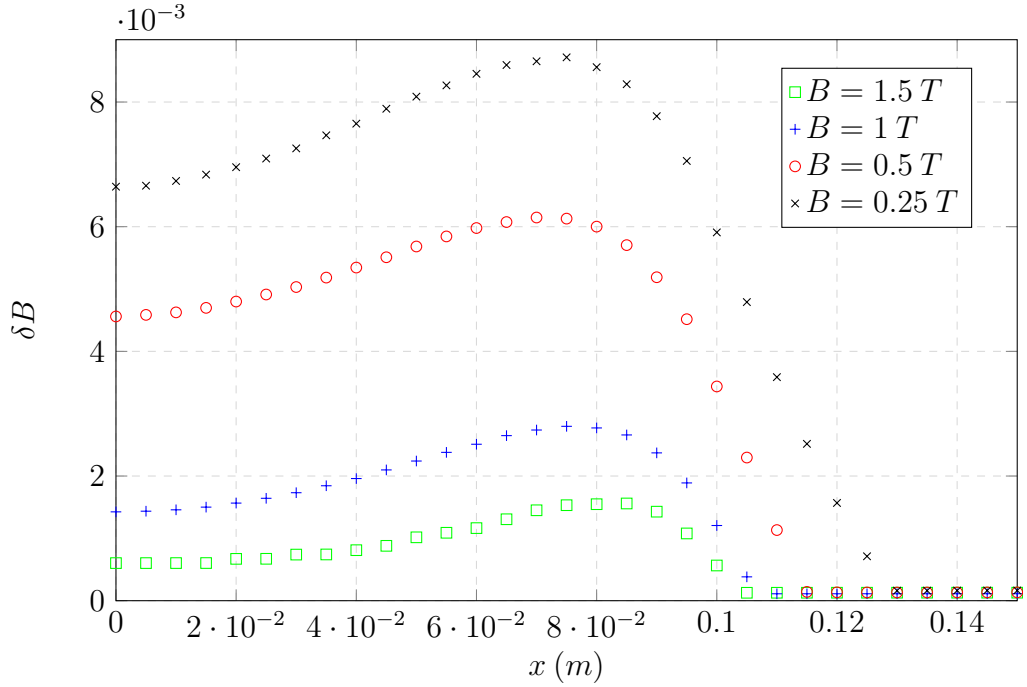

Figure 4.36: Relative induced magnetic field along an horizontal line (maximum instant).

4.6 Laboratory scale benchmark case of AC EMS

In this section we will apply different coupling schemes to a reference case; as a result of this comparison, the coupling scheme described in sections 4.2 and 4.3 has been chosen. The results obtained have been compared with experimental and numerical results, showing a good agreement. This benchmark has also been used to identify the good parameters to apply the Ω_n^m condition (equation (4.15)) to AC stirring applications. This section is based on the work published in [212, 213].

4.6.1 Description of the coupling schemes

As described in section 4.2, the EM field is not affected by the liquid metal motion when $Rem \ll R_\omega$. But the open point is about modelling or not the electromotive part of the Lorentz force is still open. In section 4.4 we showed how to explicitly model this term in the Navier-Stokes equations for a 2D case. But, when moving to 3D simulations, other phenomena have to be taken into account. Let's recap how the Lorentz force is computed:

$$\underline{f}_L = \underline{j} \times \underline{B} = -\sigma(\nabla\phi + \partial_t \underline{A} - \underline{u} \times \nabla \times \underline{A}) \times \nabla \underline{A}. \tag{4.36}$$

Since for 2D applications $\Delta\phi \equiv 0$, the mechanical influence of the magnetic field on the fluid motion is the term $\underline{u} \times \nabla \times \underline{A}$. However, in the general case, the conservation of charge has to be guaranteed, thus:

$$\Delta\phi = \underline{u} \times \nabla \times \underline{A}. \tag{4.37}$$

In other words, the conductive fluid motion creates an electric potential gradient, thus equation (4.37) has to be solved before solving each time-step of the Navier-Stokes resolution. We have decided to compare three different approaches to model this phenomenon:

(A) The convective term has been neglected, thus the Lorentz force has been computed independently from the mechanical solution as $\underline{f}_L = -\sigma(\nabla\phi + \partial_t \underline{A}) \times \nabla \underline{A}$. The algorithm is composed by the following steps:

(1). Solve $\nabla \cdot \sigma \left(-\nabla\phi - \dfrac{\partial \underline{A}}{\partial t} \right) = 0.$

(2). Solve $\nabla \times \mu^{-1} \nabla \times \underline{A} = \sigma \left(-\nabla\phi - \dfrac{\partial \underline{A}}{\partial t} \right)$ at the steady state.

(3). Solve $\rho\left(\partial_t \underline{u} + \underline{u} \cdot \nabla \underline{u}\right) - 2\mu \nabla \cdot \underline{\underline{\varepsilon}}(\underline{u}) + \nabla p = \underline{f}_L$ at the steady state, where $\underline{f}_L = \sigma \left(-\nabla\phi - \dfrac{\partial \underline{A}}{\partial t} \right) \times \nabla \times \underline{A}$ is obtained by post-processing the results obtained at step (2).

(B) The correct value of $\underline{j}$ has been computed at each mechanical time-increment. It is important to remember that this value is used only in the CFD computation (through the term $\underline{f}_L = \underline{j} \times \underline{B}$) and not to re-compute the EM field.The algorithm is composed by the following steps:

(1). Solve $\nabla \cdot \sigma \left(-\nabla\phi - \dfrac{\partial \underline{A}}{\partial t} \right) = 0.$

(2). Solve $\nabla \times \mu^{-1} \nabla \times \underline{A} = \sigma \left(-\nabla\phi - \dfrac{\partial \underline{A}}{\partial t} \right)$ at the steady state.

(3). Solve one time-step of $\rho\left(\partial_t \underline{u} + \underline{u} \cdot \nabla \underline{u}\right) - 2\mu \nabla \cdot \underline{\underline{\varepsilon}}(\underline{u}) + \nabla p = \underline{f}_L$, where $\underline{f}_L = \sigma \left(-\nabla\phi - \dfrac{\partial \underline{A}}{\partial t} + \underline{u}^- \times \nabla \times \underline{A} \right) \times \nabla \times \underline{A}$ is obtained by post-processing

the results obtained at step (2) and $\underline{u}^-$ is the velocity field at the previous time-step.

(4). Solve $\nabla \cdot \sigma \left(-\nabla\phi - \frac{\partial \underline{A}}{\partial t} + \underline{u} \times \nabla \times \underline{A} \right) = 0$ with the updated value of $\underline{u}$.

(5). Solve the following time-step of NS equation, using the Loretz force computed with the value of $\underline{j}$ obtained in step (4).

(6). Iterate steps (4) and (5) until the the stopping criterion of the mechanical simulation is fulfilled.

(C) The braking effect has been considered in explicit, neglecting the divergence constraint (thus considering $\nabla\phi$). Hence, we obtain $\underline{j} = -\sigma(\partial_t \underline{A} - \underline{u} \times \nabla \times \underline{A})$. This is an approximation for 3D cases, since the 3D phenomena related to the formation of an electric potential gradient often balance the $\underline{u} \times \underline{B}$ term, resulting in no effect of the magnetic field on the flow developed in the planes perpendicular to the magnetic field itself.The algorithm is composed by the following steps:

(1). Solve $\nabla \cdot \sigma \left(-\nabla\phi - \frac{\partial \underline{A}}{\partial t} \right) = 0.$

(2). Solve $\nabla \times \mu^{-1} \nabla \times \underline{A} = \sigma \left(-\nabla\phi - \frac{\partial \underline{A}}{\partial t} \right)$ at the steady state.

(3). Solve $\rho \left(\partial_t \underline{u} + \underline{u} \cdot \nabla \underline{u} \right) - 2\mu \nabla \cdot \underline{\varepsilon}(\underline{u}) + \nabla p = \underline{f}_L$ at the steady state, where $\underline{f}_L = \sigma \left(-\nabla\phi - \frac{\partial \underline{A}}{\partial t} + \underline{u}^- \times \nabla \times \underline{A} \right) \times \nabla \times \underline{A}$ is obtained by post-processing the results obtained at step (2) and $\underline{u}^-$ is the velocity field at the previous time-step.

It must be remarked that the methods described in (B) and (C) use the value of velocity at the previous time step, so the time-step constraint proposed in section 4.4 has to be respected.

4.6.2 Benchmark case and validation

The benchmark used to compare and validate the coupling scheme is based on the results proposed by Musaeva et. al. in 2016 [214]. The bench case consists in a laboratory scale stirring application of Galinstan melt in a Plexiglas mould. The problem configuration and the main parameters are reported in 4.37 and table 4.4 respectively. Thanks to the axial symmetry of the problem, only a 15°-section has

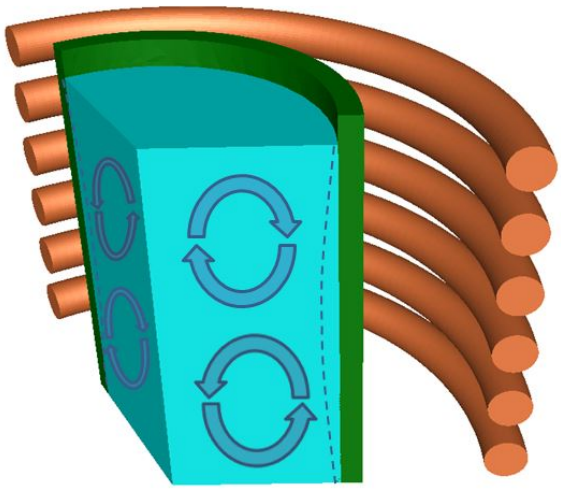

Figure 4.37: Geometry of the benchmark case

been simulated. The electromagnetic simulation has been performed in a domain which includes the inductor, the melt and a air layer $1m$ tick from the mould external surface. The input current density has been set to $I_{RMS} = 200A$ and the frequency f has been varied from $50Hz$ to $1300Hz$. The mesh (figure 4.38(a)) has been refined isotropically in the melt in order to have at least 12 elements in the skin depth. The mechanical simulation has been performed in the fluid domain. No slip boundary conditions have been imposed on the solid wall boundaries and perfectly slip boundary conditions have been imposed at the symmetry planes and the free surface. The average number of elements during the dynamic mesh adaptation is 275000. A detail of the mesh used at the steady state of the mechanical simulation is shown in figure 4.38(b). In figure 4.39, the axial velocity at the centre of the fluid cylinder is plotted. The velocity has been computed at the steady state, i.e. after $200\,s$ and the induction frequency has been set to $f = 150\,Hz$. The results have been compared to both the experimental and numerical results proposed in [214].

In table 4.5 a summary of the simulation accuracy is provided by reporting the error related to the main result variables: the maximum velocity of the fastest eddy (Ef), the maximum velocity of the slowest eddy (Es) and the position of the separation point between the eddies normalized to the maximum eddies size (Ep). Table 4.5 confirms that the use of VMS methods improves the accuracy of simulations if compared to the classic $k-\varepsilon$ method because it better models the turbulence effects. In figure 4.40, the maximum recirculation velocity over the induction frequency is plotted. For lower frequencies (where experimental data are available) both VMS and $k-\varepsilon$ are in the experimental range; however, for higher frequencies, the two solutions produce different results. In both cases the maximum velocity decreases

Table 4.4: Bench test main parameters.

Parameter	Unit	Value
Galinstan Melt		
Density	Kg/m^3	6440
Dynamic viscosity	$Pa \cdot s$	0.0024
Electric conductivity	S/m	$3.46 \cdot 10^6$
Radius	mm	31
Height	mm	70
Copper inductor		
Electric conductivity	S/m	$1.78 \cdot 10^8$
Number of turns	$-$	6
Turn diameter	mm	8
Turns distance	mm	4
Inductor radius	mm	61

after a peak, but the VMS solution decreases faster. Reference solution ($2 \cdot 10^6$ elements) also confirms this tendency. Since no experimental data are available in this region, we can not base any validation on it; but the difference in results seems to be a direct consequence of the turbulence model: in VMS a better approximation of small scale turbulence is used, thus higher energy dissipation is produced at high levels of stirring force density.

Table 4.5: Errors related to figure 4.39

Type of error	ANSYS $k-\varepsilon$	THERCAST VMS
Ef	16.1%	1.4%
Es	5.2%	1.0%
Ep	7.2%	0.4%

4.6.3 Comparison between the different coupling schemes

The three different coupling techniques described in section 4.6.1 have been tested; in figure 4.41, the error of the maximum axial velocity obtained by the different coupling schemes is shown. The error has been computed with respect to the coupling strategy (B), which is the most accurate one from the theoretical point of view. Strategy (A) results to be more accurate than (C). In both cases, the error has two peaks: one at low frequency and one at the frequency corresponding to the maximum velocity produced. This is due to the fact that the mechanical effect of the convective term (i.e. $\underline{u} \times \nabla \times \underline{A}$) depends on two different factors: by

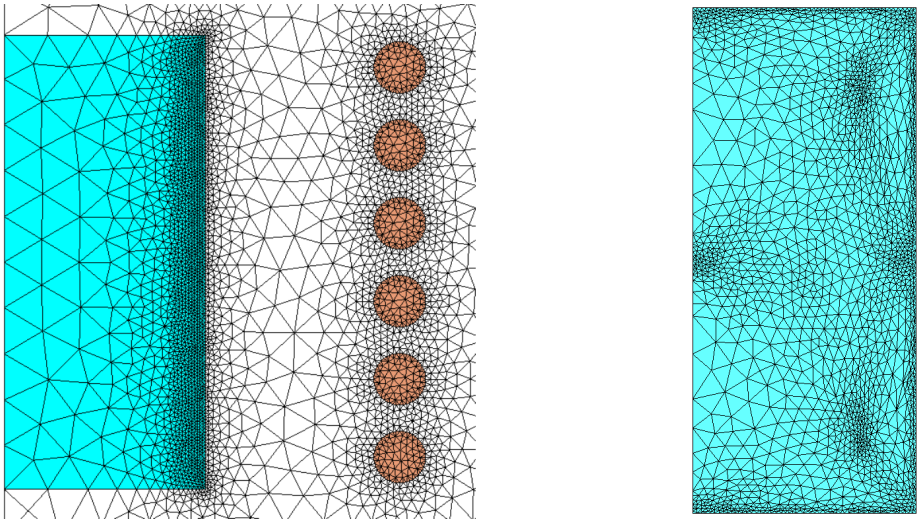

(a) Mesh used in the electro-magnetic simulation.

(b) Mesh used in the CFD simulation.

Figure 4.38: Meshes used for the EM and CFD computations.

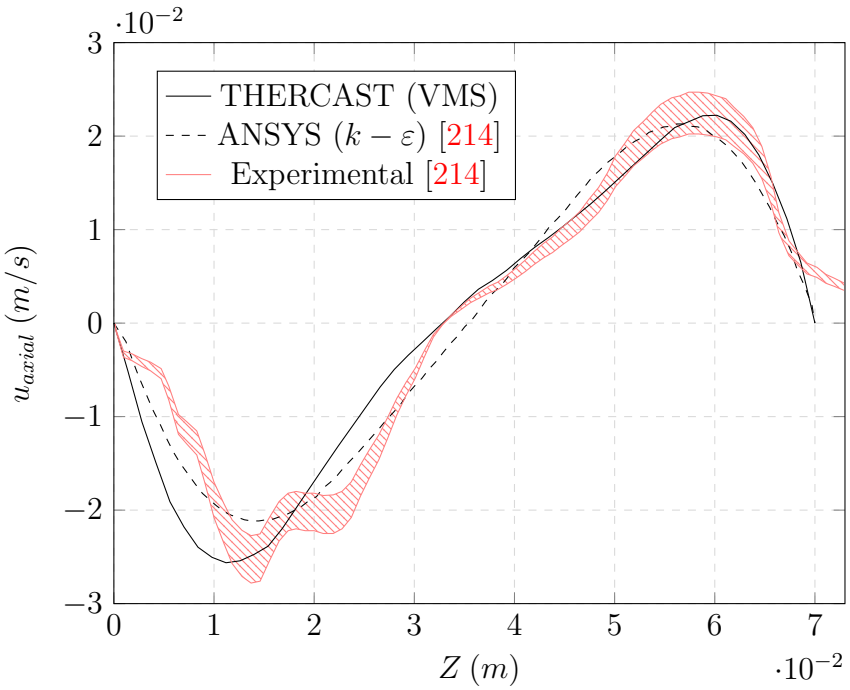

Figure 4.39: Axial velocity with frequency $h = 150\,Hz$.

increasing the frequency the velocity tends to increase (which increases the effect of the convective term), but the skin depth decreases, dumping the electromagnetic

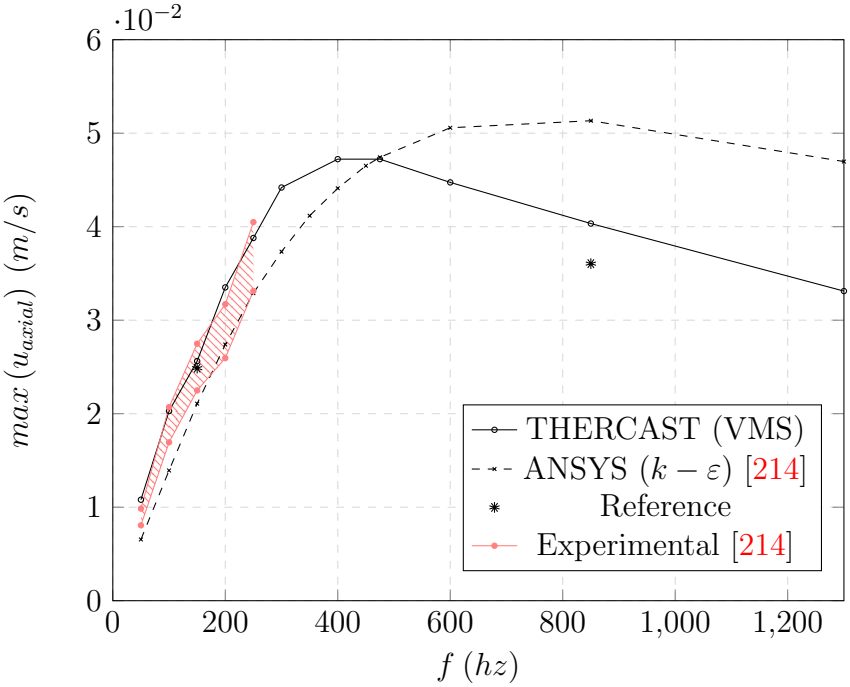

Figure 4.40: Maximum axial velocity at different frequencies.

penetration (which decreases the effect of the convective term). It is also remarkable that the approach A leads to an overestimation of the velocity because the braking effect is neglected, while approach C leads to a underestimation of the velocity since the braking term is considered without accounting for the self-balance due to the creation of an electric field $\nabla\phi$. In table 4.6, the time analysis for each coupling scheme is proposed. Let's consider strategy (A) as the reference. The resolution of Navier-Stokes equation is the most expensive part of the computation, in particular due to the long physical time to be simulated before reaching the steady state. Approach (B), which is the most accurate, is about 50% more expensive than (A), since the value of the electrical current has to be computed at each time step by solving equation (4.37). Approach (C) is the less accurate and it is slightly more expensive than (A), since the convective term of the Lorenz force has to be computed at each time step.

4.6.4 Computation of the parameters for the Ω_n^m condition

The good couple of parameters (m, n) has to be found in order to guarantee the effectiveness of the Ω_n^m-condition. Too high values (for instance $m = n = 100$) would imply that the criterion shown in equation (4.14) has to be satisfied over the whole domain: in practice, this case never takes place, so the average Lorentz

Table 4.6: Computational effort comparison between different coupling strategies.

	A	B	C
Navier-Stokes resolution	87.3%	56.6%	87%
Maxwell resolution	3.6%	2.4%	3.6%
Remeshing	8.8%	5.7%	8.7%
Coupling interface	0.3%	35.3%	0.7%
Total time	Ref.	+54%	+0.3%

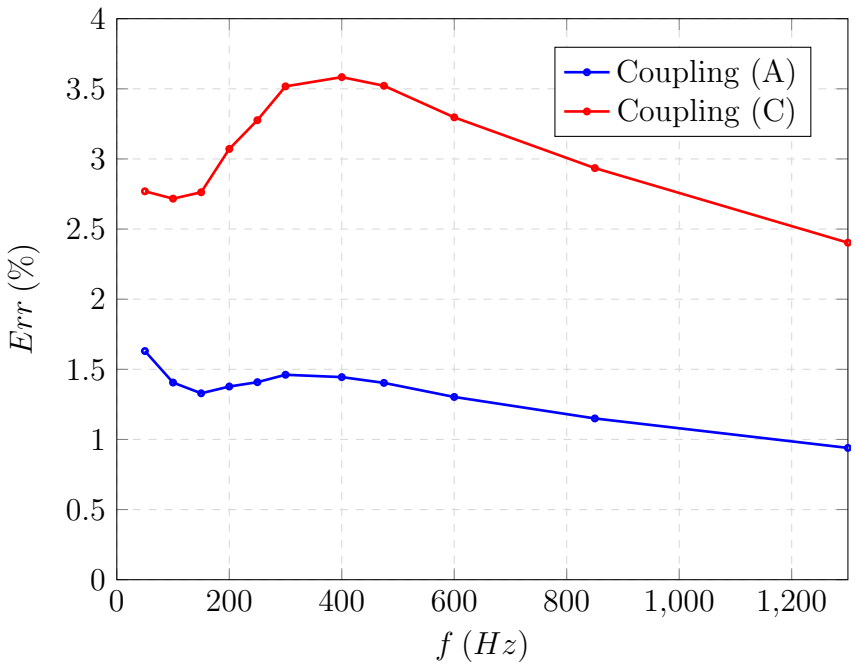

Figure 4.41: Error of the maximum axial velocity simulated with different coupling strategies.

force would be always used. On the opposite, too small values would lead to the use of the transient value of the force even when only one finite element exceeds criterion (4.14). In order to find a good couple, different stirring levels has been simulated by increasing the current density in the inductor, until reaching the lever for which the double eddy recirculation pattern is no more developed and a fully turbulent flows occurs. By increasing the stirring, the turbulence energy increases and the turbulence time scale decreases. In this way, larger parts of the domain will exhibit interaction between the turbulence and the transient part of the EM force. In figure 4.42, the (m, n) diagram is shown for three levels of stirring. For low stirring (figure 4.42(a)) the axial velocity obtained by the average Lorentz force and the one obtained with the transient part differ of 3%. This value is small, meaning

that very little interaction between the EM field and the turbulence occurs. For middle levels of stirring (figure 4.42(b)), this difference rises to 10%, while for the highest stirring level (figure 4.42(c)), the difference is 17%. The red region in the diagram represent the set of couples (m, n) for which the Ω_n^m condition is satisfied, thus the transient part of the EM force would be used. In the summary depicted in figure 4.43 we can deduce two main trends:

- When there is no need of using the transient part of the force, only few couples of (m, n) would lead to take it into account, with the consequent overuse of computational resources.
- When there is need of using the transient part of the force, a larger set of couples (coloured area) is acceptable, which makes the choice of (m, n) less delicate.
- The peak in the value of n moves towards higher m with the increasing of the stirring intensity. This means that the turbulence turnover time decreases mainly where the Lorentz force is higher. However, also for high stirring intensity, the peak does not reach $m = 100$, meaning that the region where the Lorentz force is the highest is not the region where the turbulence increased the most. This observation is important as it suggests that the choice of (m, n) depends both on the stirring intensity and the geometrical features of the specific application.

For this specific application, we propose the couple $m = 80$, $n = 5$, hence Ω_5^{80}. In this way, the average value of the force is used until it leads to a $3 - 5\%$ of error for the axial velocity, while the transient part is used above this limit.

4.7 Conclusions

In this chapter we have presented the coupling scheme between the different physics involved in EMS process.
Different numerical coupling techniques have been tested and all the factors involved in the coupling have been analysed separately.
The variation of material parameters (both from the Eulerian and Lagrangian points of view) has been included in the coupling scheme through a global condition, name Ω_n^m.
The influence of the conductive fluid motion on the EM field has been neglected, and this choice has been based on analytical considerations.
The use of the average or transient Lorentz force has been extensively analysed, because it is quite controversial in the literature. Inspired by local considerations based on the Kolmogorov theory, we proposed a global criterion to choose between

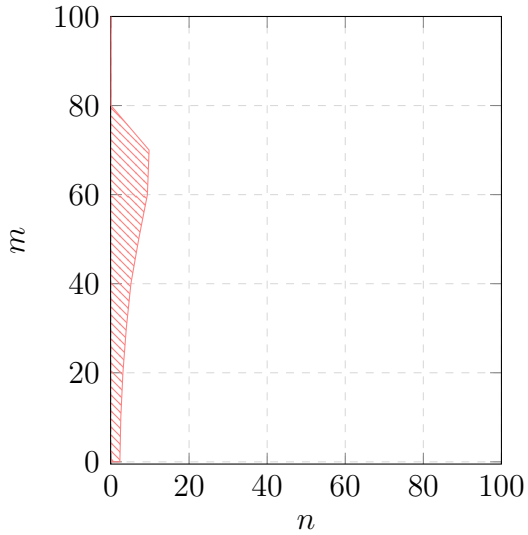

(a) Couples of parameters which lead to the use of the transient Lorentz force for low stirring.

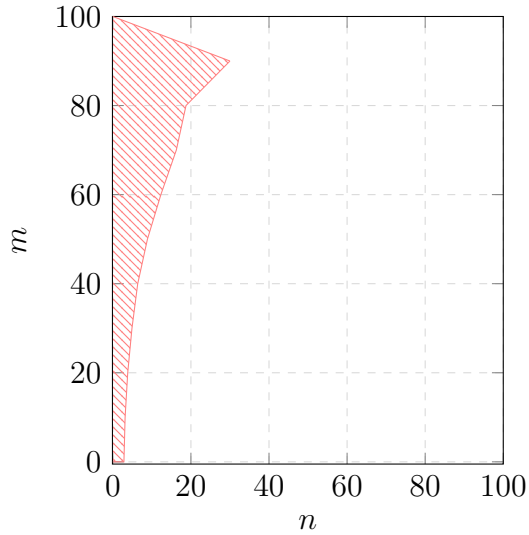

(b) Couples of parameters which lead to the use of the transient Lorentz force for medium stirring.

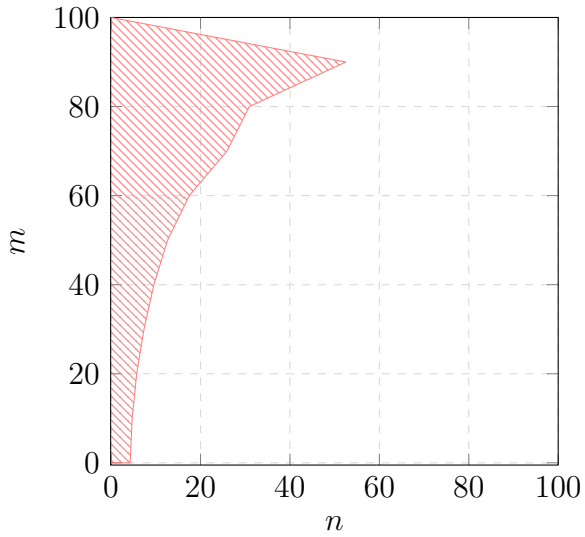

(c) Couples of parameters which lead to the use of the transient Lorentz force for high stirring.

Figure 4.42: Set of parameters couples for which the transient Lorentz force is used at different stirring intensities.

the two methods. The criterion has the same Ω_n^m structure of the one used for the material parameters' variation, in order to have a consistent and clean numerical tool.

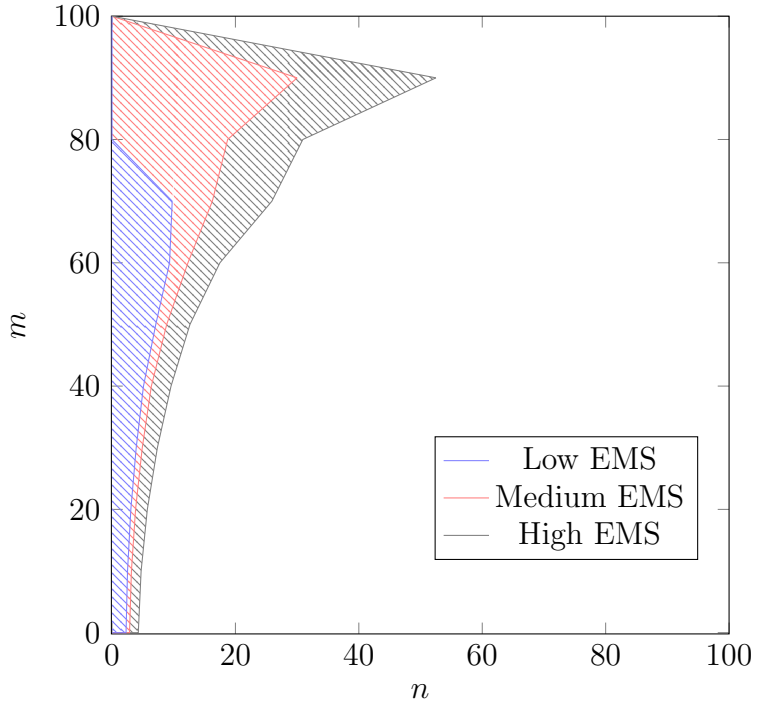

Figure 4.43: Summary of the parametric analysis for different stirring intensities.

The mechanical effect of the convective part of the eddy currents have been studied; this factor is crucial in the simulation, but different positions are present in the literature (while its omission from the EM point of view is broadly accepted). This term has been modelled explicitly in the NS equation. This choice may lead to numerical instabilities, thus a time-step-based condition has been proposed to guarantee convergence.
Hence, three different benchmarks have been used to validate the algorithm.
The first test is the well known "lid-drive cavity". After validation versus literature results, it has been used to test our code at very high turbulence level and very high magnetic field. Different configurations have been simulated and benchmarked, providing both qualitative and quantitative results. Finally, this benchmark has been used to validate the proposed critical value for the time-step, obtaining excellent agreement with the predicted and the obtained values.
The second test case consists in the enhancing of the "braking dam" case by adding EM interaction. It has been firstly validated versus numerical and experimental results in absence of magnetic field. Then, several EM configurations have been tested and benchmarked. As a result, we propose a fully benchmarked multiphase-MHD test case for future applications.
The third case is the simulation of a laboratory-scale EMS application. The results

are in good agreement with experimental and numerical results found in the literature. This test has also been used to test the coupling strategy described in the first part of the chapter and to justify the choices made in it.

Chapter 5

Industrial applications

Contents

5.1 Résumé du chapitre en français

Ce dernier chapitre montre comment l'outil développé et décrit dans les chapitres précédents a été appliqué a deux problèmes industriels. Le premier problème concerne l'application du brassage électromagnétique dans le procédé de coulée continue d'acier. L'écoulement transitoire dans le moule ainsi que la possibilité de contrôler l'écoulement et de réduire la turbulence en utilisant un brasseur électromagnétique au niveau de l'ajutage sont étudiés. Le deuxième cas est une étude de l'applicabilité de la technique de brassage électromagnétique dans la production de larges lingots par l'intermédiaire de lingotières en fonte. Cette situation est assez problématique, parce que la fonte, étant ferromagnétique, agit comme un blindage magnétique. La lingotière empêche la pénétration du champ magnétique et ne permet donc pas le brassage du métal liquide à l'intérieur du lingot. Dans cette étude, on considère plusieurs choix de conception de l'application (différentes positions et types de brasseurs). Les résultats électromagnétiques et mécaniques confirment qu'il est

possible de pénétrer dans la zone liquide, mais que la force de brassage obtenue est trop faible pour contrôler l'écoulement dans le lingot.

5.2 Introduction

In this chapter we will present two industrial applications of simulations done with the new electromagnetic module of THERCAST®. The first application (whose results are published in [215, 216]) consists in the simulation of M-EMS for a real caster used in the literature for other works. The second case is a feasibility study for an EMS system applied to large ingot casting at Industeel. Unfortunately we have not been able to retrieve full information about a real M-EMS, because data are often confidential, and experiments are very expensive to be carried out. For this reason, we limited our validation to the laboratory scale (chapter 4) and apply the developed simulation tool to open industrial problems to show how this tool can be used as support of real industrial-scale processes.

5.3 M-EMS effect of in-mould transient flow

5.3.1 Simulation layout

The studied case is a slab casting process and the mould's geometry has been taken from literature (Singh's work [46]), but only a quarter of it has been included in the simulation (see figure 5.1). A simplified electromagnetic stirrer has been positioned $3\,cm$ away from the mould in the direction of the narrow face and between 50 and $70\,cm$ under the free surface level. The EMS device is a solenoid fed by a pulsating AC current and produces a horizontal pulsating magnetic field directed from the narrow face in the direction of the nozzle plan. The geometry of the device is simplified since available data on commercial stirrers were not accurate enough to perform a simulation. In the current work we restrict ourselves to simulating a realistic Lorentz force field, since the aim is to study the interaction of the stirrer on the flow more than to obtain specific industrial results. The main data used in the simulation are reported in table 5.1.

Two different strategies have been used to re-mesh:

- Implicit-Static adaptation: the mesh is anistropically adapted to the boundaries and in the weak regions. The obtained mesh is then used as a fixed mesh during the whole computation.
- Explicit-Dynamic adaptation: the mesh is dynamically adapted during the computation according to the multicriteria vector (equation (3.85)) computed from the solution.

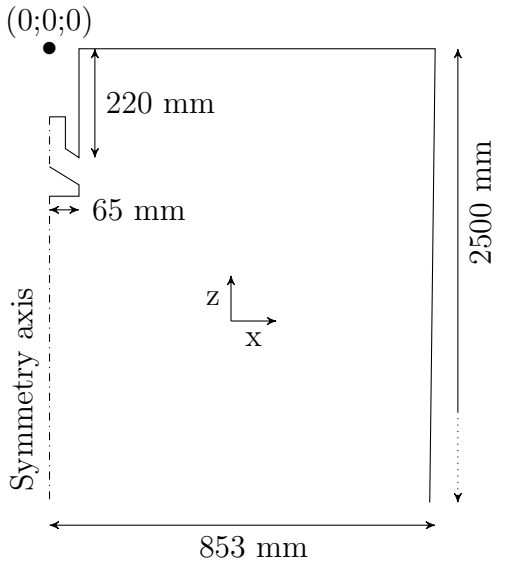

(a) Mould geometry (one quarter of the commercial mould)

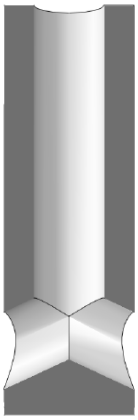

(b) Section of the Submerged Entry Nozzle (SEN).

Figure 5.1: Geometrical features of the simulated process.

In figure 5.2 we can see how the mesh is anisotropically adapted to the flow in the nozzle area. A summary of the meshes used in the simulations is proposed in table 5.2; two reference simulations obtained by using different meshing techniques have been performed to check the convergence of results. All the results in the following are taken from the static anisotropic adapted simulation, which is in good agreement with the dynamic re-meshing and the reference simulations. The coarse isotropic mesh shows instead sensible discrepancies with the reference simulation, because it is not fine enough in the nozzle and in the narrow face thickness.

5.3.2 Results

Flow simulation

The flow developed in the mould is the classical double-roll flow. In figure 5.3 the magnitude and the streamlines on the average velocity are plotted. The average velocity has been computed in the time interval $(30; 55)\ s$ when a nominally steady state is reached. In figure 3 the abnormal width of the injection flow can be noticed, which is an already observed drawback in symmetric simulations [217]. This average flow is predictive of the macro-phenomena occurring in the mould, but lacks information regarding localized turbulence, which has a strong impact on metallurgical properties. The turbulence leads to short-time sub-flows detected by the

Table 5.1: Process parameters.

Simulated mould width	$853\,mm$
Simulated mould thickness	$101.6\,mm$
Nozzle port diameter	$75\,mm$
Nozzle bore diameter (inner)	$70\,mm$
Nozzle bore diameter (outer)	$130\,mm$
Nozzle port angle	$25\,deg$
SEN submerged depth	$22\,cm$
Casting speed	$1.4\,m/min$
Bulk velocity in SEN cross section	$2.1\,m/s$
Thickness of the solidified shell	$k_s\sqrt{(z[mm])}\,mm$
k_s	$0.57\,mm^{0.5}$
Kinematic viscosity of molten steel	$0.86 \times 10^{-6}\,m^2/s$
Density of molten steel	$7000\,kg/m^3$
Resistivity of molten steel	$1.4 \times 10^{-6}\,(\Omega m)^{-1}$
Resistivity of solid parts	$2 \times 10^{-8}\,(\Omega m)^{-1}$
Inlet Reynolds number	2171000
Inlet magnetic Reynolds number	0.13
Eddy magnetic Reynolds number	0.15
Intensity of current	$300\,A$
Frequency of induction	$3\,Hz$

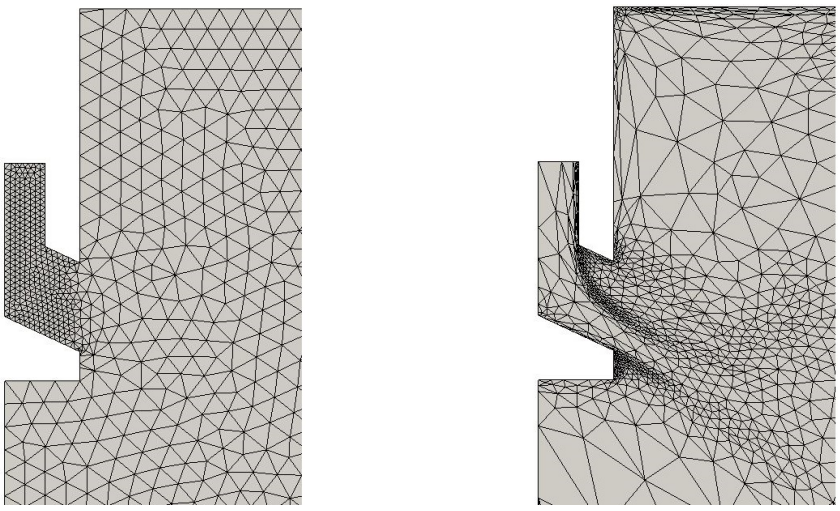

(a) Isotropic starting mesh. (b) Anisotropic adapted mesh.

Figure 5.2: Mesh at the SEN's port.

Table 5.2: Meshes details.

Number of elements (including boundary elements)	Details
230258	Static anisotropic mesh generation
229169	Isotropic non-structured mesh
230000 (average over the time-steps)	Dynamically and anisotropically adapted mesh
1136972	Static anisotropic mesh generation (reference simulation)
1534290	isotropic, non-structured mesh (reference simulation)

non-average solution; this difference can be measured in term of velocity pulsations, defined as:

$$\sigma_u = \sqrt{\frac{\sum_{T_i=0}^{T_f} \left(|\underline{u}|_i - |\bar{\underline{u}}|\right)^2}{N}} \tag{5.1}$$

where $\bar{\underline{u}}$ is the average velocity, N is the number of time-steps and T_i represents the *i-th* time-step.

In figure 5.4 the normalized velocity pulsations during the nominal steady state regime is plotted. We see that a large deviation is present in the main flow region and the maximum deviation occurs where the injected flow impacts on the narrow face; the flow in this region is highly turbulent and this turbulence has effect on the mushy zone. When the stirrer is turned on (figure 4 right) the velocity pulsations is decreased in the meniscus zone, which implies the flow to be closer to the steady state. Despite the low level of the magnetic field in the inner zone of the mould, EMS affects the injection flow as well. The flow is smoother and easily turns in the double-roll pattern, while in the non-stirred simulation the unstable flow close to the narrow face led to dynamic effects in the main injection flow. A second effect of the stirrer is to decrease the global velocity of the flow, which is important especially from a simulation point of view.

In figure 5.5(a) the velocity profile along a vertical line locater $5\,cm$ from the central axis is plotted. We see that the horizontal velocity related to the main eddy ($z \cong 2\,m$) is high, especially when compared to the vertical velocity. This means that the simulated flow and its symmetric one (in the second half of the mould) would have a strong impact in this area, which would create turbulence and lead the global flow to be non-symmetric. For this reason, the flow with no EMS should be simulated without any symmetry condition. On the contrary, we see that the

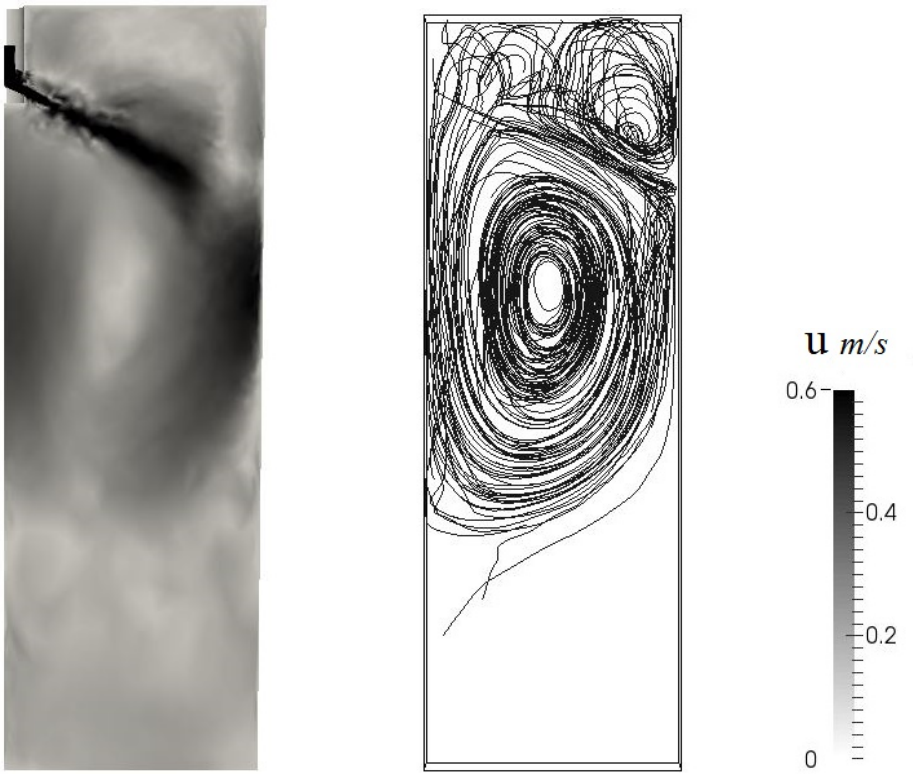

(a) Average velocity magnitude. (b) Average velocity streamlines.

Figure 5.3: Flow results without EMS in the double-roll area.

horizontal velocity in the flow with EMS is lower as well as its ratio with the vertical velocity. This result implies that in the stirred case, the geometrical symmetry plane is more likely to behave like a mechanical symmetry plane. In figure 5.6, the velocity normal to the narrow face is plotted along the middle axix of the narrow face itself. It must be remarked how EMS leads to low impact velocity on the solidifying shell, which is beneficial from a micro-structural point of view. It is also interesting to see how the use of the transient value of the Lorentz force or its average value do not affect the results sensibly. The main effects of the stirrer can be detected close to the narrow face, along the symmetry plane and on the injection flow, but not in nozzle area. In figure 5.5(b) the velocity across the exit central line of the nozzle is plotted and no sensible differences between the stirred and non-stirred solution are predicted.

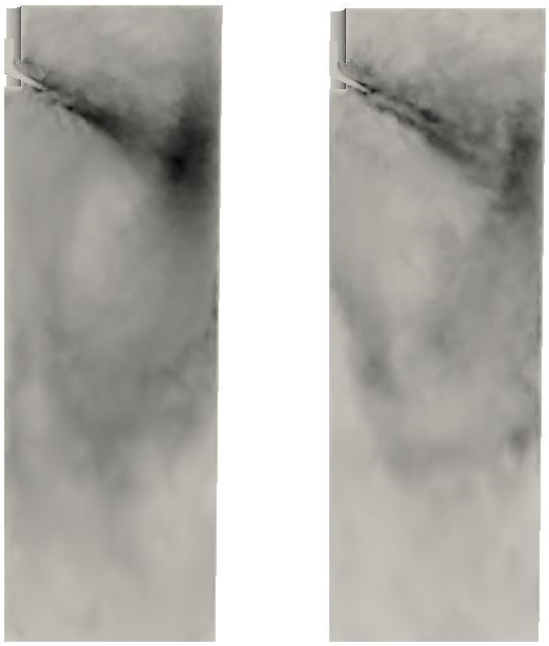

(a) EMS off. (b) EMS on.

Figure 5.4: Velocity pulsations.

Coupling scheme

The computational effort of the simulation is not highly affected by the weak coupling between the EM and CFD simulations: in figure 5.7 an analysis of the computing time is presented. The dynamic mesh adaptation is computationally expensive even if the re-meshing has been performed every 14 time steps. As we can see in figure 5.8, this choice is not good in terms of optimization. The anisotropic adaptation stretches the elements in the same direction as velocity: this means that the elementary stiffness contribution is the same for every direction and the final system is well conditioned. In-mould flow is far from being steady, so the velocity field can significantly change at every time step; therefore the mesh, which was optimized for the solution at a certain time-step, does not fit the new solution field. For this reason the obtained linear system is ill conditioned, except from the time-step when re-meshing is done, and a large number of iteration is needed to reach the convergence. On the contrary, the statically anisotropic mesh provides a mesh which is generally good for all the time steps and leads to a better conditioned system: the number of required iterations is decreased by 25% with respect to the isotropic mesh (with the same number of elements).

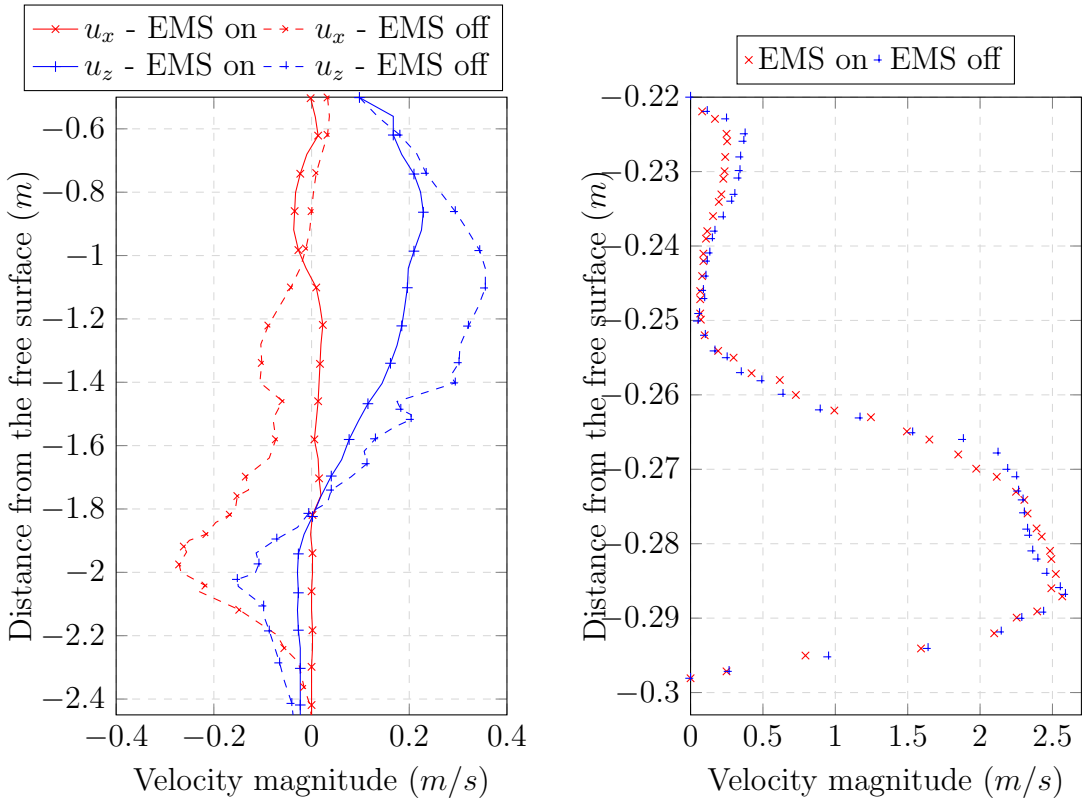

(a) Velocity profile at $5\,cm$ to the central plane.

(b) Velocity magnitude at the nozzle exit port.

Figure 5.5: Flow velocity comparison

5.4 Feasibility study for EMS in large ingot casting

In this section we will show the results obtained in the framework of an industrial partnership with Arcelormittal. The objective of the work is to understand the potential application of EMS technologies to large ingots casting processes in the site of Industeel. The process is shown in figure 5.9; a set of 4 to 8 large ingots ($5\,t$) is bottom cast in parallel, fed by a $75\,t$ ladle.

The problem to solve is that natural convective flow is developed within the ingot during solidification, thus macrosegregation occurs, leading to poor mechanical properties. By controlling the natural convection inside the ingot, higher uniformity and better microstructure is expected in the final product. In order to achieve this result, two technological applications have been proposed: vibration via ultra-sound and electromagnetic stirring. In the rest of this section, the results of the application of EMS are treated.

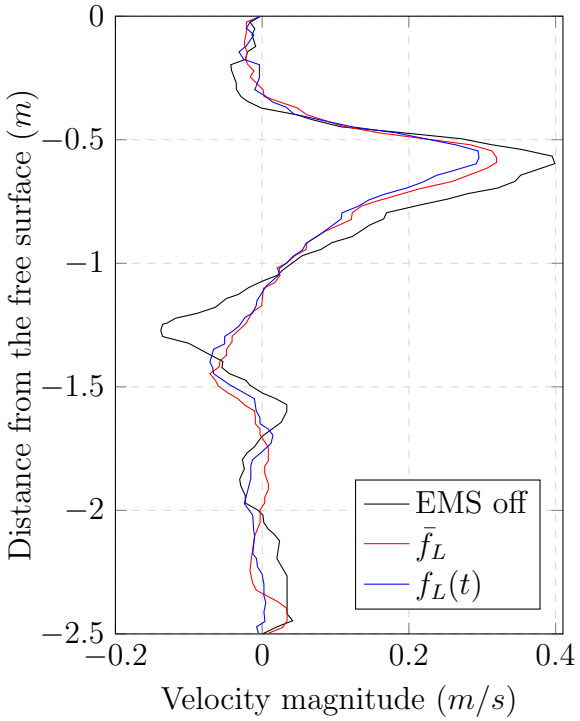

Figure 5.6: Impact velocity on the narrow face.

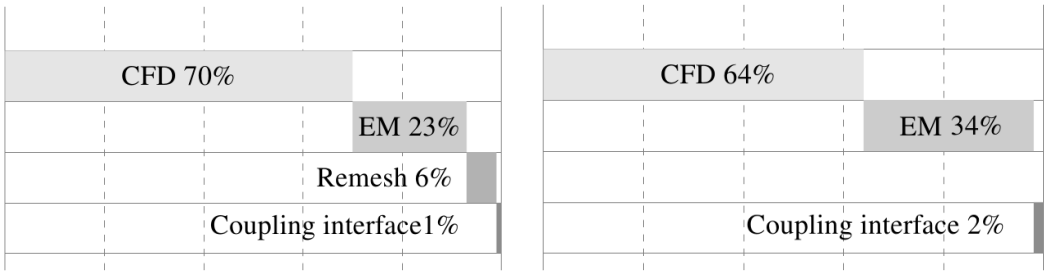

(a) Dynamic remesh.

(b) Static remesh.

Figure 5.7: Time analysis for different remeshing strategies.

5.4.1 Feasibility study

As stated in chapter 1, EMS is often applied to ingot casting to obtain uniform composition and good microstructure in the final product. However, the case proposed by Industeel presents a few important differences with respect to standard applications.

The first difference is the size; the ingot is about $2\,m$ tall and its section is about $60 \times 60\,cm$, while the $4\,t$ mould is $15\,cm$ thick. On the one hand, the high section

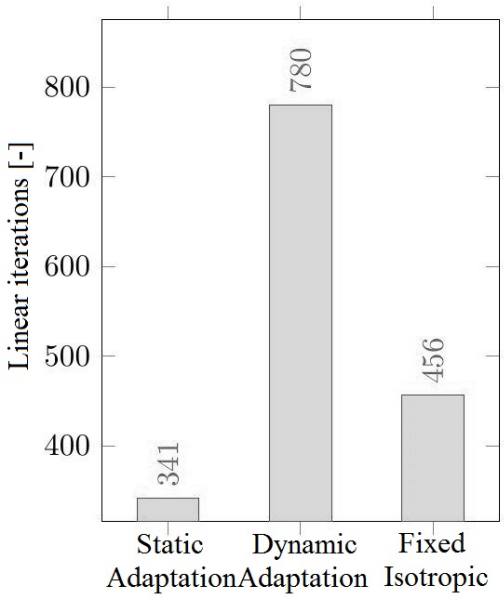

Figure 5.8: Iterations for the linear algebraic system needed to reach convergence with different remeshing strategies.

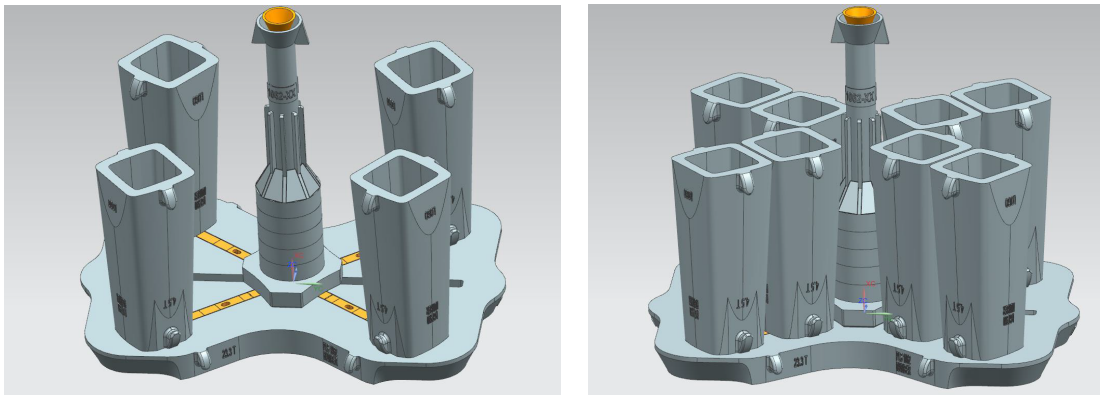

(a) Configuration of the 4-ingots cast.

(b) Configuration of the 8-ingots cast.

Figure 5.9: Possible configuration of the ingot casting process (courtesy of Industeel).

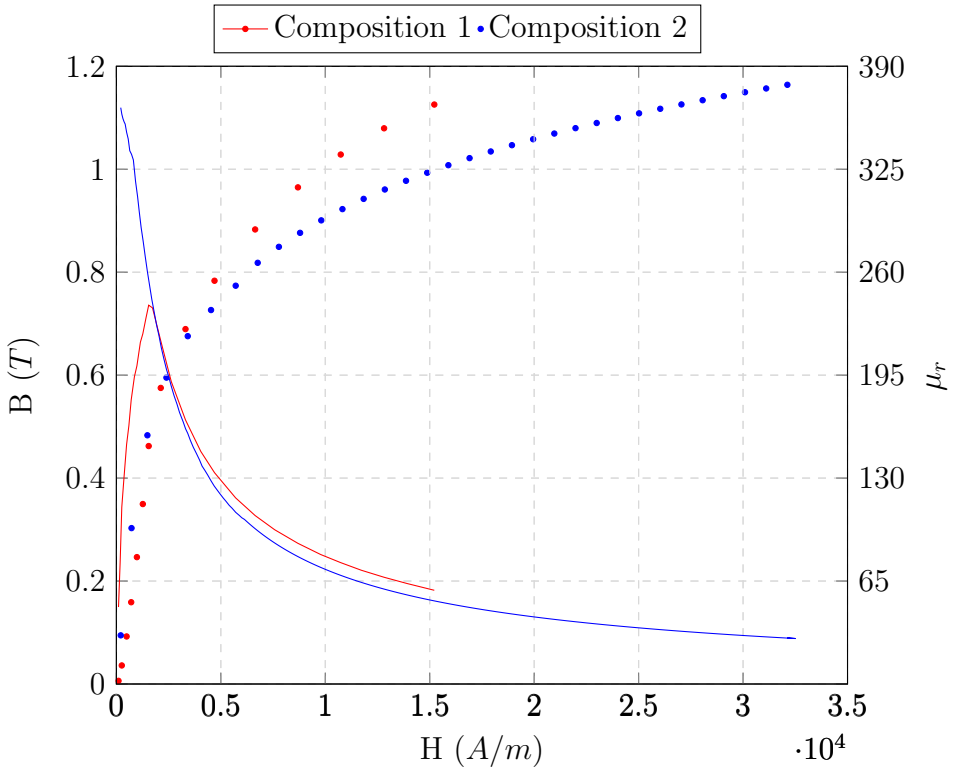

Figure 5.10: Cast Iron magnetization curve and relative magnetic permeability.

thickness limits the possible induction frequency (because a high skin/penetration depth is needed); on the other hand, a strong EM influence is needed to control the re-circulation of the $5\,t$ melt. EMS has been applied to laboratory scale problems or small industrial cases, but no extensive work has been done regarding the influence of such application on the macrosegregation of large ingots. Research in this particular application is rare because the experimental validation is extremely expensive and takes time, since the ingot has to be cut vertically (section $60 \times 200\,\mathrm{m}$) and the large obtained section has to be analysed to measure components' segregation. The second issue is that the mould is made of cast iron. Cast iron is highly ferromagnetic and its maximum relative magnetic permeability varies between $\mu_r = 200$ and $\mu_r = 360$, depending on the Ferrite content (figure 5.10). Thus, the mould works as a magnetic shield, preventing the induction fields to penetrate into the melt.
Given these issues, numerical simulation is the fastest and cheapest way to check the application's feasibility, before any industrial-scale experiment.

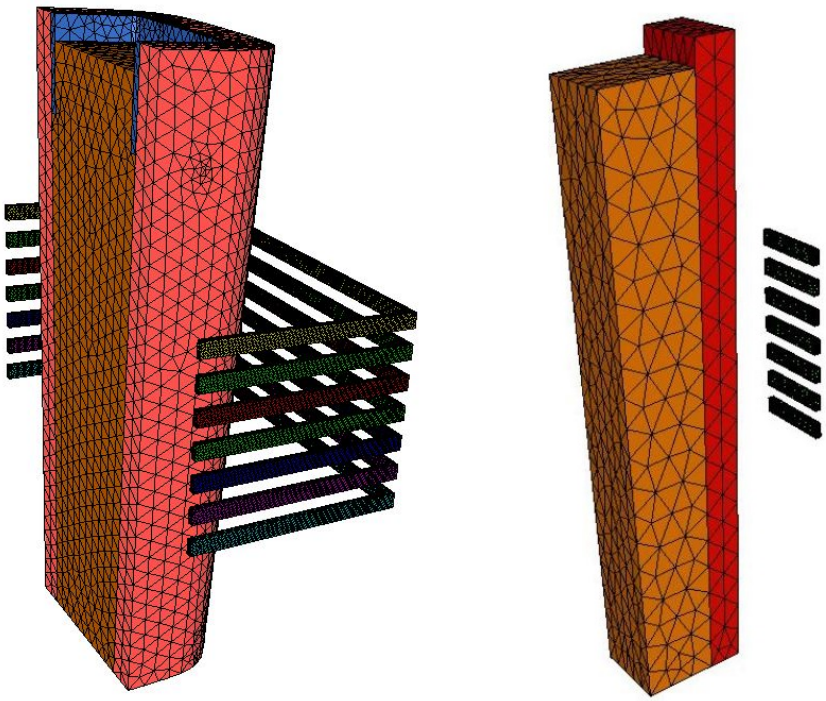

(a) Half mould geometry.

(b) Central band of the mould: simulated region.

Figure 5.11: Geometrical features of the EM simulation.

Step 1: EM penetration

At the very first stage, we need to answer to the question: can we overcome the shielding effect of the cast iron mould and have magnetic induction fields penetrated into the melt?
At this stage, very little information about the configuration and the materials were available. The stirrer has been considered as a classic AC stirrer made of a spiral coil. The frequency has been varied from $f = 4\,Hz$ to $f = 40\,Hz$. Two sets of EM computations have been performed with different magnetic permeabilities: one set with the maximum value ($\mu_r = 300$) and one set with minimum value ($\mu_r = 10$). In figure 5.11(a), the problem's geometry is shown, while figure 5.11(b) depicts the simulated domain. The choice of simulating only the central part of the mould is due to the need of performing many simulations to have a broad understanding of the problem. In addition, we were not interested in the effects due to the complete geometry because at this stage we are only interested at the penetration capability of the stirring system.

The electromagnetic results of the simulation have been plotted in figures 5.12.

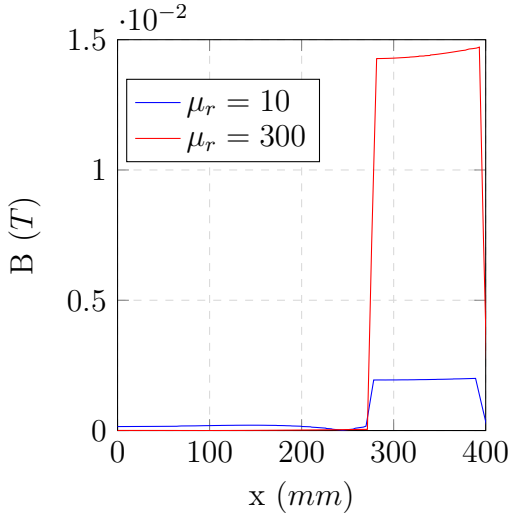

(a) Magnetic flux density vs distance from the mould's centre.

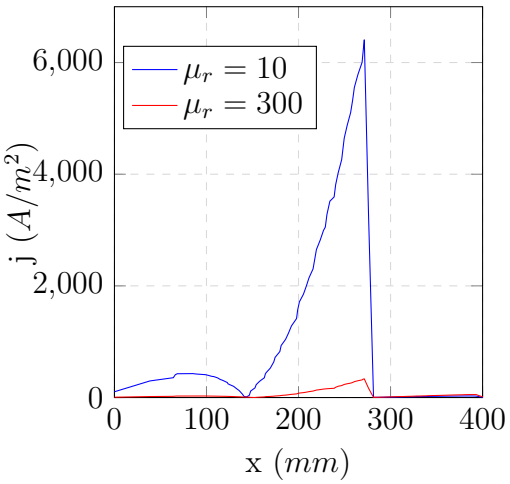

(b) Current density vs distance from the mould's centre.

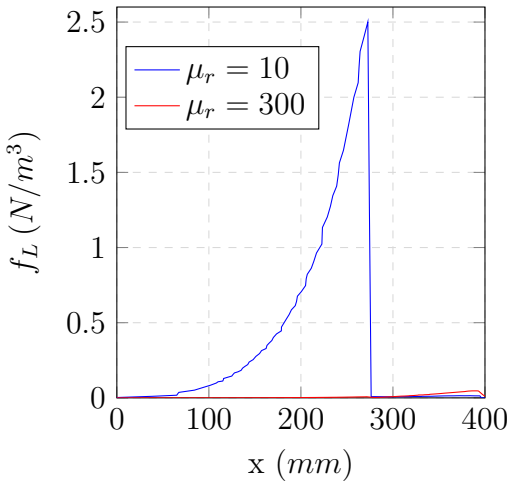

(c) Lorentz force density vs distance from the mould's centre.

Figure 5.12: Results of the EM computation of the standard stirring configuration.

The interface between the liquid metal and the mould is placed at $x = 270\,mm$. In figure 5.12(c) the Lorentz force is plotted and it is clear that no significant stirring occurs when the relative magnetic permeability of the mould is $\mu_r \gg 1$. In this case, the mould works as magnetic shield, thus the induced magnetic field is high in the mould, but totally dumped in the liquid metal region (figure 5.12(a)).

In order to improve the stirring system, some technological variations have been simulated:

Cold Mould . The principle has been inspired from the casting of high value metals and alloys by cold crucibles. The mould works as a shield because of the eddy current developed in it; by preventing these currents (by, for instance, non-conductive layers) the EMF should better penetrate into the mould with no damping. The insulating layers prevent eddy currents from developing into the mould, changing their pattern as sketched in figure 5.13. This is often done for small moulds, but it is technologically difficult for large, heavy moulds. However, we considered this option as a possible improvement. In terms of simulation, the mould has been cut with a small air layer every $30\,cm$. In figure 5.14, the isolines of the current density are plotted in the case of normal mould (figure 5.14(a)) and in the case of discontinuous mould (figure 5.14(b)). The light blue part is the liquid metal, the darker blue part is the mould section and the red area is the air domain surrounding the mould. In figure 5.15, the results of the EM simulation of the "cold mould" configuration are shown. We notice that the maximum Lorentz force induced in the liquid metal region increases of 30% when $\mu_r = 10$ (figure 5.15(e)) and 50% when $\mu_r = 300$ (figure 5.15(f)). Thus, the idea of breaking the electrical recirculation in the mould improves the stirring capability, but the obtained force density is still more than one order of magnitude lower than the necessary.

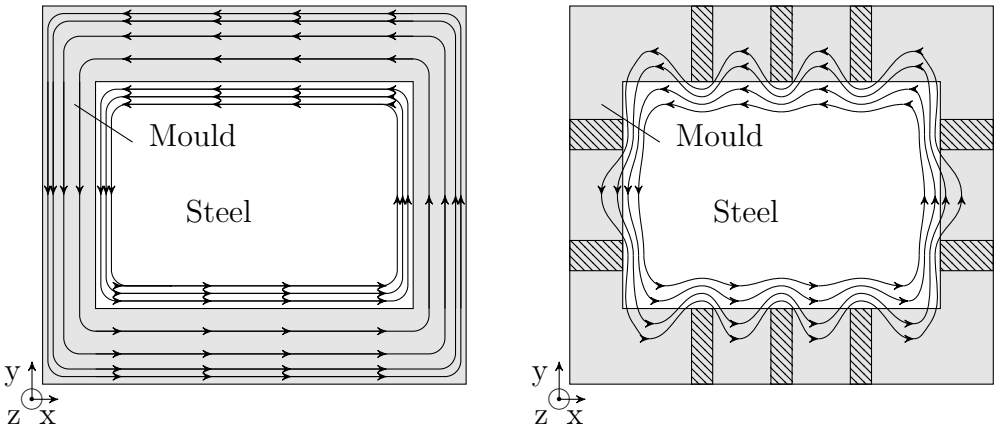

(a) Eddy currents pattern for homogeneous mould.

(b) Eddy currents pattern for non-homogeneous mould.

Figure 5.13: Electrical eddy current patter with (b) and without (a) insulating layers in the mould.

Flux concentrator . The use of a magnetic flux concentrator is a very common technique to improve induction systems' efficiency. The magnetic flux concentrator consists in a ferromagnetic shield surrounding the inductor's coil, as shown in figure 5.16. This shield leads to increase the magnetic flux density and to focus the EMF

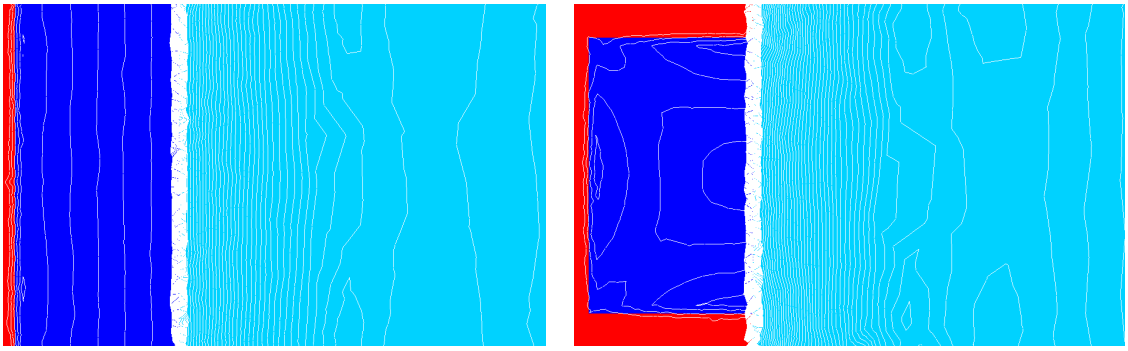

(a) Normal mould.

(b) Mould interrupted by non-conductive layers.

Figure 5.14: Current density isolines in the mould's section.

in the desired region avoiding the dispersion of magnetic energy in the air around the mould (see figure 5.17). In figure 5.18, the results of the EM simulation with the use of a flux concentrator are shown. In this case the maximum Lorentz force induced in the melt is highly increased: +168% when $\mu_r = 10$ (figure 5.18(e)), and +226% when $\mu_r = 300$ (figure 5.18(f)).

In this section we have shown that the EMF can pass through the cast iron mould and develop stirring forces inside the molten steel region. We have also shown how the use of a flux concentrator highly improves the EMS system by increasing the stirring force and the efficiency of the application. On the other hand, the shielding effect of the mould is strong and the induced stirring force is low. In addition it is clear that the material behaviour is the main factor which makes the stirring force too low to steer the flow. Thus, a second step of the feasibility study has to be done to understand the effect of the EM force on the liquid metal.

Step 2: Coupled simulation.

The second step in the feasibility study consists in analysing the impact of the EMS system on the fluid recirculation. This step requires the choice of a specific EMS system, thus the knowledge of the natural recirculation patterns is needed. The CFD/thermal analysis of the full casting process has been run with no EMS. The natural recirculation pattern when 10% of the ingot is solidified is depicted in figure 5.19. We see that, during solidification, the flow is characterized by a strong downward flow in the central axis of the mould, which is fed by a slow upward recirculation pattern along the walls. In order to block (or, at least, damp) this flow, a linear stirrer inducing a downward stirring velocity could be used. Thus, as the last step of preliminary studies, a coupled EM-CFD computation has been

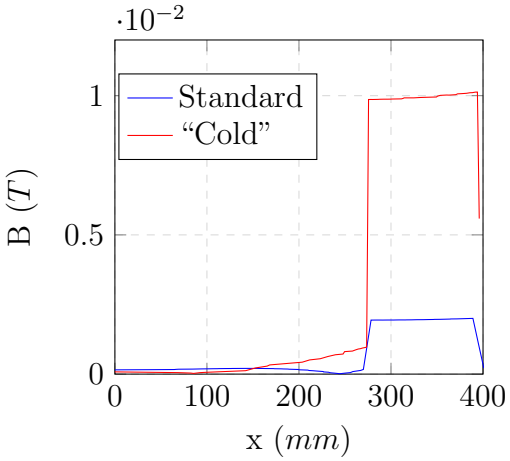

(a) Magnetic flux density vs distance from the mould's centre, $\mu_r = 10$.

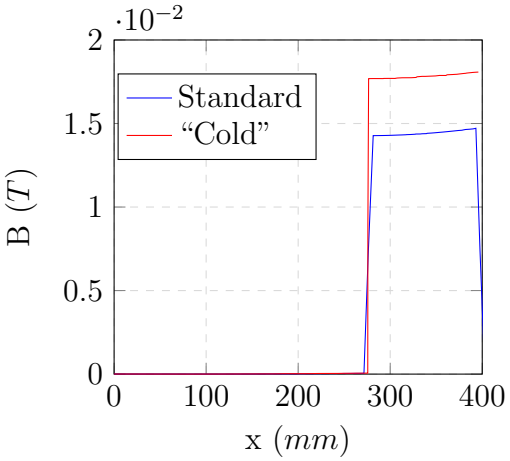

(b) Magnetic flux density vs distance from the mould's centre, $\mu_r = 300$.

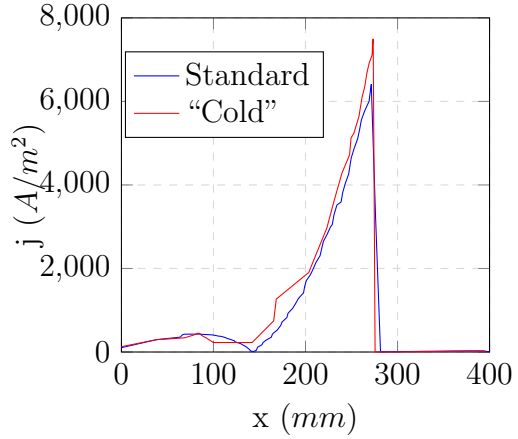

(c) Current density vs distance from the mould's centre, $\mu_r = 10$.

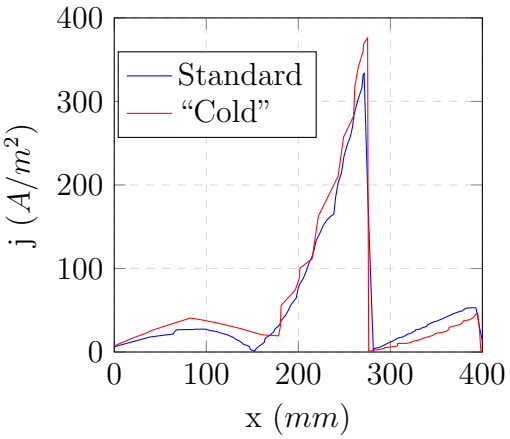

(d) Current density vs distance from the mould's centre, $\mu_r = 300$.

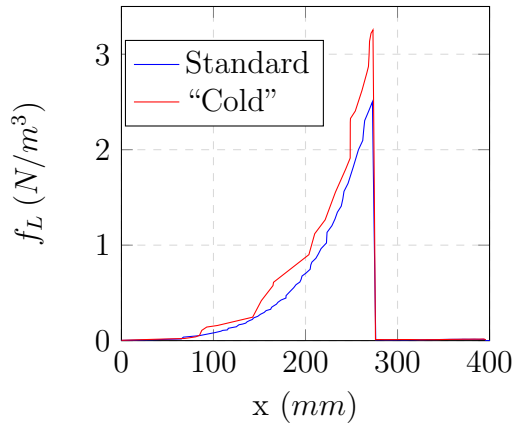

(e) Lorentz force density vs distance from the mould's centre, $\mu_r = 10$.

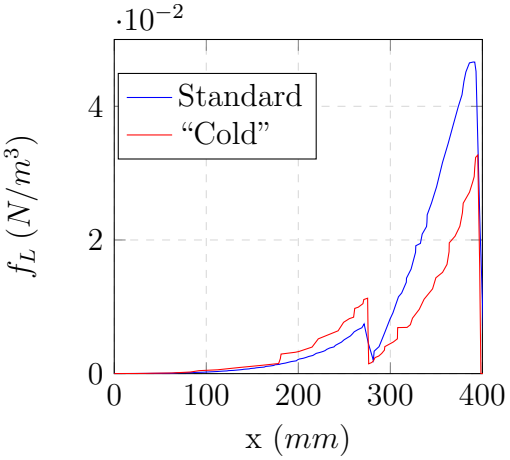

(f) Lorentz force density vs distance from the mould's centre, $\mu_r = 300$.

Figure 5.15: Results of the EM computation of the "cold mould" stirring configuration.

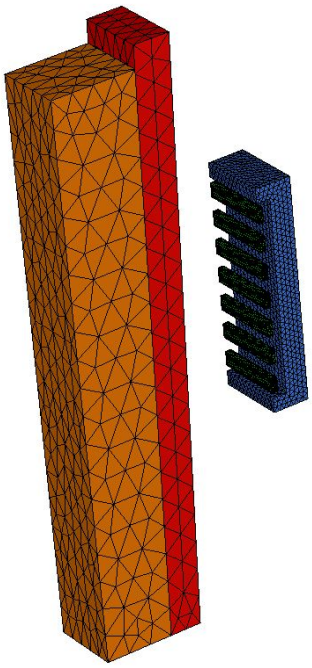

Figure 5.16: Flux concentrator surrounding the coil of the EMS.

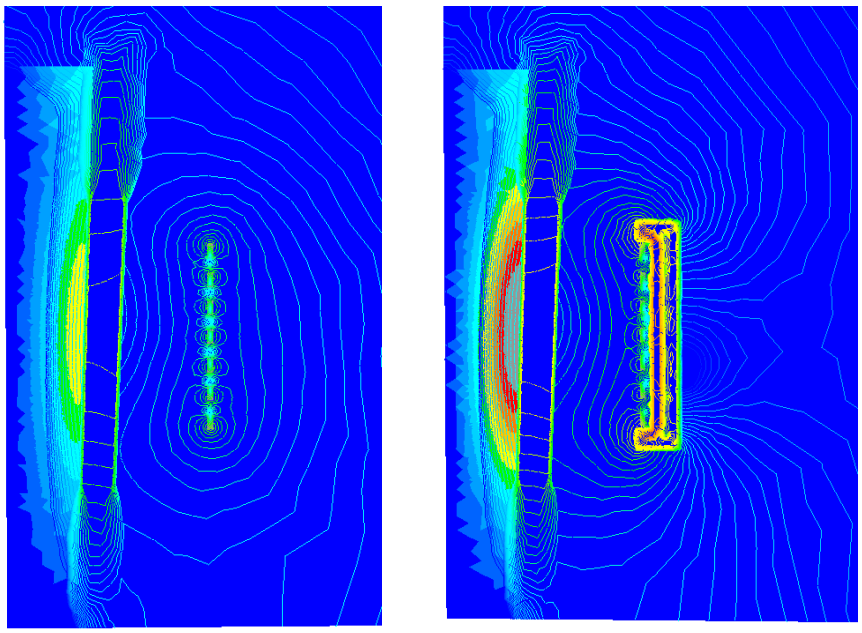

(a) Without flux concentrator. (b) with flux concentrator.

Figure 5.17: Colour plot and isolines of the magnetic flux density with and without flux concentrator.

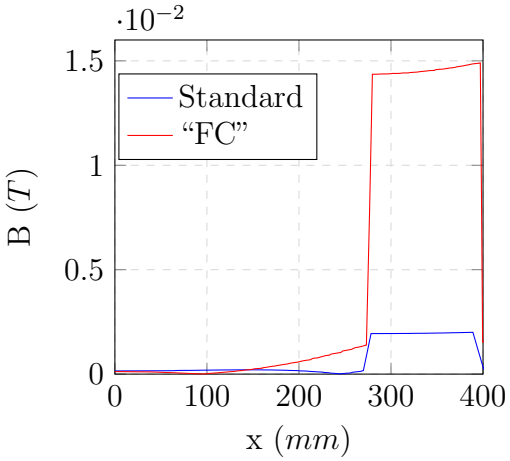

(a) Magnetic flux density vs distance from the mould's centre, $\mu_r = 10$.

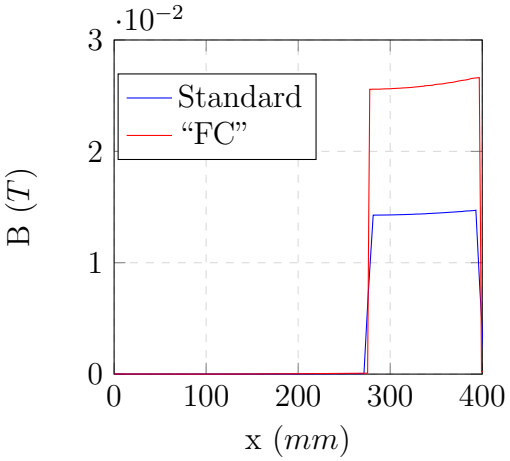

(b) Magnetic flux density vs distance from the mould's centre, $\mu_r = 300$.

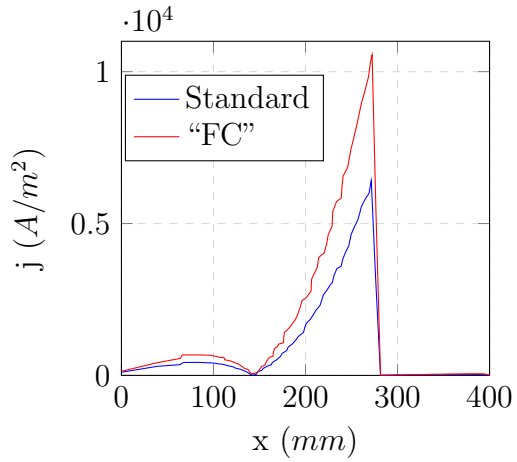

(c) Current density vs distance from the mould's centre, $\mu_r = 10$.

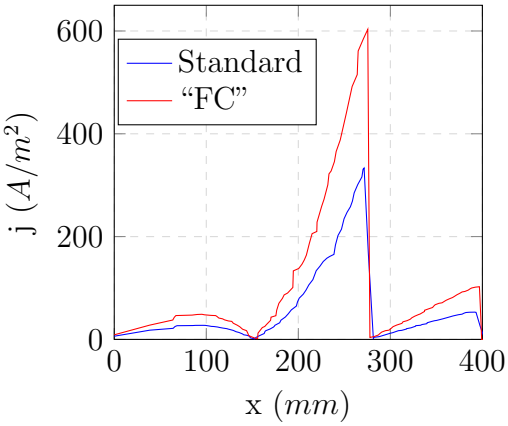

(d) Current density vs distance from the mould's centre, $\mu_r = 300$.

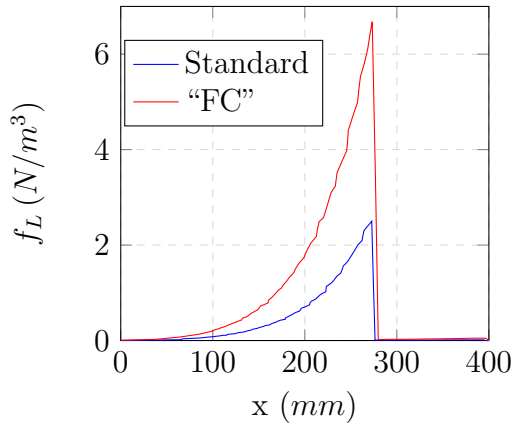

(e) Lorentz force density vs distance from the mould's centre, $\mu_r = 10$.

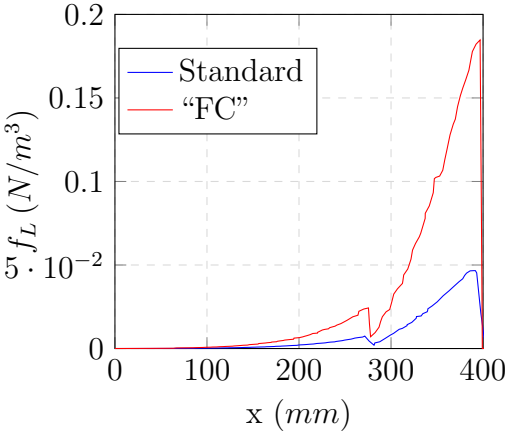

(f) Lorentz force density vs distance from the mould's centre, $\mu_r = 300$.

Figure 5.18: Results of the EM computation of the "flux concentrator" (FC) stirring configuration.

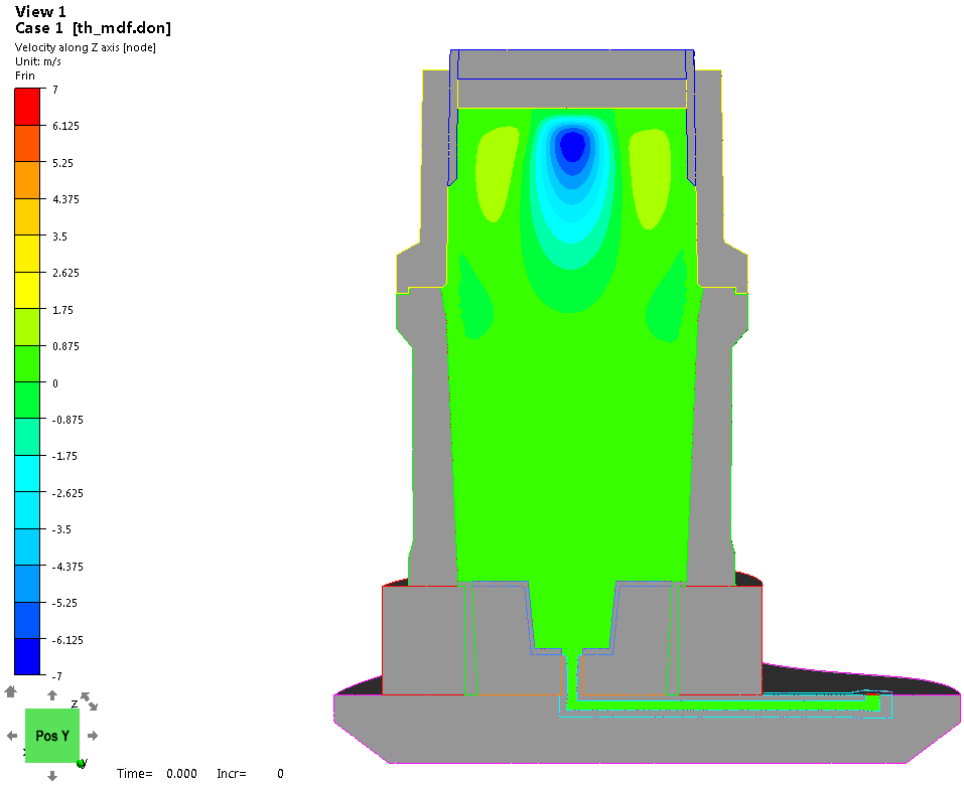

Figure 5.19: Vertical velocity during solidification due to natural convection.

performed to simulate the stirring capabilities of such a system: if the obtained velocity was of the same order of magnitude (and opposite direction) as the natural convection, the system would be feasible. On the contrary, if the induced velocity was lower, the system would be judged to be infeasible because of the dumping of the thick cast-iron mould.
The cast iron has been modelled through the model shown in equation (2.36); the flux concentrator has been hypothesized made of Fluxtrol®, which is the state-of-the-art choice for induction systems. All the simulation parameters are reported in table 5.3.

Two different positions of the inductor coil have been tested; this choice is due to the need of maximizing the flux concentration towards the mould, which can be pursued by a closer stirrer, as seen in figure 5.20. In figure 5.21, the average Lorentz force is plotted. The presence of the stirrer close to the mould (figure 5.21(b)) clearly increases the induced forces in the melt by a factor 10. On the other side, it is important to notice that the highest Lorentz forces developed in the melt are close to the free surface and their value is almost independent from the inductor position. This phenomenon is due to the EMF "escaping" from the stirrer through the air

Table 5.3: Simulation parameters.

Mould	
B_s	$0.75\,T$
μ_{rmax}	230
ρ	$9 \times 10^{-4}\Omega m$
Flux concentrator	
B_s	$1.7\,T$
μ_{rmax}	130
ρ	$1 \times 10^{-4}\Omega m$
Molten steel	
μ_r	1
ρ	$2.89 \times 10^{-7}\Omega m$
Copper coil	
μ_r	1
ρ	$5.747 \times 10^{-9}\Omega m$
f	$5Hz$
phase ϕ	$\pi/3$
j	$3\,kA/m^2$

layer between the mould and the flux concentrator (which is a magnetic shield). By reducing this air gap, the Lorentz forces induced close to the free surface are slightly reduced, but they remain the highest in the melt. This fact is the proof of the non-optimal problem configuration: the cast-iron mould is so thick and ferromagnetic, that the EMF which penetrates in the liquid metal region is too damped to induce adequate stirring force.
This lack of stirring capability is confirmed by the CFD results. In figure 5.22 the velocity vector field is plotted, while the color represents the vertical component of the velocity. In figure 5.22(a) we see that the stirring forces close to the free surface create an eddy which flows in the opposite direction than the natural convection pattern. On the opposite, no eddy is developed in the central region, where the stirring force is damped by the mould. The situation is different when the stirrer in moved closer to the mould (figure 5.22(b)). In this case, the stirring force induced in the central region is high enough to create a central recirculation flow. However, even if the result is qualitative satisfying, the magnitude of the induced velocity is 3 orders of magnitude lower than the natural convection velocity. In figures 5.23(a) and 5.23(b), the vertical velocity at the centre of the two eddies is plotted. These results show that the velocity of the stirred flow is too low with respect to the natural convection velocity, so none of the studies configurations would be able to block or invert the natural convection flow. A possible way to apply EMs to this

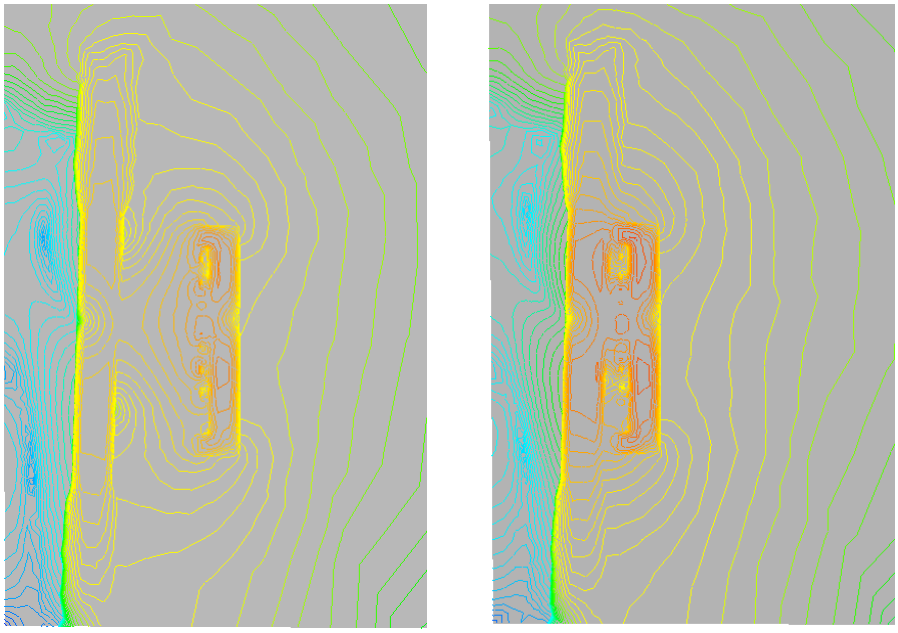

(a) Large distance between the mould and the coil.

(b) Small distance between the mould and the coil.

Figure 5.20: Isolines of the magnetic flux density in logarithmic scale corresponding to different stirrer position.

problem could be increasing the induction current density, but technological issues like excessive energy consumption and coil heating would occur. In addition, the process' efficiency would be very low because of to the dissipation due to the shielding effect of the cast-iron mould. The material of the mould is the key problem: there is no efficient way to pass energy from one side of the mould (stirrer) to the other (liquid metal) as far as this kind of mould is used.

5.5 Conclusions

In this chapter we have presented two industrial applications of the EMS simulation algorithm described in the first 4 chapters.
The first case has been found in the literature and consists in the simulation of in-mould flow. We decided to enhance the process simulated in the literature through M-EMS. The results are interesting both from the numerical and industrial point of view. From the numerical point of view, we notice the impact of anisotropic re-meshing on computation's time and accuracy. We also test VMS in the simulation of a fully turbulent flow. Finally, we analyse the computational effort related to the coupling interface, which results to be competitive. From the industrial point

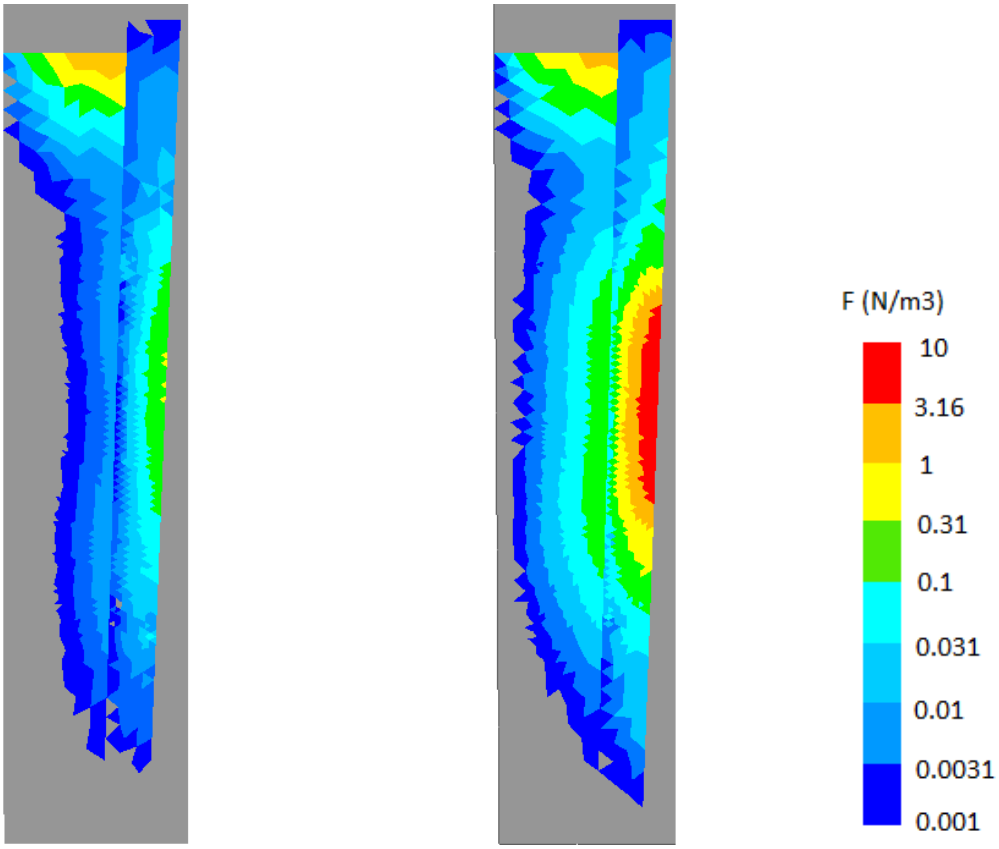

(a) Large distance between the mould and the coil.

(b) Small distance between the mould and the coil.

Figure 5.21: Lorentz force densities: vertical section at the centre of the ingot.

of view, we note how EMS decreases the turbulence in the mould; the double-roll structure is better preserved and velocity pulsations decrease. Also, the impact velocity of molten metal in the meniscus' region is lower, leading to better solidification properties.
The second industrial case consists in a feasibility study of EMS in large ingot casting. The first part consists in the study of the impact of a cast-iron mould (so, ferromagnetic) on the EM field. This is not the most efficient case for sure, but, thanks to simulations, we show how it is theoretically possible. At this stage, we also explore some possible enhancements of the EMS system, such as flux concentrators, and their effects. The second part of the study was focused on the simulation of the fully CFD-EM coupled problem. This set of simulations show that stirring Lorentz forces are developed inside the molten metal, but their magnitude is too low to produce the desired mechanical recirculation.

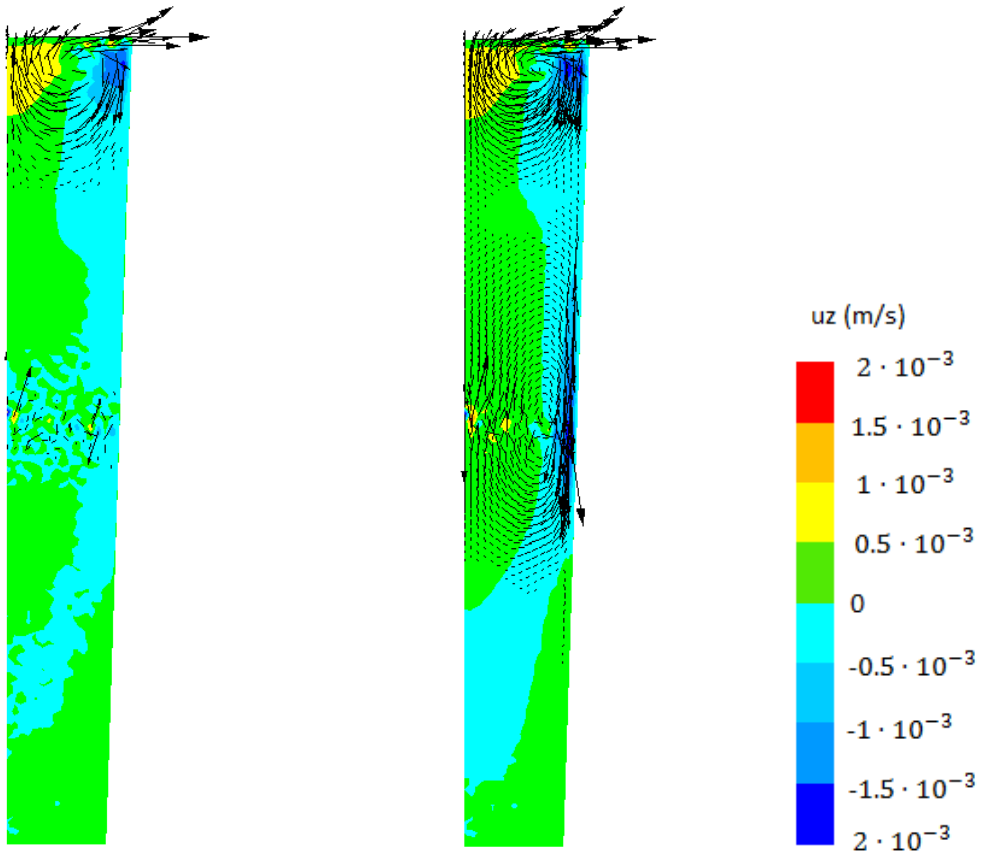

(a) Large distance between the mould and the coil.

(b) Small distance between the mould and the coil.

Figure 5.22: Stirred recirculation pattern: vector-plot of the velocity field and color-plot of the vertical component of velocity.

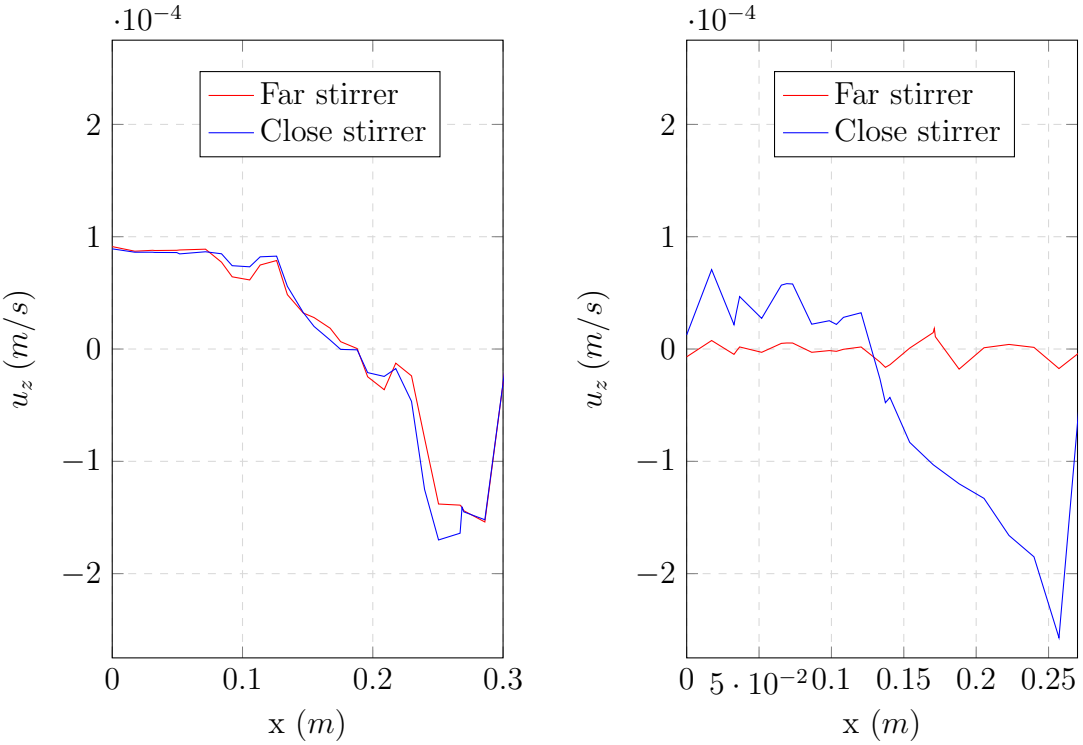

(a) Vertical velocity profile plotted at the horizontal middle-line of the ingot at $z = 1.9\,m$.

(b) Vertical velocity profile plotted at the horizontal middle-line of the ingot at $z = 1\,m$.

Figure 5.23: Vertical recirculation velocity in the ingot's middle plane.

Chapter 6

Conclusions and Perspectives

6.1 Résumé du chapitre en français

Dans ce chapitre, on souligne les principales nouveautés proposées dans ce travail de thèse. Les outils proposés et développés dans ce travail, qui ont été validés par l'expérience ou par la comparaison avec d'autres méthodes numériques, sont maintenant implémentés dans la version commerciale du logiciel THERCAST. La dernière partie de ce chapitre traite des perspectives d'évolution et d'amélioration des modèles numériques, que ce soit en matière d'efficacité dans la simulation de chacune des physiques impliquées ou en matière de couplage entre ces différentes physiques.

6.2 Conclusions

The objective of this thesis was to develop a robust, efficient and accurate numerical algorithm for the simulation of electromagnetic stirring applications, especially for in-mould stirring in the framework of continuous casting of steel. The first part of this work (chapters 2 and 3) has been dedicated to the study and modelling of each physical problem involved in the process.
The electromagnetic problems (chapter 2) has been modelled through the $(\underline{A}; \phi)$ potential formulation and a quasi-static approximation has been used. Different behaviour laws have been studied in order bot to cope with material non-linearities and have a computationally cheap and robust constitutive model. The PDE system has been solved in a de-coupled way: nodal $\mathcal{P}^1$ finite elements have been used to compute the electric potential; on the contrary, Nédélec edge finite elements have been used for the computation of the magnetic vector potential; this choice is due to the fact that edge elements better fits the PDE formulation of EM problems, which includes curl operators. Different solutions have been proposed for a time-integration. In the case of multiple induction frequencies, a *quasi-static second*

order central differences scheme has been used. In the case of unique induction frequency, the PDE system has been solved in the frequency domain, which leads to the resolution of a linear complex-valued linear system. A new approach based on real-equivalent formulations have been proposed to solve this system and improve the resolution efficiency.
In chapter 3, the fluid mechanics problem has been studied. The classic Navier-Stokes equations have been solved by a variational multistacale approach, which allows to track the effect of small scale turbulence without explicitly solving it. Being equivalent to other LES methods, VMS approach fits the studied processes which are characterised by a fully developed turbulence, but not extreme, since EMS decreases the turbulence level. This approach leads to better accuracy with respect to the broadly used k-ε model, but it requires higher computational resources. The simulation has therefore been optimized by the anisotropic mesh adaptation which uses an edge-based error estimator. Multiphase flow has been modelled through the level-set method. A convective-reinitialization approach has been proposed, hence the LS evolution is solved by a single-equation modelling, avoiding the re-initialization step. This method requires to filter the level-set function, so different filters have been compared and analysed. Also, a correction-step has been proposed to reinforce the mass conservation of each phase, which is usually not guaranteed by level-set methods.
Chapter 4 has been dedicated to the coupling scheme between the physics studied in chapters 2 and 3. Our attention has been focused on three main points:

- the influence of the time-dependent part of the Lorentz force on the fluid motion
- the variation of the computational domain and/or its material parameters.
- the effect of the convective term of the eddy currents both from the EM and the CFD point of view

These three points have both been discussed from a physical point of view by using non-dimensional numbers and from a numerical point of view. They have been studied and applied to three different benchmark cases in order to justify our choices: the lid-driven cavity, the dam-break and the ingot AC stirring of GaInSn. The influence of the time-dependent part of the Lorentz force have been considered only when the time-scale of the EM problem and the turbulence turnover time are similar, which means an interaction between the EM force and the turbulence structure may occur. A global condition (Ω_n^m condition) has been proposed and applied to a laboratory-scale case. The same approach has been used to decide when to consider the domain/material parameters variation within the coupling scheme. Finally, the convective term of the Lorentz force has been modelled from the mechanical point of view as an explicit source term. This choice makes the formulation

conditionally stable, so a limit time-step condition which guarantees the convergence of the solution has been proposed and validated. The obtained coupling scheme has been validated by comparison with experimental and numerical results provided by recognised research groups (ETP Hannover) and commercial software (ANSYS); the results are in very good agreement with the experimental data and more precise than the one obtained by the k-ε CFD module of ANSYS.
In chapter 5, industrial applications of the developed simulation tool have been shown. The first case is the application of an AC M-EMS to slab casting. At first, different meshing techniques have been compared, showing the impact of anisotropic mesh adaptation on the computational time. Then, physical results have been shown: the flow in the mould results to be less turbulent and more stable when EMS is applied; this may be linked to better solidification conditions (stable flow at the meniscus level) and regular double-roll structure. The second case is a feasibility study of EMS application to large ingot casting, in collaboration with ArcelorMittal-Industeel. The simulation tool has been used to analyse the electromagnetic condition of the process and highlight the main issues, like the presence of a thick ferromagnetic mould. The second step has been to propose possible improvements of the stirring system and to simulate the induced stirring effect on the fluid. The results are interesting and consistent with the previsions, but the application has been judged non-feasible because of the shielding effect of the mould.
As a result of this industrial-PhD, the coupling algorithm has been implemented in the commercial code THERCAST®and it is ready for the α-phase. This module can be used for any kind of EMS system, but mainly for applications in the mould, tundish and ladle for continuous casting process.

6.3 Perspectives

In chapter 3, an a-posteriori correction of the level set function has been proposed to reinforce mass conservation. This approach is effective when the different subdomains are simply connected, which is usually the case for free-surface fluctuations in steel casting. However, this correction may introduce significant numerical error for non-connected subdomains (e.g. droplet or bubble motion). The best would be to have a strong formulation which naturally reinforces mass conservation; many works have been done in this direction, but the proposed solutions are often sensitive to numerical parameters, which should be tuned for each case.
Regarding the coupling strategy, we think there is no unique direction for improvements. The coupling scheme is heavily dependent on the process to be modelled. A message-based (instead of file-based) coupling scheme would be more efficient in terms of computational time, but would require higher resources in terms of RAM.

Strong coupling strategies (i.e. coupling the EM and the CFD solvers at each time-increment) would be more precise, but significantly more time-demanding. Our algorithm is tailor-made for M-EMS applications, but it is also flexible enough to be applied to others processes. The main limitation of our approach is the impossibility to model the induced magnetic field caused by the fluid motion. This is an improvement which must be done in order to extend the simulation to braking applications. The modelling of this term implies a strong coupling between the CFD and the EM solvers; thus, the EM solver should include a term based on the liquid velocity. Also the two ways coupling may be improved; as stated before, the call of the EM solver by the CFD solver is ruled by a temperature-based condition. The best would be to base this condition directly on the variation of materials' EM parameters, in order to deal with possible material non-linearities and phase transformations, especially when these does not depend only on temperature.
From the industrial point of view, this work provided a solid tool to have an insight of the process and obtain a deep understanding of the interaction between the EM field and the fluid motion. In order to achieve the optimum simulation tool, hence able to simulate the full industrial process, the existing method should be enhanced. Different physics should be added to the proposed methodology, for instance the Argon bubbles (which are non-conductive) motion, the slag on the free surface, the tracking of inclusions and the impact of the EMF on the microstructure evolution.

Bibliography

[1] C. Li and B. G. Thomas. Maximum casting speed for continuous cast billets based on sub-mould bulging computation. In *85 th Steelmaking Conf. Proc*, pages 109–130, 2012. *Cited page 5*

[2] C. Li and B. G Thomas. Maximum casting speed for continuous cast steel billets based on sub-mold bulging computation. In *85th Steelmaking conf. proc., ISS*, pages 109–130, Nashville, 2002. *Cited page 6*

[3] J. P. Gu and C. Beckermann. Simulation of convection and macrosegregation in a large steel ingot. *Metallurgical and materials transactions A*, 30:1357–1366, 1998. *Cited page 7*

[4] H. Yang, L. Zhao, X. Zhang, K. Deng, W. Li, and Y. Gan. Mathematical Simulation on Coupled Flow, Heat, and Solute Transport in Slab Continuous Casting Process. *Metallurgical and materials transactions B*, 29:1345–1356, 1998. *Cited page 7*

[5] M. H. Bina. Homogenization heat treatment to reduce the failure of heat resistant steel castings. In Yogiraj Pardhi, editor, *Metallurgy - Advances in Materials and Processes*. InTech, Rijeka, 2012. *2 citations pages v and 7*

[6] B. Zhang, J. Cui, and G. Lu. Effects of low-frequency electromagnetic field on microstructures and macrosegregation of continuous casting 7075 aluminum alloy. *Materials Science and Engineering: A*, 355(1):325 – 330, 2003. *Cited page 8*

[7] L. Zhang and B. G. Thomas. Inclusions in continuous casting of steel. In *XXIV National Steelmaking Symposium*, pages 138–183, 2003. *Cited page 8*

[8] C. Jungwook, S. Hiroyuki, E. Toshihiko, and S. Mikio. Thermal resistance at the interface between mold flux film and mold for continuous casting of steels. *ISIJ International*, 38(5):440–446, 1998. *Cited page 6*

[9] K. Yoshiaki, E. C. Carlos, and W. C. Alan. An investigation of the crystallization of a continuous casting mold slag using the single hot thermocouple technique. *ISIJ International*, 38(4):357–365, 1998. *Cited page 6*

[10] H. Todoroki, T. Ishii, K. Mizuno, and A. Hongo. Effect of crystallization behavior of mold flux on slab surface quality of a ti-bearing fe–cr–ni super alloy cast by means of continuous casting process. *Materials Science and Engineering: A*, 413:121 – 128, 2005. *Cited page 6*

[11] I. Steinbach, M. Apel, T. Rettelbach, and D. Franke. Numerical simulations for silicon crystallization processes—examples from ingot and ribbon casting. *Solar Energy Materials and Solar Cells*, 72(1):59 – 68, 2002. *Cited page 6*

[12] A. V. Reddy and N. C. Beckermann. Modeling of macrosegregation due to thermosolutal convection and contraction-driven flow in direct chill continuous casting of an al-cu round ingot. *Metallurgical and Materials Transactions B*, 28(3):479–489, 1997. *Cited page 6*

[13] C. F. Merton. Our understanding of macrosegregation: Past and present. *ISIJ International*, 40(9):833–841, 2000. *Cited page 6*

[14] S. O. Kyung and W. C. Young. Macrosegregation behavior in continuously cast high carbon steel blooms and billets at the final stage of solidification in combination stirring. *ISIJ International*, 35(7):866–875, 1995. *Cited page 6*

[15] M. R. Aboutalebi, M. Hasan, and R. I. L. Guthrie. Coupled turbulent flow, heat, and solute transport in continuous casting processes. *Metallurgical and Materials Transactions B*, 26(4):731–744, 1995. *Cited page 6*

[16] Z. Q. Liu, F. S. Qi, B. K. Li, and S. C P Cheung. Modeling of bubble behaviors and size distribution in a slab continuous casting mold. *International Journal of Multiphase Flow*, 79:190–201, 2016. *Cited page 7*

[17] L. Zhang, J. Aoki, and B. G. Thomas. Inclusion removal by bubble flotation in a continuous casting mold. *Metallurgical and Materials Transactions B*, 37(3):361–379, 2006. *Cited page 7*

[18] B. Nagayasu, Y. Ryoji, Y. Hisao, F. Tetsuya, N. Tsutomu, and T. Seiji. Numerical analysis of fluid flow in continuous casting mold by bubble dispersion model. *ISIJ International*, 31(1):40–45, 1991. *Cited page 7*

[19] B. G. Thomas, A. Dennisov, and H. Bai. Behavior of Argon Bubbles during Continuous Casting of Steel. In *ISS 80th Steelmaking conference*, pages 375–384, 1997. *Cited page 7*

[20] B. G. Thomas, Q. Yuan, B. Zhao, and S. P. Vanka. Transient Fluid-Flow Phenomena in the Continuous Steel-Slab Casting Mold and Defect Formation. *Journal of Metals – electronic edition*, 2006. *Cited page 7*

[21] L. C. Hibbeler and B. G. Thomas. Mold slag entrainment mechanisms in continuous casting molds. In *Iron and Steel Technology Conference*, volume 10, pages 121–136, 2013. *Cited page 7*

[22] J. Nakashima and T. Toh. Improvement of continuously cast slabs by decreasing nonmetallic inclusions. Technical Report 104, Nippon Steel Technical Report, 2013. *Cited page 9*

[23] Q.T. Fang and M.J. Kinosz. Fine grain casting by mechanical stirring, October 2 1990. US Patent 4,960,163. *Cited page 9*

[24] P. Lucien. Continuous-casting method of melting metals in a slag medium by using consumable electrodes, February 15 1966. US Patent 3,234,608. *Cited page 9*

[25] X. Jian, H. Xu, T.T. Meek, and Q. Han. Effect of power ultrasound on solidification of aluminum a356 alloy. *Materials Letters*, 59(2):190 – 193, 2005. *Cited page 9*

[26] Z. Shao, Q. Le, Z. Zhang, and J. Cui. A new method of semi-continuous casting of az80 mg alloy billets by a combination of electromagnetic and ultrasonic fields. *Materials and Design*, 32(8):4216 – 4224, 2011. *Cited page 9*

[27] R. Singh, B. G. Thomas, and S. P. Vanka. Effect of electromagnetic braking (embr) on turbulent flow in continuous casting. In *AISTech 2013 - Proceedings of the Iron and Steel Technology Conference*, volume 2, pages 1323–1336, 2013. *Cited page 10*

[28] R. Chaudhary, B. G. Thomas, and S. P. Vanka. Effect of electromagnetic ruler braking (embr) on transient turbulent flow in continuous slab casting using large eddy simulations. *Metallurgical and Materials Transactions B: Process Metallurgy and Materials Processing Science*, 43(3):532–553, 2012. *2 citations pages 10 and 62*

[29] K. Cukierski and B. G. Thomas. Flow control with local electromagnetic braking in continuous casting of steel slabs. *Metallurgical and Materials Transactions B: Process Metallurgy and Materials Processing Science*, 39(1):94–107, 2008. *Cited page 10*

[30] Haiqi Yu and Miaoyong Zhu. Numerical simulation of the effects of electromagnetic brake and argon gas injection on the three-dimensional multiphase flow and heat transfer in slab continuous casting mold. *ISIJ International*, 48(5):584–591, 2008. *Cited page 10*

[31] Y. Wang and L. Zhang. Fluid flow-related transport phenomena in steel slab continuous casting strands under electromagnetic brake. *Metallurgical and Materials Transactions B*, 42(6):1319–1351, 2011. *Cited page 10*

[32] B. Rietow and B. G. Thomas. Using nail board experiments to quantify surface velocity in the cc mold. In *AISTech conference*, pages 1–11, 2008. *Cited page 10*

[33] R. Liu, D. Crosbie, S. Chung, M. Trinh, and B. G. Thomas. Measurement of molten steel surface velocity with svc and nail dipping during continuous casting process. In *Sensors, Sampling, and Simulation for Process Control*, pages 1–11, 2011. *3 citations pages v, 10, and 11*

[34] K. Timmel, M. Roder, S. Eckert, and G. Gerbeth. Flow measurements in a continuous casting model using a low temperature liquid metal. In *8th International Symposium on Ultrasonic Doppler Methods for Fluid Mechanics and Fluid Engineering*, pages 71–75, 2012. *Cited page 10*

[35] A. Pedcenko, A. Bojarevics, J. Priede, G. Gerbeth, and R. Hermann. Velocity measurements in the liquid metal flow driven by a two-phase inductor. *Experiments in Fluids*, 54(6), 2013. *Cited page 10*

[36] D. Jian and C. Karcher. Electromagnetic flow measurements in liquid metals using time-of-flight lorentz force velocimetry. *Measurement Science and Technology*, 23(7):074021, 2012. *Cited page 10*

[37] A. Thess, E. Votyakov, B. Knaepen, and O. Zikanov. Theory of the lorentz force flowmeter. *New Journal of Physics*, 9(8):299, 2007. *Cited page 10*

[38] C. Heinicke. *Local Lorentz Force Velocimetry for liquid metal duct flows*. PhD thesis, Technischen Universit¨ at Ilmenau, 2013. *Cited page 10*

[39] Q. Yuan, S. Sivaramakrishnan, S. P. Vanka, and B. G. Thomas. Computational and experimental study of turbulent flow in a 0.4-scale water model of a continuous steel caster. *Metallurgical and Materials Transactions B*, 35(B):967–982, 2004. *Cited page 10*

[40] H. Yang, M. Seden, N. Jacobson, and J.E. Eriksson. Technical review on the development of EMBR and FC Mold application in slab continuous casting at

ABB. In *XVIII International UIE-Congress: Electrotechnologies for Materials Processing*, pages 162–163, 2017. *Cited page 10*

[41] B. Zhao, B. G. Thomas, S. P. Vanka, and R. J. O'Malley. Transient fluid flow and superheat transport in continuous casting of steel slabs. *Metallurgical and Materials Transactions B: Process Metallurgy and Materials Processing Science*, 36(6):801–823, 2005. *Cited page 10*

[42] P. Ramírez-López, R. D. Morales, R. Sánchez-Pérez, L. G. Demedices, and O. Dávila. Structure of turbulent flow in a slab mold. *Metallurgical and Materials Transactions B: Process Metallurgy and Materials Processing Science*, 36(6):787–800, 2005. *Cited page 10*

[43] B. G. Thomas, R. Singh, R. Chaudhary, and P. Vanka. Flow Control with Ruler Electromagnetic Braking (EMBr) in Continuous Casting of Steel Slabs. In *Fifth Baosteel Biennial Academic Conference*, pages 1–10, 2013. *2 citations pages 10 and 11*

[44] Y. Haiqi, W. Baofeng, L. Huiqin, and L. Jianchao. Influence of electromagnetic brake on flow field of liquid steel in the slab continuous casting mold. *Journal of Materials Processing Technology*, 202(1-3):179–187, 2008. *Cited page 10*

[45] O. Sjoden and M. Venini. Use of Electromagnetic Equipment for Slab and Thin Slab Steel Continuous Caster. *Association of Metallurgical Engineers of Serbia*, 13:11–20, 2007. *Cited page 11*

[46] R. Singh, B.G. Thomas, and S.P. Vanka. Large Eddy Simulations of Double-Ruler Electromagnetic Field Effect on Transient Flow During Continuous Casting. *Metall. Mater. Trans. B*, 45(3):1098–1115, 2014. *2 citations pages 11 and 142*

[47] S. Kunstreich, T. Gautreau, J.Y. Ren, A. Codutti, F. Guastini, and M. Petronio. Development and validation of multi-mode® emb, a new electromagnetic brake for thin slab casters. *Millenium Steel*, pages 86–92, 2015. *Cited page 11*

[48] S Kunstreich, T Gautreau, J.Y. Ren, A Codutti, F Guastini, M Petronio, and F Vecchiet. Experimental approach to develop Multi-Mode® EMB, an advanced electromagnetic brake for thin slab casters. In *8th International Conference on Electromagnetic Processing of Materials*, Cannes, France, October 2015. *Cited page 11*

[49] S. Kunstreich, T. Gautreau, J. Y. Ren, A. Codutti, F. Guastini, and M. Petronio. Development and Validation of Multi-Mode EMB, a New Electromagnetic

Brake for Thin Slab Casters. In *8th European Continuous Casting Conference, 8thECCC, Graz, Austria*, pages 550–558, 2014. *Cited page 11*

[50] B.G. Thomas and R. Chaudhary. State of the art in electromagnetic flow control in continuous casting of steel slabs: modeling and plant validation. In *6th International conference electromagnetic processing of materials*, volume 6, pages 19–24, 2009. *2 citations pages v and 12*

[51] D. Musaeva, V.K. Ilin, and V. Geza. Numerical simulation of the melt flow in an induction crucible furnace driven by a lorentz force pulse at low frequency. *Magnetohydrodynamics*, 51(4):771–783, 2015. *2 citations pages 12 and 13*

[52] S. Yanqing, X. Yanjin, Z. Lei, Z. Tiejun, W. Shiping, and G. Jingjie. Study on traveling magnetic field casting of sheet component. *China foundary*, 7(3):259–264, 2010. *Cited page 12*

[53] K. Yokota and K. Fujisaki. Electromagnetic Coil Designed by Magneto-Hydro-Dynamic-Simulation. Technical Report 89, Nippon Steel Technical Report, 2004. *Cited page 12*

[54] Y. Q. Su, Y. J. Xu, L. Zhao, J. J. Guo, and H. Z. Fu. Effect of electromagnetic force on melt induced by traveling magnetic field. *Transactions of Nonferrous Metals Society of China (English Edition)*, 20(4):662–667, 2010. *Cited page 12*

[55] S. Milind. *Linear Electromagnetic Stirrer*. PhD thesis, Indian Institute of Science, 2005. *Cited page 12*

[56] K. H. Spitzer, M. Dubke, and K. Schwerdtfeger. Rotational electromagnetic stirring in continuous casting of round strands. *Metallurgical Transactions B*, 17(1):119–131, 1986. *Cited page 12*

[57] J. Stiller, K. Koal, K. Frana, and R. Grundmann. Stirring of melts using rotating and travelling magnetic fields. In *Fifth International Conference on CFD in the Process Industries*, pages 1–5, Melbourne, 2006. *Cited page 12*

[58] S. Satou and K. Fujisaki. Evaluation of the influence of the time-varying electromagnetic component in M-EMS on flow at the free surface. *Electrical Engineering in Japan (English translation of Denki Gakkai Ronbunshi)*, 177(3):62–68, 2011. *2 citations pages 13 and 23*

[59] K. Fujisaki. In-mold electromagnetic stirring in continuous casting. *IEEE Transactions on Industry Applications*, 37(4):1098–1104, 2001. *Cited page 13*

[60] M. Barna, B. Willers, M. Javurek, J. Reiter, and S. Eckert. Investigations of the liquid steel flow in slab casters with electromagnetic brakes and round bloom casters with electromagnetic stirring. In *8th European Continuous Casting Conference 2014*, page 10, 2014. *Cited page 12*

[61] C. Stelian and D. Vizman. Numerical modeling of frequency influence on the electromagnetic stirring of semiconductor melts. *Crystal Research and Technology*, 41(7):645–652, 2006. *Cited page 12*

[62] A. Cramer, V. Galindo, and M. Zennaro. Frequency dependence of an alternating magnetic field driven flow. *Magnetohydrodynamics*, 51(1):133–147, 2015. *Cited page 12*

[63] F. Santara, Y. Delannoy, and A. Autruffe. Electromagnetic stirring and retention to improve segregation in silicon for photovoltaics. *Journal of Crystal Growth*, 340(1):41 – 46, 2012. *Cited page 13*

[64] J. Meyer, F. Durand, R. Ricou, and C. Vives. Steady flow of liquid aluminum in a rectangular-vertical ingot mold, thermally or electromagnetically activated. *Metallurgical Transactions B*, 15(3):471–478, 1984. *Cited page 13*

[65] G. Zhu, J. Xu, Z. Zhang, Y. Bai, and L. Shi. Annular electromagnetic stirring-a new method for the production of semi-solid A357 aluminum alloy slurry. *Acta Metallurgica Sinica (English Letters)*, 22(6):408–414, 2009. *Cited page 13*

[66] B. I. Jung, C. H. Jung, T. K. Han, and Y. H. Kim. Electromagnetic stirring and Sr modification in A356 alloy. *Journal of Materials Processing Technology*, 111:5–9, 2001. *Cited page 13*

[67] V. Fireteanu, E. Rousset, E. Chauvin, and N. Chouard. Simultaneous Induction Heating and Electromagnetic Stirring of a Molten Glass Bath. In *8th International Conference on Electromagnetic Processing of Materials*, 2016. *Cited page 13*

[68] M. Dubke, K. H. Tacke, K. H. Spitzer, and K. Schwerdtfeger. Flow fields in electromagnetic stirring of rectangular strands with linear inductors: Part II. computation of flow fields in billets, blooms, and slabs of steel. *Metallurgical Transactions B*, 19(4):595–602, 1988. *Cited page 13*

[69] M. Dubke, K. H. Tacke, K. H. Spitzer, and K. Schwerdtfeger. Flow fields in electromagnetic stirring of rectangular strands with linear inductors: Part I. theory and experiments with cold models. *Metallurgical Transactions B*, 19(4):581–593, 1988. *Cited page 13*

[70] H. K. Moffatt. Electromagnetic stirring. *Physics Fluids A*, 3(5):1336–1343, 1991. *Cited page 13*

[71] K. Ayata, T. Mori, T. Fujimoto, T. Ohnishi, and I. Wakasugi. Improvement of Macrosegregation in Continuously Cast Bloom and Billet by Electromagnetic Stirring. Technical Report 11, Transactions ISIJ, 1984. *Cited page 13*

[72] W.D. Griffiths and D.G. McCartney. The effect of electromagnetic stirring on macrostructure and macrosegregation in the aluminium alloy 7150. *Materials Science and Engineering: A*, 222(2):140 – 148, 1997. *Cited page 13*

[73] C. Vivès. Effects of forced electromagnetic vibrations during the solidification of aluminum alloys: Part I. solidification in the presence of crossed alternating electric fields and stationary magnetic fields. *Metallurgical and Materials Transactions B*, 27(3):445–455, 1996. *Cited page 13*

[74] D. Musaeva, E. Baake, and V.K. Ilin. Experimental Investigation of Al-Alloy Directional Solidification in Pulsed Electromagnetic Field. In *Materials Science Forum*, volume 870, pages 471–476, 2016. *Cited page 13*

[75] K. Brunelli, F. Dughiero, M. Forzan, I. Lombardi, A. Marconi, S. Wen, and M. Zordan. Directional solidification experiments on g2.5 i-dss furnace - demonstrator of sikelor project. In *Internatiolnal conference on Heating by Electromagnetic Sources*, pages 633–639, 2016. *Cited page 13*

[76] F. Dughiero, M. Forzan, C. Pozza, and A. Tolomio. Experimental results in industrial environment of the i-DSS furnace. In *International Scientific Colloquium Modelling for Electromagnetic Processing*, pages 73–78, Hannover, 2014. *Cited page 13*

[77] R. Hirayama, K. Fujisaki, and T. Yamada. Dual in-mold electromagnetic stirring in continuous casting. *IEEE Transactions on Magnetics*, 40(4):2095–2097, 2004. *Cited page 13*

[78] M. Javurek, M. Barna, P. Gittler, K. Rockenschaub, and M. Lechner. Flow modelling in continuous casting of round bloom strands with electromagnetic stirring. *Steel Res. Int.*, 79(August):617–626, 2008. *Cited page 14*

[79] Y. Miki, S. Ogura, and T. Fujii. Separation of inclusions from molten steel in a tundish by use of rotating electromagnetic field. Technical Report 35, Kawasaki steel technical report, 1996. *Cited page 14*

[80] V. Dubodelov, O. Smirnov, M. Goryuk, V. Pogorsky, Seredenko V., and V. Buryak. Features of functioning of magnetodynamic tundish at continuous

casting of stee. In *8th International Conference on Electromagnetic Processing of Materials*, 2015. *Cited page 14*

[81] M Pal. *Modeling of Induction Stirred Ladles*. PhD thesis, Royal Institute of Technology, 2012. *Cited page 14*

[82] A. Einstein. On the electrodynamics of moving objects. *Annalen de Physik*, 1905. *Cited page 21*

[83] C. Christov. Hidden in plan view: the material invariance of Maxwell-Hertz-Lorentz electrodynamics. *Apeiron*, 13(2):129–161, 2004. *Cited page 21*

[84] J. R. Zapata A. *Magnetic pulse forming processes: computational modelling and experimental validation*. PhD thesis, MINES Paristech, 2016. *2 citations pages 21 and 39*

[85] N. El-Kaddah and T.T. Natarajan. Electromagnetic stirring of steel: Effect of stirrer design on mixing in horizontal electromagnetic stirring of steel slabs. In *Second International Conference on CFD in the Minerals and Process Industries*, pages 339–344, 1999. *Cited page 23*

[86] John F. Schenck. The role of magnetic susceptibility in magnetic resonance imaging: Mri magnetic compatibility of the first and second kinds. *Medical Physics*, 23(6):815–850, 1996. *Cited page 26*

[87] R. P. Feynman, R. B. Leighton, and M. L. Sands. *The Feynman lectures on physics*. Addison-Wesley Pub. Co., 1963. *Cited page 26*

[88] Q. Tang, Z. Wang, P. I. Anderson, P. Jarman, and A. J. Moses. Approximation and prediction of ac magnetization curves for power transformer core analysis. *IEEE Transactions on Magnetics*, 51(5):1–8, May 2015. *2 citations pages 31 and 32*

[89] P. Di Barba, M.E. Mognaschi, D.A. Lowther, and F. Dughiero. A benchmark problems of induction heating analysis. In *HES 16 - Heating by Electromagnetic Sources*, pages 233–240, 2016. *Cited page 32*

[90] J. Jin. *The finite element method in electromagnetics*. Wiley, 2 edition, 2002. *Cited page 36*

[91] J. C. Nedelec. Mixed finite elements in $\mathbb{R}^3$. *Numerische Mathematik*, 35(3):315–341, September 1980. *Cited page 36*

[92] J.P. Webb. Edge elements and what they can do for you. *IEEE transactions on magnetics*, MAG-29(2):1460–1465, March 1993. *Cited page 36*

[93] A. Bossavit. Solving Maxwell equations in a closed cavity, and the question of spurious modes. *IEEE transactions on magnetics*, MAG-26(2):702–705, March 1990. *Cited page 36*

[94] A. Bossavit and A. Mayergoyz. Edge elements for scattering problemss. *IEEE transactions on magnetics*, MAG-25(4):2816–2821, July 1989. *Cited page 36*

[95] J.S. Wang and N. Ida. Eigenvalues analysis in electromagnetic cavities using divergence free finite elements. *IEEE transactions on magnetics*, MAG-27(5):3978–3981, September 1991. *Cited page 36*

[96] G. Mur. Compatibility relations and the finite-element formulation of electromagnetic field problems. *IEEE transactions on magnetics*, 30(5):2972–2975, September 1994. *Cited page 38*

[97] G. Mur and A. T. de Hopp. A finite element method for computing three-dimensional electromagnetic fields in inhomogeneous media. *IEEE transactions on magnetics*, MAG-21(6):2188–2191, November 1985. *Cited page 38*

[98] G. Mur. Edge elements, their advantages and their disadvantages. *IEEE transactions on magnetics*, 30(5):3552–3557, September 1994. *Cited page 38*

[99] P. Monk. An analysis of Nedelec's method for spatial discretization of Maxwell's equations. *Journal of Computational and Applied Mathematics*, 47:101–121, 1993. *Cited page 39*

[100] C.M. Pinciuc, A. Konrad, and J.D. Lavers. Basis functions with divergence constraints for the finite element method. *IEEE transactions on magnetics*, 50(4):7200113, 2014. *Cited page 39*

[101] O. Biro and K Preis. On the use of magnetic vector potential in the finite-element analysis of three-dimensional eddy currents. *IEEE transactions on magnetics*, 25(4):3145–3159, 1989. *Cited page 40*

[102] J. Alves and F. Bay. Modelling and analysis of the electromagnetism in magnetic forming process. *IEEE Transactions on Magnetics*, 52(5):7004011, May 2015. *3 citations pages 42, 49, and 91*

[103] S. J. Salon, L. Ovacik, and J. F. Balley. Finite element calculation of harmonic losses in ac machine windings. *IEEE Transactions on Magnetics*, 29(2):1442–1445, March 1993. *Cited page 43*

[104] V. Hill, O. Farle, and R. Dyczij-Edlinger. A stabilized multilevel vector finite-element solver for time-harmonic electromagnetic waves. *IEEE Transactions on Magnetics*, 39(3):1203–1206, May 2003. *Cited page 43*

[105] R. U. Börner, O. G. Ernst, and K. Spitzer. Fast 3-D simulation of transient electromagnetic fields by model reduction in the frequency domain using Krylov subspace projection. *Geophysical Journal International*, 173:766–780, 2008. *Cited page 43*

[106] J. Chen, Z. Chen, T. Cui, and L.B. Zhang. An adaptive finite element method for the eddy current model with circuit/field couplings. *SIAM Journal on Scientific Computing*, 32(2):1020–1042, 2010. *Cited page 43*

[107] A. Grayver and T. Kolev. Large-scale 3D geoelectromagnetic modeling using parallel adaptive high-order finite element method. *Geophysics*, 80(6):E277–E291, 2015. *Cited page 43*

[108] S. Balay, Abhyankar S., M.F. Adams, J. Brown, P. Brune, K. Buschelman, L. Dalcin, V. Eijkhout, W.D. Gropp, D. Kaushik, M.G. Knepley, L.C. McInnes, K. Rupp, B.F. Smith, S. Zampini, and H. Zhang. PETSc users manual. Technical Report ANL-95/11 - Revision 3.6, Argonne National Laboratory, 2015. *Cited page 43*

[109] R. S. Tuminaro, M. A. Heroux, S. A. Hutchinson, and J. N. Shadid. Aztecoo user guide. Technical Report Version 3.6, Sandia National Laboratories, 2007. *Cited page 43*

[110] D. Day and M. Heroux. Solving complex-valued linear systems via equivalent real formulations. *SIAM Journal on Scientific Computing*, 23(2):480–498, 2006. *2 citations pages 44 and 45*

[111] A. Munankarmy and M. Heroux. A comparison of two equivalent real formulations for complex-valued linear systems part 1: Introduction and method. *American Journal of Undergraduate Research*, 1(3):17–26, 2002. *Cited page 44*

[112] O. Axelsson, M. Neytcheva, and B. Ahmad. A comparison of iterative methods to solve complex valued linear algebraic systems. *Numerical Algorithms*, 66:811–841, 2014. *Cited page 44*

[113] M. Benzi and D. Bertaccini. Block preconditioning of real-valued iterative algorithms for complex linear systems. *IMA Journal of Numerical Analysis*, 28:598–618, January 2008. *Cited page 45*

[114] O. Axelsson and A. Kucherov. Real valued iterative methods for solving complex symmetric linear systems. *Numerical Linear Algebra With Applications*, 7:197–218, 2000. *Cited page 45*

[115] Z. Z. Bai, M. Benzi, and F. Chen. On preconditioned MHSS iteration methods for complex symmetric linear systems. *Numerical Algorithms*, 56:297–317, January 2010. *Cited page 45*

[116] Z. Z. Bai, M. Benzi, and F. Chen. Modified HSS iteration methods for a class of complex symmetric linear systems. *Computing*, 87:93–111, February 2010. *Cited page 45*

[117] L. Marioni, J. R. Alves Z., E. Hachem, and F. Bay. A new approach to solve complex valued systems arising from the solution of Maxwell equations in the frequency domain through real-equivalent formulations. *Numerical Linear Algebra with Applications*, 24(2):e2079, 2017. *Cited page 45*

[118] R. W. Freund. Conjugate gradient-type methods for linear systems with complex symmetric coefficient matrix. *SIAM Journal on Scientific and Statistical Computing*, 13:425–448, 1992. *Cited page 46*

[119] Y. Saad and M. H. Schultz. A comparison of iterative methods to solve complex valued algebric systems. *SIAM Journal on Scientific and Statistical Computing*, 7(3):856–869, July 1986. *Cited page 49*

[120] F. Brezzi. On the existence, uniqueness and approximation of saddle-point problems arising from lagrangian multipliers. *ESAIM: Mathematical Modelling and Numerical Analysis - Modélisation Mathématique et Analyse Numérique*, 8(R2):129–151, 1974. *Cited page 64*

[121] D. N. Arnold, F. Brezzi, and M. Fortin. A stable finite element for the stokes equations. *CALCOLO*, 21(4):337–344, Dec 1984. *Cited page 64*

[122] L. P. Franca and C. Farhat. Bubble functions prompt unusual stabilized finite element methods. *Computer Methods in Applied Mechanics and Engineering*, 123(1):299 – 308, 1995. *Cited page 64*

[123] T.E. Tezduyar, S. Mittal, S.E. Ray, and R. Shih. Incompressible flow computations with stabilized bilinear and linear equal-order-interpolation velocity-pressure elements. *Computer Methods in Applied Mechanics and Engineering*, 95(2):221 – 242, 1992. *Cited page 64*

[124] E. Hachem. *Stabilized finite element method for heat transfer and turbulent flows inside industrial furnaces*. Theses, École Nationale Supérieure des Mines de Paris, September 2009. *Cited page 64*

[125] T. Hughes. Multiscale phenomena: Green's functions, the Dirichlet-to-Neumann formulation, subgrid scale models, bubbles and the origins of stabilized methods. *Computer Methods in Applied Mechanics and Engineering*, 127:387–401, 1995. *Cited page 65*

[126] T. Hughes, G.R. Feijóo, L. Mazzei, and J.B. Quincy. The variational multiscale method - a paradigm for computational mechanics. *Computer Methods in Applied Mechanics and Engineering*, 166:3–24, 1998. *Cited page 65*

[127] E. Hachem, B. Rivaux, T. Kloczko, H. Digonnet, and T. Coupez. Stabilized finite element method for incompressible flows with high Reynolds number. *Journal of computational physics*, 229:8643–8665, 2010. *3 citations pages 65, 66, and 101*

[128] O. Colomés and S. Badia and R. Codina and J. Principe. Assessment of variational multiscale models for the large eddy simulation of turbulent incompressible flows. *Computer Methods in Applied Mechanics and Engineering*, 285(Supplement C):32 – 63, 2015. *2 citations pages 65 and 67*

[129] T. Coupez and E. Hachem. Solution of high-reynolds incompressible flow with stabilized finite element and adaptive anisotropic meshing. *Computer Methods in Applied Mechanics and Engineering*, 267:65 – 85, 2013. *3 citations pages 67, 87, and 101*

[130] S. Osher and J. A. Sethian. Fronts propagating with curvature-dependent speed: Algorithms based on hamilton-jacobi formulations. *Journal of Computational Physics*, 79(1):12 – 49, 1988. *Cited page 68*

[131] Y.C. Chang, T.Y. Hou, B. Merriman, and S. Osher. A level set formulation of eulerian interface capturing methods for incompressible fluid flows. *Journal of Computational Physics*, 124(2):449 – 464, 1996. *Cited page 68*

[132] E. Hachem, R. Valette, and M. Khalloufi. High fidelity anisotropic adaptive fem towards physical couplings occurring in turbulent boiling. In *Numerical Modeling of Liquid-Vapor Interfaces in Fluid Flows*, 2016. *Cited page 68*

[133] E. Hachem, M. Khalloufi, J. Bruchon, R. Valette, and Y. Mesri. Unified adaptive variational multiscale method for two phase compressible–incompressible flows. *Computer Methods in Applied Mechanics and Engineering*, 308(Supplement C):238 – 255, 2016. *Cited page 68*

[134] F. Gibou and R. Fedkiw. A fast hybrid k-means level set algorithm for segmentation. In *4th Annual Hawaii International Conference on Statistics, Mathematics and Related Fields*, pages 281–291, 2005. *Cited page 68*

[135] C. Li, C. Xu, C. Gui, and M. D. Fox. Distance regularized level set evolution and its application to image segmentation. *IEEE Transactions on Image Processing*, 19(12):3243–3254, Dec 2010. *Cited page 68*

[136] L. Vese and T. Chan. A multiphase level-set framework for image segmentation using the Mumford and Shah model. *International Journal of Computer Vision*, 50(3):271–279, 2002. *Cited page 68*

[137] G.-H. Cottet and E. Maitre. A semi-implicit level set method for multiphase flows and fluid–structure interaction problems. *Journal of Computational Physics*, 314:80 – 92, 2016. *Cited page 68*

[138] D. Enright, S. Marschner, and R. Fedkiw. Animation and rendering of complex water surfaces. *ACM Trans. Graph.*, 21(3):736–744, July 2002. *Cited page 68*

[139] Mark Sussman, Peter Smereka, and Stanley Osher. A level set approach for computing solutions to incompressible two-phase flow. *Journal of Computational Physics*, 114(1):146 – 159, 1994. *2 citations pages 68 and 69*

[140] D. Polychronopoulou, N. Bozzolo, D. P. Munoz, J. Bruchon, M. Shakoor, G. Millet, I. F. von Thungen C. Dumont, R. Benard, and M. Bernacki. Introduction to the level-set full eld modeling of laths spheroidization phenomenon in alpha/beta titanium alloys. In *NUMIFORM*, page 02003, 2016. *Cited page 68*

[141] M. Shakoor, B. Scholtes, P.-O.Bouchard, and M. Bernacki. An efficient and parallel level set reinitialization method – application to micromechanics and microstructural evolutions. *Applied Mathematical Modelling*, 39(23):7291 – 7302, 2015. *Cited page 68*

[142] F. Gibou, R. Fedkiw, R. Caflisch, and S. Osher. A level set approach for the numerical simulation of dendritic growth. *Journal of Scientific Computing*, 19(1):183–199, Dec 2003. *Cited page 68*

[143] E. Olsson and G. Kreiss. A conservative level set method for two phase flow. *Journal of Computational Physics*, 210(1):225 – 246, 2005. *2 citations pages 72 and 82*

[144] E. Olsson, G. Kreiss, and S. Zahedi. A conservative level set method for two phase flow ii. *Journal of Computational Physics*, 225(1):785 – 807, 2007. *2 citations pages 72 and 82*

[145] O. Desjardins, V. Moureau, and H. Pitsch. An accurate conservative level set/ghost fluid method for simulating turbulent atomization. *Journal of Computational Physics*, 227(18):8395 – 8416, 2008. *2 citations pages 72 and 83*

[146] D. H. Pino Munoz. *High-performance computing of sintering process at particle scale*. PhD thesis, Ecole Nationale Superieure des Mines, 2012. *Cited page 73*

[147] L. Ville, L. Silva, and T. Coupez. Convected level set method for the numerical simulation of fluid buckling. *International Journal for Numerical Methods in Fluids*, 66(3):324–344, 5 2011. *Cited page 74*

[148] M. Sanchez, O. Fryazinov, P.-A. Fayolle, and A. Pasko. Convolution filtering of continuous signed distance fields for polygonal meshes. *Computer Graphics Forum*, 34(6):277–288, 2015. *2 citations pages 74 and 75*

[149] T. Coupez. Convection of local level set function for moving surfaces and interfaces in forming flow. In *NUMIFORM 07: 9th International Conference on Numerical Methods in Industrial Forming Processes*, volume 908, pages pages 61–66, Porto, Portugal, June 2007. *Cited page 77*

[150] L. Zhao, X. Bai, T. Li, and J. J. R. Williams. Improved conservative level set method. *International Journal for Numerical Methods in Fluids*, 75(8):575–590, 2014. FLD-13-0333.R1. *Cited page 83*

[151] M. Sussman and E. G. Puckett. A coupled level set and volume-of-fluid method for computing 3d and axisymmetric incompressible two-phase flows. *Journal of Computational Physics*, 162(2):301 – 337, 2000. *Cited page 83*

[152] D. Enright, R. Fedkiw, J. Ferziger, and I. Mitchell. A hybrid particle level set method for improved interface capturing. *Journal of Computational Physics*, 183(1):83 – 116, 2002. *Cited page 83*

[153] L. F. S. Betancourt. *Modeling of High Performance SMC Behavior Applications to 3D Compression Molding Simulation*. PhD thesis, MINES Paristech, 2017. *Cited page 84*

[154] J. Baiges, R. Codina, A. Pont, and E. Castillo. An adaptive fixed-mesh ale method for free surface flows. *Computer Methods in Applied Mechanics and Engineering*, 313:159 – 188, 2017. *Cited page 84*

[155] T. Coupez. Metric construction by length distribution tensor and edge based error for anisotropic adaptive meshing. *Journal of computational physics*, 230:2391–2405, 2011. *2 citations pages 86 and 87*

[156] M. Barna, M. Javurek, J. Reiter, J. Watzinger, B. Kaufmann, and M. Kirschen. Numerical Simulations of the Continuous Casting of Steel with Electromagnetic Braking and Stirring. *International Journal of Multiphysics*, 2:231–238, 2010. *Cited page 90*

[157] J Barglik, D Dołęga, and A Smagór. Coupled temperature-electromagnetic–flow fields in electro- magnetic stirrer with rotating magnetic field. *Modelling for material processing*, 8:299–304, 2010. *Cited page 91*

[158] H. Zhang, H. Nagaumi, Y. Zuo, and J. Cui. Coupled modeling of electromagnetic field, fluid flow, heat transfer and solidification during low frequency electromagnetic casting of 7XXX aluminum alloys. Part 1: Development of a mathematical model and comparison with experimental results. *Materials Science and Engineering A*, 448(1-2):189–203, 2007. *Cited page 91*

[159] H. D. Wang, M. Y. Zhu, and H. Q. Yu. Numerical analysis of electromagnetic field and flow field in high casting speed slab continuous casting mold with traveling magnetic field. *Journal of Iron and Steel Research International*, 17(9):25–30, 2010. *Cited page 91*

[160] Y. Haiqi and Z. Miaoyong. Three-dimensional magnetohydrodynamic calculation for coupling multiphase flow in round billet continuous casting mold with electromagnetic stirring. *IEEE Transactions on Magnetics*, 46(1):82–86, 2010. *Cited page 91*

[161] T. T. Natarajan and N. El-Kaddah. Finite element analysis of electromagnetic and fluid flow phenomena in rotary electromagnetic stirring of steel. *Applied Mathematical Modelling*, 28(1):47–61, 2004. *Cited page 91*

[162] G. Haijun, L. Xinzhong, F. Xueyi, Q. Juhong, X. Daming, and G. Jingjie. Numerical simulation of flow and heat transfer of continous cast steel slab under traveling magnetic field, 2013. *2 citations pages 91 and 94*

[163] K. Fujisaki, K. Wajima, and M. Ohki. 3D magnetohydrodynamics analysis method for free surface molten metal. *IEEE Transactions on Magnetics*, 36(4):1325–1328, 2000. *Cited page 91*

[164] J. Vencels, A. Jakovics, V. Geza, and M. Scepanskis. EOF library: open-source Elmer and OpenFOAM coupler for simulation of MHD with free surface. In *XVIII International UIE Congress: Electrotechnologies for Material Processing*, pages pages 312–318, Hannover, Germany, June 2017. *2 citations pages 91 and 96*

[165] R. Moreau. *Magnetohydrodynamics*. Springer Science+Business Media Dordrecht, 1990. *Cited page 94*

[166] J.D. Lavers. State of the Art of Numerical Modelling for Electromagnetic Processing of Metallic Material. In *International Scientific Colloquium Modelling for Electromagnetic Processing*, volume 1, pages 5–10, Hannover, 2008. *Cited page 94*

[167] M. Barna, M. Javurek, J. Reiter, and M. Lechner. Numerical simulations of mould electromagnetic stirring for round bloom strands. In *Bhm*, pages 518–522, 2009. *Cited page 95*

[168] F. Felten, Y. Fautrelle, Y. Du Terrail, and O. Metais. Numerical modelling of electromagnetically-driven turbulent flows using les methods. *Applied Mathematical Modelling*, 28(1):15 – 27, 2004. *2 citations pages 95 and 96*

[169] J.L. Lumley H. Tennekes. *A first course in Turbulence*. The MIT press, 1972. *Cited page 95*

[170] L. Marioni, F. Bay, and E. Hachem. Numerical stability analysis and flow simulation of lid-driven cavity subjected to high magnetic field. *Physics of Fluids*, 28(5):057102, 2016. *Cited page 100*

[171] L. Marioni, F. Bay, and E. Hachem. Lid-driven cavity highly turbulent flow subjected to high magentic field: Determination of critical time-step for explicit MHD schemes. In *10th PAMIR International Conference - Fundamental and Applied MHD*, 2016. *Cited page 100*

[172] U. Ghia, K. N. Ghia, and C. Shin. High-resolution for incompressible flow using the navier-stokes equations and a multigrid method. *Journal of computational physics*, 48(3):387–411, 1982. *Cited page 101*

[173] M. Sahin and N.G. Owens. A novel fully-implicit finite volume method applied to the lid-driven cavity problem. part i: high reynolds number flow calculations. *International Journal for Numerical Methods in Fluids*, 42:57–77, 2003. *Cited page 101*

[174] J. Zhang. Numerical simulation of 2d square driven cavity using fourth-order compact finite difference schemes. *Computers & Mathematics with Applications*, 45(1):43–52, 2003. *Cited page 101*

[175] O. Botella and R. Peyret. Benchmark spectral results on the lid-driven cavity flow. *Computers & Fluids*, 27(4):421–433, 1998. *Cited page 101*

[176] C.H. Bruneau and M. Saad. The behaviour of high reynolds flows in a driven cavity. *ColdFusion Developer's Journal (CFDJ)*, 15(3), 2006. *Cited page 101*

[177] V. Gravemeier, W. A. Wall, and E. Ramm. A three-level finite element method for the instationary incompressible navier-stokes equations. *Computer Methods in Applied Mechanics and Engineering*, 193(15-16):1323–1366, 2004. *Cited page 101*

[178] A. Masud and R. A. Khurram. A multiscale finite element method for the incompressible navier-stokes equations. *Computer Methods in Applied Mechanics and Engineering*, 195:1750–1777, 2006. *Cited page 101*

[179] Y. F. Peng, Y. H. Shiau, and R. R. Hwang. Transition in a 2-d lid-driven cavity flow. *Computers & Fluids*, 32:337–352, 2003. *Cited page 101*

[180] Y. Yu, B.W. Li, and A. Thess. The effect of a uniform magnetic field on vortex breakdown in a cylinder with rotating upper lid. *Computers & Fluids*, 88:510–523, 2013. *Cited page 101*

[181] E.E. Tzirtzilakis and M.A. Xenos. Biomagnetic fluid flow in a driven cavity. *Meccanica*, 48:187–200, 2013. *Cited page 101*

[182] G.R. Kefayati. Lattice boltzmann simulation of natural convection in nanofluid-filled 2d long enclosures at presence of magnetic field. *Theoretical and Computational Fluid Dynamics*, 27(6):865–883, November 2013. *Cited page 101*

[183] V. Shatrov, G. Mutschke, and G. Gerbeth. Three-dimensional linear stability analysis of lid-driven magnetohydrodynamic cavity flow. *Physics of Fluids*, 15(8):2141–2151, 2003. *2 citations pages 101 and 103*

[184] S. Sivasankaran, A. Malleswaran, Jinho Lee, and Pon Sundar. Hydro-magnetic combined convection in a lid-driven cavity with sinusoidal boundary conditions on both sidewalls. *International Journal of Heat and Mass Transfer*, 54:512–525, 2011. *Cited page 101*

[185] A. Yu. Gelfgat and P. Z. Bar-Yoseph. The effect of an external magnetic field on oscillatory instability of convective flows in a rectangular cavity. *Physics of Fluids*, 13(8):2269–2278, August 2001. *Cited page 101*

[186] Hakan F. Oztop, Khaled Al-Salem, and Ioan Pop. Mhd mixed convection in a lid-driven cavity with corner heater. *International Journal of Heat and Mass Transfer*, 54(15–16):3494–3504, July 2011. *Cited page 101*

[187] J. P. Garandet, T. Alboissiere, and R. Moreau. Buoyancy driven convection in a rectangular enclosure with a transverse magnetic field. *International Journal of Heat and Mass Transfer*, 35(4):741–748, 1992. *Cited page 101*

[188] H. Ozoe and K. Okada. The effect of the direction of the external magnetic field on the three-dimensional natural convection in a cubical enclosure. *International Journal of Heat and Mass Transfer*, 32:1075–1084, 1989. *Cited page 101*

[189] P.X. Yu, J.X. Qiu, Q. Qin, and Z. F. Tian. Numerical investigation of natural convection in a rectangular cavity under different directions of uniform magnetic field. *International Journal of Heat and Mass Transfer*, 67:1131–1144, 2013. *Cited page 101*

[190] L. Davoust, M.D. Cowley, R. Moreau, and R. Bolcato. Buoyancy-driven convection with a uniform magnetic field. part 2. experimental investiga- tion. *Journal of Fluid Mechanics*, 400(59), 1999. *Cited page 101*

[191] L. Marioni, M. Khalloufi, F. Bay, and E. Hachem. Two-fluid flow under the constraint of external magentic field: revisiting the dam-break benchmark. *International Journal of Numerical Methods for Heat and Fluid Flow*, 27(11), 2017. *Cited page 116*

[192] N. B. Salah, A. Soulaimani, and W. G. Habashi. A finite element method for magnetohydrodynamic. *Computer Methods in Applied Mechanics and Engineering*, 190(43):5867–5892, 2001. *Cited page 118*

[193] J.C. Martin and W.J. Moyce. An experimental study of the collapse of liquid columns on a rigid horizontal plane. *Philosophical Transactions of the Royal Society of London. Series A, Mathematical and Physical Sciences*, 244:312–324, 1952. *2 citations pages 119 and 121*

[194] S. Koshizuka and Y. Oka. Moving-particle semi-implicit method for fragmentation of incompressible fluid. *Nuclear Science and Engineering*, 123:421–434, 1996. *Cited page 119*

[195] J. Wang, Z. Ruizhi, and D. Wan. Numerical simulation of 3d dam-break flow by fem-level set method. In *Twenty-second International Offshore and Polar Engineering Conference*, pages 1080–1087, June 2012. *Cited page 119*

[196] A. Balabel. Numerical simulation of turbulent dam-break flow using the level set method. *International Journal of Modern Physics and Applications*, 1(3):112–117, 2015. *Cited page 119*

[197] K. Abdolmaleki, K. P. Thiagarajan, and M. T. Morris-Thomas. Simulation of The Dam Break Problem and Impact Flows Using a Navier-Stokes Solver. In *15th Australasian Fluid Mechanics Conference*. The University of Sydney, December 2004. *Cited page 119*

[198] E. F. Lins, R. N. Elias, F. A. Rochinha, and A. Coutinho. Residual-based variational multiscale simulation of free surface flows. *Computational Mechanics*, 46:545–557, 2010. *Cited page 119*

[199] A. Shakibaeinia and Y.C. Jin. A mesh-free particle model for simulation of mobile-bed dam break. *Advances in Water Resources*, 34:794–807, 2011. *Cited page 119*

[200] C. B. Liao, M. S. Wu, and S.J. Liang. Numerical simulation of a dam break for an actual river terrain environment. *Hydrological processes*, 21:447–460, 2007. *Cited page 119*

[201] T.J. Chang, H.M. Kao, K.H. Chang, and M.H. Hsu. Numerical simulation of shallow-water dam break flows in open channels using smoothed particle hydrodynamics. *Journal of Hydrology*, 408:78–90, 2011. *Cited page 119*

[202] A. Murrone and H. Guillard. A five equation reduced model for compressible two phase flow problems. *Journal of Computational Physics*, 202:664–698, 2005. *3 citations pages 119, 121, and 122*

[203] D. M. Greaves. Simulation of viscous water column collapse using adapting hierarchical grids. *International Journal of Numerical Methods in Fluids*, 50(6):693–711, 2010. *Cited page 119*

[204] Y. Zhang, Z. Zeng, and J. Chen. The improved space–time conservation element and solution element scheme for two dimensional dam break flow simulation. *International Journal for Numerical Methods in Fluids*, 68(5):605–624, 2012. *Cited page 119*

[205] P. A. Caron, M. A. Cruchaga, and A. Larreteguy. Sensitivity analysis of finite volume simulations of a breaking dam problem. *International Journal of Numerical Methods for Heat & Fluid Flow*, 25(7):1718–1745, 2015. *Cited page 119*

[206] T. Fondelli, A. Andreini, and B. Facchini. Numerical simulation of dam-break problem using an adaptive meshing approach. *Energy Procedia*, 82:309–315, 2015. *Cited page 119*

[207] M. L. Garcia. Adaptive mesh refinement in the dam-break problems. In *World Congress on Computational Mechanics*, May 2014. *Cited page 119*

[208] E. Marchandise and J.F. Remacle. A stabilized finite element method using a discontinuous level set approach for solving two phase incompressible flows. *Journal of Computational Physics*, 219:780–800, 2006. *Cited page 119*

[209] A. G. B. Mowat, W. J. van den Bergh, A. G. Malan, and D. Wilke. An AMG strategy for efficient solution of free-surface flows. *International Journal of Numerical Methods for Heat & Fluid Flow*, 26(3/4):1172–1186, 2016. *Cited page 119*

[210] E. Jahanbakhsh, R. Panahi, and M. S. Seif. Numerical simulation of three-dimensional interfacial flows. *International Journal of Numerical Methods for Heat & Fluid Flow*, 17(4):384–404, 2007. *Cited page 119*

[211] R. N. Elias and A. Coutinho. Stabilized edge-based finite element simulation of free-surface flows. *International Journal of Numerical Methods in Fluids*, 54:965–993, 2007. *2 citations pages 119 and 121*

[212] L. Marioni, E. Hachem, and F. Bay. Numerical simulation of electromagnetic stirring. In *XVIII UIE-Congress - Electrotechnologies for material forming*, 2017. *Cited page 129*

[213] L. Marioni, E. Hachem, and F. Bay. Numerical coupling strategy for the simulation of electromagnetic stirring . *Magnetohydrodynamics*, 53(3):547–557, 2017. *Cited page 129*

[214] D. Musaeva, V. K. Ilyin, V. Geža, and E. Baake. Experimental investigation of low-frequency pulsed Lorentz force influence on the motion of Galinstan melt. *St. Petersburg Polytechnical University Journal: Physics and Mathematics*, 2(3):193–200, 2016. *4 citations pages 131, 132, 134, and 135*

[215] L. Marioni, J. Alves, F. Bay, and E. Hachem. Effect of M-EMS on in-mould transient flow during continuous casting. *International Journal of Applied Electromagnetics and Mechanics*, 2016. *Cited page 142*

[216] L. Marioni, J. Alves, F. Bay, and E. Hachem. Effect of M-EMS on in-mould transient flow during continuous casting. In *International Conference on Heating by Electromagnetic sources*, pages 3–10, 2016. *Cited page 142*

[217] Q. Yuan, B. Zhao, S. P. Vanka, and B. G. Thomas. Study of computational issues in simulation of transient flow in continuous casting. *Steel Research International, Special Issue: Simulation of Fluid Flow in Metallurgy*, 76(1):33–43, 2005. *Cited page 143*

Résumé

Beaucoup de procédés utilisés dans l'industrie sidérurgique (coulée de lingots, coulée continue, …) peuvent générer des défauts : macro-ségrégation, mauvaises propriétés de la microstructure, défauts surfaciques. Ces problèmes peuvent être résolus par un contrôle de la température et de l'écoulement d'acier liquide. Le brassage électromagnétique (EMS) est une technique largement utilisée pour contrôler l'écoulement d'acier liquide par l'imposition d'un champ électromagnétique. Cette technique est complexe car elle couple plusieurs types de problèmes physiques: écoulement multiphasique, solidification, transfert de chaleur et induction électromagnétique à basse fréquence. En outre, l'approche expérimentale est difficile de par la dimension, l'environnement et le coût des procédés considérés. Pour ces raisons, des simulations numériques efficaces sont nécessaires pour comprendre les applications EMS et améliorer les procédés évoqués. L'objectif de cette thèse est de développer une méthodologie numérique robuste, efficace et précise pour la simulation multi-physique de l'EMS, en particulier pour le brassage dans le moule dans le cadre de la coulée continue d'acier. Cette méthodologie a été mise en œuvre dans le code commercial THERCAST® pour être utilisée dans le cadre d'applications industrielles.

Mots Clés

Méthode des éléments finis, méthode multiéchelle variationnelle, level-set, formulation équivalente réelle pour systèmes linéaires complexes, adaptation anisotrope de maillage, modélisation multiphysique, brassage électromagnétique, coulée continue, magnétohydrodynamique numérique.

Abstract

Many of the processes used in the steelmaking industry (e.g. ingot casting, continuous casting, …) can lead to defects: macro-segregation, poor microstructure properties, surface defects. These issues can be solved by controlling the temperature and the flow of molten steel. Electromagnetic stirring (EMS) is a widely used technique to steer the flow of liquid steel by the superimposition of an electro-magnetic field. This application is complex because it couples several physical problems: multi-phase flow, solidification, heat transfer and low frequency electro-magnetic induction. In addition, experimental work is difficult because of the size, environment and cost of the considered processes. For these reasons, efficient and effective numerical simulations are needed to understand EMS applications and improve the aforementioned processes.
The objective of this thesis is to develop a robust, efficient and accurate numerical procedure for the multi-physics simulation of EMS, especially for in-mold stirring in the framework of continuous casting of steel. This procedure has been implemented in the commercial code THERCAST® in order to be used for industrial applications.

Keywords

Finite element method, variational multiscale method, level-set, real equivalent formulation for complex linear systems, anisotropic mesh adaptation, multi-physics modelling, electromagnetic stirring, continuous casting, numerical magneto-hydrodynamics.